Theoretical investigations of orbital and spin-orbital effects in functionalized graphene

DISSERTATION ZUR ERLANGUNG DES DOKTORGRADES DER NATURWISSENSCHAFTEN (DR. RER. NAT.) DER FAKULTÄT FÜR PHYSIK
DER UNIVERSITÄT REGENSBURG

vorgelegt von

Susanne Irmer aus
Hirschau

im Jahr 2018

Promotionsgesuch eingereicht am: 17.01.2018
Die Arbeit wurde angeleitet von: Prof. Dr. Jaroslav Fabian

Prüfungsausschuss:
Vorsitzender: Prof. Dr. Dieter Weiss
1. Gutachter: Prof. Dr. Jaroslav Fabian
2. Gutachter: Prof. Dr. John Schliemann
Weiterer Prüfer: Prof. Dr. Vladimir Braun

Termin Promotionskolloquium: 13.06.2018

Contents

List of Figures

List of Tables

1 | Introduction

In the year 2004, the first exfoliation and characterization of the carbon allotrope graphene [1] heralded a new era of research in the realm of two-dimensional crystal materials. Graphene is a semimetal with its electrons obeying a linear dispersion relation at low energies. As in this energy regime the description of graphene bears resemblance with an effective Dirac equation for massless fermions, this material suggested the possibility to study relativistic effects such as Klein tunneling or zitterbewegung in condensed matter [2].

Graphene offers remarkable qualities regarding its mechanical, optical, thermal and electric properties [3] so that applications of this astonishing material were explored for such diverse topics as flexible electronics [4], chemical sensors [5, 6], or nanopore templates for DNA sequencing [7]. Besides high electron mobilities at room temperature [3], graphene shows a strong ambipolar electric field effect [1] allowing to tune the charge carrier density in graphene by a gate voltage. Furthermore, the sublattice degree of freedom in graphene gives rise to fascinating pseudospin physics and an unconventional integer quantum Hall effect [8, 9].

Bilayer (BL) graphene, two sheets of graphene stacked on top of each other, shares many of the qualities of its single layer (SL) counterpart [10]. However, as BL graphene's low-energy physics is dictated by a quadratic dispersion relation, also important differences between the BL and SL cases appear, for example, in the form of a third kind of quantum Hall effect [11, 12]. Moreover, the two graphene layers in the BL structure can be addressed separately and a tunable band gap can be introduced by doping or gating [10, 13, 14]. Recently, experimental indications were found that twisted BL graphene exhibits superconductivity [15]. This is a clear difference to SL graphene, where the introduction of superconductivity in the material relies on proximity to superconductors [16–19] and intercalation [20].

Early on, also the research field of spintronics evinced large interest in graphene (SL and BL). This interest was mainly motivated by the negligible hyperfine interaction in graphene and its small spin-orbit coupling (SOC) on the order of 10 μeV [21] due to carbon's small atomic number[1]. Long spin relaxation lengths on the scale of μm were found at room temperature [23–28] and the successful injection of spins to

[1] Carbon has the atomic number $Z = 6$. The SOC energy of an electron close to the atomic core can be estimated to scale like SOC$\propto Z^4$ [22].

graphene and its detection were early demonstrated [23, 24, 29, 30], accompanied by large spin signals in the nonlocal resistance of the spin valve experiments [31]. On the other hand, the hope for long spin relaxation times, based on graphene's small SOC, was not fulfilled. The experimental observations disagree in general with the theoretical predictions by about three orders of magnitude [31–33]. Not only because of this discrepancy but also to realize graphene spintronics devices on the wafer scale, efforts were taken to improve the quality of the graphene samples in order to study spin injection and transport in high-mobility and large-area graphene samples [31].

Spintronics aims to utilize not only the electronic properties of a material but also the spin degree of freedom for fast and efficient memory storage and quantum computing [31]. Therefore, apart the injection and detection of spins, graphene based spintronics devices need to allow for an efficient manipulation of the electron spin.

Both proximitized graphene and graphene functionalized with adsorbates offer ways to manipulate spin and, furthermore, to tailor existing or introduce new feasible properties to graphene, such as superconductivity (see above) and magnetism. For example, exchange interaction can be induced in the nonmagnetic graphene by placing it on a ferromagnetic insulator [34], or, separated by a tunnel barrier, on a ferromagnetic metal [35]. If also strong SOC is induced, transport magnetoanisotropies [36] are predicted to occur.

Large attention was recently drawn to graphene substrates based on transition metal dichalcogenides (TMDC). These substrates were shown to induce large SOC in graphene giving rise to the spin Hall effect[2] observable at room temperature [38–41]. This aspect opens the way for spin field effect transistors [42] involving graphene. Also charge-to-spin conversion, relying on the strong Rashba coupling in the TMDC material, was demonstrated experimentally [43] and the occurrence of topological effects in graphene are predicted [44]. The rise of spin-valley locking in graphene on a TMDC allows moreover for optical spin injection into graphene [45–47]. Recently, giant spin lifetime anisotropy was predicted and demonstrated [48–50]. The possibility to access and control the relaxation times for different spin orientations proposes graphene-TMDC systems for new spintronics logic devices.

Graphene can be further functionalized locally by adsorbates. Adatoms such as hydrogen [51, 52] and copper enhance graphene's small intrinsic SOC by factors of 100 (hydrogen) to 1000 (copper) and large spin Hall angles were observed in Refs. [53, 54]. Neutral adatoms with large SOC, such as indium, were predicted to stabilize the quantum spin Hall state in graphene [55]. However, in both the case of the analysis of the spin Hall effect as the experimental verification of the quantum spin Hall state issues remain [56–61].

In this thesis, we concentrate on the theoretical view on both orbital and spin-

[2]The interested reader can find a review on the spin Hall effect, for example, in Ref. [37].

orbital effects in functionalized graphene, with an emphasis on SOC, the role of specific adsorbates for the latter, resonant scattering off adsorbates, and, finally, a new spin relaxation mechanism for bilayer graphene.

In Ch. 2, we first consider pristine graphene and graphene-like systems which exhibit the honeycomb structure. In particular, we take into account two-dimensional lattices described by the point group symmetries D_{6h}, D_{3d}, D_{3h}, C_{6v}, and C_{3v}, and derive effective SOC Hamiltonians by applying simple symmetry arguments. With this, the ab- or presence of different SOC couplings, such as the well-known intrinsic one, the Rashba-like coupling, and the PIA term [52], is motivated by intuitive arguments. The second part of this chapter concentrates on SOC in graphene in the presence of the local point group symmetries C_{6v}, C_{3v}, and C_{2v}. These modifications to the local symmetry in graphene are introduced by single adsorbates on the hexagonal lattice in the hollow, the bridge, and the top position, respectively. Considering the given local changes in the symmetry, we identify and describe the emerging local SOC hoppings in the vicinity of the impurity.

In the following chapter, Ch. 3, we use the insights of the previous chapter and analyze three specific adsorbates on graphene, which are the methyl group, fluorine, and copper. These adsorbates settle down in the top (methyl and fluorine), as well the top and bridge position (copper) on graphene. In order to extract, on the one hand, the local SOC strength and, on the other hand, to identify the microscopic origin of it, we combine tight-binding (TB) models and density functional theory (DFT) calculations.

Chapter 4 is devoted to the orbital impact of hollow, top, and bridge adsorbates with s or p orbital character on scattering resonances in graphene. We choose as a theoretical tool for the investigation the T-matrix approach and complement it with TB calculations of large supercells. This topic has already received large attention throughout the past years due to the prediction of zero-energy states arising, for example, from vacancies. As the density of states (DOS) of pristine graphene vanishes at the charge neutrality point, a strong impact on the orbital quantities such as the conductivity is expected. As we will see in Ch. 5, also the spin relaxation in graphene is largely influenced by adsorbates representing resonant scatterers. In Ch. 4 we concentrate on the orbital aspects of single adsorbates in the three different adsorption positions and the formation of resonance levels. We furthermore compare the case of a general adsorbate to the models of strong midgap scatterers and vacancies and outline the differences between them.

Spin relaxation in graphene and a possible mechanism to explain the observed difference in magnitude between theory and experiment are the topic of Ch. 5. We first explain a new spin relaxation mechanism which relies on resonant scattering off magnetic moments in SL [62] and BL graphene. These local magnetic moments are likely introduced in small concentrations in experimental graphene samples due to vacancies or contaminating adsorbates such as hydrogen or methyl. We concentrate in particular on BL graphene and find that an hydrogen amount of about

1 ppm is sufficient to recover the experimental spin relaxation data of Refs. [26, 27]. The distinct dependence of the spin relaxation rate on the charge carrier density observed in SL and BL graphene samples can be explained by the presence of electron-hole puddles. In the second part, the focus lies on fluorinated SL and BL graphene as fabricated and measured in the group of Jun Zhu at Penn State University. By applying our spin relaxation model, which is supported by DFT calculations of fluorine, we aim to resolve the theoretical debate on whether fluorine induces local magnetic moments in graphene or not. We report here on the current status of this ongoing project and present the discrepancies found so far between the experimental observations and our model predictions.

The results of this thesis are summarized in Ch. 6.

2 Spin-orbit coupling in graphene systems from symmetry arguments

This chapter is based on the paper "Model spin-orbit coupling Hamiltonians for graphene systems", PRB 95, 165415 (2017), by Denis Kochan, Susanne Irmer, and Jaroslav Fabian.

2.1 Spin-orbit coupling in graphene

The first theoretical description of the electronic band structure of graphene goes back to the work of Philip R. Wallace in 1947 [63]. Neglecting the coupling between graphite's single layers, he essentially derived a TB model for graphene. Furthermore, he showed that the conduction and valence band touch at the six corners of the Brillouin zone, the $\boldsymbol{K}$ points, which makes graphene a semimetal. In the fifties and the following years, the attention was drawn to the effect of SOC in graphene. Slonczewski [64], McClure and Yafet [65], and Dresselhaus and Dresselhaus [66] argumented on a group theoretical basis that the SOC intrinsic to graphene introduces a gap at the corners of the Brillouin zone. However, it took about fifty years to obtain realistic estimates for this spin-orbit gap. Intense studies on the SOC of graphene had been resumed after graphene's exfoliation in 2004 [1]. Kane and Mele [67] revived the studies in 2005 by estimating the spin-orbit gap Δ_{so} to be about $200\,\mu$eV. This was a promising prediction since it inferred that the quantum spin Hall state should be observable in graphene at low temperatures of a few Kelvins.

In the subsequent years, it was shown by several groups that the value of Δ_{so} had been significantly overestimated in Ref. [67] by a factor of 10-100. Specifically, the contribution of the mixing of σ and π states to the SOC is very weak and of the order of $1\,\mu$eV [21, 68–70]. The low energy states of graphene, i.e., the occupied states forming the π bands around the $\boldsymbol{K}$ points, are mainly built from the $2p_z$ orbitals of the carbon atoms. These p_z orbitals, having zero magnetic quantum number, have to couple to states with nonzero magnetic quantum number in order to induce a finite SOC gap at $\boldsymbol{K}$. Possible candidates are the p_x and p_y orbitals of the σ band, or orbitals with even higher magnetic quantum number such as the d orbitals.

In flat graphene, the p_z orbitals are orthogonal to the p_x and p_y orbitals. However, the intra-atomic SOC allows for a spin-flipping hopping of electrons between the p_z and the p_x or p_y orbital on the same carbon atom. It can be shown by group theoretical arguments (see for example Sec. 2.4.1) that the intrinsic SOC of graphene is described by an overall spin-conserving hopping process, which couples next-nearest neighbor carbon atoms. Therefore, the spin-orbit gap will depend in leading order on the square of the spin-flip hopping strength between the p levels [21, 68–71]. Although the spin-orbit splitting of the $2p$ states (entering the σ band) of an isolated carbon atom is about $\Delta_p \approx 10\,\mathrm{meV}$ [21, 67], the spin-orbit gap at the $\boldsymbol{K}$ points resulting from this σ-π mixing process[1] is in total only of the order of $1\,\mu\mathrm{eV}$ [21, 71].

The importance of the d orbitals for the SOC in graphene was already pointed out by Slonczewski [64] and McClure and Yafet [65]. Indeed, the states around the Fermi level show a small contribution of the unoccupied $3d_{xz}$ and $3d_{yz}$ levels of carbon [21]. This allows for a direct overlap between the p_z and d_{xz} or d_{yz} states on neighboring carbon atoms in graphene. The atomic SOC between d_{xz} and d_{yz} is of spin-conserving nature and, therefore, contributes in the first order to the intrinsic SOC of graphene. Although the atomic SOC hopping strength between the d orbitals is smaller than the one between the p orbitals, the small but direct overlap of the p_z and d states on the neighboring carbon atoms is important and the d levels cause about 96% of the spin-orbit gap observed in the DFT calculations of Gmitra *et al.* [21]. The gap opened at the $\boldsymbol{K}$ points was found in this work to be about $24\,\mu\mathrm{eV}$. In an earlier DFT work, Boettger and Trickey [72], who employed a different approximation for the treatment of the SOC, found a gap of about $50\,\mu\mathrm{eV}$. In the rest of this thesis, we will consider the spin-orbit gap of $24\,\mu\mathrm{eV}$ as the reference value for the intrinsic SOC gap in graphene.

Placing graphene in an external electric field or on a substrate, a so-called Rashba SOC emerges in the graphene system. This coupling is of extrinsic nature and, thus, can be tuned by modifying the external conditions, for example by changing the electric field strength. The Rashba SOC is described as a spin-flipping hopping between nearest carbon neighbors and causes a spin splitting of the otherwise twofold degenerate bands of graphene. The microscopic origin of the Rashba coupling is found in the σ-π mixing in combination with the atomic Stark effect [21, 68, 69, 71] which couples the s orbital with the p_z orbital within the same carbon atom. The d orbitals are of less importance for the magnitude of the Rashba coupling [21, 71]. Gmitra *et al.* [21] found in their DFT study that the Rashba strength grows linearly with the electric field strength, yielding the value of $5\,\mu\mathrm{eV}$ for typical electric field strengths of $1\,\mathrm{V/nm}$. Previously, Kane and Mele [67] estimated the Rashba

[1] Explicitly, Konschuh *et al.* [71] find that the σ-π mixing contribution to the spin-orbit gap is $4\,(\Delta_p/3)^2\,(\varepsilon_p - \varepsilon_s)/(9V_{sp\sigma}^2)$. From a DFT analysis, they obtain for the difference of the on-site energies of the s and p orbitals $|\varepsilon_p - \varepsilon_s| \approx 10\,\mathrm{eV}$ and for the overlap parameter $V_{sp\sigma} \approx 6\,\mathrm{eV}$. This leads to the spin-orbit gap magnitude of $1\,\mu\mathrm{eV}$ considering only σ-π mixing.

coupling to be an order of magnitude smaller, while other works [68, 69] predicted it to be one order of magnitude larger compared to the DFT result of Gmitra *et al.* [21].

Modifications to graphene's crystal structure directly affect the SOC, both in strength and in the underlying origin or mechanism. Proximity effects from different substrate materials [45, 73–76], for example, can transfer strong SOC to the graphene band structure. Furthermore, curvature effects [21, 68] are well-known from the SOC studies of carbon nanotubes and are predicted to enhance the effect of σ-π mixing by an order of magnitude [68] in undulating graphene [77–79]. Locally, adsorbates binding to graphene [51] can also lead to a notable enhancement of the SOC of about a factor of 10 to 100 through sp^3 distortion in the σ network of graphene [51]. As another mechanism, depending on the adsorbate, also the intra-atomic SOC of the impurity can locally influence the SOC strength, see for example Ch. 3.

In this chapter, we concentrate on the SOC in graphene systems, i.e., systems with a hexagonal honeycomb structure under specific global and local structural modifications. The structural modifications reduce the point group symmetry of the system and can, therefore, give rise to new SOC mechanisms. Explicitly, we study in the first part of this chapter the point groups D_{6h}, D_{3d}, D_{3h}, C_{6v}, and C_{3v}. In the second half, we focus on local adsorbates binding in the hollow, top, and bridge positions and the allowed SOC hoppings in the vicinity of the impurity. Examples of adatoms together with realistic estimates of the local SOC strength will be treated in Ch. 3. We close the chapter with a short summary and a comparison to the approach and results of three other works [55, 80, 81] on the impact of adsorbates on graphene's SOC.

2.2 Tight-binding model for graphene and effective Hamiltonians

Graphene and the graphene systems, which we will consider in the following sections, have a hexagonal lattice structure with a two-atomic basis. Equivalently, the lattice structure can be described by two interpenetrating hexagonal sublattices (each with a one-atomic basis) labeled by A and B, which form the well-known honeycomb lattice. Figure 2.1(a) shows our choice of the unit cell together with three Bravais lattice vectors

$$\boldsymbol{R}_\alpha = a_\mathrm{L}\big(\cos\tfrac{2\pi(\alpha-1)}{3}, \sin\tfrac{2\pi(\alpha-1)}{3}\big)\,,\ \alpha = 1,2,3\,, \tag{2.1}$$

where a_L is the lattice constant. In graphene we have $a_\mathrm{L} = 2.46\,\text{Å}$. Selecting for the two primitive translation vectors $\tilde{\boldsymbol{R}}_1 = \boldsymbol{R}_1$ and $\tilde{\boldsymbol{R}}_2 = -\boldsymbol{R}_3$, we obtain the basis

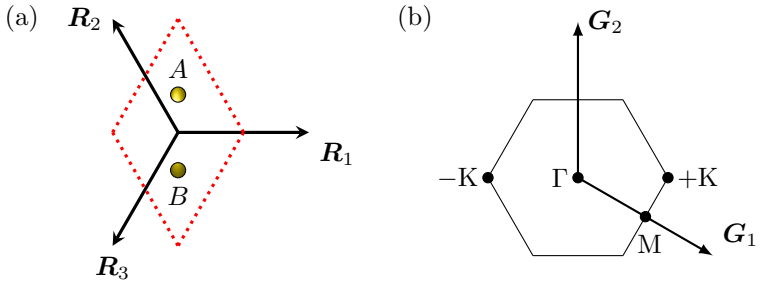

Figure 2.1: (a) Unit cell of the hexagonal graphene lattice with the two-atomic basis A and B and the Bravais lattice vectors $\boldsymbol{R}_\alpha$ ($\alpha = 1, 2, 3$). (b) Hexagonal Brillouin zone of graphene with the reciprocal lattice vectors $\boldsymbol{G}_{1/2}$ and the high symmetry points $\boldsymbol{\Gamma}$, $\boldsymbol{M}$, and $\tau\boldsymbol{K}$ ($\tau = \pm$).

vectors of the reciprocal lattice,

$$\boldsymbol{G}_\alpha = \frac{4\pi}{\sqrt{3}a_\mathrm{L}}\left(\cos\tfrac{\pi(4\alpha-5)}{6}, \sin\tfrac{\pi(4\alpha-5)}{6}\right), \ \alpha = 1, 2\,, \tag{2.2}$$

which obey the orthogonality relation $\boldsymbol{G}_\alpha.\tilde{\boldsymbol{R}}_\beta = 2\pi\delta_{\alpha,\beta}$. The corresponding maximally symmetric unit cell in reciprocal space, the first Brillouin zone, is shown Fig. 2.1(b). The first Brillouin zone contains the high symmetry points $\boldsymbol{\Gamma}$, $\boldsymbol{M}$, and $\tau\boldsymbol{K}$, which are invariant under specific subgroups of the full point group describing the direct lattice. The points $\boldsymbol{\Gamma}$ and $\boldsymbol{M}$ are the so-called time reversal symmetric points, as their time reversal counterparts differ only by a reciprocal lattice vector[2]. The points $\tau\boldsymbol{K}$ ($\tau = \pm$) are defined as the corners of the Brillouin zone and result from the two sublattices A and B. In graphene, they are also known as the Dirac points or Dirac valleys. The term "Dirac" is borrowed from the famous relativistic Dirac equation: Around the two $\tau\boldsymbol{K}$ points, graphene's dispersion is linear and can be described by a relation that looks similar[3] to the Dirac equation in the limit of zero mass.

The low-energy physics of graphene is well-described within a TB description based on π orbitals. The TB method, which is closely related to the LCAO method from chemistry, describes single-electron states which are localized at the atomic sites in the crystal lattice so that their wave functions reflect the atomic orbital of the ion. Leaving SOC aside for this moment, the Hamiltonian describing the orbital motion of an electron in the crystal lattice is given by

$$\hat{H}_\mathrm{orb} = -\frac{\hbar^2}{2m}\boldsymbol{\nabla}^2 + V_0(\boldsymbol{r}) + \sum_{i\neq 0} v_i(\boldsymbol{r})\,. \tag{2.3}$$

[2]The time reversal symmetry is introduced in Sec. 2.3.3 and its influence on the spectrum is shortly commented in Sec. 2.4.1

[3]With this analogy one has to keep in mind that the itinerant electrons in graphene are not relativistic. Their Fermi velocity is about 10^6 m/s.

The second and third term in the Hamiltonian build the crystal potential which is formed of the potential of the ionic site hosting the electron, V_0, and the contribution of the remaining ionic sites and electrons, $\sum_{i\neq 0} v_i(\boldsymbol{r})$. We choose the basis to be composed of single (real-valued) π-orbital states $|X_n\,\sigma\rangle$ with spin σ per lattice site n and take the matrix elements of $\hat{H}_{\mathrm{orb}}$ with all possible combinations of $|X_n\,\sigma\rangle$. Neglecting the overlap of atomic orbitals on different lattice sites, $\langle X_m\,\sigma|X_n\,\sigma'\rangle \approx \delta_{m,n}\delta_{\sigma,\sigma'}$, two kinds of terms appear: the on-site energy on lattice sites n, represented by the matrix element $\langle X_n\,\sigma|-\frac{\hbar^2}{2m}\boldsymbol{\nabla}^2+V_0(\boldsymbol{r}-\boldsymbol{r}_n)|X_n\,\sigma\rangle$, and the hopping integrals, $\langle X_m\,\sigma|\sum_{i\neq 0} v_i(\boldsymbol{r}-\boldsymbol{r}_n)|X_n\,\sigma\rangle$, connecting sites n and m. We determine our reference zero energy by setting the on-site energy of all π-orbitals to zero. Furthermore, we neglect all hopping integrals going beyond nearest neighbor contributions[4]. Within this nearest neighbor approximation, the orbital TB Hamiltonian for graphene reads

$$\mathcal{H}_0 = -t \sum_{\sigma} \sum_{\langle m,n\rangle} \big|X_m\,\sigma\big\rangle\big\langle X_n\,\sigma\big|\,, \tag{2.4}$$

where the positive quantity t is the nearest neighbor hopping strength, for which one finds in the literature for graphene a value of about 3 eV [3, 71, 82]. Throughout this thesis, we fix the nearest neighbor hopping strength to $t = 2.6\,\mathrm{eV}$. To obtain the band structure of graphene, we transform $\mathcal{H}_0$ from the local atomic into the Bloch basis, $|X_m\,\sigma\rangle \to |X_{\boldsymbol{q}}\,\sigma\rangle$,

$$\big|X_{\boldsymbol{q}}\,\sigma\big\rangle = \frac{1}{\sqrt{N}} \sum_{\boldsymbol{R}_m} e^{i\boldsymbol{q}.\boldsymbol{R}_m}\,\big|X_m\,\sigma\big\rangle\,. \tag{2.5}$$

Here, we set $X \in \{A, B\}$ according to the sublattice of the site and measure the quasi-momentum $\boldsymbol{q}$ from the center of the hexagonal Brillouin zone at the $\boldsymbol{\Gamma}$ point. The number of graphene unit cells enters Eq. (2.5) as the quantity N. Note that $\boldsymbol{R}_m$ is the lattice vector pointing to the m-th unit cell that hosts the orbital $|X_m\,\sigma\rangle$. We can now express the orbital Hamiltonian in the Bloch form, $\mathcal{H}_0 = \sum_{\boldsymbol{q}} \mathcal{H}_0(\boldsymbol{q})$, with

$$\mathcal{H}_0(\boldsymbol{q}) = -t \sum_{\sigma} f_{\mathrm{orb}}(\boldsymbol{q})\,\big[\hat{s}_0\big]_{\sigma\sigma}\big|A_{\boldsymbol{q}}\,\sigma\big\rangle\big\langle B_{\boldsymbol{q}}\,\sigma\big| + \mathrm{H.c.}\,, \tag{2.6}$$

where $\hat{s}_0$ represents the unit matrix in spin space (see below) and the orbital structural function is given by

$$f_{\mathrm{orb}}(\boldsymbol{q}) = \left\{1 + \mathrm{e}^{i\boldsymbol{q}.\boldsymbol{R}_2} + \mathrm{e}^{-i\boldsymbol{q}.\boldsymbol{R}_3}\right\}. \tag{2.7}$$

Diagonalizing Eq. (2.6), we obtain the dispersion relation for the π states of graphene which form the conduction ($n = +1$) and the valence band ($n = -1$),

$$\epsilon_n(\boldsymbol{q}) = n\,t|f_{\mathrm{orb}}(\boldsymbol{q})|\,. \tag{2.8}$$

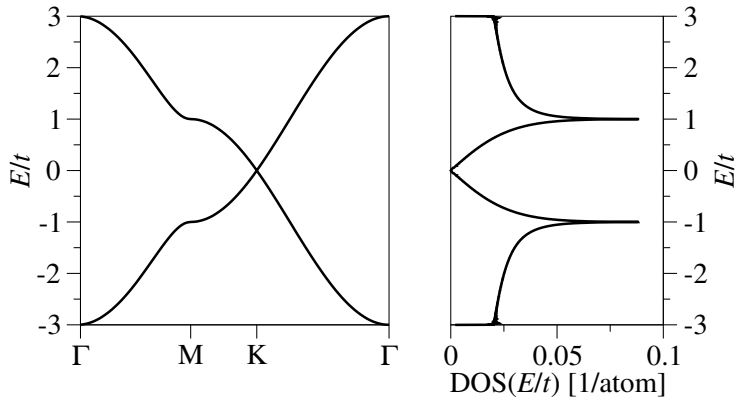

Figure 2.2: (a) Band Structure of graphene with the linear dispersion around the $\boldsymbol{K}$ point and, (b), corresponding DOS of graphene.

Figure 2.2 shows the energy dispersion of graphene in momentum space resulting from the diagonalization of Eq. (2.4) together with the DOS[5].

In pristine (undoped) graphene, the Fermi level lies at zero energy, i.e., it crosses the energy dispersion directly at the Dirac points where the valence and conduction band meet. The linear dispersion, which appears at nearby energies, can be further investigated by considering quasi-momenta $\boldsymbol{q} = \tau\boldsymbol{K} + \boldsymbol{k}$ around the Dirac point

$$\tau\boldsymbol{K} = \tau\,\frac{4\pi}{3a_{\mathrm{L}}}(1,0)\,. \tag{2.9}$$

Keeping the first nonzero term in the expansion of Eq. (2.7) in $\boldsymbol{k}$, we obtain

$$f_{\mathrm{orb}}(\tau\boldsymbol{K}+\boldsymbol{k}) \simeq \frac{\sqrt{3}a_{\mathrm{L}}}{2}\left(-\tau k_x - ik_y\right), \tag{2.10}$$

and the orbital Hamiltonian, Eq. (2.6), reduces in the low-energy limit to

$$\mathcal{H}_{\mathrm{eff}}(\tau\boldsymbol{K}+\boldsymbol{k}) = \hbar v_F\left(\tau k_x\hat{\sigma}_x - k_y\hat{\sigma}_y\right)\hat{s}_0\,. \tag{2.11}$$

Here, we introduced the Fermi velocity $v_F = \sqrt{3}a_{\mathrm{L}}t/2\hbar$ which has for graphene the value of about $v_F \approx 10^6$m/s. The sublattice degree of freedom is described by the Pauli matrices $\hat{\sigma}_i$ acting on the sublattice space, whereas for the spin degree of freedom we use the Pauli matrices $\hat{s}_i$ in the spin space. We choose as the ordering of the sublattices $\{A, B\}$ and for the spins $\sigma = \{\uparrow, \downarrow\}$ with spin quantization axis along z. The spin-Pauli matrices are given by

$$\hat{s}_0 = \begin{pmatrix} 1 & 0 \\ 0 & 1 \end{pmatrix},\ \hat{s}_x = \begin{pmatrix} 0 & 1 \\ 1 & 0 \end{pmatrix},\ \hat{s}_y = \begin{pmatrix} 0 & -\mathrm{i} \\ \mathrm{i} & 0 \end{pmatrix},\ \hat{s}_z = \begin{pmatrix} 1 & 0 \\ 0 & -1 \end{pmatrix} \tag{2.12}$$

[4]The next-nearest neighbor hopping term, for example, induces electron-hole asymmetry in the spectrum of graphene.

[5]For the diagonalization, the LAPACK [83] routine zheevx is employed. The DOS is calculated applying the triangle method [84] for the integration over the two-dimensional Brillouin zone.

and are equivalently defined for the sublattice degree of freedom, for example $[\hat{\sigma}_z]_{AA} = 1 = -[\hat{\sigma}_z]_{BB}$ and $[\hat{\sigma}_z]_{AB} = 0 = [\hat{\sigma}_z]_{BA}$. The linear dispersion relation appears then after diagonalizing Eq. (2.11) and reads

$$\epsilon_n(\tau \boldsymbol{K} + \boldsymbol{k}) = n\,\hbar v_F |\boldsymbol{k}|\,. \tag{2.13}$$

In graphene, the π-orbitals are primarily built of the carbon $2p_z$ orbitals, though all TB and symmetry discussions of the following sections are valid for any atomic orbital with quantum numbers n, $l \neq 0$, $m_l = 0$. We further note that for hexagonal systems other than pristine graphene the value of t might differ and its magnitude needs to be re-estimated or fitted for a quantitative analysis of those systems. Additional terms in Eq. (2.4) can arise if A and B sublattice atoms are distinct or feel different electrostatic potential; see the examples of planar hexagonal boron nitride (hBN), Sec. 2.4.4, or graphene on a TMDC, Sec. 2.4.6.

In the subsequent sections we focus on the following question: Given a graphene system (and its point group symmetry) what can we predict for the SOC? Concentrating on the modeling site of this problem, we will derive effective Hamiltonians describing the spin-degree of freedom in the structure. We consider one effective orbital per lattice site from which we demand invariance under certain symmetries. The approach is symmetry based which enables us to make general statements for different structural realizations of graphene systems with the same point group symmetry and provides us with a first intuitive view on the subject. The effective description incorporates the microscopic origin of the SOC but does not rely on a detailed description of the SOC in the vicinity of the atomic cores. The study of specific systems may call in a second step for multi-orbital TB models, e.g. in the Koster-Slater two-center approximation, and, for a quantitative analysis of the spin-orbit strength, DFT calculations. The effective SOC Hamiltonians for the local adsorbates will be applied to three specific impurities in Ch. 3, which also supports the validity of our following statements.

2.3 Spin-orbit coupling from symmetry

2.3.1 Microscopic SOC Hamiltonian

SOC appears as a relativistic correction in the Schrödinger equation at the atomic level and can be directly observed in the fine structure of atomic spectra. It describes the coupling of an electron's momentum to its spin degree of freedom as it moves under the influence of the gradient of an electric potential. For atoms in a lattice, the potential is represented by the effective crystal field potential V. The Hamiltonian for this microscopic spin-orbit interaction is given by

$$\hat{H}_{\mathrm{so}} = \frac{\hbar}{4m^2\mathrm{c}^2}\big(\boldsymbol{\nabla} V \times \hat{\boldsymbol{p}}\big).\hat{\boldsymbol{s}}\,, \tag{2.14}$$

where m is the vacuum rest mass of the electron, c the speed of light, $\hat{\boldsymbol{p}}$ the momentum operator, and $\hat{\boldsymbol{s}} = (\hat{s}_x, \hat{s}_y, \hat{s}_z)$ represents the array of Pauli matrices acting on the spin degrees of freedom. For the discussions below, it is useful to expand the Hamiltonian in spin-raising and spin-lowering operators, $\hat{s}_\pm = \hat{s}_x \pm i\hat{s}_y$,

$$\hat{H}_{\mathrm{so}} = \hat{\mathcal{L}}_+ \hat{s}_- + \hat{\mathcal{L}}_- \hat{s}_+ + \hat{\mathcal{L}}_z \hat{s}_z \,. \tag{2.15}$$

The $\hat{\mathcal{L}}$'s are differential operators which act only on the orbital part of the wave function[6].

2.3.2 Symmetry approach

Starting point for the derivation of an effective, system-specific SOC Hamiltonian is the system's (local) symmetry which is described by a set of symmetry operations and their respective representations $\mathcal{S}$. The symmetry allows or forbids certain spin-orbit mediated hopping terms between lattice sites. Thus, we need to investigate the behavior of the matrix elements $\langle X_m\,\sigma \,|\, \hat{H}_{\mathrm{so}} \,|\, X_n\,\sigma' \rangle$ of the microscopic SOC Hamiltonian under symmetry in our effective one-particle Hilbert space. As the gradient of the crystal field potential ∇V is largest around the atomic cores, the magnitude of the matrix elements decreases strongly with increasing distance between sites n and m. Our analysis of SOC mediated hoppings is therefore restricted to on-site, nearest neighbors, and next-nearest neighbors. Let us first give general relations that will facilitate our SOC studies.

If the system's structure is invariant under a symmetry operation $\mathcal{S}$ ($\mathcal{S}$ is a group element of the structure's point or space group) then both orbital and spin-orbital Hamiltonian have to commute with $\mathcal{S}$. In particular, this means that the effective SOC matrix element between states $|X_m\sigma\rangle$ and $|X_n\sigma'\rangle$ fulfills[7] for unitary $\mathcal{S}$

$$\begin{aligned} \langle \mathcal{S}[X_m\,\sigma] \,|\, \hat{H}_{\mathrm{so}} \,|\, \mathcal{S}[X_n\,\sigma'] \rangle &= \langle \mathcal{S}[X_m\,\sigma] \,|\, \mathcal{S}[\hat{H}_{\mathrm{so}}\, X_n\,\sigma'] \rangle \\ &= \langle X_m\,\sigma \,|\, \hat{H}_{\mathrm{so}} \,|\, X_n\,\sigma' \rangle \,. \end{aligned} \tag{2.16}$$

We further impose time reversal $\mathcal{T}$ symmetry on our systems which is represented by an antiunitary operator and can therefore be written as the product of a unitary operator and complex conjugation. From this follows directly how the matrix

[6] The operators $\hat{\boldsymbol{\mathcal{L}}}$ transform under space and time reversal symmetry as the standard angular momentum operators $\hat{\boldsymbol{L}}$ but do not fulfill their SU(2)-commutation relations. In a microscopic treatment of the SOC, the SOC is most efficient in the vicinity of the atomic core. There, the crystal field potential can be approximated by the spherically symmetric atomic potential. With $V(\boldsymbol{r}) = V(|\boldsymbol{r}|)$ and $\nabla V = (\boldsymbol{r}/r)(\mathrm{d}V/\mathrm{d}r)$, the Hamiltonian of Eq. (2.14) reduces to $\hat{H}_{\mathrm{so}} = \xi(r)\hat{\boldsymbol{L}}.\hat{\boldsymbol{s}}$ [85]. The factor $\xi(r)$ incorporates all of the radial information.

[7] We employ the notation $|\alpha\mathcal{S}[X_n\,\sigma]\rangle \equiv \alpha\mathcal{S}|X_n\,\sigma\rangle$ to denote a state $|X_n\,\sigma\rangle$ after transformation under the operation $\alpha\mathcal{S}$.

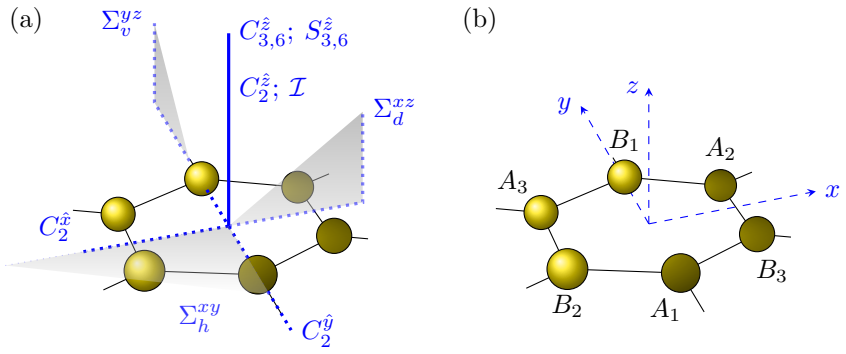

Figure 2.3: (a) Symmetries of the point group D_{6h}, which leave the honeycomb lattice structure invariant. (b) Chosen coordinate system and labeling of the carbon sites on one hexagon ring.

elements for the self-adjoint Hamiltonian transform under time reversal symmetry[8],

$$\begin{aligned}\left\langle \mathcal{T}[X_m\,\sigma] \,|\, \hat{H}_{\mathrm{so}} \,|\, \mathcal{T}[X_n\,\sigma'] \right\rangle &= \left\langle \mathcal{T}[X_m\,\sigma] \,|\, \mathcal{T}[\hat{H}_{\mathrm{so}}\, X_n\,\sigma'] \right\rangle \\ &= \overline{\left\langle X_m\,\sigma \,|\, \hat{H}_{\mathrm{so}} \,|\, X_n\,\sigma' \right\rangle} \\ &= \left\langle X_n\,\sigma' \,|\, \hat{H}_{\mathrm{so}} \,|\, X_m\,\sigma \right\rangle . \end{aligned} \tag{2.17}$$

2.3.3 Point group symmetries and transformation of spin

We have to specify from which pool of symmetries we can select $\mathcal{S}$. Pristine graphene is invariant under the crystallographic point group[9] D_{6h}, which comprises the 24 group elements of unity E, rotations C_l, space inversion $\mathcal{I}$, reflections Σ and improper rotations S_m in 12 classes,

$$D_{6h} = \{E; 2C_6^{\hat{z}}; 2C_3^{\hat{z}}; C_2^{\hat{z}}; 3C_2^{\hat{x}}; 3C_2^{\hat{y}}; \mathcal{I}; \Sigma_h^{xy}; 3\Sigma_v^{yz}; 3\Sigma_d^{xz}; 2S_3^{\hat{z}}; 2S_6^{\hat{z}}\}. \tag{2.18}$$

Here, each class is represented by one symmetry operation and the numbers in front specify the total number of equivalent elements contained in the respective class. Representative operations of each class are shown in Fig. 2.3(a) and we use the following notation: Superscripts xy, yz, and xz identify the location of reflection planes in our coordinate system, which is shown in Fig. 2.3(b), and we add for emphasis the attributes *horizontal* (h), *vertical* (v), and *diagonal*[10] (d), respectively. Superscripts $\hat{x}$, $\hat{y}$, and $\hat{z}$ specify the axes of spatial rotations. The

[8] By $\overline{a}$ we denote the complex conjugate of the quantity a.

[9] We label the point groups according to the Schönflies notation [86].

[10] This plane is commonly called a *dihedral* plane since it contains the principal axis (axis with highest rotational symmetry) and bisects the angle between two C_2 axes that are perpendicular to the principal axis [86].

angle of rotation $\Phi_l = 2\pi/l$ is encoded in the subscript l. Apart of proper rotations C_l, D_{6h} also contains improper rotations S_l, which involve a proper rotation, C_l, followed by reflection about the horizontal plane, Σ_h^{xy}. Note that the π-orbitals are odd under horizontal reflections, inversion, and π-rotations around in-plane axes. Throughout the first part of this chapter we will study and compare SOC in systems with the point group D_{6h} and its subgroups D_{3d}, D_{3h}, C_{6v}, and C_{3v}. Depending on the system, we will apply only a subset of the symmetry operations contained in D_{6h}.

For our spin-orbit analysis we further need to know, how spin $\uparrow$ and $\downarrow$ components transform under a symmetry operator $\mathcal{S}$. With the help of the unit matrix and the spin-Pauli matrices, one can write down a two-dimensional representation of the operator for rotation of spin by angle Φ_l around the axis $\hat{\boldsymbol{n}}_\alpha$ [22],

$$C_l^{\hat{\alpha}} = e^{-i\frac{\Phi_l}{2}\hat{\boldsymbol{n}}_\alpha.\hat{\boldsymbol{s}}} = \cos\left(\frac{\Phi_l}{2}\right) - i\,\hat{\boldsymbol{n}}_\alpha.\hat{\boldsymbol{s}}\sin\left(\frac{\Phi_l}{2}\right), \tag{2.19}$$

and reflection of spin in a plane with plane normal $\hat{\boldsymbol{n}}_\alpha$,

$$\sigma_\alpha = -i\,\hat{\boldsymbol{n}}_\alpha.\hat{\boldsymbol{s}}\,. \tag{2.20}$$

Specifically, we choose for the reflection planes xy, yz, and xz the plane normals $\hat{n}_\alpha$ pointing along the (positive) cartesian axes α displayed in Fig. 2.3(b).

For one-particle spin-1/2 states, the time reversal operator fulfills $\mathcal{T}^2 = -1$ [86]. We choose as a specific representation for the anti-unitary operator $\mathcal{T} = -i\hat{s}_y\hat{\mathcal{C}}$ where $\hat{\mathcal{C}}$ indicates complex conjugation. As we are considering real (effective) orbitals the time reversal operator only affects the spin part of the wave function.

We can now write down transformation rules for our π-orbital states $|X_m\sigma\rangle$ under the symmetry operations $\mathcal{S}$ presented in Fig. 2.3(a), time reversal $\mathcal{T}$ and translations $T_{\vec{a}}$ along $\vec{a}$,

$$|X_m\,\sigma\rangle \xrightarrow{C_l^{\hat{z}}} e^{-i\sigma\Phi_l/2}\,|X_{C_l^{\hat{z}}(m)}\,\sigma\rangle\,, \tag{2.21a}$$

$$|X_m\,\sigma\rangle \xrightarrow{C_2^{\hat{x}}} i\,|X_{C_2^{\hat{x}}(m)}\,(-\sigma)\rangle\,, \tag{2.21b}$$

$$|X_m\,\sigma\rangle \xrightarrow{C_2^{\hat{y}}} (-1)^{\frac{1-\sigma}{2}}\,|X_{C_2^{\hat{y}}(m)}\,(-\sigma)\rangle\,, \tag{2.21c}$$

$$|X_m\,\sigma\rangle \xrightarrow{\Sigma_h^{xy}} i(-1)^{\frac{1+\sigma}{2}}\,|X_m\,\sigma\rangle\,, \tag{2.21d}$$

$$|X_m\,\sigma\rangle \xrightarrow{\Sigma_v^{yz}} -i\,|X_{\Sigma_v^{yz}(m)}\,(-\sigma)\rangle\,, \tag{2.21e}$$

$$|X_m\,\sigma\rangle \xrightarrow{\Sigma_d^{xz}} (-1)^{\frac{1+\sigma}{2}}\,|X_{\Sigma_d^{xz}(m)}\,(-\sigma)\rangle\,, \tag{2.21f}$$

$$|X_m\,\sigma\rangle \xrightarrow{S_l^{\hat{z}}} i(-1)^{\frac{1+\sigma}{2}}e^{-i\sigma\Phi_l/2}\,|X_{S_l^{\hat{z}}(m)}\,\sigma\rangle\,, \tag{2.21g}$$

$$|X_m\,\sigma\rangle \xrightarrow{\mathcal{T}} (-1)^{\frac{1-\sigma}{2}}\,|X_m\,(-\sigma)\rangle\,, \tag{2.21h}$$

$$|X_m\,\sigma\rangle \xrightarrow{\mathcal{I}} -|X_{\mathcal{I}(m)}\,\sigma\rangle\,, \tag{2.21i}$$

$$|X_m\,\sigma\rangle \xrightarrow{T_{\vec{a}}} |X_{m+\vec{a}}\,\sigma\rangle\,. \tag{2.21j}$$

The transformation properties under improper rotations follow directly from $S_l^{\hat{z}} = \Sigma_h^{xy} \circ C_l^{\hat{z}}$ and we can rewrite space inversion as $\mathcal{I} = \Sigma_v^{yz} \circ \Sigma_h^{xy} \circ \Sigma_d^{xz}$.

Equivalently, we could do our symmetry analysis in the space of quasi-momenta by transforming the local atomic basis $|X_m\,\sigma\rangle$ to the Bloch basis $|X_{\boldsymbol{q}}\,\sigma\rangle$. One obtains similar transformation rules as in Eqs. (2.21) where it has to be taken into account that both time reversal and inversion cause $\boldsymbol{q} \mapsto -\boldsymbol{q}$. We focus in our symmetry analysis on the states in Wannier space as we will discuss both systems with and without translational symmetry (Sec. 2.4 and Sec. 2.5, respectively). In the first case we will express our effective SOC Hamiltonians also in the Bloch basis to show the impact of the SOC terms on the band structure at low energies.

2.3.4 Practical relations

Time reversal symmetry and the properties of $\hat{H}_{\mathrm{so}}$, Eq. (2.15), alone provide already important information about the nature of SOC terms in graphene-like systems. Time reversal symmetry, for example, connects SOC matrix elements with opposite spin projections,

$$\begin{aligned}
&\big\langle X_m\,\sigma\big|\hat{H}_{\mathrm{so}}\big|X_n\,\sigma'\big\rangle = \\
&\overset{(2.21h)}{=} \big\langle (-1)^{-\frac{1-\sigma}{2}}\mathcal{T}[X_m(-\sigma)]\big|\hat{H}_{\mathrm{so}}\big|(-1)^{-\frac{1-\sigma'}{2}}\mathcal{T}[X_n(-\sigma')]\big\rangle \\
&= -(-1)^{\frac{\sigma+\sigma'}{2}}\big\langle \mathcal{T}[X_m(-\sigma)]\big|\hat{H}_{\mathrm{so}}\big|\mathcal{T}[X_n(-\sigma')]\big\rangle \\
&\overset{(2.17)}{=} -(-1)^{\frac{\sigma+\sigma'}{2}}\big\langle X_n(-\sigma')\big|\hat{H}_{\mathrm{so}}\big|X_m(-\sigma)\big\rangle\,.
\end{aligned} \tag{2.22}$$

We will exploit this relation frequently in our SOC analysis. In particular, it follows that on-site spin-flipping SOC terms, i.e., $n = m$ and $\sigma' = -\sigma$, are equal to zero:

$$\big\langle X_m\,\sigma\big|\hat{H}_{\mathrm{so}}\big|X_m(-\sigma)\big\rangle \overset{(2.22)}{=} -\big\langle X_m\,\sigma\big|\hat{H}_{\mathrm{so}}\big|X_m(-\sigma)\big\rangle\,. \tag{2.23}$$

Furthermore, as $\big\langle\sigma\big|\hat{s}_\pm\big|\sigma\big\rangle = 0$, Eq. (2.15) indicates that a spin-conserving hopping changes sign under an overall flip of the spins,

$$\big\langle X_m\,\sigma\big|\hat{H}_{\mathrm{so}}\big|X_n\,\sigma\big\rangle = -\big\langle X_m(-\sigma)\big|\hat{H}_{\mathrm{so}}\big|X_n(-\sigma)\big\rangle\,. \tag{2.24}$$

Getting time reversal symmetry involved in the game, we find

$$\begin{aligned}
\big\langle X_m(-\sigma)\big|\hat{H}_{\mathrm{so}}\big|X_n(-\sigma)\big\rangle &\overset{(2.22)}{=} \big\langle X_n\,\sigma\big|\hat{H}_{\mathrm{so}}\big|X_m\,\sigma\big\rangle \\
&= \overline{\big\langle X_m\,\sigma\big|\hat{H}_{\mathrm{so}}\big|X_n\,\sigma\big\rangle}\,,
\end{aligned} \tag{2.25}$$

which, together with Eq. (2.24), implies that a spin-conserving SOC term coupling sites n and m is purely imaginary. Though, in the case of $n = m$ we see that

$$\begin{aligned}\langle X_m\,\sigma|\hat{H}_{\mathrm{so}}|X_m\,\sigma\rangle &\overset{(2.22)}{=} \langle X_m(-\sigma)|\hat{H}_{\mathrm{so}}|X_m(-\sigma)\rangle \\ &\overset{(2.24)}{=} -\langle X_m\,\sigma|\hat{H}_{\mathrm{so}}|X_m\,\sigma\rangle\,. \end{aligned} \tag{2.26}$$

Thus, on-site spin-conserving SOC terms vanish for all sites m.

So far, we have not used any point-group specific symmetries. As we will see in the following, we can make three statements about the absence of SOC terms related to the presence of specific symmetries. In detail, the statements explain why we find for pristine graphene, point group D_{6h}, only the intrinsic SOC term.

Statement 1. *Spin-flipping SOCs are inhibited by horizontal reflection Σ_h^{xy}.*

With a glance at Eq. (2.21d), we write

$$\begin{aligned}&\langle X_m\,\sigma|\hat{H}_{\mathrm{so}}|X_n(-\sigma)\rangle \\ &\overset{(2.21d)}{=} \langle i(-1)^{\frac{1-\sigma}{2}}\Sigma_h^{xy}[X_m\,\sigma]|\hat{H}_{\mathrm{so}}|i(-1)^{\frac{1+\sigma}{2}}\Sigma_h^{xy}[X_n(-\sigma)]\rangle \\ &= -\langle\Sigma_h^{xy}[X_m\,\sigma]|\hat{H}_{\mathrm{so}}|\Sigma_h^{xy}[X_n(-\sigma)]\rangle \\ &\overset{(2.16)}{=} -\langle X_m\,\sigma|\hat{H}_{\mathrm{so}}|X_n(-\sigma)\rangle\,, \end{aligned} \tag{2.27}$$

which is fulfilled only if $\langle X_m\,\sigma|\hat{H}_{\mathrm{so}}|X_n(-\sigma)\rangle = 0$.

Statement 2. *Nearest neighbor spin-flip SOCs are inhibited by a combination of space inversion $\mathcal{I}$, translation $T_{\vec{a}}$, and time reversal $\mathcal{T}$.*

We show the effect of the symmetries, as an example, on one matrix element $\langle A_2\,\sigma|\hat{H}_{\mathrm{so}}|B_3(-\sigma)\rangle$ [see Fig. 2.3(b)]. All other nearest neighbor spin-flip matrix elements can be treated analogously. Under space inversion and translation along $\vec{a} = \overrightarrow{A_3A_2} = \overrightarrow{B_2B_3}$ the matrix element transforms to

$$\begin{aligned}\langle A_2\,\sigma|\hat{H}_{\mathrm{so}}|B_3(-\sigma)\rangle &\overset{(2.21i)}{=} \langle -\mathcal{I}[B_2\,\sigma]|\hat{H}_{\mathrm{so}}|-\mathcal{I}[A_3(-\sigma)]\rangle \\ &= \langle\mathcal{I}[B_2\,\sigma]|\hat{H}_{\mathrm{so}}|\mathcal{I}[A_3(-\sigma)]\rangle \\ &\overset{(2.16)}{=} \langle B_2\,\sigma|\hat{H}_{\mathrm{so}}|A_3(-\sigma)\rangle \\ &\overset{(2.21j)}{=} \langle T_{\vec{a}}[B_3\,\sigma]|\hat{H}_{\mathrm{so}}|T_{\vec{a}}[A_2(-\sigma)]\rangle \\ &\overset{(2.16)}{=} \langle B_3\,\sigma|\hat{H}_{\mathrm{so}}|A_2(-\sigma)\rangle\,. \end{aligned} \tag{2.28a}$$

The right side of Eq. (2.28a) is distinct from the initial matrix element by complex conjugation and interchange of spin. This calls for applying time reversal symmetry,

$$\langle B_3\,\sigma|\hat{H}_{\mathrm{so}}|A_2(-\sigma)\rangle \overset{(2.22)}{=} -\langle A_2\,\sigma|\hat{H}_{\mathrm{so}}|B_3(-\sigma)\rangle\,, \tag{2.28b}$$

and thus we showed that the nearest neighbor SOC mediated spin-flip hopping is zero due to the presence of space inversion, translation, and time reversal.

Statement 3. *Nearest neighbor spin-conserving SOCs are inhibited by a combination of vertical reflection Σ_v^{yz} and translation $T_{\vec{a}}$.*

We first translate the states $|A_3\,\sigma\rangle$ and $|B_2\,\sigma\rangle$ along $\vec{a} = \overrightarrow{A_2A_3} = \overrightarrow{B_3B_2}$ and go back to the initial position by Σ_v^{yz}, i.e.,

$$\begin{aligned}\big\langle A_2\,\sigma\big|\hat{H}_{\mathrm{so}}\big|B_3\,\sigma\big\rangle &= \big\langle A_3\,\sigma\big|\hat{H}_{\mathrm{so}}\big|B_2\,\sigma\big\rangle \\ &\overset{(2.21e)}{=} \big\langle i\Sigma_v^{yz}[A_2\,(-\sigma)]\big|\hat{H}_{\mathrm{so}}\big|i\Sigma_v^{yz}[B_3\,(-\sigma)]\big\rangle \\ &= \big\langle A_2\,(-\sigma)\big|\hat{H}_{\mathrm{so}}\big|B_3\,(-\sigma)\big\rangle \end{aligned} \tag{2.29a}$$

With help of Eq. (2.24) we finally obtain, in accordance with our third statement,

$$\big\langle A_2\,\sigma\big|\hat{H}_{\mathrm{so}}\big|B_3\,\sigma\big\rangle \overset{(2.24)}{=} -\big\langle A_2\,\sigma\big|\hat{H}_{\mathrm{so}}\big|B_3\,\sigma\big\rangle = 0\,. \tag{2.29b}$$

When we consider subgroups of D_{6h}, i.e., we explicitly lower the symmetry in our system, certain symmetry operations are absent and, thus, specific statements are not fulfilled. In particular, the third statement does not necessarily hold in the case of local adsorbates where translational invariance is absent. We will nevertheless first consider systems with translational invariance.

2.4 Spin-orbit coupling under global symmetries

2.4.1 Pristine graphene and the point group D_{6h}

In the previous section we showed that the π-states in D_{6h} invariant graphene mediate only a next-nearest neighbor spin-conserving SOC term. This is the so-called intrinsic SOC and we will label its strength by λ_{I}. It enters the SOC Hamiltonian as

$$\mathcal{H}_{D_{6h}} = \frac{i\lambda_{\mathrm{I}}}{3\sqrt{3}} \sum_{\sigma} \sum_{\langle\langle m,n\rangle\rangle} \nu_{m,n} \big[\hat{s}_z\big]_{\sigma\sigma} \big|X_m\,\sigma\big\rangle \big\langle X_n\,\sigma\big|\,. \tag{2.30}$$

Here, the summation over $\langle\langle m,n\rangle\rangle$ addresses all second nearest neighbor sites m and n which are members of the same sublattice. By convention, the SOC strength λ_{I} enters Eq. (2.30) with the numerical prefactor $(3\sqrt{3})^{-1}$ which simplifies the form of the low-energy expansion in Bloch space (see below). The imaginary unit i reflects the purely imaginary nature of spin-conserving hoppings in graphene, Eqs. (2.24) and (2.25). As seen before in Eq. (2.24), the intrinsic SOC comes with opposite sign

for pairs of sites on the opposite sublattice which is encoded in $[\hat{s}_z]_{\sigma\sigma}$. Finally, the symbol $\nu_{m,n} = +1\ (-1)$ specifies whether the next-nearest neighbor hopping $n \to m$ via a common neighbor on the opposite sublattice is counter clockwise (clockwise). Let us motivate why ν_{mn} captures the sublattice dependent sign factors. First, we define

$$\frac{i\lambda_{\mathrm{I}}}{3\sqrt{3}} = \big\langle A_3\uparrow\big|\hat{H}_{\mathrm{so}}\big|A_2\uparrow\big\rangle \overset{(2.24)}{=} -\big\langle A_3\downarrow\big|\hat{H}_{\mathrm{so}}\big|A_2\downarrow\big\rangle\,. \tag{2.31a}$$

By vertical reflection Σ_d^{xz}, we connect A sites to B sites, i.e., $|A_2\uparrow\rangle = \Sigma_d^{xz}|B_3\downarrow\rangle$ and $|A_3\uparrow\rangle = \Sigma_d^{xz}|B_2\downarrow\rangle$, where the site labeling follows the conventions of Fig. 2.3(b). We obtain

$$\begin{aligned}\frac{i\lambda_{\mathrm{I}}}{3\sqrt{3}} &= \big\langle A_3\uparrow\big|\hat{H}_{\mathrm{so}}\big|A_2\uparrow\big\rangle \overset{(2.21f)}{=} \big\langle \Sigma_d^{xz}[B_2\downarrow]\big|\hat{H}_{\mathrm{so}}\big|\Sigma_d^{xz}[B_3\downarrow]\big\rangle \\ &\overset{(2.16)}{=} \big\langle B_2\downarrow\big|\hat{H}_{\mathrm{so}}\big|B_3\downarrow\big\rangle \overset{(2.24)}{=} -\big\langle B_2\uparrow\big|\hat{H}_{\mathrm{so}}\big|B_3\uparrow\big\rangle\,.\end{aligned} \tag{2.31b}$$

Indeed, for the counter clockwise path $A_2 \to (B_1) \to A_3$ it is $\nu_{A_3A_2} = +1$, while for the clockwise path $B_3 \to (A_1) \to B_2$ we have $\nu_{B_2B_3} = -1$.

To see the effect of the intrinsic SOC on the graphene band structure we transform $\mathcal{H}_{D_{6h}}$ to the Bloch basis as specified in Eq. (2.5). With the explicit choice of the unit cell shown in Fig. 2.1(a), we obtain $\mathcal{H}_{D_{6h}} = \sum_{\boldsymbol{q}} \mathcal{H}_{D_{6h}}(\boldsymbol{q})$, where

$$\mathcal{H}_{D_{6h}}(\boldsymbol{q}) = \lambda_{\mathrm{I}}\, f_{\mathrm{I}}(\boldsymbol{q}) \sum_{X,\sigma} \big[\hat{\sigma}_z\big]_{XX} \big[\hat{s}_z\big]_{\sigma\sigma} \big|X_{\boldsymbol{q}}\,\sigma\big\rangle\big\langle X_{\boldsymbol{q}}\,\sigma\big|\,. \tag{2.32}$$

The sign dependence of the intrinsic SOC on the sublattice was described by ν_{mn} in Eq. (2.30) and is now encoded in $[\hat{\sigma}_z]_{AA} = 1 = -[\hat{\sigma}_z]_{BB}$, and $[\hat{\sigma}_z]_{AB} = 0 = [\hat{\sigma}_z]_{BA}$. Defining the lattice vectors $\boldsymbol{R}_\alpha$ according to Eq. (2.1), the Fourier transform introduces the intrinsic structural function in the form

$$f_{\mathrm{I}}(\boldsymbol{q}) = -\frac{2}{3\sqrt{3}}\big\{\sin\boldsymbol{q}.\boldsymbol{R}_1 + \sin\boldsymbol{q}.\boldsymbol{R}_2 + \sin\boldsymbol{q}.\boldsymbol{R}_3\big\}\,. \tag{2.33}$$

The intrinsic SOC opens a band gap in the Dirac-cone spectrum of pristine graphene, which is described by Eq. (2.4), as can be seen from the low-energy dispersion around the $\pm\boldsymbol{K}$ points in the Brillouin zone. Defining $\boldsymbol{q} = \pm\boldsymbol{K} + \boldsymbol{k}$, we expand Eq. (2.33) in the quasi-momentum $\boldsymbol{k}$ and keep the first nonzero term. This leads to

$$f_{\mathrm{I}}(\tau\boldsymbol{K} + \boldsymbol{k}) \simeq \tau\,, \tag{2.34}$$

and, in the ordered Bloch basis $\{|A_{\boldsymbol{q}}\uparrow\rangle, |A_{\boldsymbol{q}}\downarrow\rangle, |B_{\boldsymbol{q}}\uparrow\rangle, |B_{\boldsymbol{q}}\downarrow\rangle\}$, we can write the effective low-energy Hamiltonian for a D_{6h} graphene system as

$$\mathcal{H}_{\mathrm{eff}}(\tau\boldsymbol{K} + \boldsymbol{k}) = \hbar v_F \big(\tau k_x\hat{\sigma}_x - k_y\hat{\sigma}_y\big)\hat{s}_0 + \tau\lambda_{\mathrm{I}}\hat{\sigma}_z\hat{s}_z\,. \tag{2.35}$$

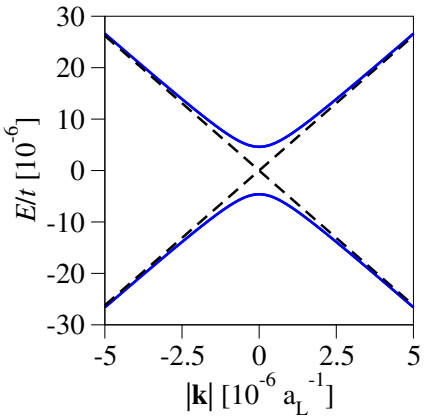

Figure 2.4: Electronic band structure of a graphene-like system around the $\boldsymbol{K}$ point. The linear, gapless spectrum (dashed) is transformed to a gapped spectrum upon including the intrinsic SOC term λ_{I}. Here, λ_{I} has the graphene value of $\lambda_{\mathrm{I}} = 12\,\mu\mathrm{eV}$ and $t = 2.6\,\mathrm{eV}$.

The intrinsic SOC gives rise to a mass term in Eq. (2.35) which opens a gap of $2\lambda_{\mathrm{I}}$ in the spectrum at $\boldsymbol{k} = 0$. As only $\hat{s}_0$ and $\hat{s}_z$ appear in $\mathcal{H}_{\mathrm{eff}}(\tau\boldsymbol{K}+\boldsymbol{k})$, we can directly infer that both conduction and valence band stay twofold degenerate and are built, for $\tau = +1$, from the states $\{|A_{\boldsymbol{K}}\uparrow\rangle, |B_{\boldsymbol{K}}\downarrow\rangle\}$ and $\{|A_{\boldsymbol{K}}\downarrow\rangle, |B_{\boldsymbol{K}}\uparrow\rangle\}$, respectively[11]. Note that we label the eigenstates of Eq. (2.35) by the spin $\uparrow$ and $\downarrow$ projections along the z spin quantization axis. The eigenenergies of the Hamiltonian are given by

$$\epsilon_{n,\sigma}(\tau\boldsymbol{K}+\boldsymbol{k}) = n\sqrt{\lambda_{\mathrm{I}}^2 + \hbar^2 v_F^2(k_x^2+k_y^2)}\,. \tag{2.36}$$

In graphene, the SOC induced gap is $2\lambda_{\mathrm{I}} = 24\,\mu\mathrm{eV}$ [21]. Figure 2.4 displays the graphene spectrum around $\boldsymbol{K}$ with and without intrinsic SOC.

The spin-degeneracy of the conduction and valence band follows directly from the presence of time reversal and space inversion symmetry,

$$\epsilon_{n,\sigma}(\boldsymbol{q}) \overset{\mathcal{T}}{=} \epsilon_{n,-\sigma}(-\boldsymbol{q}) \overset{\mathcal{I}}{=} \epsilon_{n,-\sigma}(\boldsymbol{q})\,. \tag{2.37}$$

The first relation, based on the time reversal symmetry, is reflecting Kramers' theorem. From the first part of Eq. (2.37) it is also clear why the energy bands in general can not be spin-split at the time reversal symmetric points $\boldsymbol{\Gamma}$ and $\boldsymbol{M}$ in the Brillouin zone. In the first case, we have $\epsilon_{n,\sigma}(\boldsymbol{\Gamma}) \overset{\mathcal{T}}{=} \epsilon_{n,-\sigma}(-\boldsymbol{\Gamma}) \equiv \epsilon_{n,-\sigma}(\boldsymbol{\Gamma})$. In the second case, it holds that $\epsilon_{n,\sigma}(\boldsymbol{M}) \overset{\mathcal{T}}{=} \epsilon_{n,-\sigma}(-\boldsymbol{M}) = \epsilon_{n,-\sigma}(\boldsymbol{M}-\boldsymbol{G}_1) \equiv \epsilon_{n,-\sigma}(\boldsymbol{M})$. It is important to note that not all subgroups of D_{6h} contain the space inversion symmetry. Systems, which lack this symmetry, will exhibit in general a lifting of the band degeneracy.

[11] For $\tau = -1$, the conduction band is composed of the states $\{|A_{-\boldsymbol{K}}\downarrow\rangle, |B_{-\boldsymbol{K}}\uparrow\rangle\}$ and the valence band of $\{|A_{-\boldsymbol{K}}\uparrow\rangle, |B_{-\boldsymbol{K}}\downarrow\rangle\}$.

Group/$\mathcal{S}$	E	$2C_6^{\hat{z}}$	$2C_3^{\hat{z}}$	$C_2^{\hat{z}}$	$3C_2^{\hat{x}}$	$3C_2^{\hat{y}}$	$\mathcal{I}$	Σ_h^{xy}	$3\Sigma_v^{yz}$	$3\Sigma_d^{xz}$	$2S_3^{\hat{z}}$	$2S_6^{\hat{z}}$
D_{6h}	✓	✓	✓	✓	✓	✓	✓	✓	✓	✓	✓	✓
D_{3d}	✓	—	✓	—	✓	—	✓	—	✓	—	—	✓
D_{3h}	✓	—	✓	—	—	✓	—	✓	✓	—	✓	—
C_{6v}	✓	✓	✓	✓	—	—	—	—	✓	✓	—	—
C_{3v}	✓	—	✓	—	—	—	—	—	✓	—	—	—

Table 2.1: Symmetry elements of the point group D_{6h} and its subgroups D_{3d}, D_{3h}, C_{6v}, and C_{3v}. See Fig. 2.9 on page 36 for a visualization of the point group symmetries.

2.4.2 Subgroups of D_{6h}

In this section we will give a short overview of graphene systems having a point group symmetry lower than D_{6h}. The lower point group symmetries, which we will address here, arise from structural modifications of the pristine hexagonal symmetry due to (1) *rippling*, (2) *sublattice asymmetry*, and (3) *a transverse electric field or a substrate*:

- *Rippling* reduces $D_{6h} \to D_{3d}$, which is the point group of graphene miniripple, graphane [87], silicene and 'gelicene' [88, 89], etc.;
- *Sublattice inversion asymmetry* reduces $D_{6h} \to D_{3h}$, which is the point group of planar hBN, aluminum nitride, or any other planar hexagonal system with two non-equivalent sublattices A and B;
- *Transverse electric field* reduces $D_{6h} \to C_{6v}$, which is the point group of pristine graphene in an external perpendicular electric field or graphene deposited on a substrate which does not break the sublattice symmetry, as for example SiO_2.

The point groups D_{3d}, D_{3h}, and C_{6v} are subgroups of D_{6h}, each of the three having group order[12] 12. An intersection of any two of the point groups D_{3d}, D_{3h}, C_{6v} is isomorphic [90] to the smaller non-abelian subgroup $C_{3v} \subset D_{6h}$ which has the group order 6. This implies that a graphene system formed by an arbitrary combination of two of the structural modifications (1)-(3) possesses global C_{3v} invariance. The same effective SOC Hamiltonian is valid for all possible combinations. From the effective SOC point of view, graphene miniripple (or graphane, silicene, gelicene) placed in a transverse electric field, $D_{3d} \cap C_{6v}$, is equivalent to a miniripppled boron nitride without the field or free standing graphone (semihydrogenated graphene) [91], $D_{3d} \cap D_{3h}$. Table 2.1 summarizes the symmetries of the respective point groups.

Although the point groups D_{3d}, D_{3h}, and C_{6v} are all subgroups of D_{6h} with the same group order, they result in different SOC phenomena. From the SOC

[12]The group order counts the number of elements in the group [86].

symmetry statements in Sec. 2.3.4, we can conclude on the SOCs that arise in the system of consideration.

2.4.3 SOC and the point group D_{3d}

We consider graphene miniripple as a representative system for the point group D_{3d} in the following. The point group D_{3d} is a subgroup of D_{6h} and thus it "inherits" the intrinsic SOC of graphene, λ_{I}. Additionally, the broken symmetries (see Tab. 2.1) give rise to a second SOC term, λ_{PIA}, which is a spin-flipping contribution that appears in next-nearest neighbor hoppings. The following discussion will clearify the origin of the term and its properties.

Apart from the intrinsic SOC, other spin-conserving contributions are prohibited by the vertical reflection Σ_v^{yz} and translation $T_{\vec{a}}$. Furthermore, the rippled structure breaks the horizontal reflection symmetry, Σ_h^{xy}. Our first symmetry statement in Sec. 2.3.4 predicts the occurrence of a spin-flipping mechanism. According to the second statement, presence of $\mathcal{I}$, $T_{\vec{a}}$, and $\mathcal{T}$, the spin-flipping SOC cannot act between nearest neighbors. All in all, a D_{3d} symmetric structure is subject to two next-nearest neighbor SOCs, a spin-conserving intrinsic SOC and a spin-flipping one. Space inversion $\mathcal{I}$ interchanges sublattices $|A_i\,\sigma\rangle = -\mathcal{I}|B_i\,\sigma\rangle$ and, therefore, both the next-nearest neighbor spin-conserving and spin-flipping SOC terms are not sublattice resolved,

$$\left\langle A_i\,\sigma\middle|\hat{H}_{\mathrm{so}}\middle|A_j\,\sigma'\right\rangle \overset{(2.16)}{=} \left\langle B_i\,\sigma\middle|\hat{H}_{\mathrm{so}}\middle|B_j\,\sigma'\right\rangle . \tag{2.38}$$

As space inversion symmetry is present, see Tab. 2.1, we know from Eq. (2.37) that the bands stay spin-degenerate under the influence of SOC in this system.

How can we label the next-nearest neighbor spin-flipping SOC term in the D_{3d} structure? This SOC matrix element already appeared in the discussion of SOC in bilayer graphene [92], which has the same point group symmetry. At this point in time, its effect was not investigated further. In the study of SOC in silicene (D_{3d}) in Ref. [93], the authors used the term "intrinsic Rashba" to describe the next-nearest neighbor spin-flipping SOC. This terminology can be confusing as the Rashba [94] SOC gives rise to band splittings in graphene which is not the case in the graphene systems with D_{3d} symmetry due to inversion symmetry. In a study of the C_{3v} symmetric semi-hydrogenated graphene, the acronym PIA was introduced for the next-nearest neighbor spin-flipping SOC. In that specific graphene system, the sublattice symmetry is explicitly broken as the point group C_{3v} does not contain a group element which maps sites on sublattice A to sites on sublattice B, see Tab. 2.1, and the SOC coupling is sublattice resolved. The label PIA was introduced there as an abbreviation for "pseudospin (sublattice) inversion asymmetry". Actually, the sublattice inversion asymmetry is not the crucial symmetry which is at the origin of the PIA coupling. For example, in a system with D_{3h} symmetry the sublattice

inversion symmetry is explicitly broken but the PIA coupling does not exist there; it is forbidden by the horizontal reflection Σ_h^{xy}. The same reflection plane is absent in D_{3d} (and C_{3v}) symmetric structures and gives rise to the discussed next-nearest neighbor spin-flipping SOC. We will still employ the label PIA for this coupling although we have to keep in mind that the label PIA is not a suitable acronym to describe the origin of this specific SOC term.

We define the PIA SOC matrix element as the spin-flipping hopping from site A_2 to site A_3,

$$\frac{2}{3}\lambda_{\mathrm{PIA}} \equiv \big\langle A_3\uparrow\big|\hat{H}_{\mathrm{so}}\big|A_2\downarrow\big\rangle\,. \tag{2.39}$$

The prefactor 2/3 is chosen such that the low-energy expansion in the Bloch space is simplified. The matrix element $\langle A_3\uparrow|\hat{H}_{\mathrm{so}}|A_2\downarrow\rangle$ is purely real due to the vertical reflection $\Sigma_v^{yz} \in D_{3d}$,

$$\begin{aligned}\big\langle A_3\uparrow\big|\hat{H}_{\mathrm{so}}\big|A_2\downarrow\big\rangle &\overset{(2.21e)}{=} \big\langle i\Sigma_v^{yz}[A_2\downarrow]\big|\hat{H}_{\mathrm{so}}\big|i\Sigma_v^{yz}[A_3\uparrow]\big\rangle \\ &\overset{(2.16)}{=} \big\langle A_2\downarrow\big|\hat{H}_{\mathrm{so}}\big|A_3\uparrow\big\rangle = \overline{\big\langle A_3\uparrow\big|\hat{H}_{\mathrm{so}}\big|A_2\downarrow\big\rangle}\,.\end{aligned} \tag{2.40}$$

Furthermore, it follows from time reversal symmetry $\mathcal{T}$, Eq. (2.22), for the interchange of lattice sites

$$\frac{2}{3}\lambda_{\mathrm{PIA}} = \big\langle A_3\uparrow\big|\hat{H}_{\mathrm{so}}\big|A_2\downarrow\big\rangle \overset{(2.22)}{=} -\big\langle A_2\uparrow\big|\hat{H}_{\mathrm{so}}\big|A_3\downarrow\big\rangle\,. \tag{2.41}$$

Applying rotations $C_3^{\hat{z}}$, we obtain the remaining PIA related hoppings on the sublattice A,

$$\begin{aligned}\big\langle A_1\uparrow\big|\hat{H}_{\mathrm{so}}\big|A_3\downarrow\big\rangle &\overset{(2.21a)}{=} e^{-i\frac{2\pi}{3}}\big\langle \mathcal{C}_3^{\hat{z}}[A_3\uparrow]\big|\hat{H}_{\mathrm{so}}\big|\mathcal{C}_3^{\hat{z}}[A_2\downarrow]\big\rangle \\ &\overset{(2.16)}{=} e^{-i\frac{2\pi}{3}}\,\frac{2}{3}\lambda_{\mathrm{PIA}}\,,\end{aligned} \tag{2.42}$$

$$\begin{aligned}\big\langle A_2\uparrow\big|\hat{H}_{\mathrm{so}}\big|A_1\downarrow\big\rangle &\overset{(2.21a)}{=} e^{i\frac{2\pi}{3}}\big\langle (\mathcal{C}_3^{\hat{z}})^{-1}[A_3\uparrow]\big|\hat{H}_{\mathrm{so}}\big|(\mathcal{C}_3^{\hat{z}})^{-1}[A_2\downarrow]\big\rangle \\ &\overset{(2.16)}{=} e^{i\frac{2\pi}{3}}\,\frac{2}{3}\lambda_{\mathrm{PIA}}\,.\end{aligned} \tag{2.43}$$

The spin-flipping matrix elements between B sublattice sites follow directly from the A sublattice terms with the help of Eq. (2.38) (space inversion). For a general matrix element, we express the occurring phase factors by writing

$$\big\langle X_m\,\sigma\,\big|\hat{H}_{\mathrm{so}}\big|X_n\,\sigma'\big\rangle = \big[\sigma_z\big]_{XX}\big[i\hat{\boldsymbol{s}}\times\boldsymbol{d}_{m,n}\big]_{z,\sigma\sigma'}\,\frac{2}{3}\,\lambda_{\mathrm{PIA}}\,. \tag{2.44}$$

Here, the quantity $\boldsymbol{d}_{m,n} = \overrightarrow{mn}/|\overrightarrow{mn}|$ is a unit vector in the horizontal xy-plane and points from the lattice site n to the next nearest neighbor site m, and $\hat{\boldsymbol{s}}$ stands

for the array of spin-Pauli matrices. Note that the relation between the matrix elements for sites on the sublattices A and B, Eq. (2.38), is incorporated in the above formula. Under interchange of sublattices, we have $[\hat{\sigma}_z]_{AA} = -[\hat{\sigma}_z]_{BB}$, or equivalently $[\hat{\sigma}_z]_{\mathcal{I}(X)\mathcal{I}(X)} = -[\hat{\sigma}_z]_{XX}$, and $\boldsymbol{d}_{\mathcal{I}(m),\mathcal{I}(n)} = -\boldsymbol{d}_{m,n}$. In total, the two minus signs cancel.

We keep the conventions for the intrinsic coupling λ_{I} as introduced for the D_{6h} invariant graphene, Eqs. (2.30) and (2.31). The SOC Hamiltonian for the D_{3d} invariant system of graphene miniripple is then given by

$$\begin{aligned}\mathcal{H}_{D_{3d}} = {} & \frac{i\lambda_{\mathrm{I}}}{3\sqrt{3}} \sum_{\sigma} \sum_{\langle\langle m,n \rangle\rangle} \nu_{m,n} \left[\hat{s}_z\right]_{\sigma\sigma} \left|X_m\,\sigma\right\rangle \left\langle X_n\,\sigma\right| \\ & + \frac{2\lambda_{\mathrm{PIA}}}{3} \sum_{\sigma\neq\sigma'} \sum_{\langle\langle m,n \rangle\rangle} \left[\hat{\sigma}_z\right]_{XX} \left[i\hat{\boldsymbol{s}} \times \boldsymbol{d}_{m,n}\right]_{z,\sigma\sigma'} \left|X_m\,\sigma\right\rangle \left\langle X_n\,\sigma'\right| , \end{aligned} \tag{2.45}$$

and we obtain for the Bloch form, $\mathcal{H}_{D_{3d}} = \sum_{\boldsymbol{q}} \mathcal{H}_{D_{3d}}(\boldsymbol{q})$,

$$\begin{aligned}\mathcal{H}_{D_{3d}}(\boldsymbol{q}) = \sum_{X,\sigma,\sigma'} \left[\hat{\sigma}_z\right]_{XX} \Big\{ & \lambda_{\mathrm{I}} f_{\mathrm{I}}(\boldsymbol{q}) \left[\hat{s}_z\right]_{\sigma\sigma'} + \lambda_{\mathrm{PIA}} f_{\mathrm{P}}(\boldsymbol{q}) \left[\hat{s}_+\right]_{\sigma\sigma'} \\ & + \lambda_{\mathrm{PIA}} \overline{f_{\mathrm{P}}(\boldsymbol{q})} \left[\hat{s}_-\right]_{\sigma\sigma'} \Big\} \left|X_{\boldsymbol{q}}\,\sigma\right\rangle \left\langle X_{\boldsymbol{q}}\,\sigma'\right| , \end{aligned} \tag{2.46}$$

with the structural SOC functions $f_{\mathrm{I}}(\boldsymbol{q})$, Eq. (2.33), and $f_{\mathrm{P}}(\boldsymbol{q})$,

$$f_{\mathrm{P}}(\boldsymbol{q}) = \frac{4i}{3} \Big\{ \sin \boldsymbol{q}.\boldsymbol{R}_1 + \mathrm{e}^{-i\frac{2\pi}{3}} \sin \boldsymbol{q}.\boldsymbol{R}_2 + \mathrm{e}^{+i\frac{2\pi}{3}} \sin \boldsymbol{q}.\boldsymbol{R}_3 \Big\} . \tag{2.47}$$

The structural function $f_{\mathrm{P}}(\boldsymbol{q})$ vanishes at the high symmetry points $\boldsymbol{\Gamma}$ and $\tau\boldsymbol{K}$ but has a finite value at $\boldsymbol{M}$.

As the conduction and valence bands are twofold degenerate, Eq. (2.37), the spin quantization axis can be chosen freely. For $\lambda_{\mathrm{PIA}} \neq 0$, we see that $\mathcal{H}_{D_{3d}}(\boldsymbol{q})$ commutes with the spin operator (given here in units of $\hbar/2$)

$$\mathrm{Spin}(\boldsymbol{q}) = \hat{\sigma}_0 \left[f_{\mathrm{P}}(\boldsymbol{q})\, \hat{s}_+ + \overline{f_{\mathrm{P}}(\boldsymbol{q})}\, \hat{s}_- + \frac{\lambda_{\mathrm{I}}}{\lambda_{\mathrm{PIA}}}\, f_{\mathrm{I}}(\boldsymbol{q})\, \hat{s}_z \right] , \tag{2.48}$$

which depends on the quasi-momentum $\mathbf{q}$. This is a conserved spin-quantity and we therefore describe the eigenstates of $H_{\mathrm{orb}}(\boldsymbol{q}) + \mathcal{H}_{D_{3d}}(\boldsymbol{q})$ as "spin-up" and "spin-down" states with respect to the momentum dependent quantization axis

$$\boldsymbol{n}(\boldsymbol{q}) = \frac{\Big(\mathrm{Re}\big[f_{\mathrm{P}}(\boldsymbol{q})\big], -\mathrm{Im}\big[f_{\mathrm{P}}(\boldsymbol{q})\big], \frac{\lambda_{\mathrm{I}}}{\lambda_{\mathrm{PIA}}} f_{\mathrm{I}}(\boldsymbol{q})\Big)}{\sqrt{\big|f_{\mathrm{P}}(\boldsymbol{q})\big|^2 + \frac{\lambda_{\mathrm{I}}^2}{\lambda_{\mathrm{PIA}}^2} \big|f_{\mathrm{I}}(\boldsymbol{q})\big|^2}} . \tag{2.49}$$

For $\lambda_{\mathrm{PIA}} = 0$, we have $\mathrm{Spin}(\boldsymbol{q}) = \lambda_{\mathrm{I}} f_{\mathrm{I}}(\boldsymbol{q}) \hat{\sigma}_0 \hat{s}_z$ and the spin quantization axis is oriented along z, $\boldsymbol{n}(\boldsymbol{q}) = (0, 0, \tau)$. We recover the limit of a D_{6h} invariant system.

Directly at the Dirac points, we have $f_{\mathrm{P}}(\tau\boldsymbol{K}) = 0$ and $f_{\mathrm{I}}(\tau\boldsymbol{K}) = \tau$ and again $\boldsymbol{n}(\tau\boldsymbol{K}) = (0, 0, \tau)$. At the $\boldsymbol{M}$ point, where $f_{\mathrm{I}}(\boldsymbol{M}) = 0$ the PIA structure function remains finite and $\boldsymbol{n}(\boldsymbol{M})$ is still well defined. However, at the $\boldsymbol{\Gamma}$ point ($\boldsymbol{q} = 0$) both f_{P} and f_{I} vanish and $\boldsymbol{n}(\boldsymbol{\Gamma})$ is not well defined.

In the following we will concentrate on the region around the Dirac points, $\boldsymbol{q} = \tau\boldsymbol{K} + \boldsymbol{k}$. Up to the first non-vanishing term, the expansion of f_{P} is given by

$$f_{\mathrm{P}}(\tau\boldsymbol{K} + \boldsymbol{k}) \simeq -(ik_x + k_y)a_{\mathrm{L}}\,, \tag{2.50}$$

where a_{L} is the lattice constant. Going to the ordered Bloch basis $\{|A_{\boldsymbol{q}}\uparrow\rangle, |A_{\boldsymbol{q}}\downarrow\rangle, |B_{\boldsymbol{q}}\uparrow\rangle, |B_{\boldsymbol{q}}\downarrow\rangle\}$, we obtain the effective D_{3d} invariant low-energy Hamiltonian around the $\tau\boldsymbol{K}$ valley,

$$\begin{aligned}\mathcal{H}_{\mathrm{eff}}(\tau\boldsymbol{K} + \boldsymbol{k}) = \hbar v_F \left(\tau k_x\hat{\sigma}_x - k_y\hat{\sigma}_y\right)\hat{s}_0 + \tau\lambda_{\mathrm{I}}\hat{\sigma}_z\hat{s}_z \\ + \lambda_{\mathrm{PIA}}\hat{\sigma}_z(k_x\hat{s}_y - k_y\hat{s}_x)a_{\mathrm{L}}\,.\end{aligned} \tag{2.51}$$

With the spin σ determined with respect to the momentum dependent spin quantization axis,

$$\boldsymbol{n}(\tau\boldsymbol{K} + \boldsymbol{k}) = \frac{\left(-k_y a_{\mathrm{L}}, k_x a_{\mathrm{L}}, \tau\frac{\lambda_{\mathrm{I}}}{\lambda_{\mathrm{PIA}}}\right)}{\sqrt{(k_x^2 + k_y^2)a_{\mathrm{L}}^2 + \frac{\lambda_{\mathrm{I}}^2}{\lambda_{\mathrm{PIA}}^2}}}\,, \tag{2.52}$$

the eigenspectrum of $\mathcal{H}_{\mathrm{eff}}(\tau\boldsymbol{K} + \boldsymbol{k})$ is given by

$$\epsilon_{n,\sigma}(\tau\boldsymbol{K} + \boldsymbol{k}) = n\sqrt{\lambda_{\mathrm{I}}^2 + \left(\hbar^2 v_F^2 + \lambda_{\mathrm{PIA}}^2 a_{\mathrm{L}}^2\right)\left(k_x^2 + k_y^2\right)}\,. \tag{2.53}$$

Both conduction ($n = +1$) and valence band ($n = -1$) are spin degenerate as expected from space inversion symmetry, Eq. (2.37). Figure 2.5 displays the electronic band structure resulting from $\epsilon_{n,\sigma}(\tau\boldsymbol{K} + \boldsymbol{k})$ and the momentum dependent spin quantization axis $\boldsymbol{n}(\tau\boldsymbol{K} + \boldsymbol{k})$. The PIA SOC gives rise to two effects: On the one hand, λ_{PIA} effectively renormalizes the Fermi velocity $v_F \to \sqrt{v_F^2 + \lambda_{\mathrm{PIA}}^2 a_{\mathrm{L}}^2/\hbar^2}$, or equivalently, the orbital nearest neighbor hopping $t \to \sqrt{t^2 + 4\lambda_{\mathrm{PIA}}^2/3}$ when we use the equality $v_F = \sqrt{3}a_L t/2$. The effect of λ_{PIA} is marginal for $\lambda_{\mathrm{PIA}} \ll t$, as for example in silicene [93] $t \simeq 1.1\,\mathrm{eV}$ and $\lambda_{\mathrm{PIA}} \simeq 0.7\,\mathrm{meV}$, but can become important for $\lambda_{\mathrm{PIA}} \sim t$. For example, in gelicene [93] with $t \simeq 0.9\,\mathrm{eV}$ and $\lambda_{\mathrm{PIA}} \simeq 10.7\,\mathrm{meV}$ the effect of λ_{PIA} on the band dispersion should be more pronounced. On the other hand, as seen from Eq. (2.52), λ_{PIA} gives rise to the in-plane component of $\boldsymbol{n}(\boldsymbol{q}).\hat{\boldsymbol{s}}$, see Fig. 2.5(b).

2.4.4 SOC and the point group D_{3h}

Instead of rippling, as discussed in the previous section, we consider in the following the effect of sublattice inversion asymmetry on the SOC terms. Planar hBN represents a hexagonal structure with a two-atomic basis formed of boron and nitrogen

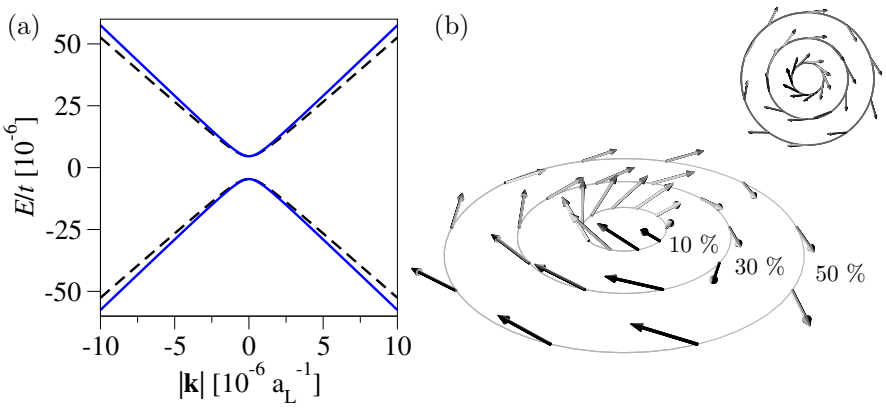

Figure 2.5: Electronic band structure and conserved spin quantity around the $\boldsymbol{K}$ point for a D_{3d} invariant SOC Hamiltonian. Panel (a) shows the electronic band structure for $t = 2.6\,\mathrm{eV}$, $\lambda_\mathrm{I} = 12\,\mu\mathrm{eV}$, and $\lambda_\mathrm{PIA} = 0.1\,\mathrm{eV}$ (black dashed) and $\lambda_\mathrm{PIA} = 1\,\mathrm{eV}$ (blue solid), respectively. The coupling λ_PIA renormalizes the Fermi velocity. Panel (b) displays the momentum dependent quantization axis $\boldsymbol{n}(\boldsymbol{q})$ defined by the conserved spin quantity, Eq. (2.49), around the $\boldsymbol{K}$ point along circles with the radius measuring 10%, 30%, and 50% of the distance $\overline{\boldsymbol{KM}}$. The chosen parameters are $t = 2.6\,\mathrm{eV}$, $\lambda_\mathrm{I} = 12\,\mu\mathrm{eV}$, and $\lambda_\mathrm{PIA} = 60\,\mu\mathrm{eV}$. Away from the $\boldsymbol{K}$ point, the in-plane components of $\boldsymbol{n}(\boldsymbol{q})$ increase. A top view of the orientation of the spin quantization axis is shown in the inset, which reveals that the circular low energy symmetry changes to the triangular one for larger radii.

atoms. The resulting two triangular sublattices are distinct, and any symmetry operation which could connect the non-equivalent sites is absent. The structure of hBN is invariant under the point group symmetry D_{3h}, see Tab. 2.1. Then, according to the symmetry statements in Sec. 2.3.4, we know that spin-flipping SOC terms do not occur (forbidden by Σ_h^{xy}) and also nearest neighbor spin-conserving SOCs are not present (forbidden by Σ_v^{yz} and $T_{\vec{a}}$). We are left with the intrinsic SOC, the next-nearest neighbor spin-conserving term which is allowed already by the D_{6h} symmetry. However, the intrinsic SOC is here sublattice dependent, and in general we have $\lambda_\mathrm{I}^\mathrm{A} \neq \lambda_\mathrm{I}^\mathrm{B}$ due to the sublattice inversion asymmetry. Furthermore, as space inversion $\mathcal{I}$ is not a symmetry of the system, spin-orbit induced band splittings can occur in a D_{3h} symmetric system. The statement of Eq. (2.37) is in general not fulfilled.

We define the intrinsic SOC couplings with the matrix elements,

$$\frac{i\lambda_\mathrm{I}^\mathrm{A}}{3\sqrt{3}} = \big\langle A_3\uparrow \big| \hat{H}_\mathrm{so} \big| A_2\uparrow \big\rangle, \tag{2.54a}$$

$$\frac{i\lambda_\mathrm{I}^\mathrm{B}}{3\sqrt{3}} = \big\langle B_3\uparrow \big| \hat{H}_\mathrm{so} \big| B_2\uparrow \big\rangle\,. \tag{2.54b}$$

As in the previous sections, we use the site labeling convention shown in Fig. 2.3(b). In the special case $\lambda_{\mathrm{I}}^{\mathrm{A}} = \lambda_{\mathrm{I}}^{\mathrm{B}}$, we recover our conventions introduced for the case of D_{6h}. Taking into account the sublattice resolved nature of the intrinsic SOC, we obtain analogously to Eq. (2.30) the D_{3h} invariant SOC Hamiltonian,

$$\begin{aligned}\mathcal{H}_{D_{3h}} = &\frac{i\lambda_{\mathrm{I}}^{\mathrm{A}}}{3\sqrt{3}} \sum_{\sigma} \sum_{\langle\langle m,n \rangle\rangle} \nu_{m,n} \left[\hat{s}_z\right]_{\sigma\sigma} \left|A_m\,\sigma\right\rangle \left\langle A_n\,\sigma\right| \\ &+ \frac{i\lambda_{\mathrm{I}}^{\mathrm{B}}}{3\sqrt{3}} \sum_{\sigma} \sum_{\langle\langle m,n \rangle\rangle} \nu_{m,n} \left[\hat{s}_z\right]_{\sigma\sigma} \left|B_m\,\sigma\right\rangle \left\langle B_n\,\sigma\right| . \end{aligned} \tag{2.55}$$

As A and B sublattice sites are nonequivalent, they can have in general different on-site energies which, for example, reflect a different electrostatic environment for the atoms boron and nitride in hBN. As A and B sites appear alternating in the lattice, the alternating on-site energies are described by a so-called staggered potential[13] Δ. Including this potential term in the orbital Hamiltonian, we obtain the low-energy Bloch representation of $\mathcal{H}_0(\tau\boldsymbol{K}+\boldsymbol{k}) + \mathcal{H}_{D_{3h}}(\tau\boldsymbol{K}+\boldsymbol{k})$,

$$\begin{aligned}\mathcal{H}_{\mathrm{eff}}(\tau\boldsymbol{K}+\boldsymbol{k}) = &\hbar v_F \left(\tau k_x \hat{\sigma}_x - k_y \hat{\sigma}_y\right)\hat{s}_0 + \Delta\,\hat{\sigma}_z \hat{s}_0 + \\ &+ \frac{\tau}{2}\left[\lambda_{\mathrm{I}}^{\mathrm{A}}(\hat{\sigma}_z + \hat{\sigma}_0) + \lambda_{\mathrm{I}}^{\mathrm{B}}(\hat{\sigma}_z - \hat{\sigma}_0)\right]\hat{s}_z\,. \end{aligned} \tag{2.56}$$

Note that in the second line a combination of $\hat{\sigma}_z$ and $\hat{\sigma}_0$ is introduced to obtain (for spin up) $\tau\lambda_{\mathrm{I}}^{\mathrm{A}}$ as the coupling between A sublattice sites and $-\tau\lambda_{\mathrm{I}}^{\mathrm{B}}$ as the coupling between B sublattice sites, in agreement with Eqs. (2.54) and (2.55). We label the eigenstates of $\mathcal{H}_{\mathrm{eff}}$ by the spin up and spin down projections along the z spin quantization axis, as the spin operator $\hat{\sigma}_0\,\hat{s}_z$ commutes with the Hamiltonian. We obtain then for the eigenspectrum around a Dirac point

$$\begin{aligned}\epsilon_{n,\sigma}(\tau\boldsymbol{K}+\boldsymbol{k}) = &\tfrac{\sigma}{2}(\lambda_{\mathrm{I}}^{\mathrm{A}} - \lambda_{\mathrm{I}}^{\mathrm{B}}) \\ &+ n\sqrt{\left[\Delta + \tfrac{\sigma}{2}(\lambda_{\mathrm{I}}^{\mathrm{A}} + \lambda_{\mathrm{I}}^{\mathrm{B}})\right]^2 + \hbar^2 v_F^2 (k_x^2 + k_y^2)}\,. \end{aligned} \tag{2.57}$$

As before, conduction and valence bands are labeled with $n = +1$ and $n = -1$, respectively, and the spin index is given by $\sigma = \{\uparrow, \downarrow\} = \{+1, -1\}$. Equation (2.57) reveals that for $\lambda_{\mathrm{I}}^{\mathrm{A}} \neq \lambda_{\mathrm{I}}^{\mathrm{B}}$ the bands are spin-split.

Figure 2.6 displays the electronic band structure around the $\boldsymbol{K}$ point for various realizations of $\lambda_{\mathrm{I}}^{\mathrm{A}}$, $\lambda_{\mathrm{I}}^{\mathrm{B}}$, and the influence of the staggered potential strength Δ. We can distinguish two "spectral" cases, the band-inverted (gapless) and the insulating (gapped) one. For $\Delta = 0$, the gapless regime is realized for all intrinsic

[13] The zero energy reference point is chosen to lie in the middle of the two on-site energies ε_A and ε_B, and the staggered potential takes the two values $+\Delta$, $-\Delta$ depending on the sublattice. The staggered potential strength is defined as $\Delta = |\varepsilon_A - \varepsilon_B|/2$.

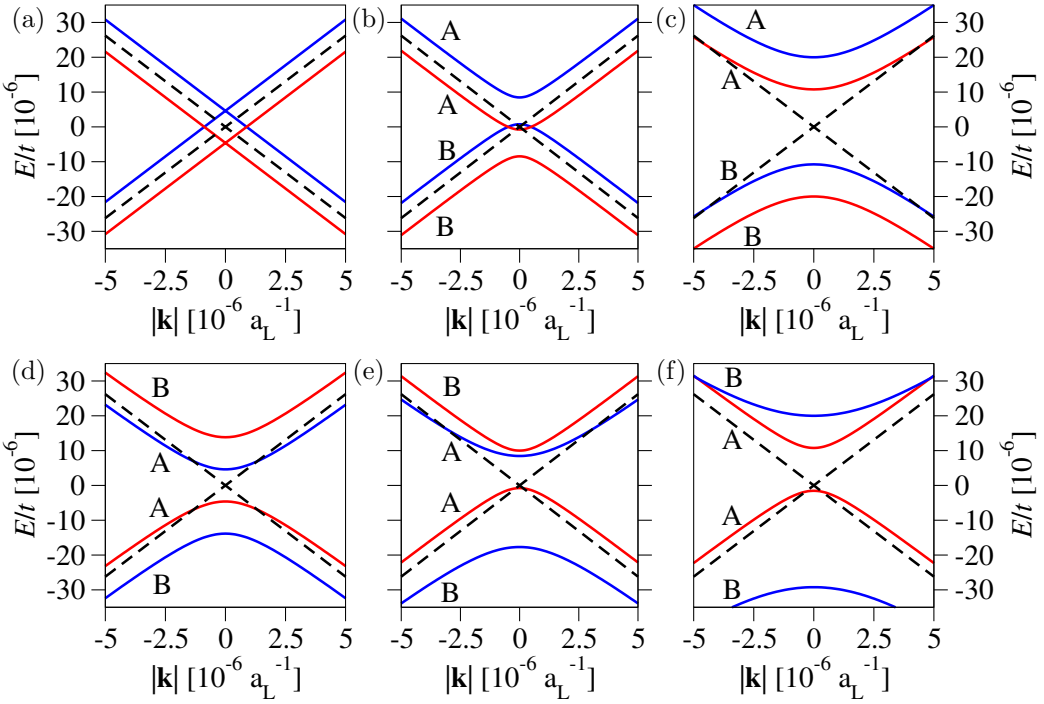

Figure 2.6: Electronic band structure around the $\boldsymbol{K}$ point for a D_{3h} invariant SOC Hamiltonian. For $t = 2.6\,\mathrm{eV}$ and $\lambda_\mathrm{I}^\mathrm{A} = 12\,\mu\mathrm{eV}$, a band-inverted regime is observed for (a) $\lambda_\mathrm{I}^\mathrm{A} = -\lambda_\mathrm{I}^\mathrm{B}$, $\Delta = 0$. The spectrum remains inverted for (b) $\Delta = 10\,\mu\mathrm{eV} < \max(|\lambda_\mathrm{I}^\mathrm{A}|, \lambda_\mathrm{I}^\mathrm{B}|)$. (c) The system is insulating for larger $\Delta = 40\,\mu\mathrm{eV}$. If (d) $\lambda_\mathrm{I}^\mathrm{B} = 3\lambda_\mathrm{I}^\mathrm{A}$ and $\Delta = 0$, the spectrum is gapped and stays gapped for larger Δ, such as (e) $\Delta = 10\,\mu\mathrm{eV}$ and (f) $\Delta = 40\,\mu\mathrm{eV}$. A crossing between the two conduction bands occurs in case (f). Blue and red lines indicate the $\uparrow$ and $\downarrow$ spin projections of the bands, respectively. The dominant sublattice population is indicated by the labels A and B and extracted for momenta close to the $\boldsymbol{K}$ point. In case (a), the A and B sublattices are equally occupied for all electronic bands. For comparison, the energy dispersion of pristine graphene without SOC and $\Delta = 0$ is displayed with black dashed lines.

couplings with $\mathrm{sign}(\lambda_\mathrm{I}^\mathrm{A}) \neq \mathrm{sign}(\lambda_\mathrm{I}^\mathrm{B})$ and, accordingly, the gapped regime is reached for $\mathrm{sign}(\lambda_\mathrm{I}^\mathrm{A}) = \mathrm{sign}(\lambda_\mathrm{I}^\mathrm{B})$. Representative examples are shown in Fig. 2.6(a) and (d). Varying the staggered potential, $\Delta \neq 0$, one can drive a transition between the two regimes. For $|\Delta| < \max(|\lambda_\mathrm{I}^\mathrm{A}|, |\lambda_\mathrm{I}^\mathrm{B}|)$ [and $\mathrm{sign}(\lambda_\mathrm{I}^\mathrm{A}) \neq \mathrm{sign}(\lambda_\mathrm{I}^\mathrm{B})$] we stay in the band-inverted case, Fig. 2.6(b); for $|\Delta|$ exceeding this threshold value a band gap opens, Fig. 2.6(c). If we start in the gapped regime, $\mathrm{sign}(\lambda_\mathrm{I}^\mathrm{A}) = \mathrm{sign}(\lambda_\mathrm{I}^\mathrm{B})$, the gap cannot be closed with varying Δ, Fig. 2.6(e) and (f). Furthermore, if $|\Delta| > |\lambda_\mathrm{I}^\mathrm{A} - \lambda_\mathrm{I}^\mathrm{B}|/2 \neq 0$ in the gapped regime, the two conduction (or depending on the parameter values, the two valence) bands cross, Fig. 2.6(f). In the two-dimensional Brillouin zone, the crossing occurs along a circle with its center placed at the Dirac point and a radius of

$$k_\mathrm{cr} = \frac{\sqrt{\lambda_\mathrm{I}^\mathrm{A}\lambda_\mathrm{I}^\mathrm{B}}}{\hbar v_F}\sqrt{\frac{4\Delta^2}{(\lambda_\mathrm{I}^\mathrm{A} - \lambda_\mathrm{I}^\mathrm{B})^2} - 1}\,. \tag{2.58}$$

2.4.5 SOC and the point group C_{6v}

As a third example, we consider SOC in graphene under the influence of an external transverse electric field. The point group for such a minimal structural modification of pristine graphene is C_{6v}. With a glance at Tab. 2.1, we know that the two sublattices A and B are connected by symmetry, e.g. by the diagonal reflection Σ_d^{xz}, or the rotations $C_2^{\hat{z}}$ and $C_6^{\hat{z}}$. This means that any next-nearest neighbor SOC will not be sublattice resolved, in contrast to the previous section. The transverse electric field assigns an effective orientation to the graphene system so that C_{6v} does not contain any symmetry element which would flip the orientation of the z axis, i.e., Σ_h^{xy} and $\mathcal{I}$ are not present. The first symmetry statement predicts that spin-flipping SOCs are allowed due to absence of Σ_h^{xy}. Furthermore, we have no restriction on the kind of neighbors that are coupled by the SOC since the second symmetry statement does not take effect. Space inversion $\mathcal{I}$ is not a symmetry of the system. In general, graphene in a transverse electric field is subject to both nearest neighbor and next-nearest neighbor spin-flipping SOC. Nearest neighbor spin-conserving SOC is forbidden due to the presence of Σ_v^{yz} (third symmetry statement). In total, we expect three SOC terms: spin-conserving intrinsic λ_I, spin-flipping PIA λ_PIA [see Eqs. (2.31) and (2.41)], and a third one which resembles the nearest neighbor spin-flipping interaction. By convention, we call this third term the Rashba SOC [67, 94].

For the Rashba coupling λ_R we take as the defining matrix element

$$\frac{2}{3}i\lambda_\mathrm{R} \equiv \big\langle A_2\uparrow\big|\hat{H}_\mathrm{so}\big|B_3\downarrow\big\rangle \overset{(2.22)}{=} -\big\langle B_3\uparrow\big|\hat{H}_\mathrm{so}\big|A_2\downarrow\big\rangle\,. \tag{2.59}$$

This coupling is purely imaginary, as can be shown by diagonal reflection Σ_d^{xz},

$$\begin{aligned}\big\langle A_2\uparrow\big|\hat{H}_{\mathrm{so}}\big|B_3\downarrow\big\rangle &\overset{(2.21f)}{=} \big\langle\Sigma_d^{xz}[B_3\downarrow]\big|\hat{H}_{\mathrm{so}}\big|-\Sigma_d^{xz}[A_2\uparrow]\big\rangle \\ &\overset{(2.16)}{=} -\big\langle B_3\downarrow\big|\hat{H}_{\mathrm{so}}\big|A_2\uparrow\big\rangle = -\overline{\big\langle A_2\uparrow\big|\hat{H}_{\mathrm{so}}\big|B_3\downarrow\big\rangle}\,. \end{aligned} \tag{2.60}$$

By rotation $C_3^{\hat{z}}$ and translation, we can relate the matrix element $\big\langle A_2\uparrow\big|\hat{H}_{\mathrm{so}}\big|B_3\downarrow\big\rangle$ to any general nearest neighbor spin-flipping element $\big\langle X_m\,\sigma\,\big|\hat{H}_{\mathrm{so}}\big|X_n\,\sigma'\big\rangle$. Similar as in the case of the PIA SOC (next-nearest neighbor spin-flipping SOC), Eq. (2.44), we describe the phase factors for a general Rashba-like hopping by

$$\big\langle X_m\,\sigma\,\big|\hat{H}_{\mathrm{so}}\big|X_n\,\sigma'\big\rangle = \big[\hat{\boldsymbol{s}}\times\boldsymbol{d}_{m,n}\big]_{z,\sigma\sigma'}\big\langle A_2\uparrow\big|\hat{H}_{\mathrm{so}}\big|B_3\downarrow\big\rangle = \big[\hat{\boldsymbol{s}}\times\boldsymbol{d}_{m,n}\big]_{z,\sigma\sigma'}\frac{2}{3}i\lambda_{\mathrm{R}}\,. \tag{2.61}$$

As previously, $\boldsymbol{d}_{m,n} = \overrightarrow{mn}/|\overrightarrow{mn}|$ is the unit vector in the horizontal xy-plane pointing now from lattice site n to a nearest neighbor site m.

In the case of graphene miniripple (D_{3d}) the PIA coupling on the A sublattice was connected to the coupling on the B sublattice by inversion symmetry, Eq. (2.38). Here, in C_{6v}, the inversion symmetry is absent. However, the A and B sublattices are connected by $C_2^{\hat{z}}$. The relative phase factor between the PIA couplings on opposite sublattices (with $\sigma\neq\sigma'$) is therefore accompanied by an additional minus sign compared to Eq. (2.38),

$$\big\langle A_i\,\sigma\,\big|\hat{H}_{\mathrm{so}}\big|A_j\,\sigma'\big\rangle \overset{(2.21a)}{=} \big\langle e^{i\frac{\pi}{2}\sigma}C_2^{\hat{z}}[B_i\,\sigma]\,\big|\hat{H}_{\mathrm{so}}\big|e^{i\frac{\pi}{2}\sigma'}C_2^{\hat{z}}[B_j\,\sigma']\big\rangle \tag{2.62}$$

$$\overset{(2.16)}{=} e^{i\frac{\pi}{2}(\sigma'-\sigma)}\big\langle B_i\,\sigma\,\big|\hat{H}_{\mathrm{so}}\big|B_j\,\sigma'\big\rangle = -\big\langle B_i\,\sigma\,\big|\hat{H}_{\mathrm{so}}\big|B_j\,\sigma'\big\rangle\,. \tag{2.63}$$

Accordingly, the phase factor description of Eq. (2.44) has to be modified for the PIA coupling in the C_{6v} invariant structure,

$$\big\langle X_m\,\sigma\,\big|\hat{H}_{\mathrm{so}}\big|X_n\,\sigma'\big\rangle = \big[i\hat{\boldsymbol{s}}\times\boldsymbol{d}_{m,n}\big]_{z,\sigma\sigma'}\frac{2}{3}\lambda_{\mathrm{PIA}}\,. \tag{2.64}$$

All in all, the SOC terms originating from the π-states in a C_{6v} invariant system (in presence of translational and time reversal symmetry) are described by the SOC Hamiltonian,

$$\begin{aligned}\mathcal{H}_{C_{6v}} = {}& \frac{i\lambda_{\mathrm{I}}}{3\sqrt{3}}\sum_{\sigma}\sum_{\langle\langle m,n\rangle\rangle}\nu_{m,n}\big[\hat{s}_z\big]_{\sigma\sigma}\big|X_m\,\sigma\big\rangle\big\langle X_n\,\sigma\big| \\ &+\frac{2\lambda_{\mathrm{PIA}}}{3}\sum_{\sigma\neq\sigma'}\sum_{\langle\langle m,n\rangle\rangle}\big[i\hat{\boldsymbol{s}}\times\boldsymbol{d}_{m,n}\big]_{z,\sigma\sigma'}\big|X_m\,\sigma\big\rangle\big\langle X_n\,\sigma'\big| \\ &+\frac{2i\lambda_{\mathrm{R}}}{3}\sum_{\sigma\neq\sigma'}\sum_{\langle m,n\rangle}\big[\hat{\boldsymbol{s}}\times\boldsymbol{d}_{m,n}\big]_{z,\sigma\sigma'}\big|X_m\,\sigma\big\rangle\big\langle X_n\,\sigma'\big|\,. \end{aligned} \tag{2.65}$$

In the literature, see for example Refs. [67, 95], the C_{6v} invariant SOC Hamiltonian often contains only the intrinsic and Rashba SOC. However, the symmetries of C_{6v} do not forbid the existence of the PIA coupling. In order to prohibit the PIA term $\lambda_{\mathrm{PIA}} \sim \langle A_3 \uparrow |\hat{H}_{\mathrm{so}}| A_2 \downarrow\rangle$ by symmetry arguments, we would have to find a combination of symmetries $\mathcal{S}_i$ in Tab. 2.1 which maps the real matrix element $\langle A_3 \uparrow |\hat{H}_{\mathrm{so}}| A_2 \downarrow\rangle \xrightarrow{\prod_i \mathcal{S}_i} -\langle A_3 \uparrow |\hat{H}_{\mathrm{so}}| A_2 \downarrow\rangle$. A candidate would be, for example, the combined operation $\mathcal{S} = \Sigma_v^{yz} \circ \Sigma_d^{xz} \circ C_2^{\hat{z}}$. However, this operation acts as an identity on the orbital and spin space as $C_2^{\hat{z}} \equiv \Sigma_d^{xz} \circ \Sigma_v^{yz}$. Employing only rotations $C_3^{\hat{z}}$ and $C_6^{\hat{z}}$ does not bring about the desired minus sign since the arising phase factors add up to unity. Symmetry combinations that effectively reduce to Σ_v^{yz}, e.g. $\Sigma_d^{xz} \circ C_3^{\hat{z}} \circ C_6^{\hat{z}}$, only show that the matrix element $\langle A_3 \uparrow |\hat{H}_{\mathrm{so}}| A_2 \downarrow\rangle$ is a real quantity, see Eq. (2.40). Therefore, PIA cannot be neglected in general.

For the Bloch form of the C_{6v} invariant SOC Hamiltonian, $\mathcal{H}_{C_{6v}} = \sum_{\boldsymbol{q}} \mathcal{H}_{C_{6v}}(\boldsymbol{q}) = \sum_{\boldsymbol{q}} \mathcal{H}_{\mathrm{I}}(\boldsymbol{q}) + \mathcal{H}_{\mathrm{P}}(\boldsymbol{q}) + \mathcal{H}_{\mathrm{R}}(\boldsymbol{q})$, we already know the intrinsic term and, omitting in the spin-flip related part of Eq. (2.46) the factor $[\hat{\sigma}_z]_{XX}$, also the PIA contribution,

$$\mathcal{H}_{\mathrm{I}}(\boldsymbol{q}) = \sum_{X,\sigma,\sigma'} \big[\hat{\sigma}_z\big]_{XX} \lambda_{\mathrm{I}} f_{\mathrm{I}}(\boldsymbol{q}) \big[\hat{s}_z\big]_{\sigma\sigma'} \big|X_{\boldsymbol{q}}\,\sigma\big\rangle\big\langle X_{\boldsymbol{q}}\,\sigma'\big|\,, \tag{2.66a}$$

$$\mathcal{H}_{\mathrm{P}}(\boldsymbol{q}) = \sum_{X,\sigma,\sigma'} \lambda_{\mathrm{PIA}} \Big\{ f_{\mathrm{P}}(\boldsymbol{q}) \big[\hat{s}_+\big]_{\sigma\sigma'} + \overline{f_{\mathrm{P}}(\boldsymbol{q})} \big[\hat{s}_-\big]_{\sigma\sigma'} \Big\} \big|X_{\boldsymbol{q}}\,\sigma\big\rangle\big\langle X_{\boldsymbol{q}}\,\sigma'\big|\,. \tag{2.66b}$$

For the part related to the Rashba SOC, we obtain

$$\begin{aligned}\mathcal{H}_{\mathrm{R}}(\boldsymbol{q}) =& i\lambda_{\mathrm{R}} \sum_{\sigma,\sigma'} \sum_{X,X'} \Big\{ \big[\hat{\sigma}_+\big]_{XX'} \Big(f_{\mathrm{R}}(\boldsymbol{q}) \big[\hat{s}_+\big]_{\sigma\sigma'} + \overline{f_{\mathrm{R}}(-\boldsymbol{q})} \big[\hat{s}_-\big]_{\sigma\sigma'} \Big) \\ &- \big[\hat{\sigma}_-\big]_{XX'} \Big(\overline{f_{\mathrm{R}}(\boldsymbol{q})} \big[\hat{s}_-\big]_{\sigma\sigma'} + f_{\mathrm{R}}(-\boldsymbol{q}) \big[\hat{s}_+\big]_{\sigma\sigma'} \Big) \Big\} \big|X_{\ q}\,\sigma\big\rangle\big\langle X'_{\boldsymbol{q}}\,\sigma'\big|\,,\end{aligned} \tag{2.67}$$

with the structural function

$$f_{\mathrm{R}}(\boldsymbol{q}) = \frac{2}{3}\Big\{ 1 + \mathrm{e}^{-i\frac{2\pi}{3}} \mathrm{e}^{-i\boldsymbol{q}.\boldsymbol{R}_3} + \mathrm{e}^{i\frac{2\pi}{3}} \mathrm{e}^{i\boldsymbol{q}.\boldsymbol{R}_2} \Big\}\,. \tag{2.68}$$

In analogy to the spin-raising $[\hat{s}_+]$ and spin-lowering $[\hat{s}_-]$ operators, we used in Eq. (2.67) the sublattice (pseudospin) lowering and raising operators $\hat{\sigma}_\pm = \frac{1}{2}(\hat{\sigma}_x \pm i\hat{\sigma}_y)$, where $\big[\hat{\sigma}_+\big]_{AB} = 1 = \big[\hat{\sigma}_-\big]_{BA}$ and $\big[\hat{\sigma}_+\big]_{BA} = 0 = \big[\hat{\sigma}_-\big]_{AB}$.

Directly at the Dirac point $\tau\boldsymbol{K}$, the Rashba structural function reduces to

$$f_{\mathrm{R}}(\tau\boldsymbol{K}) = \begin{cases} 2 & \text{for } \tau = +1\,, \\ 0 & \text{for } \tau = -1\,. \end{cases} \tag{2.69}$$

The effective low energy Hamiltonian for the C_{6v} invariant graphene system is then given by

$$\begin{aligned}\mathcal{H}_{\mathrm{eff}}(\tau\boldsymbol{K} + \boldsymbol{k}) = \hbar v_F \big(\tau k_x \hat{\sigma}_x - k_y \hat{\sigma}_y\big)\hat{s}_0 + \tau\lambda_{\mathrm{I}}\hat{\sigma}_z\hat{s}_z + \\ + \lambda_{\mathrm{PIA}}\hat{\sigma}_0(k_x\hat{s}_y - k_y\hat{s}_x)a_{\mathrm{L}} - \lambda_{\mathrm{R}}(\tau\hat{\sigma}_x\hat{s}_y + \hat{\sigma}_y\hat{s}_x)\,.\end{aligned} \tag{2.70}$$

Note that in contrast to the case of point group D_{3d}, Eq. (2.51), the PIA SOC $\sim \hat{\sigma}_0$ acts now on both sublattices in the same way. Furthermore, the PIA SOC vanishes directly at a Dirac point, $\boldsymbol{k} = 0$, whereas the intrinsic and Rashba SOC remain finite there. The eigenspectrum is given by

$$\begin{aligned}\epsilon_{n,n'}(\tau\boldsymbol{K}+\boldsymbol{k}) = n'\lambda_{\mathrm{R}} + \\ + n\sqrt{(\lambda_{\mathrm{I}}+n'\lambda_{\mathrm{R}})^2 + (\hbar v_F - n'\lambda_{\mathrm{PIA}}a_{\mathrm{L}})^2(k_x^2+k_y^2)}\,,\end{aligned} \tag{2.71}$$

where $n = \pm$ labels the conduction and valence bands and $n' = \pm$ is a band index which indicates the spin polarization. From Eq. (2.71) we see that both Rashba and PIA SOC induce band spin splittings in the spectrum. However, the PIA does not contribute to the spin splitting directly at the Dirac point. The reason why the PIA contribution induces band spin splitting at all, is the lack of inversion symmetry [see Eq. (2.37)] in the point group C_{6v}. PIA SOC is also present in a D_{3d} symmetric system but there, the bands stay spin degenerate. We can further relate the observed spin splitting to the results of Bychkov and Rashba [94], who showed in 1983 that band spin splittings occur in systems with a single high symmetry axis, at least threefold, and an invariant vector pointing along this axis. In our case of the point group C_{6v}, we have the transverse rotation axis along z, allowing for six-fold rotations, and an electric field oriented in this direction.

Unlike in the previously studied graphene systems, we do not find a spin-conserved quantity of the simple form $\hat{\sigma}_0\,[\boldsymbol{n}(\boldsymbol{q}).\hat{\boldsymbol{s}}]$, which commutes with $\mathcal{H}_{C_{6v}}(\boldsymbol{q})$. Instead, we compute the spin expectation value $\langle\hat{\boldsymbol{s}}\rangle \equiv \langle \boldsymbol{q}, n, n'|\hat{\boldsymbol{s}}|\boldsymbol{q}, n, n'\rangle$ from the eigenstates $|\boldsymbol{q}, n, n'\rangle$. In the low energy limit, $\boldsymbol{q} = \tau\boldsymbol{K} + \boldsymbol{k}$, we obtain

$$\begin{pmatrix}\langle\hat{s}_x\rangle\\ \langle\hat{s}_y\rangle\\ \langle\hat{s}_z\rangle\end{pmatrix} = \alpha_{n,n'}.\beta_{n'}\begin{pmatrix}-n'k_y/k\\ +n'k_x/k\\ 0\end{pmatrix}. \tag{2.72}$$

Here, we introduced $\alpha_{n,n'} = \mathrm{sign}(\tau\lambda_{\mathrm{I}} + 2n'\lambda_{\mathrm{R}} - \epsilon_{n,n'})$, $\beta_{n'} = \mathrm{sign}(\hbar v_F - n'\lambda_{\mathrm{PIA}}a_L)$, $k = \sqrt{k_x^2+k_y^2}$, and the abbreviation $\epsilon_{n,n'} \equiv \epsilon_{n,n'}(\tau\boldsymbol{K}+k)$. For all energy bands, the spins are lying in the plane for quasi-momenta around the $\tau\boldsymbol{K}$ point.

Figure 2.7 displays the band structure around the $\tau = +1$ Dirac point for different parameter values as well as the spin texture around this Dirac point. The bands are spin-split and two bands out of four are always degenerate at the Dirac point. By tuning the strength of the Rashba SOC with respect to the intrinsic one, both gapped and gapless spectra can be acchieved. For $|\lambda_{\mathrm{I}}| > |\lambda_{\mathrm{R}}|$, a gap of $2(|\lambda_{\mathrm{I}}| - |\lambda_{\mathrm{R}}|)$ occurs between the valence and conduction bands. As it was already pointed out by Kane and Mele [67], this condition is necessary to observe the quantized spin Hall phase in the graphene structure. For $|\lambda_{\mathrm{I}}| = |\lambda_{\mathrm{R}}|$, the gap closes and a triple degeneracy occurs at the Dirac point. Depending on the relative sign of the SOC parameters, the degeneracy is formed either by two valence bands and

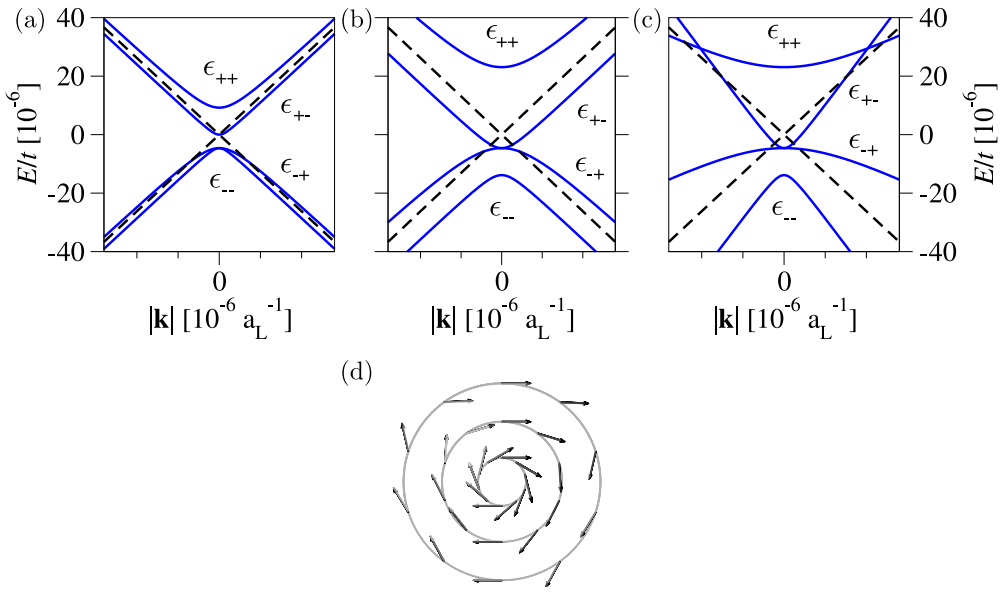

Figure 2.7: Electronic band structure and spin texture around the $\boldsymbol{K}$ point for a C_{6v} invariant SOC Hamiltonian. The parameters $t = 2.6\,\mathrm{eV}$ and $\lambda_\mathrm{I} = 12\,\mu\mathrm{eV}$ are fixed. For $\lambda_\mathrm{PIA} = 0$ and (a) $\lambda_\mathrm{R} = 6\,\mu\mathrm{eV} < \lambda_\mathrm{I}$ the spectrum is gapped. (b) The spectrum is gapless for $\lambda_\mathrm{R} = 24\,\mu\mathrm{eV} > \lambda_\mathrm{I}$. A finite $\lambda_\mathrm{PIA} = 1\,\mathrm{eV}$, see (c), leads to a crossing between the two conduction bands due to renormalization of the Fermi velocities in the bands. Panel (d) displays the spin expectation value along circles around the K-point for the energy band ϵ_{--} of panel (b). The circles radii correspond to 10%, 30% and 50% of the distance $\overline{\boldsymbol{KM}}$. For comparison, the energy dispersion of pristine graphene without SOC is displayed with black dashed lines.

one conduction band or two conduction bands and one valence band. For $|\lambda_\mathrm{I}| < |\lambda_\mathrm{R}|$, the spectrum remains gapless with a double degeneracy at the Dirac point. Figure 2.7(a) and (b) display the transition from a gapped to gapless spectrum. The spin expectation value for the valence band of the gapless spectrum shown in (b) is in-plane only, see Fig. 2.7(d). Finite PIA SOC renormalizes the Fermi velocities of the spin-split branches $n' = \pm$ of a band with fixed index n, $v_{F\pm} = v_F \mp \lambda_\mathrm{PIA} a_L/\hbar$. This can induce a crossing between the two branches $\epsilon_{n,\pm}$ [see Fig. 2.7(c) for an example]. To find the critical k-value k_cr at which the crossing occurs, we define the quantity

$$\Omega = 1 + 2\frac{\lambda_\mathrm{I}}{\lambda_\mathrm{R}}\frac{\lambda_\mathrm{PIA} a_L}{\hbar v_F} + \left(\frac{\lambda_\mathrm{PIA} a_L}{\hbar v_F}\right)^2 \approx 1 + 2\frac{\lambda_\mathrm{I}}{\lambda_\mathrm{R}}\frac{\lambda_\mathrm{PIA} a_L}{\hbar v_F}\,. \tag{2.73}$$

If $\Omega > 0$, the two spin-split bands $\epsilon_{n,\pm}(\tau\boldsymbol{K} + \boldsymbol{k})$ cross along a circle in momentum space, centered at $\tau\boldsymbol{K}$, having the radius

$$k_\mathrm{cr} = \left|\frac{\lambda_\mathrm{R}}{\lambda_\mathrm{PIA} a_L}\sqrt{\Omega}\right| \approx \left|\frac{\lambda_\mathrm{R}}{\lambda_\mathrm{PIA} a_L} + \frac{\lambda_\mathrm{I}}{\hbar v_F}\right|. \tag{2.74}$$

However, it is worth to notice that for realistic graphene-like values of the orbital and SOC parameters, i.e., $\lambda_\mathrm{I} \ll \hbar v_F$ and $\lambda_\mathrm{R} \sim \lambda_\mathrm{PIA}$, $k_\mathrm{cr} \approx 1/a_L$. At this wavevector, we are already far away from the Dirac valleys where the linear approximation, which was used for the derivation of the crossing condition, is no longer valid[14].

2.4.6 SOC and the point group C_{3v}

The point group C_{3v} describes graphene systems where both the transverse direction is fixed, as in the previous section, and the sublattice symmetry is broken. Semihydrogenated graphene (graphone) [52], graphene/TMDC heterostructures [76, 96], silicene on a substrate, hBN in a transverse electric field, etc., are representative examples of such systems. Only threefold rotations $C_3^{\hat{z}}$ and vertical reflections Σ_v^{yz} leave these structures invariant, see Tab. 2.1. As C_{3v} is isomorphic to any intersection of the previously discussed point groups D_{3d}, D_{3h}, and C_{6v}, we know that all SOC terms that appeared in the latter point groups (intrinsic, PIA, and Rashba) will also appear in C_{3v}. From this argument and also from the lack of a symmetry operation that connects the two different sublattices, we introduce for the next-nearest neighbor SOC terms, intrinsic and PIA, sublattice resolved parameters, i.e., $\lambda_\mathrm{I} \to \{\lambda_\mathrm{I}^\mathrm{A}, \lambda_\mathrm{I}^\mathrm{B}\}$ and $\lambda_\mathrm{PIA} \to \{\lambda_\mathrm{PIA}^\mathrm{A}, \lambda_\mathrm{PIA}^\mathrm{B}\}$. We define the SOC parameters via the following matrix elements:

$$\frac{i\lambda_\mathrm{I}^\mathrm{A}}{3\sqrt{3}} = \left\langle A_3\uparrow \middle| \hat{H}_\mathrm{so} \middle| A_2\uparrow \right\rangle, \ \frac{i\lambda_\mathrm{I}^\mathrm{B}}{3\sqrt{3}} = \left\langle B_3\uparrow \middle| \hat{H}_\mathrm{so} \middle| B_2\uparrow \right\rangle, \tag{2.75a}$$

$$\frac{2}{3}\lambda_\mathrm{PIA}^\mathrm{A} = \left\langle A_3\uparrow \middle| \hat{H}_\mathrm{so} \middle| A_2\downarrow \right\rangle, \ \frac{2}{3}\lambda_\mathrm{PIA}^\mathrm{B} = \left\langle B_3\uparrow \middle| \hat{H}_\mathrm{so} \middle| B_2\downarrow \right\rangle, \tag{2.75b}$$

$$\frac{2}{3}i\lambda_\mathrm{R} = \left\langle A_2\uparrow \middle| \hat{H}_\mathrm{so} \middle| B_3\downarrow \right\rangle. \tag{2.75c}$$

The SOC Hamiltonian for the C_{3v} invariant graphene system with π orbitals is, in analogy to the results of preceding sections, given by

$$\begin{aligned}\mathcal{H}_{C_{3v}} = &\frac{i\lambda_\mathrm{I}^\mathrm{A}}{3\sqrt{3}} \sum_\sigma \sum_{\langle\langle m,n\rangle\rangle} \nu_{m,n} \left[\hat{s}_z\right]_{\sigma\sigma} \left|A_m\,\sigma\right\rangle \left\langle A_n\,\sigma\right| \\ &+ \frac{i\lambda_\mathrm{I}^\mathrm{B}}{3\sqrt{3}} \sum_\sigma \sum_{\langle\langle m,n\rangle\rangle} \nu_{m,n} \left[\hat{s}_z\right]_{\sigma\sigma} \left|B_m\,\sigma\right\rangle \left\langle B_n\,\sigma\right| \\ &+ \frac{2\lambda_\mathrm{PIA}^\mathrm{A}}{3} \sum_{\sigma\neq\sigma'} \sum_{\langle\langle m,n\rangle\rangle} \left[i\hat{\boldsymbol{s}} \times \boldsymbol{d}_{m,n}\right]_{z,\sigma\sigma'} \left|A_m\,\sigma\right\rangle \left\langle A_n\,\sigma'\right|\end{aligned}$$

[14] The linear approximation on the orbital part of the graphene band structure is valid up to energies of the order of $100\,\mathrm{meV} \approx 0.04\,t$. Therefore, the value of the critical wave vector should be about $k_\mathrm{cr} = 0.01 - 0.1\,\text{Å}^{-1} \approx 0.004 - 0.04\,a_\mathrm{L}^{-1}$ or less.

$$+\frac{2\lambda_{\mathrm{PIA}}^{\mathrm{B}}}{3}\sum_{\sigma\neq\sigma'}\sum_{\langle\langle m,n\rangle\rangle}\left[i\hat{\boldsymbol{s}}\times\boldsymbol{d}_{m,n}\right]_{z,\sigma\sigma'}\left|B_m\,\sigma\right\rangle\left\langle B_n\,\sigma'\right|$$
$$+\frac{2i\lambda_{\mathrm{R}}}{3}\sum_{\sigma\neq\sigma'}\sum_{\langle m,n\rangle}\left[\hat{\boldsymbol{s}}\times\boldsymbol{d}_{m,n}\right]_{z,\sigma\sigma'}\left|X_m\,\sigma\right\rangle\left\langle X_n\,\sigma'\right|. \tag{2.76}$$

We already know all structural functions for the different SOC terms which we need for the Bloch form of $\mathcal{H}_{C_{3v}}$. Collecting all SOC contributions with the proper sublattice resolved couplings we have

$$\begin{aligned}
\mathcal{H}_{C_{3v}}(\boldsymbol{q}) =& \sum_{\sigma,\sigma'}\lambda_{\mathrm{I}}^{\mathrm{A}}f_{\mathrm{I}}(\boldsymbol{q})\left[\hat{s}_z\right]_{\sigma\sigma'}\left|A_{\boldsymbol{q}}\,\sigma\right\rangle\left\langle A_{\boldsymbol{q}}\,\sigma'\right| \\
&+\sum_{\sigma,\sigma'}\lambda_{\mathrm{I}}^{\mathrm{B}}f_{\mathrm{I}}(\boldsymbol{q})\left[\hat{s}_z\right]_{\sigma\sigma'}\left|B_{\boldsymbol{q}}\,\sigma\right\rangle\left\langle B_{\boldsymbol{q}}\,\sigma'\right| \\
&+\sum_{\sigma,\sigma'}\lambda_{\mathrm{PIA}}^{\mathrm{A}}\left\{f_{\mathrm{P}}(\boldsymbol{q})\left[\hat{s}_+\right]_{\sigma\sigma'}+\overline{f_{\mathrm{P}}(\boldsymbol{q})}\left[\hat{s}_-\right]_{\sigma\sigma'}\right\}\left|A_{\boldsymbol{q}}\,\sigma\right\rangle\left\langle A_{\boldsymbol{q}}\,\sigma'\right| \\
&+\sum_{\sigma,\sigma'}\lambda_{\mathrm{PIA}}^{\mathrm{B}}\left\{f_{\mathrm{P}}(\boldsymbol{q})\left[\hat{s}_+\right]_{\sigma\sigma'}+\overline{f_{\mathrm{P}}(\boldsymbol{q})}\left[\hat{s}_-\right]_{\sigma\sigma'}\right\}\left|B_{\boldsymbol{q}}\,\sigma\right\rangle\left\langle B_{\boldsymbol{q}}\,\sigma'\right| \\
&+i\lambda_{\mathrm{R}}\sum_{\sigma,\sigma'}\sum_{X,X'}\left\{\left[\hat{\sigma}_+\right]_{XX'}\left(f_{\mathrm{R}}(\boldsymbol{q})\left[\hat{s}_+\right]_{\sigma\sigma'}+\overline{f_{\mathrm{R}}(-\boldsymbol{q})}\left[\hat{s}_-\right]_{\sigma\sigma'}\right)\right. \\
&\left.-\left[\hat{\sigma}_-\right]_{XX'}\left(\overline{f_{\mathrm{R}}(\boldsymbol{q})}\left[\hat{s}_-\right]_{\sigma\sigma'}+f_{\mathrm{R}}(-\boldsymbol{q})\left[\hat{s}_+\right]_{\sigma\sigma'}\right)\right\}\left|X_{\boldsymbol{q}}\,\sigma\right\rangle\left\langle X'_{\boldsymbol{q}}\,\sigma'\right|.
\end{aligned} \tag{2.77}$$

The orbital Hamiltonian contains in general also a staggered potential term Δ [similar to the discussions of point group D_{3d}, Eq. (2.56)] which energetically distinguishes between sites of sublattices A and B. At low energies, i.e., close to the Dirac point $\tau\boldsymbol{K}$, the effective C_{3v} symmetric Hamiltonian reads

$$\begin{aligned}
\mathcal{H}_{\mathrm{eff}}(\tau\boldsymbol{K}+\boldsymbol{k}) =& \hbar v_F\left(\tau k_x\hat{\sigma}_x-k_y\hat{\sigma}_y\right)\hat{s}_0+\Delta\hat{\sigma}_z\hat{s}_0 \\
&+\frac{\tau}{2}\left[\lambda_{\mathrm{I}}^{\mathrm{A}}\left(\hat{\sigma}_z+\hat{\sigma}_0\right)+\lambda_{\mathrm{I}}^{\mathrm{B}}\left(\hat{\sigma}_z-\hat{\sigma}_0\right)\right]\hat{s}_z \\
&+\frac{1}{2}\left[\lambda_{\mathrm{PIA}}^{\mathrm{A}}\left(\hat{\sigma}_z+\hat{\sigma}_0\right)+\lambda_{\mathrm{PIA}}^{\mathrm{B}}\left(\hat{\sigma}_z-\hat{\sigma}_0\right)\right](k_x\hat{s}_y-k_y\hat{s}_x)a_{\mathrm{L}} \\
&-\lambda_{\mathrm{R}}(\tau\hat{\sigma}_x\hat{s}_y+\hat{\sigma}_y\hat{s}_x).
\end{aligned} \tag{2.78}$$

There is no simple analytic form for the dispersion relation resulting from this general effective Hamiltonian. Due to lack of inversion symmetry, the spectrum is composed of spin-split bands. The spin splitting is, similar as in the C_{6v} symmetric case, due to both the Rashba and PIA SOC whereas the latter is unimportant for investigations directly at the Dirac point. Figure 2.8 displays the band structure of a C_{3v} invariant graphene system for the simplified case of $\Delta=0$ and $\lambda_{\mathrm{PIA}}^{\mathrm{A}}=0=\lambda_{\mathrm{PIA}}^{\mathrm{B}}$ and different magnitudes of the intrinsic and Rashba SOC, which results in inverted,

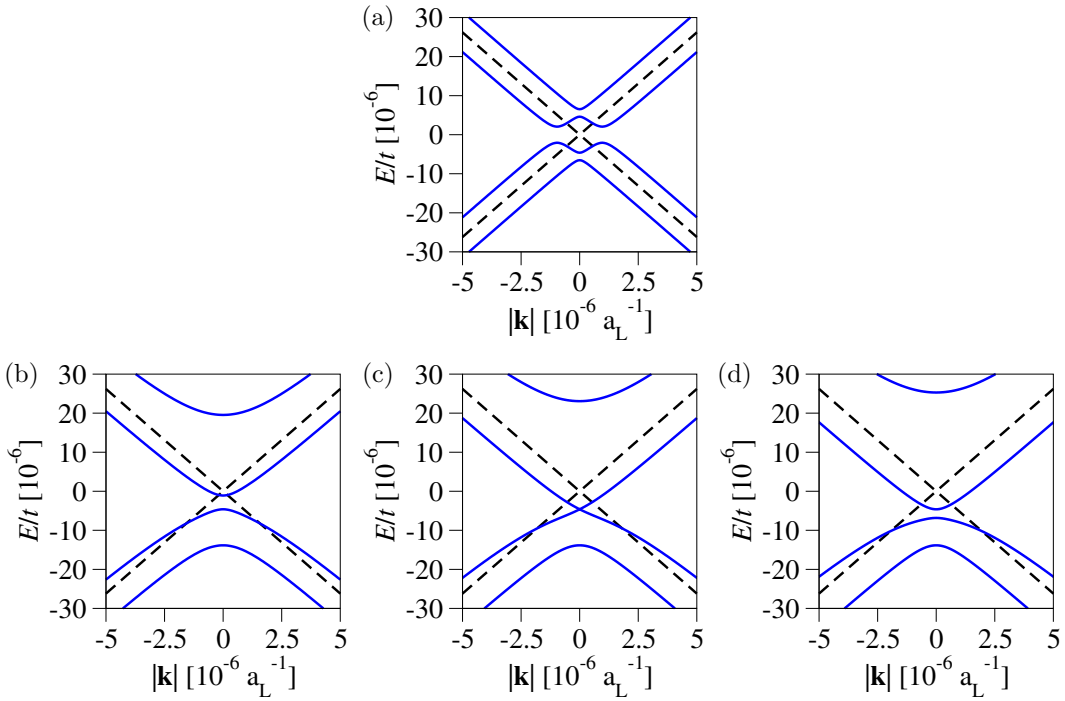

Figure 2.8: Electronic band structure around the $\boldsymbol{K}$ point for a C_{3v} invariant SOC Hamiltonian for $t = 2.6\,\mathrm{eV}$, $\Delta = 0$, $\lambda_{\mathrm{PIA}}^{\mathrm{A/B}} = 0$, and $\lambda_{\mathrm{I}}^{\mathrm{A}} = 12\,\mu\mathrm{eV}$. (a) For $\lambda_{\mathrm{I}}^{\mathrm{B}} = -\lambda_{\mathrm{I}}^{\mathrm{A}}$, a finite $\lambda_{\mathrm{R}} = 6\,\mu\mathrm{eV}$ lifts the band degeneracy observed in the D_{3h} case of Fig. 2.6. A gapped spectrum, (b) $\lambda_{\mathrm{I}}^{\mathrm{B}} = 3\lambda_{\mathrm{I}}^{\mathrm{A}}$, $\lambda_{\mathrm{R}} = 6\,\mu\mathrm{eV}$, can be tuned to gapless, (c), for $\lambda_{\mathrm{R}} = \sqrt{2}\lambda_{\mathrm{I}}^{\mathrm{A}}$, and (d) back to gapped, $\lambda_{\mathrm{I}}^{\mathrm{B}} = 3\lambda_{\mathrm{I}}^{\mathrm{A}}$, $\lambda_{\mathrm{R}} = 20\,\mu\mathrm{eV}$. For comparison, the energy dispersion of pristine graphene without SOC is displayed with black dashed lines.

gapped and gapless spectra. Directly at the Dirac point, $\boldsymbol{k} = 0$, the four energy bands lie at the energies $-\lambda_{\mathrm{I}}^{\mathrm{A}}$, $-\lambda_{\mathrm{I}}^{\mathrm{B}}$, and $\left(\lambda_{\mathrm{I}}^{\mathrm{A}} + \lambda_{\mathrm{I}}^{\mathrm{B}} \pm \sqrt{(\lambda_{\mathrm{I}}^{\mathrm{A}} - \lambda_{\mathrm{I}}^{\mathrm{B}})^2 + 16\lambda_{\mathrm{R}}^2}\right)/2$. For given intrinsic SOC strengths $\lambda_{\mathrm{I}}^{\mathrm{A}}$, $\lambda_{\mathrm{I}}^{\mathrm{B}}$, the Rashba SOC λ_{R} can be used as a tuning parameter[15] to drive the system through different band topologies.

The richness of SOC terms that appear in a C_{3v} symmetric graphene system, Eq. (2.78), compared to the case of the D_{6h} invariant pristine graphene, Eq. (2.35), follow the basic principle that became clear in the previous sections: The lower the point group symmetry in a graphene system is, the less symmetry restrictions are imposed on the SOC, and the more different hopping mediated SOC appear in the system. A pictorial summary of the so far discussed point group symmetries together with a list of the symmetry allowed SOC parameters is shown in Fig. 2.9.

[15] The Rashba SOC appears due to extrinsic effects such as a substrate or the transverse external electric field. As its magnitude can be changed by modifying the extrinsic influence, e.g., the magnitude or orientation of the electric field, the Rashba SOC is suited as a tuning parameter.

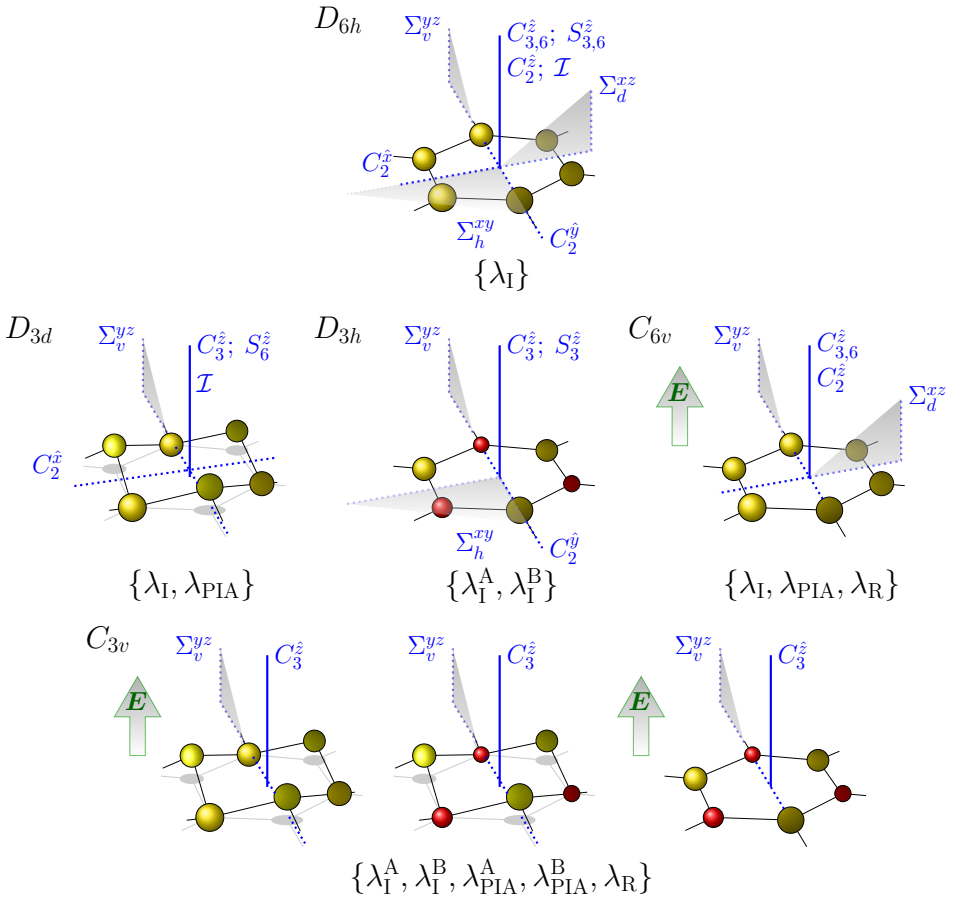

Figure 2.9: Pictorial view of the point group D_{6h} and its subgroups D_{3d}, D_{3h}, C_{6v}, and C_{3v} together with representative graphene systems. The examples cover pristine graphene (D_{6h}), graphene miniripple (D_{3d}), planar hBN (D_{3h}), graphene in a transverse, external electric field (C_{6v}), as well as graphene miniripple in a transverse external electric field, miniripple hBN, and hBN in a transverse external electric field (all C_{3v}). The smaller the point group symmetry is, the more SOC parameters are allowed.

2.5 Spin-orbit coupling under local symmetries

2.5.1 Local symmetry

In the previous sections, we discussed graphene systems that were globally invariant under specific point group symmetries. In the following, we will focus on graphene which is subject to locally adsorbed impurities or simple admolecules. We restrict our analysis to light adsorbates whereas Refs. [55, 80] treat heavy adsorbates. Furthermore, we assume that the adatom coverage on the hexagonal structure is dilute so that it is enough to investigate only the local SOC effect from a single impurity. We thus exclude from our analysis any effect of clustering or interference effects between nearby impurity centers. Under these assumptions, we can work within our symmetry based TB framework from the previous sections in the local atomic basis with broken translational symmetry.

Depending on the electronic structure of both adatom and hosting graphene, the bonding occurs in one of the three stable adsorption positions, which are called the hollow, the top, and the bridge position. These different adsorption sites are reflected in different local point group symmetries which are C_{6v}, C_{3v}, and C_{2v} for the three cases, respectively. For simplicity, we will describe the adsorbate such that it binds to the graphene system via a single effective orbital which is invariant under the local point group symmetry and time reversal symmetry. This approximation works very well for the case studies of specific adatoms presented in Ch. 3. In situations where the restriction to monovalency is not a good approximation, one might consider a multi-orbital TB study. The symmetry arguments will then have to be adapted to the different symmetries of the atomic orbitals.

To derive the adsorbate induced effective SOC Hamiltonian, we consider the local point group symmetry determined by the adsorption position. The resulting SOC terms can then be added to the orbital and spin-orbital Hamiltonians of the global translational invariant structure discussed in the previous sections. Since we focus on the local effect of the impurity, we restrict ourselves to hoppings up to next-nearest neighbors of the adsorbate. We employ the label O for the impurity and $|O\rangle$ for the corresponding atomic orbital, the labels Y_j ($|Y_j\rangle$) for the nearest neighbor sites (in the host material) to the impurity, and the labels Z_j ($|Z_j\rangle$) for the next-nearest neighbor sites. Depending on the adsorption position, the maximal number of neighbors in nearest or next-nearest sites will vary.

For all three adsorption positions, we employ the minimal orbital TB Hamiltonian [97, 98]

$$\begin{aligned}\mathcal{H}_{\mathrm{orb}}^{\mathrm{ad}} = \omega \sum_{\sigma} \sum_{\langle O, Y_j \rangle} \left(|O\,\sigma\rangle\langle Y_j\,\sigma| + |Y_j\,\sigma\rangle\langle O\,\sigma| \right) \\ + \varepsilon \sum_{\sigma} |O\,\sigma\rangle\langle O\,\sigma| \,, \end{aligned} \tag{2.79}$$

Ad-element / model parameters [eV]	ω	ε
Hydrogen (top)	7.50	0.16
Methyl (top)	7.60	-0.19
Fluorine (top)	5.50	-2.20
Copper (top)	0.81	0.08
Copper (bridge)	0.54	0.02

Table 2.2: Orbital TB parameters for different adsorbates: hydrogen, methyl, fluorine, and copper in the top and bridge position as obtained in Refs. [52, 99–101].

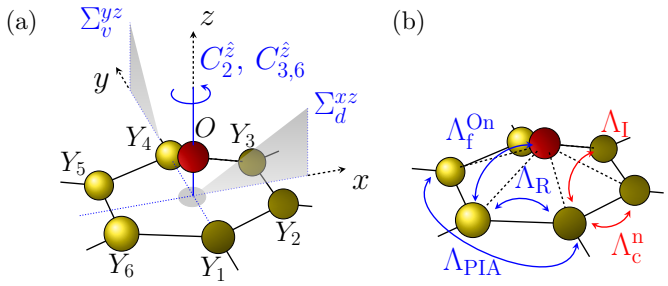

Figure 2.10: (a) Symmetry elements of the local point group symmetry C_{6v} for an adatom binding in the hollow position. The site labeling convention and the chosen coordinate system are shown as well. (b) Local SOC hoppings in the vicinity of the adatom. The spin-flipping hoppings are shown in blue, the spin-conserving hoppings in red.

which comprises the hybridization ω between the impurity and its nearest neighbors, and the adatom's on-site energy ε. Table 2.2 shows representative values for the orbital model parameters for different adatoms studied with the approach as described above and fitted against first principles data. We will meet these examples again in Ch. 3 when we consider a quantitative analysis of adatom induced local SOC in graphene.

2.5.2 Adatom in the hollow position

The center of a hexagon in graphene's honeycomb lattice is called the hollow position. As was shown by DFT studies, adsorbates which favorably bond in this position are light metallic adatoms [102] such as Li and Na from the group I-III in the periodic table of the chemical elements, heavy (post-)transition metals [55, 102, 103] such as In and Co, and light admolecules such as NH_3, H_2O, and NO_2 [104]. Figure 2.10(a) shows schematically an adatom in the hollow position and the local point group symmetries. The orientation of the z axis is fixed by the adatom positioned above the graphene plane and the local point group is C_{6v}. That is, the out-of plane adatom takes effectively the role of the transverse electric field in the

global analog of Sec. 2.4.5. We assume that the hollow adsorption induces local SOC hoppings primarly among the carbon atoms forming the hexagon ring.

The global symmetry analysis revealed the presence of several SOC terms that will occur likewise under the local symmetry. In analogy to the terms in Eq. (2.65), we call the local analogs intrinsic Λ_I, Rashba Λ_R, and PIA Λ_PIA and define them via the following matrix elements:

$$\frac{i\Lambda_\mathrm{I}}{3\sqrt{3}} = \left\langle Y_5\uparrow \,|\, \hat{H}_\mathrm{so} \,|\, Y_3\uparrow \right\rangle, \tag{2.80a}$$

$$\frac{2\Lambda_\mathrm{PIA}}{3} = \left\langle Y_5\uparrow \,|\, \hat{H}_\mathrm{so} \,|\, Y_3\downarrow \right\rangle, \tag{2.80b}$$

$$\frac{2i\Lambda_\mathrm{R}}{3} = \left\langle Y_3\uparrow \,|\, \hat{H}_\mathrm{so} \,|\, Y_2\downarrow \right\rangle. \tag{2.80c}$$

Here, we keep the same numerical prefactors introduced in Eq. (2.65) for clarity. However, the formulation in Bloch space and the low-energy expansions, from which the factors originate, is no longer meaningful due to the lack of translational symmetry. With breaking the translational symmetry, the third symmetry statement of Sec. 2.3.4 can no longer be applied, and nearest neighbor spin-conserving hoppings become allowed in general. We define the corresponding coupling via the matrix element

$$i\Lambda_\mathrm{c}^\mathrm{n} = \langle Y_2\uparrow | \hat{H}_\mathrm{so} | Y_3\uparrow \rangle, \tag{2.81}$$

which is purely imaginary as can be seen from Eqs. (2.24) and (2.25). For the spin-conserving nearest neighbor hopping between general sites Y_j, we obtain

$$\left\langle Y_j\,\sigma | \hat{H}_\mathrm{so} | Y_k\,\sigma \right\rangle = \tilde{\nu}_{Y_j,Y_k} \left[\hat{s}_z\right]_{\sigma\sigma} i\Lambda_\mathrm{c}^\mathrm{n}. \tag{2.82}$$

This parametrization is analogous to the intrinsic (next-nearest neighbor spin-conserving) hopping with $\tilde{\nu}_{Y_j,Y_k} = +1$ (-1) if the virtual hopping path from the site Y_k to Y_j via the central adatom O is counter clockwise (clockwise).

Further SOC mediated hoppings might occur between the adatom and its six carbon neighbors, which we investigate in the following. As stated before, we assume that the adatom's orbital is invariant both under the C_{6v} symmetries, $\mathcal{S}|O\rangle = |O\rangle$ for any $\mathcal{S} \in C_{6v}$, and time reversal symmetry, $\mathcal{T}|O\rangle = |O\rangle$. These conditions are met for example by alkali metal adatoms. From symmetry, we see that a spin-conserving hopping of the form $\langle O\uparrow|\hat{H}_\mathrm{so}|Y_1\uparrow\rangle$ is absent,

$$\begin{aligned}\left\langle O\uparrow|\hat{H}_\mathrm{so}|Y_1\uparrow\right\rangle &\overset{(2.21e)}{=} \left\langle i\Sigma_v^{yz}[O\downarrow]|\hat{H}_\mathrm{so}|i\Sigma_v^{yz}[Y_1\downarrow]\right\rangle \\ &\overset{(2.16)}{=} \left\langle O\downarrow|\hat{H}_\mathrm{so}|Y_1\downarrow\right\rangle \overset{(2.24)}{=} -\left\langle O\uparrow|\hat{H}_\mathrm{so}|Y_1\uparrow\right\rangle = 0\,.\end{aligned} \tag{2.83}$$

On the contrary, a spin-flipping hopping $\langle O\uparrow|\hat{H}_\mathrm{so}|Y_1\downarrow\rangle$ is allowed by symmetry

and purely imaginary,

$$\begin{aligned}\left\langle O\uparrow|\hat{H}_{\mathrm{so}}|Y_1\downarrow\right\rangle &\overset{(2.21e)}{=} \left\langle i\Sigma_v^{yz}[O\downarrow]|\hat{H}_{\mathrm{so}}|i\Sigma_v^{yz}[Y_1\uparrow]\right\rangle \\ &\overset{(2.16)}{=} \left\langle O\downarrow|\hat{H}_{\mathrm{so}}|Y_1\uparrow\right\rangle \overset{(2.22)}{=} -\overline{\left\langle O\uparrow|\hat{H}_{\mathrm{so}}|Y_1\downarrow\right\rangle}\,. \end{aligned} \tag{2.84}$$

Defining the spin-flipping SOC term as

$$i\Lambda_{\mathrm{f}}^{\mathrm{On}} = \left\langle O\uparrow|\hat{H}_{\mathrm{so}}|Y_1\downarrow\right\rangle, \tag{2.85}$$

and applying point group symmetries such as the rotation $C_6^{\hat{z}}$,

$$\begin{aligned}\left\langle O\uparrow|\hat{H}_{\mathrm{so}}|Y_2\downarrow\right\rangle &= \left\langle e^{i\frac{\pi}{6}}C_6^{\hat{z}}[O\uparrow]|\hat{H}_{\mathrm{so}}|e^{-i\frac{\pi}{6}}C_6^{\hat{z}}[Y_1\downarrow]\right\rangle \\ &\overset{(2.16)}{=} e^{-i\frac{\pi}{3}}\left\langle O\uparrow|\hat{H}_{\mathrm{so}}|Y_1\downarrow\right\rangle \overset{(2.85)}{=} e^{-i\frac{\pi}{3}}\, i\Lambda_{\mathrm{f}}^{\mathrm{On}}, \end{aligned} \tag{2.86}$$

we obtain certain phase relations that can be summarized for any Y_j and $\sigma \neq \sigma'$ as

$$\left\langle O\,\sigma|\hat{H}_{\mathrm{so}}|Y_j\,\sigma'\right\rangle = \left[\hat{\boldsymbol{s}}\times\boldsymbol{d}_{O,Y_j}\right]_{\sigma\sigma'} i\Lambda_{\mathrm{f}}^{\mathrm{On}}\,. \tag{2.87}$$

Here, the vector $\boldsymbol{d}_{O,Y_j}$ should be understood as the unit vector in the xy-plane pointing from site Y_j to O.

In summary, we find that five different SOC terms are locally induced by the hollow adatom with an effective orbital invariant under C_{6v} and time reversal. The hoppings are illustrated in Fig. 2.10(b). The corresponding local SOC Hamiltonian is therefore given by

$$\begin{aligned}\mathcal{H}_{\mathrm{so}}^{\mathrm{hol}} &= i\Lambda_{\mathrm{c}}^{\mathrm{n}} \sum_{\sigma}\sum_{\langle Y_j,Y_k\rangle} \tilde{\nu}_{Y_j,Y_k}\left[\hat{s}_z\right]_{\sigma\sigma}\left|Y_j\,\sigma\right\rangle\left\langle Y_k\,\sigma\right| \\ &+ \frac{i\Lambda_{\mathrm{I}}}{3\sqrt{3}}\sum_{\sigma}\sum_{\langle\langle Y_j,Y_k\rangle\rangle} \nu_{Y_j,Y_k}\left[\hat{s}_z\right]_{\sigma\sigma}\left|Y_j\,\sigma\right\rangle\left\langle Y_k\,\sigma\right| \\ &+ \frac{2i\Lambda_{\mathrm{R}}}{3}\sum_{\sigma\neq\sigma'}\sum_{\langle Y_j,Y_k\rangle}\left[\hat{\boldsymbol{s}}\times\boldsymbol{d}_{Y_j,Y_k}\right]_{z,\sigma\sigma'}\left|Y_j\,\sigma\right\rangle\left\langle Y_k\,\sigma'\right| \\ &+ \frac{2\Lambda_{\mathrm{PIA}}}{3}\sum_{\sigma\neq\sigma'}\sum_{\langle\langle Y_j,Y_k\rangle\rangle}\left[i\hat{\boldsymbol{s}}\times\boldsymbol{d}_{Y_j,Y_k}\right]_{z,\sigma\sigma'}\left|Y_j\,\sigma\right\rangle\left\langle Y_k\,\sigma'\right| \\ &+ i\Lambda_{\mathrm{f}}^{\mathrm{On}}\sum_{\sigma\neq\sigma'}\sum_{\langle O,Y_j\rangle}\left[\hat{\boldsymbol{s}}\times\boldsymbol{d}_{O,Y_j}\right]_{z,\sigma\sigma'}\left|O\,\sigma\right\rangle\left\langle Y_j\,\sigma'\right| + \mathrm{H.c.}\,. \end{aligned} \tag{2.88}$$

2.5.3 Adatom in the top position

We now draw our attention to the top position, i.e., the adsorption of an impurity directly above one carbon atom of the graphene lattice. According to DFT studies,

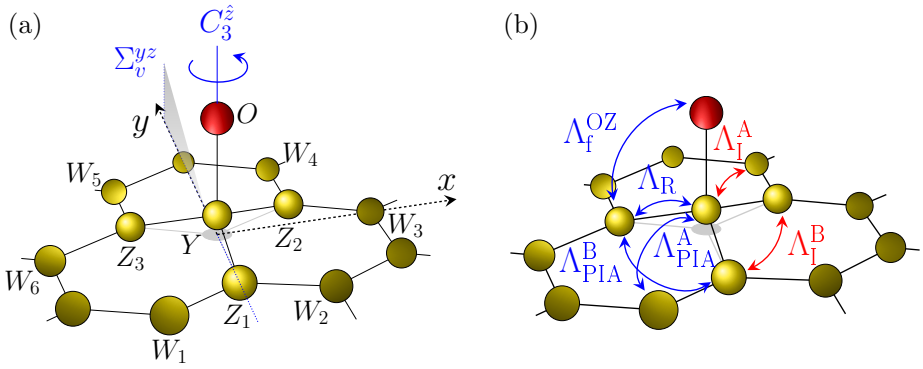

Figure 2.11: (a) Symmetry elements of the local point group symmetry C_{3v} for an adatom binding in the top position. The site labeling convention and the chosen coordinate system are shown as well. (b) Local SOC hoppings in the vicinity of the adatom. The spin-flipping hoppings are shown in blue, the spin-conserving hoppings in red.

candidates are light atoms such as hydrogen [52, 105], fluorine [100, 106, 107], and copper [101, 108, 109], the heavier gold atom [102, 109], and the light admolecule methyl [99]. As shown in Fig. 2.11(a), the local point group symmetries are those of C_{3v}. The adatom fixes both the orientation along the z axis and, by binding to one sublattice, breaks the sublattice inversion symmetry. In contrast to our global discussion (see Fig. 2.9), the high symmetry axis coincides with the bond axis between the adatom and its (single) nearest carbon neighbor. We include in our analysis of local SOC hoppings not only the three next-nearest neighbor carbon atoms Z but also the third nearest neighboring sites W.

From the global C_{3v} SOC symmetry analysis, Sec. 2.4.6 and Eq. (2.76), we expect (and can analogously derive) the appearance of sublattice resolved intrinsic $\Lambda_{\mathrm{I}}^{\mathrm{A/B}}$ and PIA couplings $\Lambda_{\mathrm{PIA}}^{\mathrm{A/B}}$, as well as the Rashba coupling Λ_{R} in the vicinity of the top adsorption site in the graphene lattice. Assuming, that the top adatom binds to the sublattice A, we define these local couplings as [cf. Fig. 2.11(b)],

$$\frac{i\Lambda_{\mathrm{I}}^{\mathrm{A}}}{3\sqrt{3}} = \langle Y\uparrow | \hat{H}_{\mathrm{so}} | W_3\uparrow\rangle , \tag{2.89a}$$

$$\frac{i\Lambda_{\mathrm{I}}^{\mathrm{B}}}{3\sqrt{3}} = \langle Z_3\uparrow | \hat{H}_{\mathrm{so}} | Z_2\uparrow\rangle , \tag{2.89b}$$

$$\frac{2i\Lambda_{\mathrm{R}}}{3} = \langle Y\uparrow | \hat{H}_{\mathrm{so}} | Z_1\downarrow\rangle , \tag{2.89c}$$

$$\frac{2\Lambda_{\mathrm{PIA}}^{\mathrm{A}}}{3} = \langle Y\uparrow | \hat{H}_{\mathrm{so}} | W_3\downarrow\rangle , \tag{2.89d}$$

$$\frac{2\Lambda_{\mathrm{PIA}}^{\mathrm{B}}}{3} = \langle Z_3\uparrow | \hat{H}_{\mathrm{so}} | Z_2\downarrow\rangle . \tag{2.89e}$$

All intrinsic couplings are purely imaginary due to the general statement of Eqs. (2.24)

and (2.25). The purely imaginary nature of the Rashba coupling is implied by the vertical reflection Σ_v^{yz},

$$\begin{aligned}\langle Y\uparrow|\hat{H}_{\mathrm{so}}|Z_1\downarrow\rangle &= \langle i\Sigma_v^{yz}[Y\downarrow]|\hat{H}_{\mathrm{so}}|i\Sigma_v^{yz}[Z_1\uparrow]\rangle \\ &\overset{(2.16)}{=} \langle Y\downarrow|\hat{H}_{\mathrm{so}}|Z_1\uparrow\rangle \overset{(2.22)}{=} -\overline{\langle Y\uparrow|\hat{H}_{\mathrm{so}}|Z_1\downarrow\rangle}\,. \end{aligned} \tag{2.90}$$

The PIA coupling $\Lambda_{\mathrm{PIA}}^{\mathrm{B}}$ is purely real since we have, equivalently to Eq. (2.40),

$$\begin{aligned}\langle Z_3\uparrow|\hat{H}_{\mathrm{so}}|Z_2\downarrow\rangle &\overset{(2.21e)}{=} \langle i\Sigma_v^{yz}[Z_2\downarrow]|\hat{H}_{\mathrm{so}}|i\Sigma_v^{yz}[Z_3\uparrow]\rangle \\ &\overset{(2.16)}{=} \langle Z_2\downarrow|\hat{H}_{\mathrm{so}}|Z_3\uparrow\rangle = \overline{\langle Z_3\uparrow|\hat{H}_{\mathrm{so}}|Z_2\downarrow\rangle}\,. \end{aligned} \tag{2.91}$$

However, we face a different situation for the coupling $\Lambda_{\mathrm{PIA}}^{\mathrm{A}}$. In the global analog, where the symmetry center was located at the center of a hexagon, the same reasoning as in Eq. (2.91) could be applied. With the high symmetry axis shifted to the bond axis between adatom and carbon atom in the local C_{3v} case, the sites Y and W are not interchangeable by symmetry. The reader can convince him- or herself that out of the symmetries E, $C_3^{\hat{z}}$, Σ_v^{yz}, and $\mathcal{T}$ one cannot find a combination that will prove that $\Lambda_{\mathrm{PIA}}^{\mathrm{A}}$ is real. Instead, this coupling is in general complex and the formula for the phase factors, Eq. (2.44), has to be adapted appropriately,

$$\langle Y\,\sigma\,|\hat{H}_{\mathrm{so}}|W_j\,\sigma'\rangle = \left[i\hat{\boldsymbol{s}}\times\boldsymbol{d}_{Y,W_j}\right]_{z,\sigma\sigma'}\frac{2}{3}\Big[\mathrm{Re}\big(\Lambda_{\mathrm{PIA}}^{\mathrm{A}}\big)+i\nu_{Y,W_j}\,\mathrm{Im}\big(\Lambda_{\mathrm{PIA}}^{\mathrm{A}}\big)\Big]\,.$$

The phase factors for the hoppings related to the intrinsic $\Lambda_{\mathrm{I}}^{\mathrm{A/B}}$, the Rashba Λ_{R}, and the PIA coupling $\Lambda_{\mathrm{PIA}}^{\mathrm{B}}$ among the sites Y remain unchanged [see for example Eq. (2.76)].

We now turn to the case of non-vanishing SOC hoppings involving the effective adatom orbital O. The SOC mediated hoppings between the adatom and its nearest carbon neighbor, $\langle O\uparrow|\hat{H}_{\mathrm{so}}|Y\uparrow\rangle$ and $\langle O\uparrow|\hat{H}_{\mathrm{so}}|Y\downarrow\rangle$, are forbidden. In the first case, we have

$$\begin{aligned}\langle O\uparrow|\hat{H}_{\mathrm{so}}|Y\uparrow\rangle &\overset{(2.24)}{=} -\langle O\downarrow|\hat{H}_{\mathrm{so}}|Y\downarrow\rangle \\ &\overset{(2.21e)}{=} -\langle i\Sigma_v^{yz}[O\uparrow]|\hat{H}_{\mathrm{so}}|i\Sigma_v^{yz}[Y\uparrow]\rangle \\ &\overset{(2.16)}{=} -\langle O\uparrow|\hat{H}_{\mathrm{so}}|Y\uparrow\rangle\,, \end{aligned} \tag{2.92}$$

and, in the second case, it follows from rotations $C_3^{\hat{z}}\in C_{3v}$ that

$$\begin{aligned}\langle O\uparrow|\hat{H}_{\mathrm{so}}|Y\downarrow\rangle &\overset{(2.21a)}{=} \langle e^{i\frac{\pi}{3}}C_3^{\hat{z}}[O\uparrow]|\hat{H}_{\mathrm{so}}|e^{-i\frac{\pi}{3}}C_3^{\hat{z}}[Y\downarrow]\rangle \\ &\overset{(2.16)}{=} e^{-i\frac{2\pi}{3}}\langle O\uparrow|\hat{H}_{\mathrm{so}}|Y\downarrow\rangle\,, \end{aligned} \tag{2.93}$$

and equivalently for $(C_3^{\hat{z}})^{-1}$, which is fulfilled only if $\langle O\uparrow|\hat{H}_{\mathrm{so}}|Y\downarrow\rangle = 0$.

For SOC hoppings of the type $\langle O\sigma|\hat{H}_{\mathrm{so}}|Z_j\sigma'\rangle$ we can use Eqs. (2.83) and (2.84) from the discussion of the hollow adatom. We then immediately know that

$$i\Lambda_{\mathrm{c}}^{\mathrm{OZ}} = \langle O\uparrow|\hat{H}_{\mathrm{so}}|Z_1\uparrow\rangle \equiv 0\,, \tag{2.94}$$

$$i\Lambda_{\mathrm{f}}^{\mathrm{OZ}} = \langle O\uparrow|\hat{H}_{\mathrm{so}}|Z_1\downarrow\rangle \neq 0\,. \tag{2.95}$$

The phase factors for the coupling $\Lambda_{\mathrm{f}}^{\mathrm{OZ}}$ are given, correspondingly, by

$$\langle O\,\sigma|\hat{H}_{\mathrm{so}}|Z_j\,\sigma'\rangle = \left[\hat{\boldsymbol{s}}\times\boldsymbol{d}_{O,Z_j}\right]_{z,\sigma\sigma'} i\Lambda_{\mathrm{f}}^{\mathrm{OZ}}\,, \tag{2.96}$$

where the vector $\boldsymbol{d}_{O,Z_j}$ is the unit vector pointing from site Z_j to the projection of O into the xy-plane, i.e., site Y. Summarizing all local contributions from above, we obtain the general Hamiltonian describing the SOC in the vicinity of an adatom binding in the top position,

$$\begin{aligned}
\mathcal{H}_{\mathrm{so}}^{\mathrm{top}} = {} & \frac{i\Lambda_{\mathrm{I}}^{\mathrm{A}}}{3\sqrt{3}}\sum_{\sigma}\sum_{\langle\langle Y,W_j\rangle\rangle}\nu_{Y,W_j}\left[\hat{s}_z\right]_{\sigma\sigma}\left|Y\,\sigma\right\rangle\left\langle W_j\,\sigma\right| + \mathrm{H.c.} \\
& + \frac{i\Lambda_{\mathrm{I}}^{\mathrm{B}}}{3\sqrt{3}}\sum_{\sigma}\sum_{\langle\langle Z_j,Z_k\rangle\rangle}\nu_{Z_j,Z_k}\left[\hat{s}_z\right]_{\sigma\sigma}\left|Z_j\,\sigma\right\rangle\left\langle Z_k\,\sigma\right| \\
& + \sum_{\sigma\neq\sigma'}\sum_{\langle\langle Y,W_j\rangle\rangle}\left[i\hat{\boldsymbol{s}}\times\boldsymbol{d}_{Y,W_j}\right]_{z,\sigma\sigma'} \\
& \qquad\times\frac{2}{3}\Big[\mathrm{Re}\big(\Lambda_{\mathrm{PIA}}^{\mathrm{A}}\big) + i\nu_{Y,W_j}\mathrm{Im}\big(\Lambda_{\mathrm{PIA}}^{\mathrm{A}}\big)\Big]\left|Y\,\sigma\right\rangle\left\langle W_j\,\sigma'\right| + \mathrm{H.c.} \\
& + \frac{2\Lambda_{\mathrm{PIA}}^{\mathrm{B}}}{3}\sum_{\sigma\neq\sigma'}\sum_{\langle\langle Z_j,Z_k\rangle\rangle}\left[i\hat{\boldsymbol{s}}\times\boldsymbol{d}_{Z_j,Z_k}\right]_{z,\sigma\sigma'}\left|Z_j\,\sigma\right\rangle\left\langle Z_k\,\sigma'\right| \\
& + \frac{2i\Lambda_{\mathrm{R}}}{3}\sum_{\sigma\neq\sigma'}\sum_{\langle Y,Z_j\rangle}\left[\hat{\boldsymbol{s}}\times\boldsymbol{d}_{Y,Z_j}\right]_{z,\sigma\sigma'}\left|Y\,\sigma\right\rangle\left\langle Z_j\,\sigma'\right| + \mathrm{H.c.} \\
& + i\Lambda_{\mathrm{f}}^{\mathrm{OZ}}\sum_{\sigma\neq\sigma'}\sum_{\langle O,Z_j\rangle}\left[\hat{\boldsymbol{s}}\times\boldsymbol{d}_{O,Z_j}\right]_{z,\sigma\sigma'}\left|O\,\sigma\right\rangle\left\langle Z_j\,\sigma'\right| + \mathrm{H.c.}\,.
\end{aligned} \tag{2.97}$$

In total, we found six SOC terms which are described by the four purely imaginary couplings $i\Lambda_{\mathrm{I}}^{\mathrm{A}}$, $i\Lambda_{\mathrm{I}}^{\mathrm{B}}$, $i\Lambda_{\mathrm{R}}$, $i\Lambda_{\mathrm{f}}^{\mathrm{OZ}}$, the purely real $\Lambda_{\mathrm{PIA}}^{\mathrm{B}}$, and one coupling that is in general complex, $\Lambda_{\mathrm{PIA}}^{\mathrm{A}}$.

2.5.4 Adatom in the bridge position

After the hollow and the top position, which are described by the local point groups C_{6v} and C_{3v}, we turn to the bridge position where the adatom sits above the center of a carbon-carbon bond. For example, the elements oxygen [106, 110] and

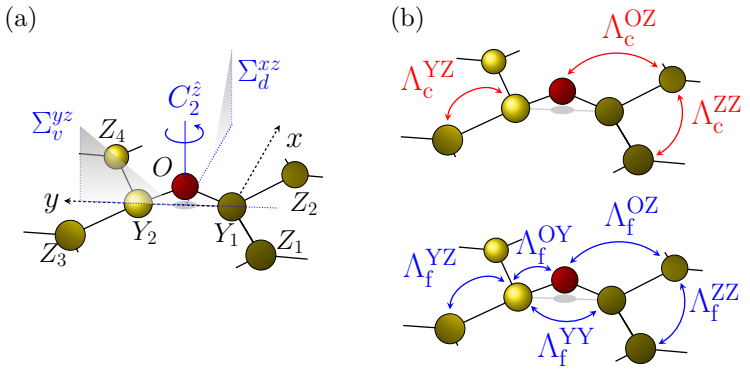

Figure 2.12: (a) Symmetry elements of the local point group symmetry C_{2v} for an adatom binding in the bridge position. The site labeling convention and the chosen coordinate system are shown as well. (b) Local SOC hoppings in the vicinity of the adatom. The spin-flipping hoppings are shown in blue, the spin-conserving hoppings in red.

nitrogen [106] are binding to graphene in this position. Comparing the adsorption energies for the elements copper [101, 108, 109] and gold [102, 109] in the bridge and top position, the bridge position is almost as energetically favorable as the top position. A similar result was found for light admolecules such as CO, NO and NO_2 [104] by comparing the adsorption energies for the bridge and hollow position. We therefore have various possible candidates of light elements to be found in the bridge position.

The effective adatom orbital has two carbon hybridization partners, see the sketch in Fig. 2.12(a). Local symmetries are, apart the identity E, two vertical reflection planes, Σ_v^{yz} and Σ_d^{xz}, and their axis of intersection $C_2^{\hat{z}}$ which allows for twofold rotations. All these symmetries are gathered in the local point group $C_{2v} = \{E, C_2^{\hat{z}}, \Sigma_v^{yz}, \Sigma_d^{xz}\}$. As C_{2v} is not a subgroup of D_{6h}, we did not discuss a global analog in the previous sections.

The low symmetry (the order of point group C_{2v} is smaller than in the previous examples) places only few restrictions on the SOC hopping in the vicinity of the adatom. Even up to (only) the next-nearest carbon neighbors Z to the adatom we find eight SOC hoppings that are in general nonzero and of different strength. We define them in the following:

$$i\Lambda_c^{YZ} = \langle Y_2 \uparrow | \hat{H}_{so} | Z_4 \uparrow \rangle , \tag{2.98a}$$
$$i\Lambda_c^{OZ} = \langle O \uparrow | \hat{H}_{so} | Z_4 \uparrow \rangle , \tag{2.98b}$$
$$i\Lambda_c^{ZZ} = \langle Z_1 \uparrow | \hat{H}_{so} | Z_2 \uparrow \rangle , \tag{2.98c}$$
$$i\Lambda_f^{OY} = \langle O \uparrow | \hat{H}_{so} | Y_1 \downarrow \rangle , \tag{2.98d}$$
$$i\Lambda_f^{YY} = \langle Y_1 \uparrow | \hat{H}_{so} | Y_2 \downarrow \rangle , \tag{2.98e}$$

$$\mathrm{Re}(\Lambda_\mathrm{f}^\mathrm{YZ}) + \mathrm{i}\,\mathrm{Im}(\Lambda_\mathrm{f}^\mathrm{YZ}) = \langle Y_2 \uparrow | \hat{H}_\mathrm{so} | Z_4 \downarrow \rangle , \tag{2.98f}$$

$$\mathrm{Re}(\Lambda_\mathrm{f}^\mathrm{OZ}) + \mathrm{i}\,\mathrm{Im}(\Lambda_\mathrm{f}^\mathrm{OZ}) = \langle O \uparrow | \hat{H}_\mathrm{so} | Z_4 \downarrow \rangle , \tag{2.98g}$$

$$\Lambda_\mathrm{f}^\mathrm{ZZ} = \langle Z_2 \uparrow | \hat{H}_\mathrm{so} | Z_1 \downarrow \rangle . \tag{2.98h}$$

A pictorial view is provided in Fig. 2.12(b). The nearest neighbor spin-conserving hopping in Eq. (2.98a) appears due to the lack of translational symmetry (third symmetry statement of Sec. 2.3.4), and is thus of the same origin as $\Lambda_\mathrm{c}^\mathrm{n}$ present in the hollow adsorption position, Sec. 2.5.2. With the horizontal reflection symmetry Σ_h^{xy} being broken, spin-flipping hoppings can occur in general (first symmetry statement). In particular, the lack of space inversion and translational symmetry gives rise to nearest spin-flipping hoppings. The nearest and next-nearest neighbor spin-flipping SOC, $\Lambda_\mathrm{f}^\mathrm{YZ}$ and $\Lambda_\mathrm{f}^\mathrm{OZ}$, respectively, are present due to the broken translationally symmetry. These couplings are in general complex-valued as there are no local symmetries that would tell us otherwise.

Summing up all terms and phase factors, we obtain the rather lengthy expression for the local C_{2v} SOC Hamiltonian which captures all symmetry allowed SOC hoppings in the vicinity of the bridge adatom,

$$\begin{aligned}
\mathcal{H}_\mathrm{so}^\mathrm{brid} = {} & i\Lambda_\mathrm{c}^\mathrm{YZ} \sum_\sigma \sum_{\langle Y_j, Z_k \rangle} \nu_{O,Z_k} \left[\hat{s}_z\right]_{\sigma\sigma} \left|Y_j\,\sigma\right\rangle\!\left\langle Z_k\,\sigma\right| + \mathrm{H.c.} \\
& + i\Lambda_\mathrm{c}^\mathrm{OZ} \sum_\sigma \sum_{\langle\langle O, Z_k \rangle\rangle} \nu_{O,Z_k} \left[\hat{s}_z\right]_{\sigma\sigma} \left|O\,\sigma\right\rangle\!\left\langle Z_k\,\sigma\right| + \mathrm{H.c.} \\
& + i\Lambda_\mathrm{c}^\mathrm{ZZ} \sum_\sigma \sum_{\langle\langle Z_j, Z_k \rangle\rangle} \nu_{Z_j,Z_k} \left[\hat{s}_z\right]_{\sigma\sigma} \left|Z_j\,\sigma\right\rangle\!\left\langle Z_k\,\sigma\right| \\
& + i\Lambda_\mathrm{f}^\mathrm{OY} \sum_{\sigma\neq\sigma'} \sum_{\langle O, Y_j \rangle} \left[\hat{\boldsymbol{s}} \times \boldsymbol{d}_{O,Y_j}\right]_{z,\sigma\sigma'} \left|O\,\sigma\right\rangle \left\langle Y_j\,\sigma'\right| + \mathrm{H.c.} \\
& + i\Lambda_\mathrm{f}^\mathrm{YY} \sum_{\sigma\neq\sigma'} \left[\hat{\boldsymbol{s}} \times \boldsymbol{d}_{Y_1,Y_2}\right]_{z,\sigma\sigma'} \left|Y_1\,\sigma\right\rangle \left\langle Y_2\,\sigma'\right| + \mathrm{H.c.} \\
& + \sum_{\sigma\neq\sigma'} \sum_{\langle Y_j, Z_k \rangle} \Big\{ \nu_{O,Z_k} \left[i\hat{s}_y\right]_{\sigma\sigma'} \mathrm{Re}\big(\Lambda_\mathrm{f}^\mathrm{YZ}\big) + i\,\mathrm{Im}\big(\Lambda_\mathrm{f}^\mathrm{YZ}\big) \Big\} \\
& \qquad \times \mathrm{sgn}\left[\boldsymbol{d}_{O,Y_j}.\boldsymbol{d}_{Y_1,Y_2}\right] \left|Y_j\,\sigma\right\rangle \left\langle Z_k\,\sigma'\right| + \mathrm{H.c.} \\
& + \sum_{\sigma\neq\sigma'} \sum_{\langle\langle O, Z_j \rangle\rangle} \Big\{ \nu_{O,Z_j} \left[i\hat{s}_y\right]_{\sigma\sigma'} \mathrm{Re}\big(\Lambda_\mathrm{f}^\mathrm{OZ}\big) + i\,\mathrm{Im}\big(\Lambda_\mathrm{f}^\mathrm{OZ}\big) \Big\} \\
& \qquad \times \mathrm{sgn}\left[\boldsymbol{d}_{O,Z_j}.\boldsymbol{d}_{Y_1,Y_2}\right] \left|O\,\sigma\right\rangle \left\langle Z_j\,\sigma'\right| + \mathrm{H.c.} \\
& + \Lambda_\mathrm{f}^\mathrm{ZZ} \sum_{\sigma\neq\sigma'} \sum_{\langle\langle Z_j, Z_k \rangle\rangle} \left[i\hat{\boldsymbol{s}} \times \boldsymbol{d}_{Z_j,Z_k}\right]_{z,\sigma\sigma'} \left|Z_j\,\sigma\right\rangle \left\langle Z_k\,\sigma'\right| .
\end{aligned} \tag{2.99}$$

All quantities, which are introduced to describe the phase factors, are to be understood in a similar manner as in the previous sections. In particular, we sum in the first and sixth line over the nearest neighbors $\langle Y_j, Z_k \rangle$ and employ the symbol ν_{O,Z_k}. There, it is $\nu_{O,Z_k} = +1$ (-1) if the path $Z_k \to Y_j$ is counter clockwise (clockwise) after extension to the next nearest neighbor path $Z_k \to Y_j \to O$.

The order of the point group C_{2v}, which is four, is lower than for the point groups C_{3v} (order six) and C_{6v} (order twelve). The lower symmetry is directly reflected in the many terms occuring in the SOC Hamiltonian.

2.6 Concluding remarks

With this section, we conclude the chapter on the derivation of effective SOC Hamiltonians from simple symmetry arguments. We considered both graphene systems with the global point group symmetries D_{6h}, D_{3d}, D_{3h}, C_{6v}, and C_{3v}, and graphene under local changes in the symmetry due to single adatoms in the hollow, bridge, and top positions. The latter give rise to the local point groups C_{6v}, C_{3v}, and C_{2v}, respectively. In the derivation of the models, we assumed effective monovalent orbitals that are invariant under the global or local point group symmetry.

Our approach does not resolve the microscopic origin of the different SOC hoppings. Such a picture would be obtained considering a multi-orbital TB description as, for example, it was done in the work by Konschuh *et al.* [71] for graphene and the work by Gúzman-Arellano *et al.* [111], where the authors investigate the effect of a gate voltage on the local SOC induced by fluorine on graphene. In the end, to obtain a model Hamiltonian, which is convenient for investigations such as spin transport, one will project the multi-orbital result to, for example, the p_z orbital sector. This projection can be acchieved with the Löwdin down-folding scheme [112].

We assumed in our discussion of local adsorbates monovalent effective atomic orbitals, which are invariant under the corresponding local point group symmetry. The last statement holds explicitly for atomic s and p_z orbitals. Depending on the adsorbate, this condition might not be met and an extension of the model would be required. The presented models nevertheless work very well for the methyl group and fluorine, binding on graphene in the top position, and copper, binding in both the top and bridge position, as can be seen in the following chapter.

Other symmetry based discussions of the SOC from local adsorbates can be found in the literature. Let us shortly comment on the approach and results of three exemplary works. Weeks *et al.* [55] investigate heavy adatoms on graphene by combining symmetry arguments, DFT calculations, and TB simulations. Explicitly, they predict that thallium and indium would stabilize the quantum spin Hall state in graphene due to their strong intrinsic SOC. These adatoms are non-magnetic and bind in the hollow position. Furthermore, they have an unfilled p-shell and the

authors conclude that the Rashba coupling will be subdominant for these hollow adatoms close to the Dirac points[16]. The exclusion of spin-flipping processes due to magnetic moments or the Rashba coupling and the presence of strong intrinsic, i.e., spin-conserving, SOC coupling in the vicinity of the adatoms is in favor of the quantum spin Hall state. We note that the SOC Hamiltonian of Ref. [55] is expressed in hoppings among the adatoms' p orbitals. Assuming a periodic pattern of non-interacting adatoms placed in each hexagon, the authors provide also a down-folded, graphene-only Hamiltonian in momentum space. We can therefore not directly compare their model with our result presented in Sec. 2.5.2. For a direct comparison, one would need to properly down-fold both our and their Hamiltonian in real space to the p_z orbital sector to bring the two models to the same form. This is, however, beyond the scope of this thesis. The prediction of Weeks *et al.* from 2011 for the indium adatom was tested in transport studies of Jia *et al.* [59] and Chandni *et al.* [60] four years later. However, both works did not find clear-cut evidence of indium induced strong SOC. A recent work by dos Santos and coworkers [61] tries to explain this discrepancy between the theoretical and experimental results. After down-folding to a graphene-only Hamiltonian, they find that the adatom induces first and second nearest neighbor hoppings between carbon atoms forming the hexagon ring around the hollow adatom. These hopping terms allow not only for intra- but also inter-valley spin-orbit scattering processes. Finally, they conclude from large-scale quantum transport simulations with randomly distributed adatoms that the valley-mixing terms cause the absence of a topological gap in the experiments.

Pachoud *et al.* [80] study also non-magnetic, heavy adsorbates on graphene, which do not induce significant local corrugation to the graphene lattice. In that case, the induced local SOC strength originates mainly from the intra-atomic SOC of the adsorbate[17]. They consider adatoms in all three adsorption positions and take into account p, d, and f orbitals on the impurity. Their derivation of the Hamiltonians is equivalent to the approach of Weeks *et al.* [55] for the hollow position, but extends the results of the latter by considering not only p orbitals. They also provide the graphene-only Hamiltonians in the momentum space by taking a continuum limit as done by dos Santos *et al.* [61]. As we mentioned already above, our models of the preceding sections are therefore not directly comparable to their results. The result for the hollow position is similar to the one of dos Santos *et al.* showing the emergence of spin-dependent inter-valley hoppings. Additional spin-flipping terms appear in the result of Pachoud *et al.*, which are neglected in the ones of dos Santos *et al.*. Within the same approach, Pachoud *et al.* investigate the top and bridge position. In the top position, they find second nearest intrinsic and Rashba-like first nearest neighbor hoppings. The PIA coupling, whose presence was shown in

[16] In Ch. 4, we will encounter the basic and simple argument behind this conclusion.
[17] We will learn more about the microscopic origin of local SOC in the next chapter.

Sec. 2.5.3 and preceding sections, does not occur in the presented result. For the bridge position, they do not find any SOC terms at all. This is in clear contrast with our findings of Sec. 2.5.4. In the next chapter, we will successfully apply our SOC model to a copper adatom binding in the bridge position. We find that the copper adatom also does not induce significant corrugation in the graphene lattice, which meets the prerequisite of the work of Pachoud *et al.*.

As a last example, we want to mention the SOC analysis by Brey [81] of adatoms with outer-shell p orbitals in the hollow and top positions. Brey considers the atomic SOC between the orbitals of the adatom, and considers tunneling between the orbitals of the adatom and graphene in second order perturbation theory. For an effective Hamiltonian, Brey concentrates on Bloch states directly at the Dirac point. For the hollow position, he finds spin-conserving hoppings only between next-nearest carbon neighbors in contrast to our additional nearest neighbor contribution in Sec. 2.5.2. Furthermore, no spin-flipping contributions related to the Rashba coupling are found. As the analysis concentrates to states directly at the $\boldsymbol{K}$ point, a momentum-dependent contribution as, for example, our PIA term does not appear. For the top position, Brey resolves the contribution of the next-nearest neighbor intrinsic SOC and the nearest neighbor Rashba coupling.

Our effective SOC Hamiltonians, presented in this chapter, are useful for spin-transport studies and are easy to implement in quantum transport simulation packages such as Kwant [113]. However, there are two issues which have to be dealt with. On the one hand, we saw especially in the case of the local symmetries that many SOC parameters can occur in the vicinity of the adsorbate. For a convenient use of the model, the pool of free parameters should be reduced to a minimal set. On the other hand, one has to find realistic estimates for the SOC strengths. Combining the derived effective Hamiltonians with the results of DFT calculations can resolve both problems. Essentially, the next chapter shows this approach at work for three local adsorbates, the methyl group, fluorine, and copper on graphene.

3 Local spin-orbit coupling from adatoms: Case studies

This chapter is divided into three parts relying on three publications: Section "Methyl functionalized graphene" is based on the paper "Spin-orbit coupling in methyl functionalized graphene", PRB 93, 045423 (2016), by Klaus Zollner, Tobias Frank, Susanne Irmer, Martin Gmitra, Denis Kochan, and Jaroslav Fabian. Section "Fluorine functionalized graphene" is based on the paper "Spin-orbit coupling in fluorinated graphene", PRB 91, 115141 (2015), by Susanne Irmer, Tobias Frank, Sebastian Putz, Martin Gmitra, Denis Kochan, and Jaroslav Fabian. Section "Copper functionalized graphene" is based on the paper "Copper adatoms on graphene: Theory of orbital and spin-orbital effects", PRB 95, 035402 (2017), by Tobias Frank, Susanne Irmer, Martin Gmitra, Denis Kochan, and Jaroslav Fabian. In all three publications, I was contributing to the development of the effective SOC Hamiltonians and the TB simulations, including the fitting of the DFT results.

3.1 Adatoms on graphene

Placing adsorbates on graphene offers a way to tailor graphene's qualities, for example, in the electronic and optical area. While graphene functionalized with $FeCl_3$ represents an excellent transparent electrical conductor, full fluorination transforms graphene to a wide-bandgap semiconductor [136]. It was also demonstrated that graphene based circuits can be patterned by local functionalization with adsorbates (see Ref. [136] and references therein). It is important, however, to realize the strong influence of the degree of functionalization, i.e. the adsorbate concentration, on the induced properties as well as other extrinsic effects such as temperature or gating of the graphene samples [111, 114, 127, 137, 138].

For experiments, it is important to have tools at hand for the detection and characterization of adsorbates on graphene. Adsorbates can induce changes in the crystal structure (e.g., by covalent bonding) and the transport properties of graphene (e.g., by a local charge transfer between adsorbate and graphene). Consequently, scanning tunneling microscopy (STM) [127, 139–142], Raman spectroscopy [143, 144], electrostatic force microscopy [145], and electron diffraction [146] are, among others, convenient approaches to quantify or classify the impurities. Recently, Hal-

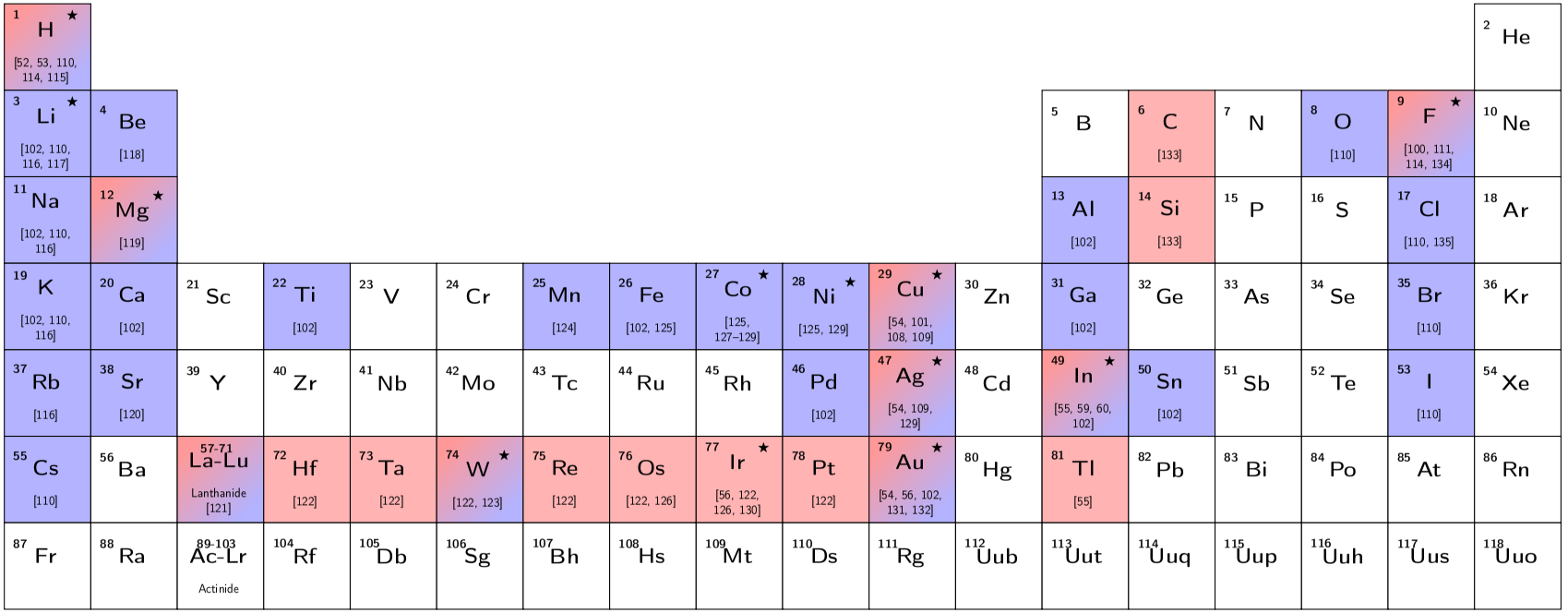

Figure 3.1: Periodic system of adsorbates on (single layer) graphene studied in the literature. Adatoms which are investigated with a focus on the impact on the orbital electronic structure (DFT, TB or experimental studies) are marked in blue. Investigations of the SOC, magnetic moments, and spin relaxation due to the adsorbate are marked in red. A combination of orbital and spin physics is indicated by a gradient between blue and red. Experimental works are stressed by a star symbol. References to the corresponding works are shown together with each element. This list does not claim to be complete but is intended to give the reader a first clue about existing works.

bertal *et al.* [147] managed to image individual atomic defects on graphene by scanning nanothermometry. Not least because of graphene's sensitivity to adsorbates, graphene-based gas or chemical sensors represent an interesting field of research [5, 6].

Several works, both experimental and theoretical, have focused on small or dilute concentrations of adsorbates on graphene. Figure 3.1 presents a list[1] of adatom studies on graphene where the authors focused on different aspects of adatom induced properties, such as the impact on the electronic structure of graphene and spin-related phenomena due to locally induced magnetic moments or strong SOC. Let us comment on some works which are important for or related to our considerations in the following sections and chapters.

Understanding the binding of the adatom to graphene is important in view of strong or weak bonding, thermal stability, charge transfer, and adsorption position, to name only a few. For example, while hydrogen establishes a strong covalent bond to graphene [52], copper is only weakly bonding to graphene and van der Waals interactions have to be included in the theoretical DFT calculations to obtain a satisfying description [101, 109]. The binding behavior influences also the thermal stability of the adatom on graphene and is related to the strengths of migration barriers for the specific adsorbate [110] and its tendency to clustering. Depending on the electronegativity of the element, less or more significant charge transfer occurs between graphene and the impurity (see for example hydrogen [52] and fluorine [100], respectively).

We already saw in Ch. 2 that the adsorption position plays an important role for considerations of SOC. Depending on whether the adsorbate prefers the hollow, top, or bridge position, spin-conserving and spin-flipping hoppings occur. For example, Weeks *et al.* [55] predicted that the adatoms indium and thallium are found in the hollow position and induce large intrinsic SOC. Correspondingly, they concluded that these elements stabilize the quantum spin Hall state in graphene. However, up to now this promising theoretical vision was not observed in experiments [59, 60]. Local enhancement of the SOC in graphene was studied in several works, for example the light adatom hydrogen [52], or the more heavier gold [131]. Spin Hall effect studies of experimental groups [53, 54] extracted large spin Hall angles indicating strong SOC for hydrogen, gold, silver, and copper and seem to be in line[2] with the theoretical works.

The spin-physics in graphene is also significantly influenced by the formation of local magnetic moments in graphene [115]. For example, it was shown [137, 148,

[1] Due to the huge literature on the subject, this list is not complete but may give the interested reader a first impression on the large variety of approaches and results, and encourage him or her to inquire further.

[2] References [56–58] pointed out recently the importance of multiple background contributions (not necessarily spin-dependent) to non-local resistance signals. These findings indicate that the analysis of the spin Hall effect might need refinement.

149] that sp^3 defects such as hydrogen give rise to such local magnetic moments. If the adatom furthermore induces a strong resonant state (see Ch. 4) close to the Fermi level, already a small amount of impurities contributes significantly to the spin relaxation in graphene as was shown by Refs. [26, 27, 62] (see Ch. 5).

In this chapter, we concentrate on the local SOC induced by three adsorbates, which are the methyl group CH_3, and the adatoms fluorine F and copper Cu. In all cases, our focus lies on the dilute limit of adsorbate concentration so that we can exclude interactions between the adsorbates or clustering effects. In order to extract the local SOC strengths we rely on a combination of the symmetry analysis described in Ch. 2 and DFT calculations performed by Klaus Zollner, Tobias Frank, and Martin Gmitra. In Sec. 3.2 we will first address the possible origin for locally enhanced SOC in graphene, before we describe our approach for unraveling the SOC mechanisms for the studied adsorbates in Sec. 3.3. With the Secs. 3.4, 3.5, and 3.6, we turn to the qualitative and quantitative study of local SOC for CH_3, F, and Cu, respectively. Section 3.7 concludes our case studies on local SOC from adsorbates in graphene.

3.2 Mechanisms for local spin-orbit coupling in graphene

The binding of adatoms to graphene impacts locally the SOC in graphene in mainly two ways. The first mechanism is introduced by the covalent bonding of adatoms, for example, in the top position on graphene, as it is the case for hydrogen [52]. The sp^2 network of graphene is locally disturbed due to a sp^3 rehybridization of the atomic orbitals on the carbon site to which the adatom binds to. As a result, this carbon atom is lifted out of the graphene plane. Castro Neto and Guinea [51] argued in 2009 that the local disturbance of the graphene orbital structure can lead to strong enhancement of the local spin-orbit strength in the π sector, reaching values of about 7.5 meV. Due to the sp^3 hybridization, the p_z orbitals of carbon experience a nonzero overlap with the p_x and p_y orbitals on the same atom[3]. We will recapitulate the results of Ref. [51] in the following.

Castro Neto and Guinea build their local orbital basis out of directed orbitals allowing for a tuning between the two extreme cases of sp^2 and sp^3 hybridization. Following Pauling [150], they employ the basis

$$|\pi\rangle = A|s\rangle + \sqrt{1-A^2}|p_z\rangle\,,$$
$$|\sigma_1\rangle = \sqrt{\frac{1-A^2}{3}}|s\rangle - \frac{A}{\sqrt{3}}|p_z\rangle + \sqrt{\frac{2}{3}}|p_x\rangle\,,$$

[3] In flat graphene, the p_z orbitals are orthogonal to the p_x, p_y orbitals on the same atom. This is the main reason why the σ-π mixing in graphene is subdominant for the SOC. For more details see Sec. 2.1.

$$|\sigma_2\rangle = \sqrt{\frac{1-A^2}{3}}|s\rangle - \frac{A}{\sqrt{3}}|p_z\rangle - \frac{1}{\sqrt{6}}|p_x\rangle + \frac{1}{\sqrt{2}}|p_y\rangle\,,$$
$$|\sigma_3\rangle = \sqrt{\frac{1-A^2}{3}}|s\rangle - \frac{A}{\sqrt{3}}|p_z\rangle - \frac{1}{\sqrt{6}}|p_x\rangle - \frac{1}{\sqrt{2}}|p_y\rangle\,. \tag{3.1}$$

For a tuning parameter of $A = 0$, the basis describes sp^2 hybridization, for $A = 0.5$ the sp^3 configuration is realized. The value of A is related to the angle θ between the direction of the σ_i $(i = 1, 2, 3)$ orbitals and the plane normal via $\cos\theta = -A/\sqrt{A^2+2}$. Investigating the propagator from a π state at one atomic site, to the π' state at another site, they find a relation between the emerging effective non-local SOC strength $\Delta_{\mathrm{SO}}^{\mathrm{eff}}$ and the atomic one of the carbon $2p$ orbitals, Δ_p,

$$\frac{\Delta_{\mathrm{SO}}^{\mathrm{eff}}}{\Delta_p} \approx A\sqrt{3(1-A^2)}\,. \tag{3.2}$$

In the limit of full sp^3 hybridization, this formula estimates $\Delta_{\mathrm{SO}}^{\mathrm{eff}} = 75\%$ and $\Delta_p \approx 7.5\,\mathrm{meV}$.

Clearly, if the local SOC strengths exceed the value of 7.5 meV, the local sp^3 distortion can not be the only cause. In this case, the second possibility of enhancing SOC in graphene by adsorbates has to be considered. The intra-atomic SOC of the adatom might be significantly stronger than the one of the carbon atoms in the graphene lattice[4]. The hybridization between the adatom's orbitals and the underlying graphene structure can infer a partial transfer of the strong SOC to the graphene π bands.

3.3 Methods

We tackle the origin and magnitude of the local SOC from adatoms in graphene by a combination of two convenient tools: On the one hand, we consider the local symmetry, i.e., the point group which describes the lattice symmetries in the vicinity of the adatom. We then directly profit from our symmetry analysis of the local SOC in the previous Secs. 2.5.2, 2.5.3, and 2.5.4. On the other hand, we are interested in specific adatoms. Their binding properties, the local changes in the electronic structure and, most importantly, the SOC can be nicely analyzed by (spin-unpolarized) DFT calculations of the (local and projected) DOS and the band structure. With this "realistic" data input, we can test and, if necessary, adjust the models and fit the SOC parameters in our effective TB model.

We will investigate in the following three adsorbates: the admolecule methyl CH_3 in the top position, the adatom fluorine F in the top position, and copper Cu in

[4] As the SOC energy of an electron close to the atomic core scales like SOC$\propto Z^4$ [22], heavy adatoms such as indium ($Z = 49$) exhibit strong intra-atomic SOC.

the top and bridge positions. Our interest in these impurity studies is twofold. Firstly, we would like to extract the strength of the SOC locally induced by a single adsorbate and, secondly, we want to discover the origin of the local SOC. In order to do this, we study a dilute adatom (or admolecule) concentration (typically of about 1%) on graphene within the supercell approach. Note that the supercells reproduce a periodic pattern of adatoms on the graphene surface (we do not study a random distribution of the adsorbates). Unwanted (but in general present) interaction between the periodic images of the adsorbates requires us to choose the supercells to be big enough. Neglecting at first SOC effects, we perform least-square fits[5] of the TB to the DFT band structure and extract the orbital TB parameters hybridization strength and on-site energy. Keeping this result fixed, we fit the SOC strengths to the spin splitting of the bands close to the Fermi level. This approach is justified due to the different energy scales of the orbital level of the band structure (order of 1 eV) and the spin splitting of the bands (order of 1 meV). Since the number of symmetry allowed local SOC parameters can be quite extensive, the fits are performed such that we reduce the number of fitting parameters to a minimal set. At the same time, this set is required to reflect the spin splitting of the bands best. Note that the spin splittings of the bands depend on the supercell size and decrease with decreasing adsorbate concentration. The representative magnitude of the local SOC is reflected in the SOC strengths extracted from the TB model. Once interaction effects between the adatoms can be excluded, these values are rather robust to a further increase of the supercell size.

3.4 Methyl functionalized graphene

In the following section we study in detail the local SOC induced by the methyl group on graphene. In particular, we use the TB models derived in the previous chapter and rely on the support of DFT calculations by Klaus Zollner, Martin Gmitra, and Tobias Frank [99].

The methyl group is the most simple organic molecule. It is of special interest for experiments where chemical vapor deposition is employed to grow graphene, as during the growth process a H_2/CH_4 gas mixture is used [152]. With this, CH_3 appears to be a likely contaminant to clean graphene samples. In those systems, the influence of the methyl group on the spin physics needs to be considered as this adsorbate was shown, for example, to induce local magnetic moments in graphene [99, 148], similarly as in the case of the hydrogen adatom. From experiences with hydrogen on graphene [52, 53], one might also expect some influence of local SOC induced by CH_3.

The similarity of methyl and hydrogen on graphene could be also deduced from

[5]For the least-square fitting method see for example Ref. [151].

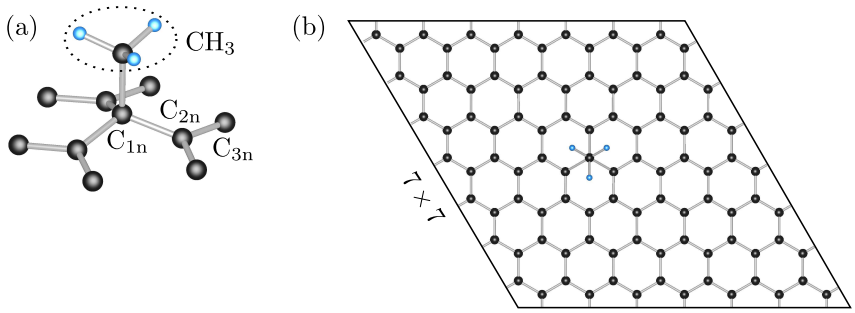

Figure 3.2: (a) Geometric structure close to the admolecule CH_3 binding in the top position. CH_3 binds to the carbon atom C_{1n}, has three second nearest neighbors C_{2n}, and six third nearest neighbors C_{3n}. In equilibrium, the three hydrogen atoms (blue) of methyl point towards the centers of the graphene hexagons lying underneath. Panel (b) shows the 7×7 supercell, which is used to realize the dilute limit of admolecule coverage. Adapted from [99].

the respective values of the effective Pauling electronegativity, which are very close for the two adsorbates [153, 154]. This indicates similar binding behavior of methyl and hydrogen. Whether the resemblance also extends to the regime of SOC, cannot be directly concluded without further thorough analysis which is the topic of this section.

Indeed, we find that, as in the case of hydrogen on graphene [52, 53], the local SOC strengths reach values which are about 100 times larger than in pristine graphene. The local sp^3 distortion, introduced by the impurity covalently bonding to graphene, can be accounted for this effect.

3.4.1 Structure and orbital physics

Figure 3.2 provides a pictorial view of the geometric structure in the vicinity of CH_3, adsorbing on graphene, as well as the 7×7 supercell, which is chosen to represent the limit of dilute admolecule coverage on graphene. In equilibrium, the hydrogen atoms of the methyl molecule point towards the center of the three subjacent graphene hexagons. Furthermore, a small pyramidal (instead of trigonal) configuration of the molecule appears. A significant structural distortion can be observed only very close to the adsorption position of CH_3 and is manifested in a local stretching of the carbon-carbon bonds and a lifting of the carbon atom C_{1n} out of the graphene plane by about 0.4 Å [99]. The methyl molecule sits about 1.6 Å above C_{1n}.

The bonding of CH_3 to graphene leaves structural signatures in graphene very alike to those of the hydrogen adatom [52], which enters a strong covalent bond with graphene. The binding energy of methyl on graphene is with 2.46 eV [99] furthermore very close to the hydrogen related value [52]. The covalent bonding

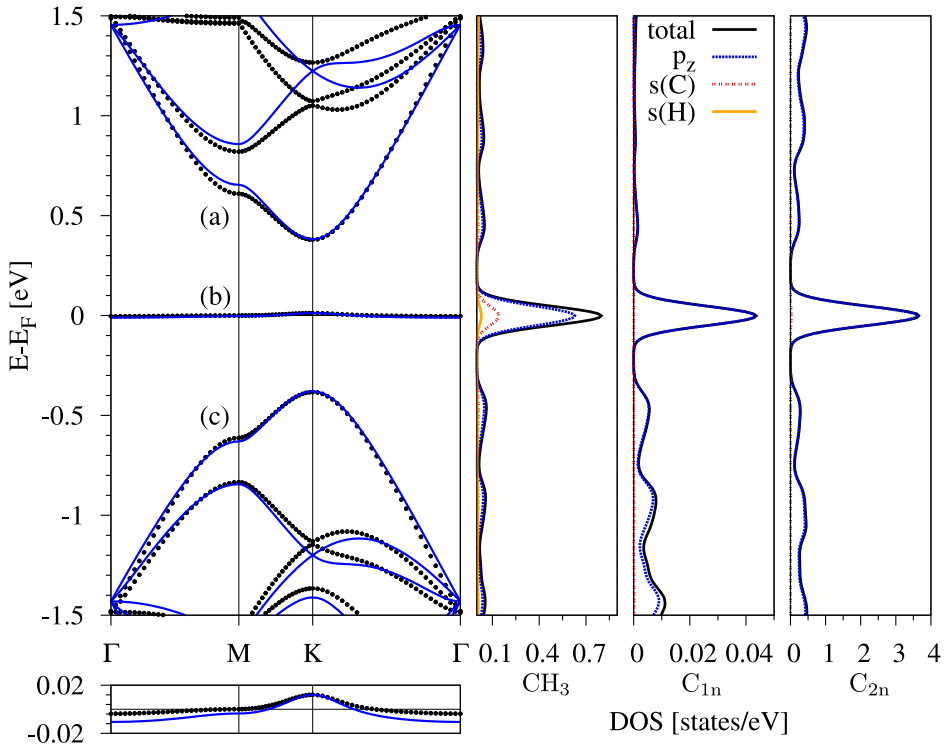

Figure 3.3: Electronic band structure and DOS of methyl functionalized graphene for a 7×7 DFT supercell calculation. A zoom to the midgap band is shown below the band structure. The DOS is projected to the orbitals with s and p character on CH_3, C_{1n}, and C_{2n}. Together with the DFT band structure (black dotted), the band structure from the fitted TB model (blue solid) is shown. Adapted from [99].

of the admolecule is accompanied by a local sp^3 rehybridization of the atomic orbitals on its adsorption partner C_{1n}, which lifts C_{1n} out of the graphene plane. Clear signatures of the covalent bonding can be further seen in the projected DOS (PDOS) analyzed for a dense admolecule coverage (2×2 supercell) in Ref. [99].

While in the dense limit the methyl admolecules of different supercells are very close and are likely to interact, this interaction of periodic images is suppressed for large enough admolecule distances, as it is the case in the selected 7×7 supercell. This configuration models an admolecule to carbon ratio of 1%. Figure 3.3 displays the DFT calculated band structure for the dilute limit together with the PDOS for the atomic sites CH_3, C_{1n}, and C_{2n}. Close to the Fermi level appear three bands which we call the (a) conduction, (b) midgap, and (c) valence band. The midgap band is only weakly dispersive (bandwidth of about 0.01 eV). For a denser admolecule coverage, the bandwidth is by up to a factor of ten larger [99]. This implies that the Bloch modulation function of the corresponding state becomes in the dilute limit more localized within the supercell. The interaction between the supercell periodic images is weakened.

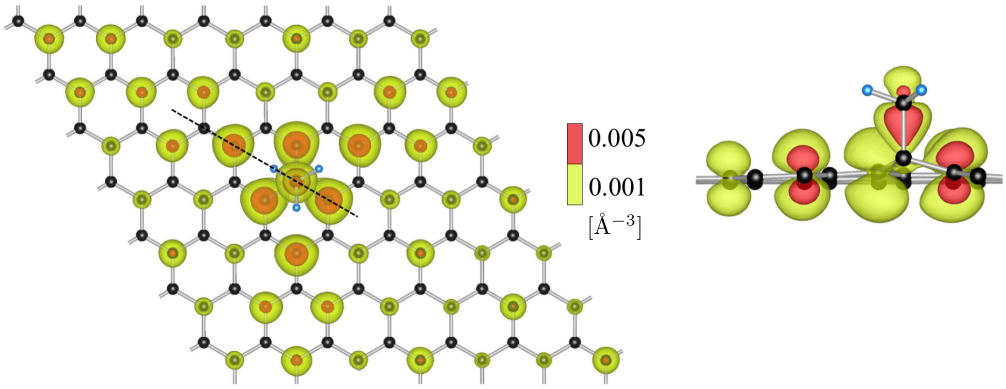

Figure 3.4: Top and side view of the electronic charge density for states in the midgap band of methyl functionalized graphene in a 7×7 DFT calculation. The dashed line in the top view indicates the line along which the cross-sectional view is extracted. Adapted from [99].

The PDOS data reveals that the bands (a)-(c) around the Fermi level are built from the p_z orbitals on C_{2n} and CH_3. Note that the states of the site C_{1n}, the adsorption position of the methyl group, contribute only by a small amount. The electronic states forming the midgap band preferably occupy sites on the graphene sublattice to which the admolecule is not adsorbing to. This fact is, for example, visualized in the plot of the charge density of Ref. [99], see Fig. 3.4. The charge density is strongly centered near the impurity which indicates suppression of the interaction between admolecules from neighboring supercells. The C_3 rotational invariance of the local point group symmetry C_{3v} is reflected in the triangular anisotropy of the charge density.

Dilute limit - orbital tight-binding model

In the previous chapter, we considered effective TB Hamiltonians which were based on atomic states with p_z or s orbital character. The above discussion of the electronic structure of methyl functionalized graphene in the dilute limit showed that this assumption is valid for the bands (a)-(c) close to the Fermi level. Indeed, the orbital band structure of the 7×7 supercell calculation for CH_3 on graphene can be nicely fit by the rather simple minimal orbital TB Hamiltonian [97, 98] given already in Eq. (2.79),

$$\begin{aligned} \mathcal{H}_{\text{orb}} = \omega \sum_{\sigma} \left(|O\,\sigma\rangle\langle Y\,\sigma| + |Y\,\sigma\rangle\langle O\,\sigma| \right) \\ + \varepsilon \sum_{\sigma} |O\,\sigma\rangle\langle O\,\sigma| \,. \end{aligned} \tag{3.3}$$

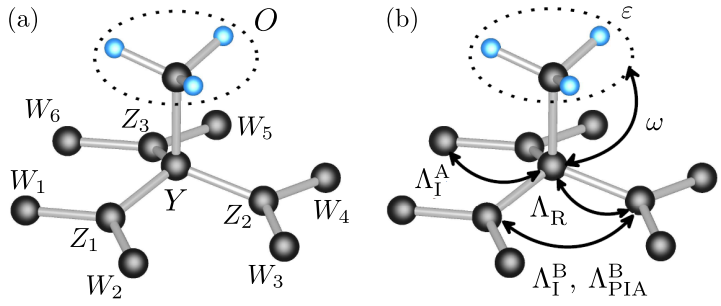

Figure 3.5: (a) Site labeling convention in the model Hamiltonians of Eq. (3.3) and Eq. (3.4). (b) Pictorial view of the local orbital and spin-orbital TB hoppings describing CH_3 on graphene in the top position. Adapted from [99].

This Hamiltonian is added to the one of pristine graphene, $\mathcal{H}_0$ in Eq. (2.4), in the nearest neighbor approximation with $t = 2.6\,\text{eV}$[6]. Here, the methyl admolecule is modeled, for simplicity, by one effective orbital with p_z character. Let us shortly remind us of the notation used in Eq. (3.3). The symbol $|O\rangle$ represents an electronic state in the effective orbital on CH_3, the symbol $|Y\rangle$ is used for a p_z orbital state on the admolecule's nearest neighbor C_{1n}. The TB parameter ω describes the hybridization between C_{1n} and CH_3, and ε parametrizes the on-site energy of the single energy level representing the methyl group. Figure 3.5(a) provides a pictorial view of the labeling conventions.

In order to extract realistic values of the parameter set (ω, ε), we perform a least-square fit of the eigenenergies of $\mathcal{H}_0 + \mathcal{H}_{\text{orb}}$ to the DFT computed bands (a)-(c). We restrict the fit to a range of momenta around the $\boldsymbol{K}$ point. This range is indicated in Fig. 3.6 as we employ it below also in the fit of the local SOC strengths. With the parameters $\omega = 7.6\,\text{eV}$ and $\varepsilon = -0.19\,\text{eV}$ we obtain good overall agreement between the DFT and TB band structure calculation, see Fig. 3.3. The magnitudes of the orbital parameters agree with the ones of Ref. [98] who finds $\omega' = 5.2\,\text{eV}$ and $\varepsilon' = -0.16\,\text{eV}$ for a 4×4 supercell calculation. The large hybridization strength and the small on-site energy reflect the strong covalent bond between CH_3 and graphene in the TB model. In fact, the extracted parameters are very close to those of hydrogenated graphene [52].

3.4.2 Spin-orbit coupling from dilute methyl coverage

Figure 3.6 displays the spin-orbit splittings of the bands (a)-(c) along the Γ-M-K-Γ line for the 7×7 supercell. We already presented a candidate for the model of the local SOC in Sec. 2.5.3. Equations (2.89) and (2.95) define six possible SOC

[6] All on-site energies aside of the one of the admolecule are set equal to zero. Furthermore, we do not take into account changes in the nearest neighbor hopping parameter t among carbon atoms in the vicinity of the impurity.

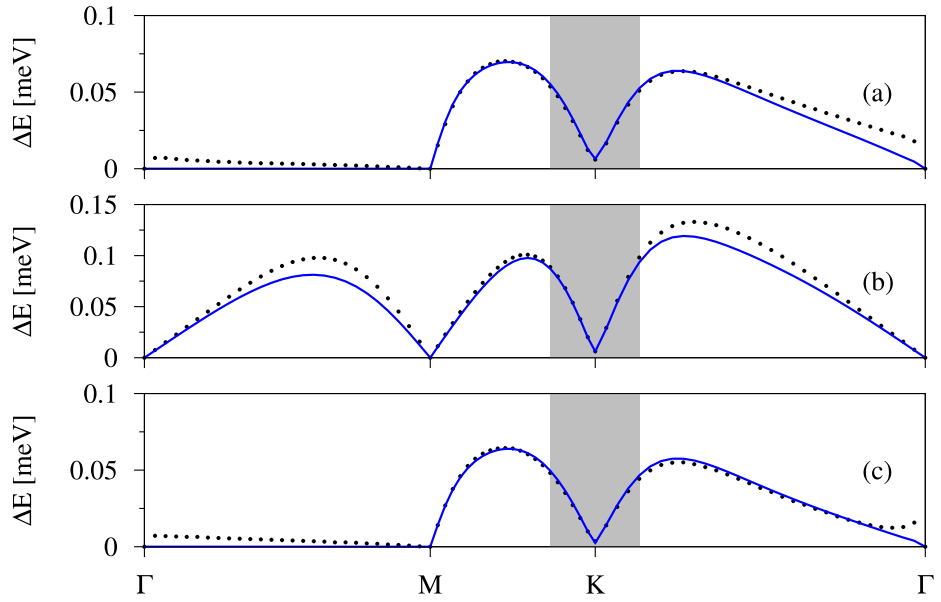

Figure 3.6: Spin splitting of the bands close to the Fermi energy of methyl functionalized graphene in the dilute limit. The splittings along the high symmetry line Γ-M-K-Γ are obtained from 7×7 supercell calculations of both DFT (black dotted) and the best-fit TB model (blue solid). The fitting was restricted to the shaded region around the $\boldsymbol{K}$ point. The labeling (a), (b), and (c) corresponds to the band labeling in Fig. 3.3. From [99].

couplings that describe the SOC in the vicinity of the admolecule based on a TB description with p_z orbitals. Minimizing the least-square differences between model and DFT calculated band splittings reduces this set to four local SOC parameters only: $\Lambda_{\mathrm{I}}^{\mathrm{A}}$, $\Lambda_{\mathrm{I}}^{\mathrm{B}}$, Λ_{R}, and $\Lambda_{\mathrm{PIA}}^{\mathrm{B}}$, see Fig. 3.5(b). During the fit of the bands (a)-(c), we concentrated, as for the orbital part, on the low energy region around the $\boldsymbol{K}$ point, see Fig. 3.6. The corresponding model Hamiltonian is given by

$$
\begin{aligned}
\mathcal{H}_{\mathrm{so}}^{\mathrm{top}} = & \frac{i\Lambda_{\mathrm{I}}^{\mathrm{A}}}{3\sqrt{3}} \sum_{\sigma} \sum_{\langle\langle Y,W_j\rangle\rangle} \nu_{Y,W_j} \left[\hat{s}_z\right]_{\sigma\sigma} \left|Y\,\sigma\right\rangle\left\langle W_j\,\sigma\right| + \mathrm{H.c.} \\
& + \frac{i\Lambda_{\mathrm{I}}^{\mathrm{B}}}{3\sqrt{3}} \sum_{\sigma} \sum_{\langle\langle Z_j,Z_k\rangle\rangle} \nu_{Z_j,Z_k} \left[\hat{s}_z\right]_{\sigma\sigma} \left|Z_j\,\sigma\right\rangle\left\langle Z_k\,\sigma\right| \\
& + \frac{2\Lambda_{\mathrm{PIA}}^{\mathrm{B}}}{3} \sum_{\sigma\neq\sigma'} \sum_{\langle\langle Z_j,Z_k\rangle\rangle} \left[i\hat{\boldsymbol{s}}\times\boldsymbol{d}_{Z_j,Z_k}\right]_{z,\sigma\sigma'} \left|Z_j\,\sigma\right\rangle\left\langle Z_k\,\sigma'\right| \\
& + \frac{2i\Lambda_{\mathrm{R}}}{3} \sum_{\sigma\neq\sigma'} \sum_{\langle Y,Z_j\rangle} \left[\hat{\boldsymbol{s}}\times\boldsymbol{d}_{Y,Z_j}\right]_{z,\sigma\sigma'} \left|Y\,\sigma\right\rangle\left\langle Z_j\,\sigma'\right| + \mathrm{H.c.} \\
& + \frac{i\lambda_{\mathrm{I}}}{3\sqrt{3}} \sum_{\sigma} {\sum_{\langle\langle m,n\rangle\rangle}}' \nu_{m,n} \left[\hat{s}_z\right]_{\sigma\sigma} \left|X_m\,\sigma\right\rangle\left\langle X_n\,\sigma\right| . \qquad (3.4)
\end{aligned}
$$

X (Adatom)	n×n	ω [eV]	ε [eV]	$\Lambda_{\mathrm{I}}^{\mathrm{A}}$ [meV]	$\Lambda_{\mathrm{I}}^{\mathrm{B}}$ [meV]	$\Lambda_{\mathrm{PIA}}^{\mathrm{B}}$ [meV]	Λ_{R} [meV]
CH_3	5×5	7.6	-0.16	-0.39	0.095	-0.71	1.01
	7×7	7.6	-0.19	-0.77	0.15	-0.69	1.02
H [52]	5×5	7.5	0.16	-0.21	-	-0.77	0.33

Table 3.1: Orbital and SOC best-fit TB parameters of 5×5 and 7×7 supercells for methyl functionalized graphene. The values are comparable, which confirms the robustness of the TB model. The parameter strengths are further close to the ones obtained for hydrogenated graphene for a 5×5 supercell of Ref. [52].

Here, the symbol $|Z_j\rangle$ denotes a p_z orbital on one of the three next-nearest neighbors C_{2n} to the admolecule, $|W_j\rangle$ similarly addresses one of the six third nearest neighbors C_{3n}. The last line represents the intrinsic SOC of graphene with the fixed parameter value $\lambda_{\mathrm{I}} = 12\,\mu$eV. The primed sum addresses only carbon sites that are not coupled by $\Lambda_{\mathrm{I}}^{\mathrm{A}}$ or $\Lambda_{\mathrm{I}}^{\mathrm{B}}$.

Local SOC strengths of the order of 0.1 to 1 meV are obtained from the fit. Specifically, we find $\Lambda_{\mathrm{I}}^{\mathrm{A}} = -0.77\,\mathrm{meV}$, $\Lambda_{\mathrm{I}}^{\mathrm{B}} = 0.15\,\mathrm{meV}$, $\Lambda_{\mathrm{R}} = 1.02\,\mathrm{meV}$, and $\Lambda_{\mathrm{PIA}}^{\mathrm{B}} = -0.69\,\mathrm{meV}$. The resulting TB band splittings are shown along with the DFT data in Fig. 3.6. The parameter $\Lambda_{\mathrm{PIA}}^{\mathrm{B}}$, denoting the spin-flipping next-nearest neighbor hopping, reproduces on its own the main shape of the spin-orbit splitting curves. This result is similar to the case of hydrogenated graphene [52] which yields also local SOC strengths of the order of up to 1 meV. We show a comparison of the SOC parameters for methyl functionalized and hydrogenated graphene in Tab. 3.1. We added also SOC results from a 5×5 supercell treatment of the methyl group on graphene, for which we do not show the actual DFT and TB data. The overall magnitude of the SOC parameters coincides for the two supercell sizes. The two intrinsic spin-conserving parameters $\Lambda_{\mathrm{I}}^{\mathrm{A}}$ and $\Lambda_{\mathrm{I}}^{\mathrm{B}}$ in the 7×7 supercell are almost twice the values of the 5×5 supercell. This might be due to the fact that the 5×5 supercell still shows effects of interaction between the supercell periodic images. We therefore focused on the 7×7 supercell calculation.

To summarize, we find that the methyl group on graphene induces local SOC strengths of up to 1 meV, corresponding to a local enhancement of graphene's SOC by a factor of 100. As in the case of hydrogenated graphene [52], the SOC enhancement is due to the local sp^3 distortion introduced by the covalent bonding of the methyl group to graphene. The formula of Castro Neto and Guinea [51], Eq. (3.2), estimates for the structural parameters[7] found in Ref. [99] an effective local SOC strength of about 6 meV due to the local corrugation. In comparison to our result, this prediction slightly overestimates the effect of CH_3 adsorption on graphene.

[7] According to Ref. [99], the C_{1n} atom is lifted out of the graphene plane by 0.41 Å, and the C_{1n}-C_{2n} bond measures 1.509 Å. This yields a value of $A \approx 0.399$ in Eq. (3.2).

3.5 Fluorine functionalized graphene

As a second adsorbate for graphene we consider fluorine, which is the most electronegative chemical element and is known to form a strong covalent bond with carbon [155, 156].

Especially interesting for experiments concentrating on the spin physics in graphene with small fluorine content are studies on magnetic moments from fluorine. Theoretically, the presence of moments due to fluorine is not yet resolved as contradicting results are found in DFT studies [148, 157–159]. Nevertheless, some experimental studies [134, 137, 160] find indications of fluorine induced magnetic moments. Ref [134], for example, investigates weak localization in the fluorinated devices and observes saturation effects, which could originate in local magnetic moments or, as another possibility, from strong local SOC.

Although we do not consider magnetic moments in this section[8], we investigate the possibility of strong local SOC enhancement in graphene due to fluorine. We believe that this is a valuable contribution to encourage further experimental studies and to help in the debate of the spin physics in fluorinated graphene samples.

We will see below that fluorine on graphene induces locally even larger SOC than methyl or hydrogen. Compared to the value of the intrinsic coupling in graphene of $10\,\mu$eV, the local SOC strength reaches up to 10 meV. This corresponds to a local enhancement by a factor 1000. Simple sp^3 distortion [51] cannot generate SOC strengths of this magnitude in graphene, and we identify fluorine's p_x and p_y orbitals as the source of this giant local SOC. Our results are based on a TB study with the SOC description of the previous chapter and DFT calculations by Tobias Frank and Martin Gmitra [100].

3.5.1 Structure and orbital physics

Fluorine preferentially chemisorbs on top of one carbon atom of graphene [107, 161], see Fig. 3.7(a). In order to mimic dilute fluorinated graphene we rely on DFT data for a 10×10 supercell [see Fig. 3.7(b) for an example of the supercell geometry], which corresponds to a fluorine concentration of 0.5%. As in the previous case of methyl on graphene, fluorine and its carbon hybridization partner form a covalent bond, which is accompanied by a local sp^3 corrugation of the lattice around the adsorption position and a vertical displacement of about 0.4 Å of the atom C_{1n} [100]. The bond length between fluorine and C_{1n} is about 1.6 Å [100]. Furthermore, the analysis of a smaller 5×5 supercell [100] showed that a charge transfer occurs from graphene to fluorine (Bader charge [162] of about $0.5\,e$).

The corresponding electronic band structure calculated from DFT is shown in

[8] We will reconsider the local magnetic moment in Ch. 5, where we study spin relaxation due to resonant scattering off magnetic moments.

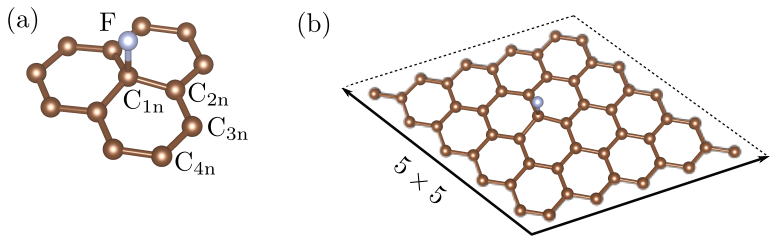

Figure 3.7: (a) Geometric structure close to the adatom F binding in the top position. Fluorine adsorbs to the carbon atom C_{1n}, has three second nearest neighbors C_{2n}, six third nearest neighbors C_{3n}, and three fourth nearest carbon neighbors C_{3n}. Panel (b) shows, as an example, a 5×5 supercell together with the corresponding lattice vectors. Adapted from [100].

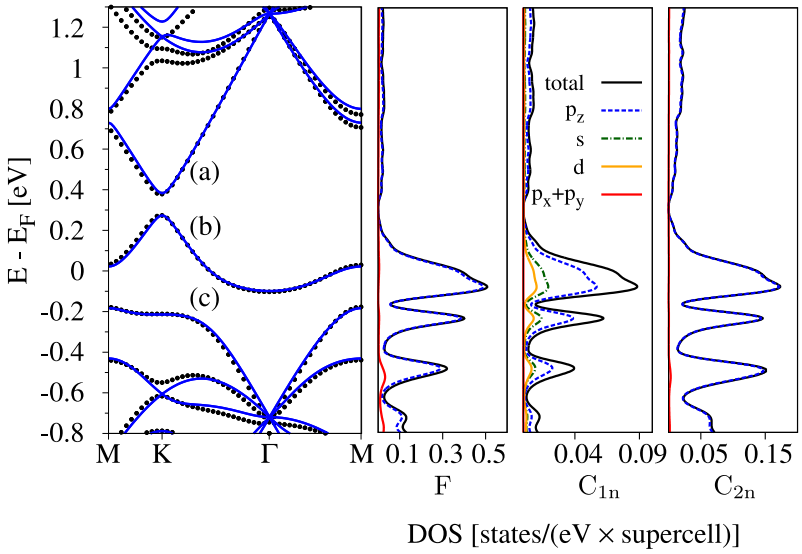

Figure 3.8: Electronic band structure and DOS of fluorinated graphene for a 10×10 DFT supercell calculation. Together with the DFT band structure (black dotted), the best-fit TB result is shown (blue solid). Close to the Fermi level, we identify the (a) conduction, (b) midgap, and (c) valence band. Adapted from [100].

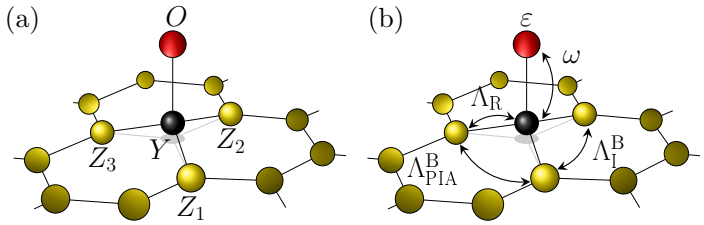

Figure 3.9: (a) Site labeling convention in the model Hamiltonians of Eq. (3.5) and Eq. (3.6). (b) Pictorial view of the local orbital and spin-orbital TB hoppings describing F on graphene in the top position.

Fig. 3.8. Next to the band structure, the PDOS for atoms in the vicinity of the impurity is shown. As in Sec. 3.4, we refer to the bands (a), (b) and (c) as the conduction, midgap and valence band in the following. We note that the width of the midgap band is with about 0.6 eV significantly larger than in the case of methyl functionalized graphene, Sec. 3.4, though it is by about a factor of five smaller than for a fluorinated 1×1 supercell (see Ref. [100]). The interaction between periodic images of the fluorine adatoms in the larger supercell treatment is suppressed. From the DOS analysis we note that the conduction, midgap, and valence bands around the Fermi level are mainly composed from states of the p_z orbitals on fluorine and its next-nearest neighbors C_{2n}. The latter kind of sites reside on the sublattice which is not fluorinated, similar as in the case of graphene functionalized with CH_3. The fluorinated carbon atom C_{1n} shows beside the p_z contribution also the presence of s and d orbitals. Below -0.4 eV, the fluorine's $p_x + p_y$ contribution to the PDOS of the valence bands increases.

The charge density calculation of a 5×5 supercell (not shown) in Ref. [100] further illustrates that the midgap state is localized on the non-fluorinated sublattice. However, the midgap state in this system is spreading out in a triangular way around the impurity and "touches" the border to the next supercells. We infer that the 5×5 supercell is still subject to significant fluorine-fluorine interaction across neighboring supercells. This supercell size is not large enough to represent the limit of dilute fluorine coverage and we therefore focus for our SOC analysis on the 10×10 supercell.

Dilute limit - orbital tight-binding model

We conclude from the previous DOS analysis that an effective TB Hamiltonian based on orbitals with p_z character is capable of describing both the orbital and spin-orbital structure of fluorinated graphene around the Fermi level. We employ

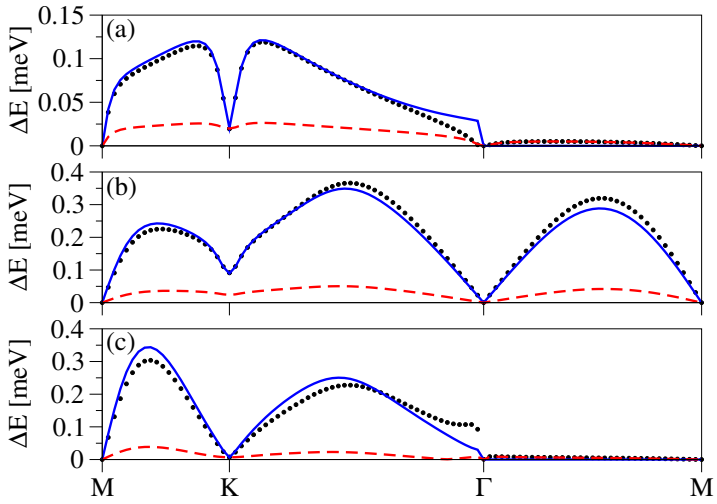

Figure 3.10: Spin splitting of the bands close to the Fermi energy of fluorinated graphene in the dilute limit. The splittings along the high symmetry line M-K-Γ-M are obtained from 10×10 supercell calculations of both DFT (black dotted) and the best-fit TB model (blue solid). The labeling (a), (b), and (c) corresponds to the band labeling in Fig. 3.8. Also shown are the reduced splittings magnitudes (red dashed), which are obtained by turning off the SOC on fluorine in the DFT calculations [100].

the local orbital Hamiltonian of Eq. (2.79),

$$\begin{aligned} \mathcal{H}_{\text{orb}} &= \omega \sum_{\sigma} \left(|O\,\sigma\rangle\langle Y\,\sigma| + |Y\,\sigma\rangle\langle O\,\sigma| \right) \\ &+ \varepsilon \sum_{\sigma} |O\,\sigma\rangle\langle O\,\sigma| \,, \end{aligned} \tag{3.5}$$

which describes fluorine on top of the atom C_{1n}. A pictorial view of the Hamiltonian is offered in Fig. 3.9. By minimizing the least-square differences between the model and DFT calculated conduction, midgap, and valence bands along the full M-K-Γ-M line, we obtain the parameter values $\varepsilon = -2.2\,\text{eV}$ and $\omega = 5.5\,\text{eV}$. The very good agreement between the model and the DFT data is shown in Fig. 3.8. Note that the negative value of the on-site energy reflects the (partial) transfer of electrons from graphene to fluorine.

3.5.2 Spin-orbit coupling from dilute fluorine coverage

Figure 3.10 displays the band splittings of the conduction, midgap, and valence bands when SOC is included in the DFT calculation. Largest splitting magnitudes are observed in the midgap and valence band, while the conduction band, composed predominantly from carbon p_z orbitals, is less split. Especially the valence band lies in energy closer to states showing contributions of fluorine's p_x and p_y orbitals

(see Fig. 3.8). To extract the local SOC strengths we use the SOC model for an adatom in the top position as introduced in Sec. 2.5.3. The set of symmetry allowed local SOC parameters reduces to three couplings upon fitting the model to the DFT splitting of all three bands along the full M-K-Γ-M line: the local intrinsic $\Lambda_{\mathrm{I}}^{\mathrm{B}}$ connecting the sites $\mathrm{C}_{2\mathrm{n}}$, the local Rashba equivalent Λ_{R} between $\mathrm{C}_{1\mathrm{n}}$ and $\mathrm{C}_{2\mathrm{n}}$ sites, and $\Lambda_{\mathrm{PIA}}^{\mathrm{B}}$, the spin-flipping PIA among sites $\mathrm{C}_{2\mathrm{n}}$. The influence of all other (symmetry allowed) local SOC couplings is found to be negligible and set to zero. The local SOC Hamiltonian therefore reads

$$\begin{aligned}\mathcal{H}_{\mathrm{so}}^{\mathrm{top}} = &\frac{i\Lambda_{\mathrm{I}}^{\mathrm{B}}}{3\sqrt{3}} \sum_{\sigma} \sum_{\langle\langle Z_j, Z_k \rangle\rangle} \nu_{Z_j,Z_k} \left[\hat{s}_z\right]_{\sigma\sigma} \left|Z_j\,\sigma\right\rangle\!\left\langle Z_k\,\sigma\right| \\ &+ \frac{2\Lambda_{\mathrm{PIA}}^{\mathrm{B}}}{3} \sum_{\sigma\neq\sigma'} \sum_{\langle\langle Z_j, Z_k \rangle\rangle} \left[i\hat{\boldsymbol{s}} \times \boldsymbol{d}_{Z_j,Z_k}\right]_{z,\sigma\sigma'} \left|Z_j\,\sigma\right\rangle \left\langle Z_k\,\sigma'\right| \\ &+ \frac{2i\Lambda_{\mathrm{R}}}{3} \sum_{\sigma\neq\sigma'} \sum_{\langle Y, Z_j \rangle} \left[\hat{\boldsymbol{s}} \times \boldsymbol{d}_{Y,Z_j}\right]_{z,\sigma\sigma'} \left|Y\,\sigma\right\rangle \left\langle Z_j\,\sigma'\right| + \mathrm{H.c.} \\ &+ \frac{i\lambda_{\mathrm{I}}}{3\sqrt{3}} \sum_{\sigma} \sum_{\langle\langle m,n \rangle\rangle}{}' \nu_{m,n} \left[\hat{s}_z\right]_{\sigma\sigma} \left|X_m\,\sigma\right\rangle \left\langle X_n\,\sigma\right| . \end{aligned} \tag{3.6}$$

The pristine intrinsic coupling $\lambda_{\mathrm{I}} = 12\,\mu\mathrm{eV}$ couples all next-nearest neighbor sites that do not participate in hoppings with $\Lambda_{\mathrm{I}}^{\mathrm{B}}$. This restriction is indicated by a prime at the corresponding summation symbol. As a best-fit result we obtain $\Lambda_{\mathrm{I}}^{\mathrm{B}} = 3.3\,\mathrm{meV}$, $\Lambda_{\mathrm{PIA}}^{\mathrm{B}} = 7.3\,\mathrm{meV}$, and $\Lambda_{\mathrm{R}} = 11.2\,\mathrm{meV}$, which yields a very good match between the TB and the DFT splittings, see Fig. 3.10. Deviations between the model and DFT results are visible close to the $\boldsymbol{\Gamma}$ point in the valence and conduction band. At energies above 0.9 eV in the conduction band and below −0.6 eV in the valence band, the $2s$ and $3d$ orbitals contribute almost as much as the p_z orbitals to the PDOS of $\mathrm{C}_{1\mathrm{n}}$ [100]. These orbital contributions are neglected in the derivation of the effective SOC Hamiltonian of Eq. (3.6).

As a cross-check we also analyzed the spin splittings in the smaller supercell 7×7 for which the explicit DFT data of band structure and spin splitting are not presented here. However, as can be seen from Tab. 3.2, the SOC parameters remain almost unchanged going from the 7×7 supercell to the 10×10 supercell, whereas the orbital parameters are more sensitive to the supercell size. The values of ε and ω change by about 30% and 10%, respectively.

Excluding the SOC on fluorine in the DFT 10×10 supercell reduces the band splittings by a factor of ten, see Fig. 3.10. This means that the observed large SOC values come dominantly from fluorine itself. Fluorine's strong intra-atomic SOC, related to its p_x and p_y orbitals, is transferred to graphene due to the hybridization of the adatom with graphene. The remaining contribution to the local SOC enhancement is attributed to the $\sigma - \pi$ hybridization induced by the structural

n×n	ω [eV]	ε [eV]	$\Lambda_{\mathrm{I}}^{\mathrm{B}}$ [meV]	$\Lambda_{\mathrm{PIA}}^{\mathrm{B}}$ [meV]	Λ_{R} [meV]
7×7	6.1	-3.3	3.2	7.9	11.3
10×10	5.5	-2.2	3.3	7.3	11.2

Table 3.2: TB parameters that fit best the orbital and spin-orbital effects of fluorinated graphene of 7×7 and 10×10 supercells, respectively. The parameter values are comparable for both supercell sizes, which confirms the robustness of the TB model.

deformation in the vicinity of the fluorine adsorption to graphene[9].

In summary, we see that fluorine induces a giant local SOC of up to 10 meV which is 10 times larger than in methyl functionalized (or hydrogenated [52]) graphene and a factor of 1000 larger than the value of the intrinsic SOC parameter in graphene. Fluorine's p orbitals are at the origin of this strong enhancement of the local SOC.

3.6 Copper functionalized graphene

The following section deals with another adatom on graphene: Copper. Although copper is only weakly bonding to graphene, still a notable enhancement of the local SOC is expected. On the one hand, graphene coupled to a Cu(111) substrate by weak van der Waals forces was shown to exhibit strong SOC [75] up to the meV scale. On the other hand, the spin Hall effect measurements of Ref. [54] on graphene, grown by chemical vapor deposition on a copper foil, estimate a spin orbit strength of about 20 meV. In this experiment, the strong SOC was attributed to residual Cu adatoms on graphene which are unintentionally introduced during the fabrication of the samples. It was furthermore shown by DFT calculations that copper's unpaired localized s state gives rise to a magnetic moment [101, 108, 125] in graphene. We, instead, focus in this section on the impact of single copper adatoms in the top and bridge position on the local SOC in graphene.

We will treat the top and the bridge adsorption position which are distinguished by the local induced point group symmetries C_{3v} and C_{2v}, respectively. Despite this fundamental difference in the local symmetry, we observe very similar orbital physics with p and d orbital contributions around the Fermi energy. Both p and d appear to be equally important for the local SOC. With the help of the TB analysis of DFT data [101] calculated by Tobias Frank and Martin Gmitra, we find SOC strengths ranging from 10 to 50 meV which are locally induced by copper.

[9] With the fluorinated C_{1n} atom being vertically displaced by 0.423 Å and the C_{1n}-C_{2n} bond being stretched to 1.469 Å [100], the formula of Castro Neto and Guinea, Eq. (3.2), estimates an enhanced SOC strength of about 6.6 meV ($A \approx 0.43$). However, as we saw in the case of methyl functionalized graphene, Sec. 3.4.2, this value has to be understood as an upper bound to the real SOC strength induced by σ-π coupling.

3.6.1 Structure and orbital physics

The bonding behavior of coinage metal atoms[10] on graphene is highly influenced by non-local interactions. This was elucidated by Amft *et al.* [109] in a DFT study including different approximations to the van der Waals interaction. They showed that the top and bridge adsorption configurations of copper on graphene are almost energetically equivalent and deviate only by few meV. The hollow adsorption position lies by about 200 meV higher in energy. Also Refs. [108, 125] predict the top and bridge adsorption positions as the ones of lowest energy although these authors were not including van der Waals corrections in their calculations. Van der Waals interactions were also taken into account in the DFT calculations which are analyzed in this section (see Ref. [101] for technical details). Since the top and bridge positions in graphene are, from an energetic point of view, equally favored by the copper adatom, we concentrate in the following on the orbital and spin-orbital analysis of Cu in both top and bridge position (see Fig. 3.11 for a schematic view). The supercell 10×10 is used for the TB analysis of SOC effects and represents the dilute limit.

The distance between copper and the graphene surface is about 2.1 and 2.2 Å for the top and bridge position (larger than the approximately 1.6 Å for methyl or fluorine), and local corrugations in both the top and bridge configurations appear to be very small, at about 0.08 Å and 0.11 Å, respectively [101]. Both the large graphene-copper distance and the negligible corrugation indicate that copper is only weakly bonding to graphene.

Dilute limit: the top position

Figure 3.12 shows the electronic band structure of a 10×10 supercell of graphene with copper in the top position. The result from the TB model is also included in the figure and the model itself is presented later below (page 69). Around the $\boldsymbol{K}$ point, from -1 to 0.75 eV with respect to the Fermi level, one can imagine remnants of the Dirac cone. Together with the modest binding energy of 0.68 eV [101] this is a further indication of the weak bond between copper and graphene. The hybridization of copper to graphene manifests itself in the hybridization gap opening around the $\boldsymbol{K}$ point: It appears due to the interaction between the states of graphene with the ones forming the flat band around the Fermi level, the midgap band.

The PDOS for the top configuration, shown in Fig. 3.13, was calculated in a smaller 7×7 supercell and is resolved according to different total (orbital+spin) angular momenta for the atoms Cu, C_{1n}, C_{2n}, C_{3n}, and C_{4n} (see Fig. 3.11 for the labeling of atomic sites). From the PDOS we see that the Cu s orbitals are very

[10] Coinage metal atoms are, for example, copper, gold, and silver. These are elements that have been historically used in alloys for the production of coins.

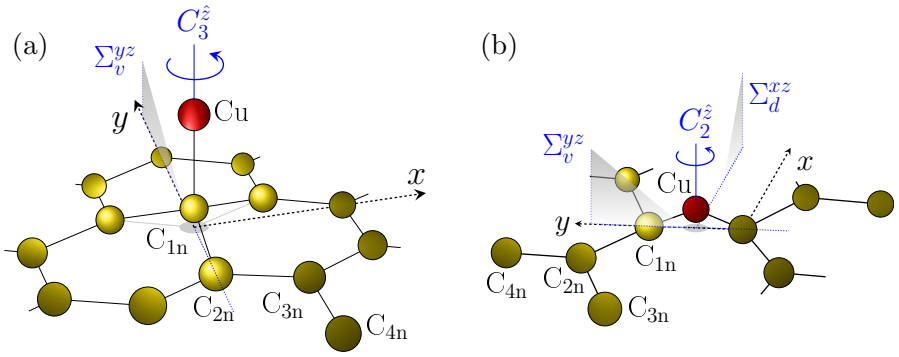

Figure 3.11: Schematic view of the copper adatom binding in the (a) top and (b) bridge position to graphene. Indicated is the labeling of the atomic sites in the vicinity of the copper adatom and the symmetry operations of the local point groups C_{3v} (top) and C_{2v} (bridge).

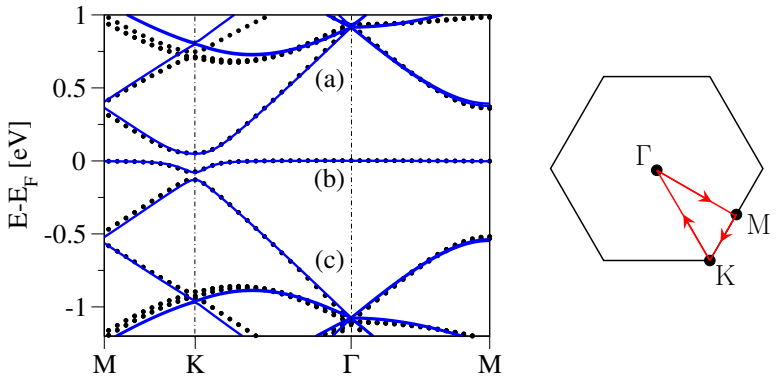

Figure 3.12: Electronic band structure of graphene functionalized with copper in the top position for a 10×10 supercell calculation from both DFT (black symbols) and TB (solid line). The TB parameters $\omega_t = 0.81\,\text{eV}$ and $\varepsilon_t = 0.08\,\text{eV}$ are obtained by fitting the (a) conduction, (b) midgap, and (c) valence band to the DFT data. The right panel displays the path chosen in the hexagonal Brillouin zone.

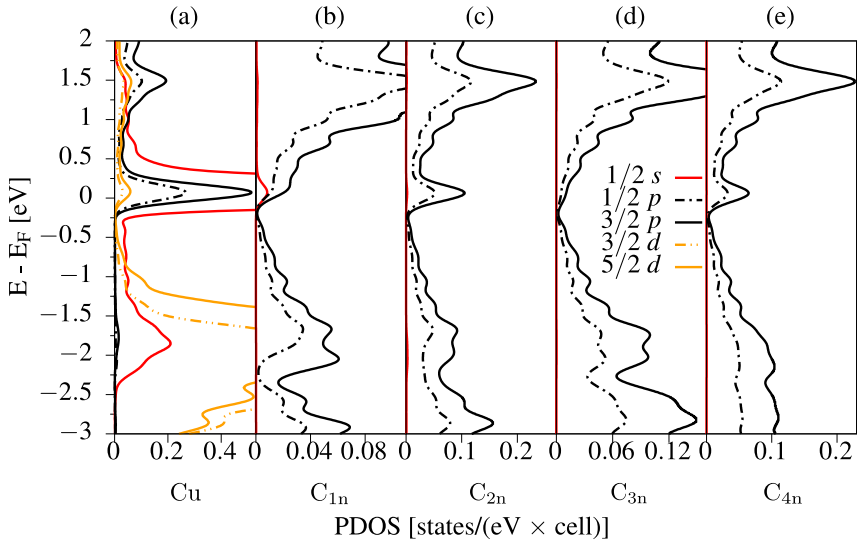

Figure 3.13: DOS of graphene functionalized with copper adatoms in the top position for a 7×7 DFT supercell calculation. The data is resolved to the total angular momenta j and the orbital quantum numbers s, p, and d, for the atomic sites (a) Cu, (b) C_{1n}, (c) C_{2n}, (d) C_{3n}, and (e) C_{4n} [see Fig. 3.11(a) for the labeling convention]. A numerical energy broadening of 130 meV was applied in the calculations. Adapted from [101].

important for the bonding. They are dominantly contributing around the Fermi level to the states of the midgap band and overlap in the same energy interval also with the s states of C_{1n}. Copper states with s character appear (with varying magnitude) throughout the energies from -2.5 to 1.5 eV. The d levels of copper, on the other hand span the range from -1 eV down to -4 eV. At -1 eV, the second valence band starts to contribute to the spectrum. The maximum contribution of d levels is found at about -2 eV. The spin-orbit interaction splits the d levels with total angular momentum $j = 3/2$ and $j = 5/2$ in energy by approximately 200 meV [101]. An experimental spectroscopic measurement of an isolated copper atom found a splitting of 253 meV [163] caused by the intra-atomic SOC. Due to the energy broadening of 130 meV in the DFT calculation the splitting of the Cu $4p$ levels by the intra-atomic SOC, 31 meV [163], is not resolved in the PDOS. Copper's $4p$ levels contribute mainly to the conduction and the midgap band at the Fermi energy. In terms of orbital angular momentum, the states around the Fermi level have mainly $m_z = 0$ character, though small contributions of states with $m_z = \pm 1$ and $m_z = \pm 2$ are also found.

The approximately linear energy dependence of the PDOS of the carbon atoms in the vicinity of the adatom reflects the almost intact linear dispersion of graphene around the Fermi level shown in Fig. 3.12. We have now seen already several indications that copper binds only weakly (and noninvasively) to graphene.

Orbital tight-binding model for the top position

Figure 3.12 already displayed the TB fit to the DFT electronic band structure. The model which forms the basis of this fit is the minimal orbital TB Hamiltonian of Eq. (2.79), which we applied successfully also for the methyl group and fluorine on graphene in the previous sections, Secs. 3.4 and 3.5. States with $m_z = 0$ character dominate for the three bands around the Fermi level. This insight gives us further motivation to use this orbital model Hamiltonian to describe the (weak) bonding of copper to graphene,

$$\begin{aligned}\mathcal{H}_{\text{orb}} = \omega_t \sum_{\sigma} \left(|O\,\sigma\rangle\langle Y\,\sigma| + |Y\,\sigma\rangle\langle O\,\sigma|\right) \\ +\varepsilon_t \sum_{\sigma} |O\,\sigma\rangle\langle O\,\sigma|\,. \end{aligned} \tag{3.7}$$

All three bands around the Fermi energy, the valence, midgap, and conduction band, are considered in the fit of the band structure along the full M-K-Γ-M line. The minimal least-square is obtained for the orbital parameters $\omega_t = 0.81\,\text{eV}$, reflecting the weak hybridization of copper to graphene, and the small on-site energy $\varepsilon_t = 0.08\,\text{eV}$. A very good agreement between TB and DFT data is obtained with this parametrization, see Fig. 3.12.

Dilute limit: the bridge position

Remarkably, copper in the top and bridge positions looks very alike on the orbital level, as we will see below. However, it is important to note that the bridge position differs from the top position by the local point group symmetry. The bridge configuration is invariant under the four symmetry operations of the point group C_{2v} (see Fig. 2.12 on page 44). This has a direct consequence on the shape of the irreducible wedge in the Brillouin zone[11]. We can identify the irreducible wedge in the bridge position as the trapezoid defined by the path Γ-M_1-K_1-K_2-Γ, which is shown in Fig. 3.14 next to the electronic band structure. Time reversal symmetry followed by the translation along a reciprocal lattice vector maps $\boldsymbol{K}_1$ to $\boldsymbol{K}_2$. It follows that the electronic spectrum is identical at these two points, although the eigenstates at these points have opposite spin-polarization. However, one fails to find a similar map between the high symmetry points $\boldsymbol{M}_1$ to $\boldsymbol{M}_2$ due to the low C_{2v} symmetry. We expect in general different spectra at the $\boldsymbol{M}_1$ and $\boldsymbol{M}_2$ points and, similarly, on the interconnecting lines of the path Γ-M_1-K_1-Γ-M_2-K_2-Γ.

The electronic band structure of copper in the bridge position, along the chosen path in the irreducible wedge of the Brillouin zone as shown in Fig. 3.14, exhibits

[11] In the top configuration, the irreducible wedge is defined by the path M-K-Γ-M (see Fig. 3.12). Applying time reversal, the local point group symmetries of C_{3v}, and translation along the reciprocal lattice vectors onto the wedge, we can cover the full hexagonal Brillouin zone.

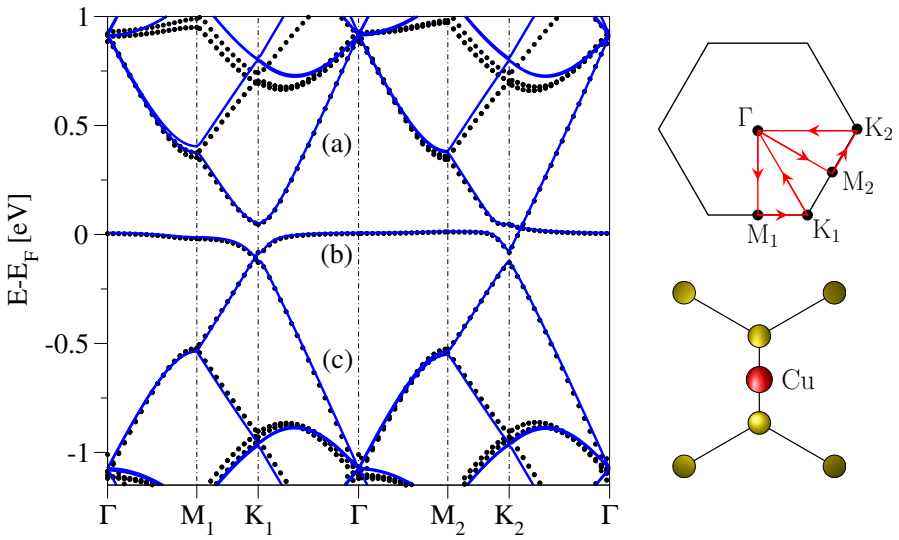

Figure 3.14: Electronic band structure of graphene functionalized with copper in the bridge position for a 10×10 supercell calculation from both DFT (black symbols) and TB (solid line). The TB parameters $\omega_t = 0.54\,\text{eV}$ and $\varepsilon_t = 0.02\,\text{eV}$ are obtained by fitting the (a) conduction, (b) midgap, and (c) valence band to the DFT data. The upper right panel displays the path chosen in the hexagonal Brillouin zone. The lower right panel presents a top view of the C_{2v} symmetric adsorption of copper in the bridge position. The orientation of the coordinate systems in both the real and the reciprocal lattice are chosen to be the same.

several similarities with copper in the top position (cf. Fig. 3.12). Around the Fermi energy, we can clearly identify three bands (a), (b), and (c), which we call the conduction, midgap, and valence band, respectively. Furthermore, traces of the Dirac cone appearing in the unperturbed graphene system can be found around $\boldsymbol{K}_1$ and $\boldsymbol{K}_2$ in the energy interval $[-1, 0.75]\,\text{eV}$. However, crossings are emerging along the paths M_1-K_1 and K_2-Γ between the valence and midgap band, and the conduction and midgap band, respectively.

Also the DOS for the bridge configuration [101] of Fig. 3.15 (7×7 supercell), projected to states with different total angular momenta on copper and neighboring carbon atoms C_{1n}, C_{2n}, C_{3n}, and C_{4n}, looks very much alike the one of the top configuration (Fig. 3.13). This appears to be natural if we consider the very similar orbital band structures in both adsorption positions. Looking closely, one sees that the PDOS for the nearest carbon neighbors to the copper adatom differs mainly in the energies from -0.5 to 0.5 eV around the Fermi level. In the top position, the copper s states hybridize with the π states on C_{2n} and C_{4n} of the opposite sublattice. Also the methyl group and fluorine in the top position exhibit this hybridization with states on the opposite sublattice (see Secs. 3.4 and 3.5). In the bridge position, on the other hand, we see peaks in the PDOS from states with p orbital character

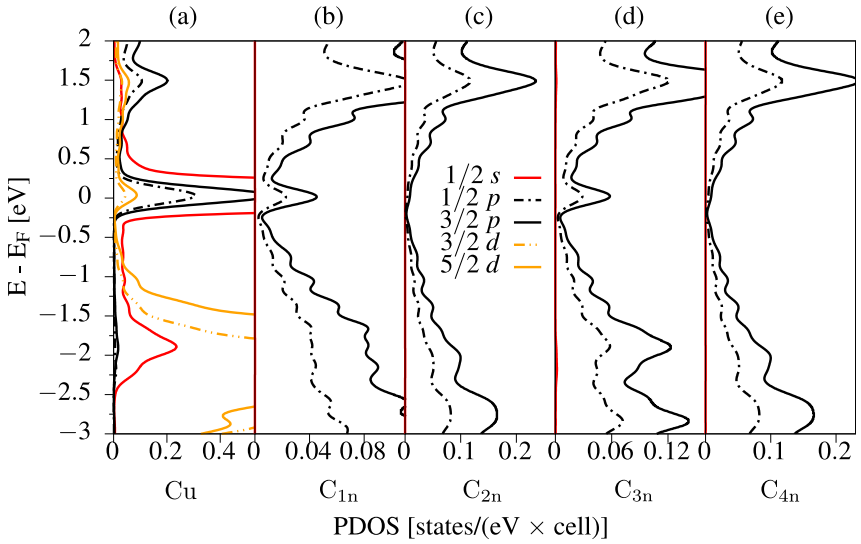

Figure 3.15: DOS of graphene functionalized with copper adatoms in the bridge position for a 7×7 DFT supercell calculation. The data is resolved to the total angular momenta j and the orbital quantum numbers s, p, and d, for the atomic sites (a) Cu, (b) C_{1n}, (c) C_{2n}, (d) C_{3n}, and (e) C_{4n} [see Fig. 3.11(b) for the labeling convention]. A numerical energy broadening of 130 meV was applied in the calculations. Adapted from [101].

on coppers carbon binding partners C_{1n} and the third nearest neighbors C_{3n}.

In total, the s, p, and d orbital states are found at the energies as in the top case. Copper's d states with $j = 3/2$ and $j = 5/2$ are split by about 0.2 eV. Furthermore, states around the Fermi level have dominantly $m_z = 0$ character (not shown in the PDOS). These results match with those of copper in the top position. We therefore expect that the local SOC has the same physical origin in both systems.

Orbital tight-binding model for the bridge position

Before changing gears and considering the SOC effects on the band structure, let us first present the orbital model Hamiltonian for the bridge position. Around the Fermi level, states with orbital angular momentum $m_z = 0$ dominate the electronic properties. Considering copper's two adsorption partners in the bridge position, we have [see Eq. (2.79)],

$$\begin{aligned} \mathcal{H}_{\text{orb}} = \omega_b \sum_{\sigma} \sum_{j=1,2} \left(|O\,\sigma\rangle\langle Y_j\,\sigma| + |Y_j\,\sigma\rangle\langle O\,\sigma| \right) \\ + \varepsilon_b \sum_{\sigma} |O\,\sigma\rangle\langle O\,\sigma| \,. \end{aligned} \tag{3.8}$$

As in the top position, we describe the binding of copper in the bridge position to graphene by two orbital parameters: the hybridization strength ω_b and the on-site

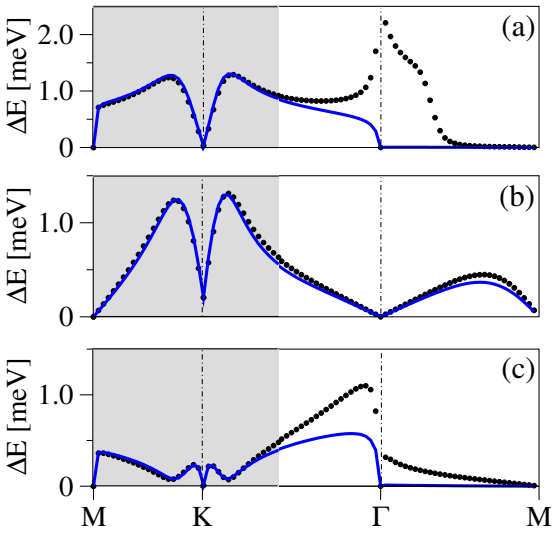

Figure 3.16: Spin splitting of the bands close to the Fermi energy of graphene functionalized with copper in the top position in the dilute limit. The splittings along the high symmetry line M-K-Γ-M are obtained for a 10×10 supercell calculation from both DFT (black dotted) and the best-fit TB model (blue solid). The labeling (a), (b), and (c) corresponds to the band labeling in Fig. 3.12. The shaded region around the $\boldsymbol{K}$ point indicates the fitting region.

energy ε_b. From the least-square fit of the valence, midgap, and conduction band along the full Γ-M_1-K_1-Γ-M_2-K_2-Γ line we obtain $\omega_b = 0.54\,\text{eV}$ and $\varepsilon_b = 0.02\,\text{eV}$. With these parameters, indicating by their small value the weak bond established between copper in the bridge position and graphene, excellent agreement between the DFT and TB calculated band structures is achieved, see Fig. 3.14.

3.6.2 Spin-orbit coupling from dilute copper coverage

In the following, we consider the effect of SOC on the band structure of copper in both the top and bridge position. First, we apply the local SOC Hamiltonians of the previous chapter, Secs. 2.5.3 and 2.5.4. Following this, we address the origin of the observed local SOC strengths.

Local spin-orbit coupling in the top position

Figure 3.16 presents the SOC induced band splittings for copper in the top position calculated from DFT [101]. To model the local SOC effects around the Fermi level, we make use of the minimal effective SOC Hamiltonian as derived in Sec. 2.5.3. We can do so as the DOS analysis revealed that the energies around the Fermi level are dominated by states with $m_z = 0$. The derivation of the model Hamiltonian in Sec. 2.5.3 relies on the assumption of effective atomic orbitals which have $m_z =$

0 character and are, therefore, invariant under all symmetries of the local point group C_{3v} (and invariant under time reversal symmetry). Similar as in the case of methyl or fluorine on graphene, we find that we can reduce the set of free SOC parameters to only three: the spin-conserving intrinsic coupling $\Lambda_{\mathrm{I}}^{\mathrm{B}}$, and the spin-flipping couplings Λ_{R} and $\Lambda_{\mathrm{PIA}}^{\mathrm{B}}$. This reduction is achieved by fitting the three bands of valence, midgap, and conduction to the DFT data for energies around the Fermi level. The quasi-momenta considered in the fitting are specified in Fig. 3.16. Defining the SOC coupling parameters according to Eq. (2.89) (Sec. 2.5.3), the model Hamiltonian for the local SOC induced by copper binding in the top position reads

$$\begin{aligned}\mathcal{H}_{\mathrm{so}}^{\mathrm{top}} = &\frac{i\Lambda_{\mathrm{I}}^{\mathrm{B}}}{3\sqrt{3}} \sum_{\sigma} \sum_{\langle\langle Z_j, Z_k \rangle\rangle} \nu_{Z_j,Z_k} \left[\hat{s}_z\right]_{\sigma\sigma} \left|Z_j\,\sigma\right\rangle\!\left\langle Z_k\,\sigma\right| \\ &+ \frac{2\Lambda_{\mathrm{PIA}}^{\mathrm{B}}}{3} \sum_{\sigma\neq\sigma'} \sum_{\langle\langle Z_j, Z_k \rangle\rangle} \left[i\hat{\boldsymbol{s}} \times \boldsymbol{d}_{Z_j,Z_k}\right]_{z,\sigma\sigma'} \left|Z_j\,\sigma\right\rangle \left\langle Z_k\,\sigma'\right| \\ &+ \frac{2i\Lambda_{\mathrm{R}}}{3} \sum_{\sigma\neq\sigma'} \sum_{\langle Y, Z_j \rangle} \left[\hat{\boldsymbol{s}} \times \boldsymbol{d}_{Y,Z_j}\right]_{z,\sigma\sigma'} \left|Y\,\sigma\right\rangle \left\langle Z_j\,\sigma'\right| + \mathrm{H.c.} \\ &+ \frac{i\lambda_{\mathrm{I}}}{3\sqrt{3}} \sum_{\sigma} {\sum_{\langle\langle m, n \rangle\rangle}}' \nu_{m,n} \left[\hat{s}_z\right]_{\sigma\sigma} \left|X_m\,\sigma\right\rangle \left\langle X_n\,\sigma\right| . \end{aligned} \tag{3.9}$$

The last term addresses the intrinsic SOC of unperturbed graphene with the fixed value $\lambda_{\mathrm{I}} = 12\,\mu\mathrm{eV}$ and couples all next-nearest neighbor sites apart of the sites $\mathrm{C}_{2\mathrm{n}}$, which are represented by the states $|Z_j\rangle$.

Fitting the band-splitting under fixed orbital parameters ω_t and ε_t, we obtain the parameter values $\Lambda_{\mathrm{I}}^{\mathrm{B}} = 9\,\mathrm{meV}$, $\Lambda_{\mathrm{R}} = 30.2\,\mathrm{meV}$, and $\Lambda_{\mathrm{PIA}}^{\mathrm{B}} = -47.4\,\mathrm{meV}$. With these parameters, the TB and DFT band-splittings align very nicely in the fitting region. While the splitting of the midgap band is also well recovered outside the fitting region, we see large deviations in the valence and conduction band when approaching the $\boldsymbol{\Gamma}$ point. At the $\boldsymbol{\Gamma}$ point, the two bands are farther away from the Fermi level and states with orbital character other than $m_z = 0$ start to contribute.

Local spin-orbit coupling in the bridge position

The form of the local SOC model Hamiltonian is very different in the bridge position, compared to the top position, as there the local point group is C_{2v}. One of the consequences is the enhanced number of free local SOC parameters, as was shown in Sec. 2.5.4. Here, comparing the model to the spin splitting of the electronic bands, found in the DFT calculations, helps a lot in reducing the number of fit parameters. We find that the local SOC is well described with three SOC parameters. The model SOC Hamiltonian, which is invariant under the local C_{2v}

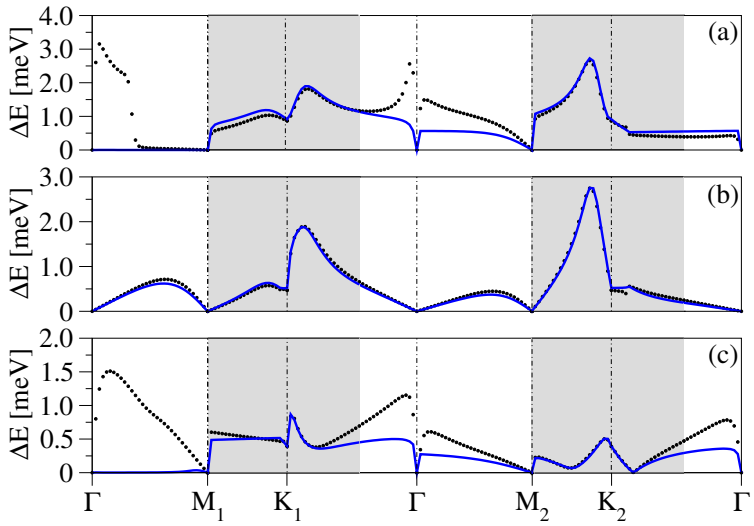

Figure 3.17: Spin splitting of the bands close to the Fermi energy of graphene functionalized with copper in the bridge position in the dilute limit. The splittings along the high symmetry line Γ-M_1-K_1-Γ-M_2-K_2-Γ are obtained for a 10×10 supercell calculation from both DFT (black dotted) and the best-fit TB model (blue solid). The labeling (a), (b), and (c) corresponds to the band labeling in Fig. 3.14. The shaded regions around the $\boldsymbol{K}_1$ and $\boldsymbol{K}_2$ points indicate the fitting regions.

symmetry and well reflects the influence of copper in the bridge position, reduces then from Eq. (2.99) to

$$\begin{aligned}\mathcal{H}_{\mathrm{so}}^{\mathrm{brid}} = {} & \mathrm{Re}\big(\Lambda_{\mathrm{f}}^{\mathrm{YZ}}\big) \sum_{\sigma\neq\sigma'} \sum_{\langle Y_j, Z_k\rangle} \nu_{O,Z_k} \big[i\hat{s}_y\big]_{\sigma\sigma'} \,\mathrm{sgn}\big[\boldsymbol{d}_{O,Y_j}.\boldsymbol{d}_{Y_1,Y_2}\big] \big|Y_j\,\sigma\big\rangle \big\langle Z_k\,\sigma'\big| + \mathrm{H.c.} \\ & + i\Lambda_{\mathrm{f}}^{\mathrm{YY}} \sum_{\sigma\neq\sigma'} \big[\hat{\boldsymbol{s}} \times \boldsymbol{d}_{Y_1,Y_2}\big]_{z,\sigma\sigma'} \big|Y_1\,\sigma\big\rangle \big\langle Y_2\,\sigma'\big| + \mathrm{H.c.} \\ & + \sum_{\sigma\neq\sigma'} \sum_{\langle\langle O,Z_j\rangle\rangle} \Big\{\nu_{O,Z_j} \big[i\hat{s}_y\big]_{\sigma\sigma'} \mathrm{Re}\big(\Lambda_{\mathrm{f}}^{\mathrm{OZ}}\big) + i\,\mathrm{Im}\big(\Lambda_{\mathrm{f}}^{\mathrm{OZ}}\big)\Big\} \\ & \qquad \times \mathrm{sgn}\big[\boldsymbol{d}_{O,Z_j}.\boldsymbol{d}_{Y_1,Y_2}\big] \big|O\,\sigma\big\rangle \big\langle Z_j\,\sigma'\big| + \mathrm{H.c.} \\ & + \frac{i\lambda_{\mathrm{I}}}{3\sqrt{3}} \sum_{\sigma} \sum_{\langle\langle m,n\rangle\rangle} \nu_{m,n} \big[\hat{s}_z\big]_{\sigma\sigma} \big|X_m\,\sigma\big\rangle \big\langle X_n\,\sigma\big|\,. \end{aligned} \tag{3.10}$$

The last term represents the spin-conserving intrinsic SOC $\lambda_{\mathrm{I}} = 12\,\mu\mathrm{eV}$ of unperturbed graphene, which couples all next-nearest carbon neighbors. To extract the values of the SOC parameters, we consider the low energy region around the $\boldsymbol{K}_1$ and $\boldsymbol{K}_2$ points. Figure 3.17 displays both the model and DFT calculated spin splitting of the valence, midgap, and conduction bands. The quasi-momenta, which are included in the fitting, are indicated in the figure. The very good agreement

between model and DFT in the fitted region is obtained with the local SOC parameters $\Lambda_{\mathrm{f}}^{\mathrm{YZ}} = (-7.5 + i\,0)\,\mathrm{meV}$, $\Lambda_{\mathrm{f}}^{\mathrm{YY}} = 41\,\mathrm{meV}$, and $\Lambda_{\mathrm{f}}^{\mathrm{OZ}} = (1.4 + i\,8.4)\,\mathrm{meV}$. As we already saw for copper in the top position, the splitting of the midgap band is well recovered along the full Γ-M_1-K_1-Γ-M_2-K_2-Γ path. Significant deviations, on the other hand, appear in the valence and conduction band around the $\boldsymbol{\Gamma}$ point. The same reason as in the top position causes our model to fail there: The two bands are farther away from the Fermi level and states with orbital character other than $m_z = 0$ start to contribute.

Microscopic origin of the local SOC

For copper in the bridge position, the local SOC terms are described by spin-flipping hoppings only. The SOC strengths lie in the range from 1 to 40 meV, with the highest value occuring for the hopping underneath the copper adatom. In the top position, both spin-flipping and spin-conserving hoppings are necessary to explain the effect of the local SOC on the band structure. The SOC parameters reach values from 10 to 50 meV. What is the origin of this strong local enhancement of SOC?

The local sp^3 distortion can be ruled out as the enhancing factor due to two reasons. First, we saw that copper is only weakly bonding to graphene and leads to very small local distortion of the graphene lattice. The observed corrugation of about 0.1 Å for both positions is negligible for the local SOC. In particular, based on Castro Neto's and Guinea's prediction, Eq. (3.2), we would expect a maximum value for the SOC of 0.7 meV for the corrugation observed in the top position[12]. Second, comparing the local SOC strengths of copper in both adsorption positions to the ones of, for example, the methyl group[13] on graphene, we have to conclude that the enhancement appears by a large portion due to the intra-atomic spin-orbit interaction of the copper adatom itself. The contributions of the p and d orbitals on copper seem to play a major role. Indeed, to entangle the influence of copper's intra-atomic SOC from the one of local sp^3 distortion, the SOC was turned off on copper for the top position in the DFT calculations of Ref. [101]. The band splittings, see Fig. 3.18, then drop down to values of the order of 10 μeV. The orbital contributions in the PDOS for both the top and bridge position are quite similar so that we can expect a similar result for the bridge position. In the case of fluorine on graphene, SOC strengths up to 10 meV were caused by fluorine's p_x and p_y orbitals. We found above in the PDOS analysis that copper contributes with both p and d orbital states close to the Fermi energy, which can therefore influence

[12] Ref. [101] reports that apart the vertical displacement of C_{1n} by 0.08 Å in the top position, the lattice constant, and thus the C_{2n}-C_{2n} bond length, remains almost unchanged ($a_{\mathrm{L}} = 2.46$ Å). From this, we estimate the C_{1n}-C_{2n} distance to be about 1.51 Å and $A \approx 0.046$ in Eq. (3.2).

[13] We saw in Sec. 3.4 for the methyl group on graphene that the local sp^3 distortion is the main mechanism behind the local SOC strengths of the order of 0.1 to 1 meV.

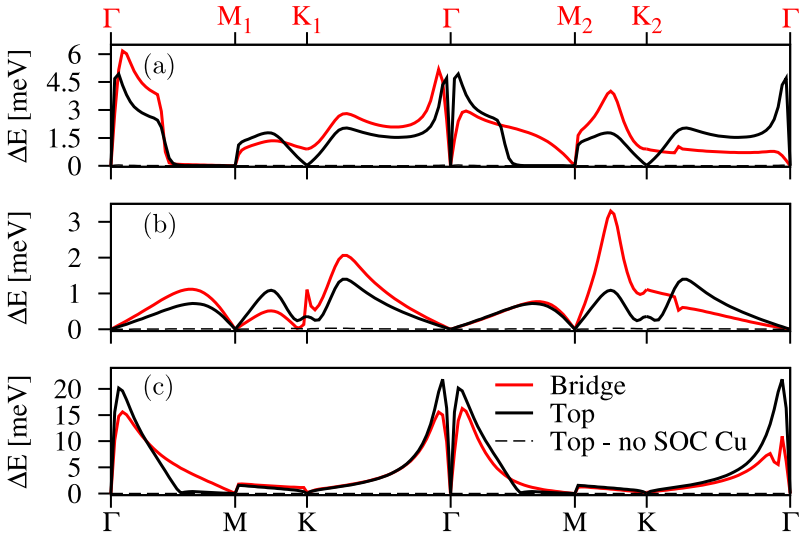

Figure 3.18: Spin splitting of the bands close to the Fermi energy of graphene functionalized with copper in the top and bridge positions for a 7×7 supercell DFT calculation. The band labeling (a), (b), and (c), as well as the labeling of the high symmetry points corresponds to those shown in Figs. 3.12 and 3.14. Turning off SOC on the copper adatom in the top position, results in a splitting shown by the black dashed line. Adapted from [101].

the local SOC.

If the d levels affect the local SOC for energies close to the Fermi level, then there would be an effect on the spin splitting of the valence, midgap, and conduction band by shifting the d levels away from the Fermi level. In the DFT calculations of Ref. [101], this is acchieved by adding a Hubbard U term to the exchange functional [164]. Practically speaking, the inclusion of a nonzero Hubbard U shifts the fully occupied copper d levels to lower energies. As shown in Ref. [101], the spin splittings decrease in all three bands of interest with increasing the U parameter. The band which is most affected by the d levels is the valence band as it lies closest in energy to the d states. Further analysis of the spin splittings [101] reveal that coppers p and d orbitals contribute by about the same magnitude to the spin splitting of the midgap band. The spin-orbit splitting of the d levels of isolated copper is with about 253 meV one order of magnitude larger than the one of the p levels with about 31 meV [163]. This factor of ten relating the intra-atomic SOC strenghts of the d and p orbitals of copper competes with the factor of 0.1 which relates the orbital contribution of the d and p states to energies around the Fermi level as found in Ref. [101]. This competition results in the approximately equal importance of the p and d levels to the SOC effects of copper on graphene.

In summary, we found that copper in both the top and bridge positions on graphene induces local strong SOC of the order of tens of meV. The adsorption of copper on graphene, therefore, locally enhances the SOC of graphene by up to a

	Orbital [eV]		SOC [meV]						
Adsorbate	ω	ε	$\Lambda_{\mathrm{I}}^{\mathrm{A}}$	$\Lambda_{\mathrm{I}}^{\mathrm{B}}$	$\Lambda_{\mathrm{PIA}}^{\mathrm{B}}$	Λ_{R}	$\Lambda_{\mathrm{f}}^{\mathrm{YZ}}$	$\Lambda_{\mathrm{f}}^{\mathrm{YY}}$	$\Lambda_{\mathrm{f}}^{\mathrm{OZ}}$
CH_3 (top)	7.6	-0.19	-0.77	0.15	-0.69	1.02	–	–	–
F (top)	5.5	-2.2	–	3.3	7.3	11.2	–	–	–
Cu (top)	0.81	0.08	–	9.0	-47.4	30.2	–	–	–
Cu (bridge)	0.54	0.02	–	–	–	–	-7.5	41	$1.4 + i\,8.4$

Table 3.3: Summary of the orbital TB parameters as well as the local SOC strengths induced by binding of the methyl group CH_3, fluorine F, and copper Cu on graphene. The parameters are extracted from fitting the orbital adatom Hamiltonian and the local, symmetry-motivated SOC models of Secs. 2.5.3 and 2.5.4 to DFT data. See Secs. 3.4, 3.5, and 3.6 for details.

factor of 1000. While the sp^3 distortion gives only a negligible contribution, we realized that coppers p and d orbitals are dominantly causing the giant local SOC enhancement. Furthermore, these orbitals appear to be equally important.

3.7 Concluding remarks

In this chapter, we have successfully applied the local, symmetry-motivated, SOC Hamiltonians of the first chapter to adsorbates in the top and bridge positions on graphene. We focused on three candidates: the methyl group CH_3 in the top position, the fluorine adatom F in the top position, and the copper adatom Cu, which appears to bind equally likely in the top and the bridge position. An important insight into the electronic structure of graphene functionalized with the considered adsorbates is given by the DFT calculations. Understanding the basic physical mechanisms on the scale of the atomic orbitals, the free TB parameters of the model Hamiltonians were found by fitting the DFT calculated band structure and, for the SOC strengths, the spin-orbit induced splitting of the bands. We concentrated our analysis on the energy bands close to the Fermi level, which we call the valence, midgap, and conduction band. Table 3.3 summarizes all obtained parameters for the different adsorbate cases.

We found that the local SOC in graphene in the vicinity of CH_3 is by a factor of 100 larger than the intrinsic SOC in pristine graphene and reaches values from 0.1 to 1 meV. The local sp^3 distortion [51] is at the basis of this observation, similar to the case of hydrogenated graphene [52]. For fluorine and copper, on the other hand, the intra-atomic SOC of the adatoms are more important. The p levels of fluorine dominate in the local SOC enhancement, giving local SOC strengths of 1 to 10 meV. In the case of copper, for the two adsorption positions top and bridge, copper's p and d orbitals bring about a large local SOC with values ranging from

about 10 to 50 meV. The effect of the small local sp^3 distortion, observed for copper, is negligible.

Locally enhanced SOC in graphene functionalized with adsorbates can have a strong impact on the spin relaxation. In this scenario, the spin relaxation rates are mainly affected from short-range scattering events off the impurities [62, 115, 165–170]. Also magnetic moments, which we have not treated in detail in this chapter, can significantly influence the spin relaxation. Virtual bound states may arise due to the adsorbate on graphene at low energies. Those states are formed by the itinerant electrons of graphene scattering resonantly off the impurity. During the resonant scattering process the electron spends a finite time in the vicinity of the adatom and can feel the spin-flip field of the local SOC or local magnetic moments. The spin-orientation of the electrons is therefore altered by the local environment and the spin relaxation rate increases. In the following chapter, we focus on the orbital aspects of resonant scattering before we present a model for spin relaxation by resonant scattering off magnetic moments in Ch. 5. In detail, we will study on the following pages adatoms with s and p_z orbital character which are adsorbed on graphene in the three positions top, bridge, and hollow. We determine the resonance characteristics of the adatoms on the DOS and the momentum relaxation rates. Furthermore, we will compare the orbital effect of a general adatom to the ones caused by vacancies.

4 Adatoms and resonant scatterers in graphene

This chapter is based on the paper "Resonant scattering due to adatoms in graphene: Top, bridge, and hollow positions", PRB 97, 075417 (2018), by Susanne Irmer, Denis Kochan, Jeongsu Lee, and Jaroslav Fabian.

4.1 Resonant scattering in graphene

An impurity in a metal can give rise to two scenarios [171, 172]. On the one hand, if the impurity potential is strongly attractive, it induces a bound state just beneath the continuum of the conduction band states. Increasing the spatial distance to the impurity, the amplitude of the bound state's wave function is exponentially decaying so that the state is strongly localized around the impurity site. On the other hand, if the impurity is of a weaker nature, the conduction electrons will spent only some finite time in its vicinity. A scattering resonance [172] is induced by the impurity which is also called a virtual bound state[1]. At large distances from the impurity site, the states have Bloch state character. The virtual bound state lies in the continuum of the conduction band states and induces, therefore, a narrow peak in the metal's DOS.

Virtual bound states represented by peaks in the DOS can also occur in graphene and are induced by short-range impurities. The wave function amplitude of those states generally decay according to a power law [173–175] and are therefore not normalizable. Strictly speaking, those states are only quasi-localized as one cannot define a localization length like for exponentially localized states [174]. We kindly ask the reader to keep this distinction in mind, but will employ the term "localized" in the rest of this chapter and use the term "resonant state" instead of virtual bound state.

In its pristine form, graphene is a semimetal and thus exhibits no band gap separating the valence and conduction band. The DOS vanishes at the charge neutrality point of pristine graphene and grows linearly for higher, but low, energies. Due to the finite but small DOS, graphene is especially sensitive to resonant states

[1] The state is not a well-defined eigenstate and therefore no true bound state.

forming in the low energy region. We refer to the energy at which the resonant state appears in the DOS as the "resonance energy". The resonance lifetime, τ, can be estimated from the width Γ (full width of half maximum) of the resonance peak appearing in the DOS, by using the relation $\tau = \hbar/\Gamma$.

The change in graphene's DOS due to the resonant state translates also to the relaxation rates measured in transport experiments [97, 176–178]. For example, Robinson *et al.* [97] predicted by a study based on the T-matrix formalism that the adsorbates H^+ and OH^{-1} (both binding to the top position) induce an asymmetry in the conductivity. However, this property crucially depends on the kind of adsorbate or short-range scatterer and needs to be distinguished [178, 179] in experiments from long-range Coulomb scattering events [59, 60, 119, 180] due to charged impurities in the sample. The short-range scattering, in contrast to charge scattering processes, plays an important role in spin relaxation experiments [62, 115, 165–169]. Local spin-orbit coupling or local magnetic moments might be induced by an impurity serving as a resonant scatterer to graphene. The local property can then efficiently affect the spin of the electrons moving through the sample in the finite time they are localized in the vicinity of the impurity during the resonant scattering event.

Different sources for resonant states in graphene have been explored throughout the past years comprising studies on the zero-energy modes arising from vacancies [173, 174, 181] and more general resonant states due to substitutional impurities [174, 182–184] and adsorbates. Regarding the latter, two main approaches were followed. Either specific adatoms were investigated [52, 98, 99, 101, 110, 139, 185, 186], often with the input of DFT calculations, or a symmetry analysis based on the difference in the adsorption positions was used [6, 55, 187, 188]. This led, for example, to the indications that an s-like orbital in the hollow position is effectively decoupled from the graphene states [55, 187].

In this chapter, we want to contribute to the already large amount of works on resonant scattering in graphene by offering a comprehensive view on single (or a dilute amount of) adsorbates binding in the different adsorption positions of top, bridge, and hollow to graphene. We restrict ourselves to adsorbates with s or p_z orbital character[2] to catch basic differences and similarities between different configurations. We will see intersections with the results of earlier theoretical works, though, by scanning a large portion of the orbital parameter space, which characterizes the impurity, we also extend and connect them.

The first part of the chapter, Sec. 4.2, addresses the employed adatom models and how one obtains through the non-perturbative T-matrix formalism the resonance characteristics in the DOS and momentum relaxation rates. In Sec. 4.3, we address and characterize adsorbates in the top, bridge, and hollow positions. For example, we will meet similarities between our results for an adsorbate in the bridge position

[2]The approach, presented in this chapter, can be straightforwardly extended to other atomic orbitals. However, this is not in the scope of the present work.

and findings of Wehling *et al.* [183] on double substitutional impurities, which they also obtained within the T-matrix formalism. We also observe the decoupling of C_{6v} symmetric atomic orbitals in the hollow position from graphene (see, e.g., Ref. [187]) regardless of the adatom's orbital parameters. After investigating the localization of the resonant states around specific impurities in Sec. 4.4, we draw in Sec. 4.5 a comparison between adsorbates, the special cases of vacancies, and the so-called strong midgap scatterers (SMS) [2, 176, 177, 189]. The SMS model is especially interesting as it provides an analytic formula for the conductivity, which is derived from partial wave analysis. This formula allows to extract the impurity concentration from experimental data in a convenient way and seems to be often used (see, for example, Refs. [134, 190, 191]). By a direct comparison of the model to the T-matrix treatment of general adatoms and vacancies, we point to the limitations of the model and the consequences for quantitative data analysis based on the conductivity model.

4.2 Methods

In this chapter, we are interested in the resonance levels induced by single monovalent adatoms on graphene, i.e., we focus on the single adatom limit. A convenient tool for these investigations is the Green's function methodology together with the fully non-perturbative T-matrix approach.

4.2.1 T-matrix formalism

Let $\mathcal{H}_0$ represent the Hamiltonian of graphene being subject to a perturbation $\mathcal{V}$. The total system is then described by $\mathcal{H} = \mathcal{H}_0 + \mathcal{V}$. The retarded Green's operator of this system satisfies

$$\left[E^+ - \mathcal{H}\right] \mathcal{G}(E^+) = \mathbb{1}\,, \tag{4.1}$$

where $E^+ = E + i\delta$ is the energy including an infinitesimal imaginary part $\delta \to 0$. Without the infinitesimal δ, the operator $[E - \mathcal{H}]$ will be singular for specific energies and, therefore, is then not invertible. Including the imaginary part and multiplying with the inverse of the operator in Eq. (4.1) results in the Dyson equation for the full retarded Green's operator,

$$\mathcal{G}(E^+) = \mathcal{G}_0(E^+) + \mathcal{G}_0(E^+)\mathcal{V}\mathcal{G}(E^+)\,, \tag{4.2}$$

where we defined the Green's operator of the unperturbed system as $\mathcal{G}_0(E^+) = [E^+ - \mathcal{H}_0]^{-1}$. Equation (4.2) can be solved iteratively and one obtains

$$\mathcal{G}(E^+) = \mathcal{G}_0(E^+) + \mathcal{G}_0(E^+)\mathcal{T}\mathcal{G}_0(E^+)\,, \tag{4.3}$$

where

$$\begin{aligned}\mathcal{T} &= \mathcal{V} + \mathcal{V}\mathcal{G}_0\mathcal{V} + \mathcal{V}\mathcal{G}_0\mathcal{V}\mathcal{G}_0\mathcal{V} + ... \\ &= \mathcal{V}\left[\mathbb{1} - \mathcal{G}_0(E^+)\mathcal{V}\right]^{-1}\end{aligned} \tag{4.4}$$

denotes the T-matrix. We would like to calculate the T-matrix in the local atomic basis, i.e., we are interested in the matrix elements $\langle X_l|\mathcal{T}|X_m\rangle$ where $|X_l\rangle$, $|X_m\rangle$ are p_z orbital states on the graphene lattice sites. In order to evaluate these matrix elements, we need to know, on the one hand, the perturbation $\mathcal{V}$ and, on the other hand, the propagators (or Green's functions) $\langle X_l|\mathcal{G}_0|X_m\rangle$.

Perturbation $\mathcal{V}$ for different adsorption positions

We obtain the perturbation term $\mathcal{V}$ by integrating out the adatom degree of freedom from the "graphene+adatom" system using the Löwdin transformation [112]. Starting point is the Hamiltonian describing graphene with a single adatom in the top, bridge, or hollow position [see Eq. (2.79) in Sec. 2.5],

$$H = \varepsilon\,|O\rangle\,\langle O| + \omega \sum_{\langle O,l\rangle} \left(|O\rangle\,\langle Y_l| + \text{H.c.}\right) + \mathcal{H}_0\,, \tag{4.5}$$

which includes the Hamiltonian of unperturbed graphene in the nearest neighbor approximation,

$$\mathcal{H}_0 = -t \sum_{\langle l,m\rangle} |X_l\rangle\,\langle X_m|\ . \tag{4.6}$$

Since we are only interested in the orbital degrees of freedom, we omit the summation over spin indices in the above and all following formulas. The first part in Eq. (4.5) describes the effective adatom orbital $|O\rangle$ characterized by an on-site energy ε and its hybridization to the nearest carbon partners $|Y_l\rangle$ in the graphene lattice. The maximal number of these hybridization partners depends on the adsorption position of the adatom and reduces to one for the top position, to two for the bridge, and to six for the hollow position. As previously in Sec. 2.5, we assume that the effective orbital on the adatom is invariant under the local point group symmetry corresponding to the adsorption position[3]. This condition is met, for all adsorption configurations, by an adatom orbital having s or p_z orbital character.

In the Löwdin down-folding procedure [112] one partitions the basis of the unperturbed eigenstates of the full system, i.e., graphene with the adatom, into two classes A and B. For our purposes, class A will describe the adatom degree of freedom and class B the graphene system. Löwdin derives in his work a perturbative formula, which describes the influence of one class of states onto the other. If we

[3] We saw in Sec. 2.5 that an adatom in the hollow position leads to local C_{6v}, an adatom in the top position to local C_{3v}, and an adatom in the bridge position to local C_{2v} symmetry.

are interested only in the B sector of states of the Hamiltonian H, we can eliminate the sector A by using[4]

$$\mathcal{H} = H_{BB} + H_{BA}(E - H_{AA})^{-1}H_{AB} \equiv \mathcal{H}_0 + \mathcal{V}(E)\,, \tag{4.7}$$

since $H_{BB} \equiv \mathcal{H}_0$ in our above notation. Thus, we obtain an effective Hamiltonian for a graphene-only system which includes an energy dependent perturbation $\mathcal{V}(E) = H_{BA}(E - H_{AA})^{-1}H_{AB}$ originating in the adatom binding to graphene. The Hamiltonian for the adatom is simply given by $H_{AA} = |O\rangle\,\varepsilon\,\langle O|$ and the hybridization of the adatom to graphene is included in $H_{AB} = \sum_l |O\rangle\,\omega\,\langle Y_l| = H_{BA}^\dagger$. We find that the energy-dependent perturbation acts on the nearest carbon neighbor(s) of the adatom,

$$\mathcal{V}(E) = \frac{|\omega|^2}{E - \varepsilon}\,\mathcal{P}\,. \tag{4.8}$$

The operator $\mathcal{P}$ projects to the space of states formed by the p_z orbitals of the hybridization partners of the adatom,

$$\mathcal{P} = \left(\sum_{\langle O,l\rangle} |Y_l\rangle\right)\left(\sum_{\langle O,m\rangle} \langle Y_m|\right)\,, \tag{4.9}$$

so that in the effective graphene-only Hamiltonian the carbon hybridization partners gain energy-dependent on-site potentials and are coupled among themselves by the same strength $|\omega|^2/(E - \varepsilon)$.

Green's functions for graphene

Having uncovered the form of the perturbation $\mathcal{V}$ needed for the T-matrix, we will now turn our attention to the Green's functions. We are interested in local impurities and aim at the real space representation of the retarded Green's functions for graphene. Nevertheless, we start from the momentum representation of the Hamiltonian of pristine graphene,

$$\mathcal{H}_0(\boldsymbol{q}) = -t\left(\tilde{f}_{\mathrm{orb}}(\boldsymbol{q})\;|A_{\boldsymbol{q}}\rangle\,\langle B_{\boldsymbol{q}}| + \mathrm{H.c.}\right)\,, \tag{4.10}$$

which can be represented by a 2×2 matrix in the Bloch basis $\{|A_{\boldsymbol{q}}\rangle\,, |B_{\boldsymbol{q}}\rangle\}$. In order to obtain Eq. (4.10) from the nearest neighbor TB Hamiltonian of graphene

[4]The interested reader is encouraged to have a look at the appendix in Löwdin's paper [112], where he gives a symbolic derivation of the basic formulas. This derivation shows the connection between Eq. (4.7) and the formulas including geometrical series in the main text of Löwdin's paper.

in real space [Eq. (2.4) on page 9] we employed a slightly different convention for the Bloch transform compared to Eq. (2.5):

$$|X_{\boldsymbol{q}}^{\alpha}\rangle = \frac{1}{\sqrt{N}} \sum_{\boldsymbol{R}_m} e^{i\boldsymbol{q}.(\boldsymbol{R}_m+\boldsymbol{\tau}_\alpha)} \, |X_m^{\alpha}\rangle \; . \tag{4.11}$$

Here, the index α indicates whether the p_z orbital state resides on the A or B sublattice where $|X_{\boldsymbol{q}}^{A}\rangle \equiv |A_{\boldsymbol{q}}\rangle$ and $|X_{\boldsymbol{q}}^{B}\rangle \equiv |B_{\boldsymbol{q}}\rangle$. Accordingly, $\boldsymbol{R}_m + \boldsymbol{\tau}_\alpha$ specifies the absolute position of the carbon atom in the graphene lattice. While the lattice vectors $\boldsymbol{R}_m$ address the m-th unit cell in which the carbon site is located, the vector $\boldsymbol{\tau}_\alpha$ takes into account the relative shift in the absolute position between the sublattice sites A and B in the same unit cell. Figure 4.1(a) displays the choice of the unit cell and the vectors $\boldsymbol{\delta}_m$ connecting nearest carbon neighbors. Explicitly, we have $\boldsymbol{\delta}_m = [\cos(m\frac{2\pi}{3} + \frac{\pi}{2}), \sin(m\frac{2\pi}{3} + \frac{\pi}{2})]a_{cc}$ with $m = 1, 2, 3$ and $a_{cc} = a_L/\sqrt{3}$ being the carbon-carbon distance. In this convention, the shifting vectors are $\boldsymbol{\tau}_A = 0$ and $\boldsymbol{\tau}_B = -\boldsymbol{\delta}_3$. We obtain the orbital structural function $\tilde{f}_{\rm orb}(\boldsymbol{q})$ entering Eq. (4.10) as

$$\tilde{f}_{\rm orb}(\boldsymbol{q}) = \exp(i\boldsymbol{q}.\boldsymbol{\delta}_1) + \exp(i\boldsymbol{q}.\boldsymbol{\delta}_2) + \exp(i\boldsymbol{q}.\boldsymbol{\delta}_3) \, . \tag{4.12}$$

The eigenenergies of pristine graphene, describing the conduction ($n = +1$) and valence band ($n = -1$), are accordingly given by

$$\epsilon_n(\boldsymbol{q}) = n\, t|\tilde{f}_{\rm orb}(\boldsymbol{q})| \, . \tag{4.13}$$

Using Eq. (4.10) and inverting $[E^+ - \mathcal{H}_0(\boldsymbol{q})]$, we find for the Green's operator of graphene

$$\begin{aligned} \mathcal{G}_0(E^+) &= \sum_{\alpha,\beta,\boldsymbol{q}} |X_{\boldsymbol{q}}^{\alpha}\rangle \, \langle X_{\boldsymbol{q}}^{\alpha}| \, [E^+ - \mathcal{H}_0(\boldsymbol{q})]^{-1} \, |X_{\boldsymbol{q}}^{\beta}\rangle \, \langle X_{\boldsymbol{q}}^{\beta}| \\ &= \sum_{\alpha,\beta,\boldsymbol{q}} |X_{\boldsymbol{q}}^{\alpha}\rangle \left[\frac{E^+\delta_{\alpha,\beta} - t\tilde{f}_{\rm orb}(\boldsymbol{q})\, \delta_{\alpha,A}\delta_{\beta,B} - t\overline{\tilde{f}_{\rm orb}(\boldsymbol{q})}\, \delta_{\alpha,B}\delta_{\beta,A}}{{E^+}^2 - t^2|\tilde{f}_{\rm orb}(\boldsymbol{q})|^2} \right] \langle X_{\boldsymbol{q}}^{\beta}| \; . \end{aligned} \tag{4.14}$$

From the matrix elements $\lim_{\delta\to 0} \langle X_l^{\alpha}| \, \mathcal{G}_0(E^+) \, |X_m^{\beta}\rangle$, after taking the continuum limit, we can identify three different kinds of Green's functions for graphene in real space, see Fig. 4.1(b). The first one is the on-site Green's function which we obtain from setting $l = m$ and $\alpha = \beta$,

$$G_{00}(E) = \lim_{\delta\to 0} G_{00}(E^+) = \lim_{\delta\to 0} \frac{V}{N} \int\limits_{\text{1st BZ}} \frac{\mathrm{d}q^2}{(2\pi)^2} \frac{E^+}{{E^+}^2 - t^2|\tilde{f}_{\rm orb}(\boldsymbol{q})|^2} \, . \tag{4.15}$$

The second type of Green's function couples two different sites on the same sublattice, i.e., $\alpha = \beta$ and $l \neq m$,

$$G_{lm}^{\rm NN}(E) = \lim_{\delta\to 0} G_{lm}^{\rm NN}(E^+) = \lim_{\delta\to 0} \frac{V}{N} \int\limits_{\text{1st BZ}} \frac{\mathrm{d}q^2}{(2\pi)^2} \frac{E^+ \mathrm{e}^{i\boldsymbol{q}.(\boldsymbol{R}_l - \boldsymbol{R}_m)}}{{E^+}^2 - t^2|\tilde{f}_{\rm orb}(\boldsymbol{q})|^2} \, . \tag{4.16}$$

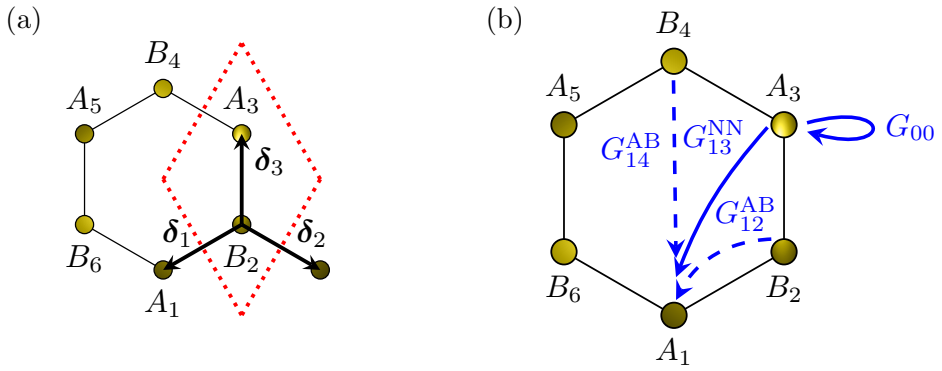

Figure 4.1: (a) Graphene unit cell (red dashed line) and the site labeling convention on a hexagon ring as used for the real space representation of the Green's functions. Bold arrows show the orientation of the nearest neighbor connection vectors $\boldsymbol{\delta}_j$, $j = 1, 2, 3$. (b) Schematic view of the relevant Green's functions coupling sites on a hexagon ring: G_{00} giving the on-site contribution, G_{12}^{AB} and G_{14}^{AB} coupling sites on the opposite sublattice, and G_{13}^{NN} coupling sites on the same sublattice.

Finally, the third kind of Green's function couples two different sites on the opposite sublattice, i.e., $\alpha \neq \beta$ and $l \neq m$,

$$G_{lm}^{\mathrm{AB}}(E) = \lim_{\delta\to 0} G_{lm}^{\mathrm{AB}}(E^+) = \lim_{\delta\to 0} \frac{V}{N} \int\limits_{1\mathrm{st\ BZ}} \frac{\mathrm{d}q^2}{(2\pi)^2} \frac{(-t)\tilde{f}_{\mathrm{orb}}(\boldsymbol{q})\, \mathrm{e}^{i\boldsymbol{q}\cdot(\boldsymbol{R}_l - \boldsymbol{R}_m - \boldsymbol{\tau}_B)}}{E^{+2} - t^2 |\tilde{f}_{\mathrm{orb}}(\boldsymbol{q})|^2}\,, \quad (4.17)$$

and

$$G_{lm}^{\mathrm{BA}}(E) = \lim_{\delta\to 0} G_{lm}^{\mathrm{BA}}(E^+) = \lim_{\delta\to 0} \frac{V}{N} \int\limits_{1\mathrm{st\ BZ}} \frac{\mathrm{d}q^2}{(2\pi)^2} \frac{(-t)\overline{\tilde{f}_{\mathrm{orb}}(\boldsymbol{q})}\, \mathrm{e}^{i\boldsymbol{q}\cdot(\boldsymbol{R}_l - \boldsymbol{R}_m + \boldsymbol{\tau}_B)}}{E^{+2} - t^2 |\tilde{f}_{\mathrm{orb}}(\boldsymbol{q})|^2}\,. \quad (4.18)$$

In the above formulas, the integration runs over the first Brillouin zone and the area of one unit cell of graphene is represented by $V/N = A_{\mathrm{uc}}$.

An analytic expression for the on-site Green's function G_{00} for small energies can be obtained by linearizing the spectrum around the $\pm\boldsymbol{K}$ points in the first Brillouin zone [185, 192, 193]. In this approach, the integral in Eq. (4.15) is transformed to two integrals around the two Brillouin zone corners. The integral spreads over all states lying in a circle of radius Λ around $\pm\boldsymbol{K}$, where the momentum cutoff Λ ensures the conservation of the number of states. One obtains

$$G_{00}(E) = \frac{E}{W^2} \ln \left| \frac{E^2}{W^2 - E^2} \right| - i\pi \frac{|E|}{W^2} \Theta(W - |E|)\,, \quad (4.19)$$

where $W = \hbar v_F \Lambda = \sqrt{\sqrt{3}\pi} t$ is the cut-off energy and $\Theta(x)$ the Heaviside step function.

A word of caution has to be voiced if one wants to repeat the same process for the other types of Green's functions. Obtaining analytic formulas for G_{lm}^{NN} and G_{lm}^{AB} requires the limit $\Lambda \to \infty$ [170, 193]. It was already noted in Refs. [185, 193] that this approximation has to be taken with a grain of salt. Indeed, a numerical comparison of Wang *et al.* [194] showed that the value of the momentum cutoff has to be selected carefully to obtain sufficiently good results. We tested the effect of the $\Lambda \to \infty$ approximation in the calculation of G_{lm}^{NN} and G_{lm}^{AB}, as given in Ref. [170], on the results of the resonance energies which will be presented below. Compared to a fully numerical integration[5] using the complete graphene spectrum we found that for the bridge position the resonance levels shift significantly. For example, for a copper adatom in the bridge position, as parametrized in Sec. 3.6, the $\Lambda \to \infty$ approach yields a resonance energy of $E_{\mathrm{res}} = 128\,\mathrm{meV}$ [101], whereas evaluating the Green's functions numerically results in $E_{\mathrm{res}} = 82\,\mathrm{meV}$. We cross-checked the fully numerical result with TB calculations for large supercells, which simulate a finite but very small adatom concentration of the order of 0.01%. For an adatom in the hollow position, no resonance level could be found in the investigated energy interval for the linearized model and $\Lambda \to \infty$. However, this is in contrast to the results of the TB supercell simulations and the numerical evaluation of the Green's functions.

To obtain reliable results, we evaluate all Green's functions by full numerical integration of the non-linearized spectrum over the 2D Brillouin zone. Throughout the calculations we keep a small energy broadening of $\delta = 1\,\mathrm{meV}$ due to numerical costs. The position of the resonance energies are affected only marginally by this factor. Changing $\delta \to \delta/2$ leads to changes of the order of 0.1%. The width of the resonance peaks is naturally the more affected by the broadening the smaller the width is. Especially, resonance widths smaller than 2 meV can not be resolved within our numerical calculations. In the top and bridge position, changing $\delta \to \delta/2$ decreases the level widths by about 1 to 2 meV. The hollow position, on the other hand, exhibits very narrow peaks of about twice the energy broadening, measuring about 2 meV. Although, we cannot extract the correct widths in the hollow position, the widths we obtain in the top and bridge positions appear to have the correct order of magnitude despite the finite energy broadening of 1 meV. Note that although we are keeping a finite imaginary part δ for the energy E^+, we omit the superscript $+$ in the following formulas.

With the help of symmetry arguments we can reduce the number of Green's functions needed for the different adsorption position and, thus, reduce the numerical costs for their calculation. Apart the translational symmetry holding for all propagators, the Green's functions G_{lm}^{AB} coupling opposite sublattices respect the threefold rotational symmetry. Green's functions for sites on the same sublattice, G_{lm}^{NN}, can be transformed to equivalent Green's functions by sixfold rotations [195].

[5] For the numerical integration we used the trapezoidal rule as described in Ref. [151].

Coupling sites on the same hexagon ring, as required by the form of $\mathcal{V}$ for the hollow position, see Eq. (4.8), needs at maximum four different Green's functions: G_{00}, $G_{12}^{\mathrm{AB}} = G_{16}^{\mathrm{AB}} = G_{32}^{\mathrm{AB}}$, $G_{13}^{\mathrm{NN}} = G_{15}^{\mathrm{NN}} = G_{35}^{\mathrm{NN}}$, and $G_{14}^{\mathrm{AB}} = G_{52}^{\mathrm{AB}} = G_{36}^{\mathrm{AB}}$. The propagators are indicated in Fig. 4.1(b).

T-matrix for different adsorption positions

With $\mathcal{V}$ of Eq. (4.8) and $G_{lm}^{\alpha\beta} = \langle X_l^\alpha | \mathcal{G}_0 | X_m^\beta \rangle$ we can evaluate the T-matrix elements $\langle X_l^\alpha | \mathcal{T} | X_m^\beta \rangle$ in the local atomic basis. Using Eq. (4.4) and the definition of the projection $\mathcal{P}$ in Eq. (4.9), we identify the non-vanishing block of the T-matrix to be

$$\mathcal{T} = \frac{|\omega|^2}{E - \varepsilon - |\omega|^2 \mathcal{A}(E)} \, \mathcal{P} \, . \tag{4.20}$$

Depending on the adsorption position, the term $\mathcal{A}$ comprises a combination of different Green's functions. Explicitly, we have

$$\mathcal{A}(E) = \begin{cases} G_{00}(E) & \text{(top)} \\ 2\left[G_{00}(E) + G_{12}^{\mathrm{AB}}(E)\right] & \text{(bridge)} \\ 6\left\{G_{00}(E) + G_{14}^{\mathrm{AB}}(E) \right. & \\ \quad \left. + 2[G_{12}^{\mathrm{AB}}(E) + G_{13}^{\mathrm{NN}}(E)]\right\} & \text{(hollow)} \end{cases} \tag{4.21}$$

4.2.2 Density of states and momentum relaxation rate

As explained at the beginning of Sec. 4.2, we will study the adatom induced resonance in the DOS and the momentum relaxation rates. Both quantities are accessible simply from knowing the T-matrix.

Density of states

From $\mathcal{T}$, we can directly calculate the full Green's function $\mathcal{G}(E)$ of graphene under the local perturbation $\mathcal{V}$. We use the quantity $\mathcal{G}(E)$ to obtain the DOS of the system defined via the imaginary part of $\mathcal{G}$, i.e.,

$$\begin{aligned} \mathrm{DOS}(E) &= -\frac{1}{\pi} \mathrm{Im}\,\mathrm{Tr}\left[\mathcal{G}(E)\right] \\ &= -\frac{1}{\pi} \mathrm{Im}\,\mathrm{Tr}\left[\mathcal{G}_0(E)\right] - \frac{1}{\pi} \mathrm{Im}\,\mathrm{Tr}\left[\mathcal{G}_0(E)\mathcal{T}(E)\mathcal{G}_0(E)\right] \\ &= -\frac{1}{\pi} \mathrm{Im}\,\mathrm{Tr}\left[\mathcal{G}_0(E)\right] - \frac{1}{\pi} \mathrm{Im}\,\mathrm{Tr}\left[\mathcal{G}_0^2(E)\mathcal{T}(E)\right] \\ &= -\frac{1}{\pi} \mathrm{Im}\,\mathrm{Tr}[\mathcal{G}_0(E)] + \frac{1}{\pi} \mathrm{Im}\,\mathrm{Tr}\left[\frac{\partial \mathcal{G}_0(E)}{\partial E} \mathcal{T}(E)\right] . \end{aligned} \tag{4.22}$$

In the last steps we used the property of the trace and, writing the Green's operator in the eigenbasis of the Hamiltonian, $\mathcal{G}_0 = \sum_n |n\rangle \langle n| / (E - \epsilon_n)$, reformulated [196]

$$\begin{aligned}\mathcal{G}_0^2(E) &= \left(\sum_n \frac{|n\rangle \langle n|}{E-\epsilon_n}\right)\left(\sum_m \frac{|m\rangle \langle m|}{E-\epsilon_m}\right) = \sum_{n,m} \frac{|n\rangle \langle n|m\rangle \langle m|}{(E-\epsilon_n)(E-\epsilon_m)} \\ &= \sum_n \frac{|n\rangle \langle n|}{(E-\epsilon_n)^2} = -\frac{\partial \mathcal{G}_0}{\partial E}\,. \end{aligned} \tag{4.23}$$

Equation (4.22) consists of two main parts: The first term is the DOS of unperturbed graphene, the second term describes the change in the DOS due to the perturbation. Normalizing the DOS to the total number of carbon atoms in the system, we obtain the DOS per atom $\nu(E) = \nu_0(E) + \Delta\nu(E)$, with the unperturbed part described by $\nu_0(E) = -\mathrm{Im}[G_{00}(E)]/\pi$ and the perturbed one given by

$$\Delta\nu(E) = \frac{\eta}{\pi}\mathrm{Im}\,\mathrm{Tr}\left[\frac{\partial \mathcal{G}_0(E)}{\partial E}\mathcal{T}(E)\right]\,. \tag{4.24}$$

Here, $\eta = 1/(2N)$ is the adatom concentration in the system and N is the number of graphene unit cells.

In Sec. 4.4 we will further use the local DOS (LDOS) to extract information about the localization behavior of the resonant states around the impurity. The LDOS can be easily obtained from the defining expression in Eq. (4.22). Therein, the trace is given by the sum over all atomic basis states, which yields

$$\begin{aligned}\mathrm{DOS}(E) &= -\frac{1}{\pi}\mathrm{Im}\,\mathrm{Tr}\left[\mathcal{G}_0(E) + \mathcal{G}_0(E)\mathcal{T}(E)\mathcal{G}_0(E)\right] \\ &= -\frac{1}{\pi}\mathrm{Im}\sum_{m,\alpha}\left[\langle X_m^\alpha|\,\mathcal{G}_0(E)\,|X_m^\alpha\rangle + \langle X_m^\alpha|\,\mathcal{G}_0(E)\mathcal{T}(E)\mathcal{G}_0(E)\,|X_m^\alpha\rangle\right] \\ &= \sum_{m,\alpha}\left(-\frac{1}{\pi}\right)\mathrm{Im}\,\langle X_m^\alpha|\,\mathcal{G}_0(E)\,|X_m^\alpha\rangle \\ &+ \sum_{m,\alpha}\left(-\frac{1}{\pi}\right)\mathrm{Im}\,\langle X_m^\alpha|\,\mathcal{G}_0(E)\mathcal{T}(E)\mathcal{G}_0(E)\,|X_m^\alpha\rangle \\ &= \sum_{m,\alpha}\left[\rho_0^{m,\alpha}(E) + \Delta\rho^{m,\alpha}(E)\right]. \end{aligned} \tag{4.25}$$

Again, we split the LDOS contributions in an unperturbed part for the lattice site X_m^α, $\rho_0^{m,\alpha}$, and a perturbed one, $\Delta\rho^{m,\alpha}(E)$, which comprises the influence of the adatom binding to graphene. Using the completeness of the atomic basis, the perturbed part can be rewritten to

$$\Delta\rho^{m,\alpha}(E) = \left(-\frac{1}{\pi}\right)\mathrm{Im}\sum_{l,\beta}\sum_{n,\tau}\langle X_m^\alpha|\mathcal{G}_0(E)|X_l^\beta\rangle\langle X_l^\beta|\mathcal{T}(E)|X_n^\tau\rangle\langle X_n^\tau|\mathcal{G}_0(E)|X_m^\alpha\rangle\,. \tag{4.26}$$

As the non-vanishing part of the T-matrix affects all nearest neighbors of the adatom, see Eq. (4.20), the evaluation of Eq. (4.26) requires the evaluation of propagators connecting any adatom neighboring site to the lattice site X_m^α at which the LDOS is to be computed. With our straightforward, though rather crude, numerical implementation of the Green's functions, the evaluation of the LDOS can be time-consuming. We will therefore employ large supercell TB calculations for a quantitative and large-scale evaluation of the LDOS in Sec. 4.4.

Momentum relaxation rate

The resonant state leaves traces not only in the DOS but also in the momentum relaxation rate. We consider in the following elastic scattering off the adatoms on graphene assuming that the adatoms have no internal excitations. Furthermore, we neglect any multiple-scattering events. The latter are suppressed in the limit of dilute adatom coverage or the case for a single adatom on graphene, but would be important for higher adatom concentrations. We start with the generalized Fermi's golden rule to obtain the transition rate between the states $|n\,q\rangle$ and $|n'q'\rangle$ of the same eigenenergy $\epsilon_{nq} \equiv \epsilon_n(\boldsymbol{q})$ given in Eq. (4.13),

$$W_{nq|n'q'} = \frac{2\pi}{\hbar} \left|\langle n'q'| \, \mathcal{T}(\varepsilon_{nq}) \, |n\,q\rangle\right|^2 \delta(\epsilon_{nq} - \epsilon_{n'q'}) \,. \tag{4.27}$$

We remember that the index n refers to the conduction ($n = +1$) or valence ($n = -1$) branch of the graphene spectrum. The (normalized) eigenstates $|n\,q\rangle$ diagonalizing the graphene Hamiltonian are given by a linear combination of the Bloch states on the two sublattices A and B of graphene,

$$|n\,q\rangle = \frac{1}{\sqrt{2}} \left(|A_{\boldsymbol{q}}\rangle - n \sqrt{\frac{\tilde{f}_{\mathrm{orb}}(\boldsymbol{q})}{\left[\tilde{f}_{\mathrm{orb}}(\boldsymbol{q})\right]}} \, |B_{\boldsymbol{q}}\rangle \right) \,. \tag{4.28}$$

Note that all information about the adatom binding to graphene is entering the transition rate of Eq. (4.27) via the T-matrix. For isotropic scattering in momentum space, we weight the transition rate with the so-called transport factor[6] $(1-\cos\phi_{qq'})$, sum over all final states $|q'n'\rangle$, and finally obtain the elastic transport scattering rate

$$\tau_{nq}{}^{-1} = \sum_{q',n'} (1 - \cos\phi_{qq'}) \, W_{nq|n'q'} \,. \tag{4.29}$$

The symbol $\phi_{qq'}$ refers here to the angle between the $\boldsymbol{q}$ and $\boldsymbol{q'}$ vectors. The momentum relaxation rate is then only one step away and found after averaging over

[6] See for the derivation of the transport factor, for example, the chapter on the Boltzmann transport theory of Ref. [85].

the Fermi contour for a given energy E,

$$\tau_{\mathrm{m}}^{-1}(E) = \frac{\sum_{q,n} {\tau_{nq}}^{-1} \delta(E - \varepsilon_{nq})}{\sum_{q,n} \delta(E - \varepsilon_{nq})} \,. \tag{4.30}$$

The momentum relaxation rate is directly proportional to the adatom concentration $\eta = 1/(2N)$. This factor emerges, on the one hand, from the normalization factor of the eigenstates of graphene in Eq. (4.28), and, on the other hand, from the Fourier transform of the atomic basis, in which we expressed the T-matrix, to the Bloch basis.

We will be mainly interested in resonances occurring at low energies, i.e., in the range of $[-0.3, 0.3]\,\mathrm{eV}$ around the Fermi level. At those energies, the graphene spectrum is well described by the linear approximation, which simplifies the numerical evaluation of the summations (integrals) needed for the calculation of τ_{m}^{-1}. The Green's functions entering the T-matrix are nevertheless computed on the full Brillouin zone as already pointed out in Sec. 4.2.1.

4.3 Resonance characteristics for adatoms in the top, bridge, and hollow positions

In the following sections, we will fall back on the DOS to investigate resonance levels in the single adatom limit induced by the adatom adsorption on graphene. In order to cover a broad variety of possible adsorbate realizations, we calculate the DOS under the variation of ε and ω, which are the orbital parameters that characterize the adatom on graphene. The resonance energies are then extracted from the adatom induced peaks in the perturbed part of the DOS $\Delta\nu$. We further read off for each peak the width at half maximum, which represents the resonance lifetime. We will refer to those scans through the parameter space as the resonance maps. To be more precise, we vary the hybridization strength from 0 to 10 eV, and the on-site parameter from -5 to 5 eV. Negative values of ω are omitted since the T-matrix depends only on $|\omega|^2$. This means that all resonance maps are symmetric with respect to the $\omega = 0$ axis. We restrict ourselves to the experimentally relevant energy range from -0.3 to 0.3 eV to check for resonance peaks[7]. We show for comparison also the momentum relaxation rates for specific parameter pairs (ω, ε) for a dilute adatom concentration of $\eta = 10^{-6} = 1\,\mathrm{ppm}$. The width of the occurring resonance peaks in the momentum relaxation rate are in general different from the peak widths which we extract from the DOS. Distinctive features for the adsorption positions of top, bridge, and hollow will be pointed out for both the DOS and τ_{m}^{-1} results.

[7] This energy range corresponds to a variation of the charge carrier density from -9.5 to $9.5 \cdot 10^{12}\,\mathrm{cm}^{-2}$, according to $n = 1/(\pi)\,(E/\hbar v_F)^2$.

4.3.1 Adatom in the top position

Figure 4.2 displays in panel (a) the aforementioned resonance maps for the resonance energy E_{res} (left) and the corresponding peak widths Γ (right) for a single adatom in the top position.

We first note a mirror symmetry with respect to the $\varepsilon = 0$ axis in the maps for Γ and, taking into account only the absolute value, also for E_{res}. We can explain this appearance by realizing that in the top position the singularity of the single non-vanishing T-matrix element mainly determines the location of the resonance. Taking Eq. (4.20) and the corresponding expression in Eq. (4.21) for the top position, this boils down to the zero of $E - \varepsilon - \omega^2 G_{00}(E)$. The real part of the on-site Green's function $G_{00}(E)$ is an odd function of E, which is also visible in Eq. (4.19). The imaginary part, on the other hand, is even with respect to E. Therefore, the quantity E_{res} undergoes a change in sign upon $\varepsilon \to -\varepsilon$ for fixed ω, while the peak width remains unchanged[8], $\Gamma \to \Gamma$ for $\varepsilon \to -\varepsilon$.

Secondly, we see that for small ω the parameter range giving rise to resonance peaks in the investigated energy interval of $[-0.3, 0.3]\,\mathrm{eV}$ is more restricted than for larger ω. Naturally, by lowering the hybridization strength ω for a fixed on-site energy ε gradually decouples the adatom from graphene. At $\omega = 0$ no hybridization between the adatom orbital and the graphene states takes place. A δ-shaped peak occurs in the DOS at $E_{\mathrm{res}} = \varepsilon$ and represents the isolated adatom level. This means that in Fig. 4.2(a) for $\omega = 0$, the on-site energies are limited to the range of the investigated energy interval, i.e., from -0.3 to $0.3\,\mathrm{eV}$.

On the other hand, if we increase ω for fixed ε, the hybridization of the impurity level with the graphene states renormalizes the resonance level energy [172]. It shifts closer to zero energy and, at the same time, the resonance width decreases. For $\omega \to \infty$ the effective potential on the adsorption site tends to infinity, $\omega^2/(E-\varepsilon) \to \infty$, and the wave function vanishes at this site. This parameter limit, therefore, effectively simulates a vacancy in graphene which induces a characteristic zero-energy mode in the graphene spectrum [173, 174, 189, 193]. We will come back to the special case of vacancies in Sec. 4.5.

For parameters representing a general top positioned adatom on graphene the resonance maps reveal that with increasing resonance energy also the width of the resonance levels grows. The DOS of unperturbed graphene scales (in good approximation) linearly with the energy. Correspondingly, the impurity level can couple to more graphene states at larger energies, which is reflected in broader resonance peaks.

The DOS and the momentum relaxation rates for exemplary parameters are shown in Fig. 4.2(b). The employed parameter sets (ω, ε) correspond to the corner points (1), (2), and (3) of the path drawn in the resonance map. Note that in the

[8] The imaginary part of the finite complex energy, at which the zero of the denominator of the T-matrix element occurs, is given by $\Gamma/2$ [196].

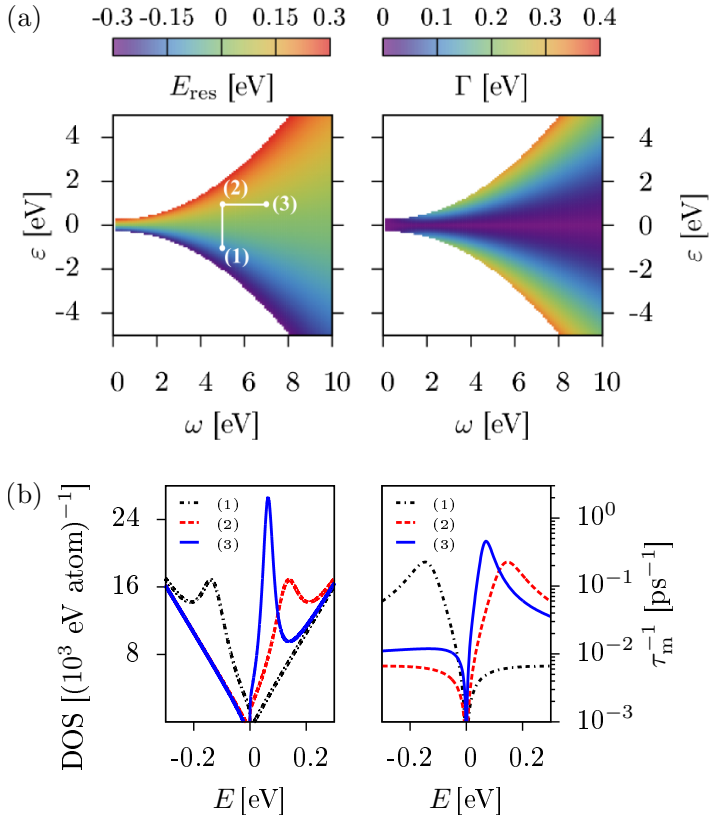

Figure 4.2: Resonance and momentum relaxation characteristics induced by adatoms in the top position. (a) Dependence of the resonance energy E_{res} and resonance width Γ on ε and ω. (b) Snapshots of DOS and τ_{m}^{-1} for the three parameter realizations (1) $\omega = 5\,\mathrm{eV}$, $\varepsilon = -1\,\mathrm{eV}$, (2) $\omega = 5\,\mathrm{eV}$, $\varepsilon = 1\,\mathrm{eV}$, and (3) $\omega = 7\,\mathrm{eV}$, $\varepsilon = 1\,\mathrm{eV}$. The chosen parameters give rise to resonance levels with (1) $E_{\mathrm{res}} = -130\,\mathrm{meV}$, $\Gamma = 109\,\mathrm{meV}$, (2) $E_{\mathrm{res}} = 130\,\mathrm{meV}$, $\Gamma = 109\,\mathrm{meV}$, and (3) $E_{\mathrm{res}} = 64\,\mathrm{meV}$, $\Gamma = 50\,\mathrm{meV}$, respectively. An adatom concentration of $\eta = 10^3$ ppm is used for the DOS data, for better resolution, and a more realistic concentration of $\eta = 1$ ppm for τ_{m}^{-1}.

DOS calculation the adatom concentration was enlarged to the value of 10^3 ppm for a better visibility of the resonance peaks. The calculation of τ_{m}^{-1}, on the other hand, uses a more realistic adatom concentration of 1 ppm. Path (1) to (2) reflects the mirror symmetry in the resonance map mentioned above. Two adatoms with the same hybridization strength, $\omega_1 = \omega_2 = \omega$, but opposite on-site energies, $\varepsilon_1 = -\varepsilon_2$, induce resonance levels on the opposite sites of the zero energy. Path (2) to (3) shows that for fixed on-site energy and increasing hybridization strength, the resonance level shifts closer to zero energy and the peak width decreases in both the DOS and τ_{m}^{-1} graphs.

Recollecting the orbital parameters of the adatoms studied for their local SOC in the previous chapter, see Tab. 3.3, we can extract the resonance levels and resonance widths for the methyl group, fluorine, and copper binding in the top position. The methyl group has a strong hybridization of $\omega = 7.6\,\mathrm{eV}$ and a small on-site energy of $\varepsilon = -0.19\,\mathrm{eV}$. Accordingly, we expect the resonance level to lie at small negative energy. Indeed, we find $E_{\mathrm{res}} = -7.9\,\mathrm{meV}$ and $\Gamma = 6\,\mathrm{meV}$ for this parameter realization. Hydrogen with $\omega = 7.5\,\mathrm{eV}$ and $\varepsilon = 0.16\,\mathrm{eV}$ [52] is very similar to the methyl group but, due to the positive on-site energy, the resonance level appears at positive energy, $E_{\mathrm{res}} = 7\,\mathrm{meV}$ and $\Gamma = 5\,\mathrm{meV}$. The fluorine adatom is described by $\omega = 5.5\,\mathrm{eV}$ and negative on-site energy of $\varepsilon = -2.2\,\mathrm{eV}$ which is significantly larger than in the case of methyl or hydrogen. The resonance level appears far away from zero energy at $E_{\mathrm{res}} = -262\,\mathrm{meV}$ and, due to the large resonance energy, is very broad having $\Gamma = 277\,\mathrm{meV}$. The copper adatom, as a third example, is only weakly binding to graphene with $\omega = 0.81\,\mathrm{eV}$ and exhibits a small on-site energy of $\varepsilon = 0.08\,\mathrm{eV}$. The resonance peak is still sufficiently narrow, $\Gamma = 9\,\mathrm{meV}$, and the resonance level occurs at $E_{\mathrm{res}} = 68\,\mathrm{meV}$. The DOS and momentum relaxation rates for these adatoms will be shown later in Sec. 4.5, Fig. 4.9(a), where we compare those adatoms to the impact of a vacancy on graphene.

In general, we observe in the momentum relaxation rate calculations of Fig. 4.2(b) a noticeable electron-hole asymmetry (see also Ref. [97]), which gets more pronounced for resonance levels shifting farther away from zero energy, as it is the case for fluorine adatoms. However, experiments with dilute adatom concentrations of $\eta \simeq 1 - 100\,\mathrm{ppm}$ often show less asymmetry in their data. For example, in the transport measurements on dilute fluorinated graphene of Refs. [134, 160] the momentum relaxation rate data appears to be rather symmetric. A possible explanation for the discrepancy between theoretical prediction and experimental observation can be masking effects by symmetric contributions to the momentum relaxation rates from charged impurities [197], clusters [198, 199], or additional SMS candidates [176], which all can contribute to the transport. We will meet the experimental data of Refs. [134, 160] on fluorine again in Sec. 5.3. In contrast, asymmetric transport behavior was observed in samples on stronger fluorinated graphene samples [200].

4.3.2 Adatom in the bridge position

Figure 4.3(a) presents the resonance maps for an adatom in the bridge position. Unlike the maps for the top position, no mirror symmetry about the $\varepsilon = 0$ axis appears. The simple symmetry arguments of the previous section are no longer valid as two Green's functions, G_{00} and G_{12}^{AB}, with different behavior under $E \to -E$ enter the term $\mathcal{A}(E)$, Eq. (4.21), in the T-matrix. The rainbow-like appearance of the resonance maps is caused by the interplay of them.

Compared to the top position, Fig. 4.2, fewer parameter pairs (ω, ε) are able to realize resonance peaks in the fixed energy interval $[-0.3, 0.3]$ eV. Moreover, negative on-site energies dominate the allowed parameter region. These observations reflect that the resonance levels from adatoms in the bridge position are more sensitive to the variation of the orbital parameters than it is the case for top adatoms. Wehling *et al.* [183] draw a similar conclusion in their study of substitutional single and double impurities. The substitutional impurities are conveniently modeled by assigning an on-site potential to those graphene lattice sites which are to be substituted by the impurity. In our adatom description, this would mean to abandon ω and ε, and add on-site potentials U_0 to the former adatom hybridization partner(s) $|Y_l\rangle$. In the case of the double substitutional impurity, the terms U_0 appear on neighboring sites and a general interaction strength U_1 between the two sites is added. For $U_1 = U_0$, the local perturbation has the form of Eq. (4.8) for the bridge position with the main difference that, in contrast to the effective potential $\omega^2/(E - \varepsilon)$ appearing for the adatom case, the local potential strength U_0 is independent of the energy E.

Panel (b) of Fig. 4.3 shows how the resonance levels for a bridge adatom develop in the DOS and momentum relaxation rate under variation of (ω, ε) along the path (1) to (3) as indicated in the resonance map. Along the line segment (1) to (2), the hybridization strength is fixed and the on-site energy is changed such that the resonance level jumps from negative to positive energies. Increasing ω but keeping ε fixed, path (2) to (3), on the other hand, shifts the resonance level to even higher energies. This is in contrast to our observation for an adatom in the top position. The effective coupling between the two hybridization sites $|Y_{1,2}\rangle$ of the bridge position is at the basis of this shift away from zero energy. The resonance peaks are broadened under increasing the resonance energy by enlarging ω, since more states are available at the higher energy and the adatom is stronger coupled to graphene. Furthermore, for the same adatom concentration, the momentum relaxation rates τ_{m}^{-1} for the bridge and top positioned adatoms are comparable in magnitude.

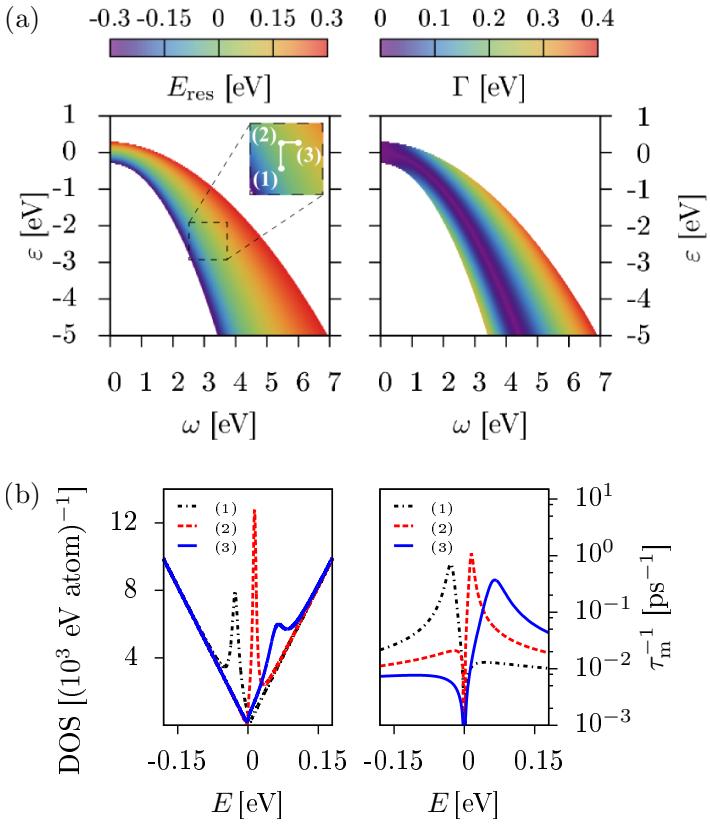

Figure 4.3: Resonance and momentum relaxation characteristics induced by adatoms in the bridge position. (a) Dependence of the resonance energy E_{res} and resonance width Γ on ε and ω. (b) Snapshots of DOS and τ_{m}^{-1} for the three parameter realizations (1) $\omega = 3\,\mathrm{eV}$, $\varepsilon = -2.5\,\mathrm{eV}$, (2) $\omega = 3\,\mathrm{eV}$, $\varepsilon = -2.2\,\mathrm{eV}$, and (3) $\omega = 3.2\,\mathrm{eV}$, $\varepsilon = -2.2\,\mathrm{eV}$. The chosen parameters give rise to resonance levels with (1) $E_{\mathrm{res}} = -27\,\mathrm{meV}$, $\Gamma = 17\,\mathrm{meV}$, (2) $E_{\mathrm{res}} = 14\,\mathrm{meV}$, $\Gamma = 9\,\mathrm{meV}$, and (3) $E_{\mathrm{res}} = 60\,\mathrm{meV}$, $\Gamma = 42\,\mathrm{meV}$, respectively. An adatom concentration of $\eta = 100\,\mathrm{ppm}$ is used for the DOS data, for better resolution, and a more realistic concentration of $\eta = 1\,\mathrm{ppm}$ for τ_{m}^{-1}.

4.3.3 Adatom in the hollow position

In the hollow position, as for the top and bridge cases, we assume that the adatom orbital respects the local point group symmetry, which is C_{6v}. This implies that the orbital has the magnetic quantum number $m_z = 0$ and couples to all six sites on the surrounding hexagon ring with the same hybridization parameter ω.

Weeks *et al.* [55] already argued in their study on strong local SOC originating from hollow adatoms in graphene that electrons which tunnel to such a $m_z = 0$ orbital[9] interfere destructively. The adatom orbital appears as effectively decoupled from the graphene states. The simple argument of Weeks is based on assuming adatoms in all hollow positions of the lattice. After Fourier transforming to the momentum space, the coupling of the adatom to the Bloch states is found to vanish at the Dirac points. The argument was later repeated by other authors, so for example by Ruiz-Tijerina *et al.* [187] where they extend the analysis to the full first Brillouin zone. The hollow adatom decouples from a large portion of the graphene continuum states in the first Brillouin zone.

The occurrence of those interference effects for the hollow position, led Duffy *et al.* [6] to the conclusion that an adatom coupling to graphene through its $m_z = 0$ orbital is, so to say, invisible. That is, the hollow adatom influences the graphene electronic properties only weakly. However, symmetry-breaking perturbations such as uniaxial strain would, according to the authors, lift the interference effects and result in graphene as a device sensing, e.g., the mentioned uniaxial strain. Other works concentrated on the signatures of such hollow adatoms in the STM spectra, for example Refs. [139–141, 188], which revealed that the C_{6v} symmetric adsorption of the hollow adatom leads to peaks in the zero-bias tunneling conductance. For adatoms in the top position, asymmetric Fano-type line shapes are observed. Classifying the adatom orbital into C_{3v} preserving and C_{3v} violating forms, the influence on the Kondo temperature and the Kondo quantum critical point were investigated [201, 202]. And, finally, studying disordered graphene with adatoms in the hollow position, Uchoa *et al.* [188] considered the influence of the orbital symmetry on Anderson localization. This list of works represents only a snapshot of peculiarities arising from the local symmetry of and around adsorbates in graphene. We will proceed in the following with our resonance analysis for the $m_z = 0$ orbital in the hollow position.

Figure 4.4(a) displays the resonance map obtained by scanning the orbital parameter space for resonance peaks in the DOS in the restricted energy range from -0.3 to $0.3\,\mathrm{eV}$. Compared to the top and bridge positions, only parameters from a small portion of all possible combinations give rise to resonance peaks in the considered energy window. As in the bridge position, the resonance map exhibits a rainbow shape. Furthermore, starting with a resonance level at negative energy

[9] In the work of Weeks *et al.* [55], the $m_z = 0$ orbital is represented by a p_z orbital.

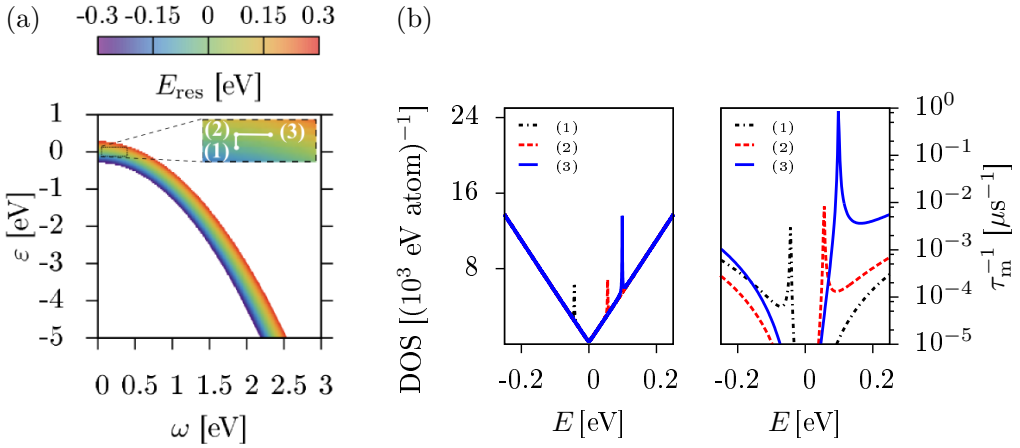

Figure 4.4: Resonance and momentum relaxation characteristics induced by adatoms ($m_z = 0$) in the hollow position. (a) Dependence of the resonance energy E_{res} on ε and ω. The resonance widths Γ (not shown) are not resolved sufficiently and are estimated to be $\Gamma \leq 2\,\mathrm{meV}$. (b) Snapshots of DOS and τ_{m}^{-1} for the three parameter realizations (1) $\omega = 0.2\,\mathrm{eV}$, $\varepsilon = -0.08\,\mathrm{eV}$, (2) $\omega = 0.2\,\mathrm{eV}$, $\varepsilon = 0.02\,\mathrm{eV}$, and (3) $\omega = 0.3\,\mathrm{eV}$, $\varepsilon = 0.02\,\mathrm{eV}$. The chosen parameters give rise to resonance levels with (1) $E_{\mathrm{res}} = -43\,\mathrm{meV}$, (2) $E_{\mathrm{res}} = 55\,\mathrm{meV}$, and (3) $E_{\mathrm{res}} = 99\,\mathrm{meV}$, respectively. An adatom concentration of $\eta = 500\,\mathrm{ppm}$ is used for the DOS data, for better resolution, and a more realistic concentration of $\eta = 1\,\mathrm{ppm}$ for τ_{m}^{-1}.

and increasing the on-site energy (for fixed hybridization strength), the resonance level is shifted to positive energies. Fixing the on-site energy and increasing the hybridization strength, on the other hand, always results in a resonance level at higher energy. Overall, the position of the resonance level is much more sensitive to variation of the orbital parameters ω and ε than in the bridge position.

We mentioned already in Sec. 4.2.1 that we use a finite energy broadening in our numerical evaluation of the Green's functions. This broadening affects the resolution of very narrow resonance peaks as it is the case for the $m_z = 0$ orbital in the hollow position. We can only estimate an upper bound for the corresponding resonance widths $\Gamma \leq 2\,\mathrm{meV}$ for all peaks observed in the interval $[-0.3, 0.3]\,\mathrm{eV}$. We, therefore, forgo displaying the map for the resonance widths in Fig. 4.4(a).

Both the restricted parameter region of the resonance map and the global appearance of very narrow resonance peaks indicate that the $m_z = 0$ orbital in the hollow position suffers from destructive interference as shown by earlier works (see above). This presumption is further supported by particular DOS and momentum relaxation rate calculations as shown in Fig. 4.4(b). The resonance levels manifest themselves as very sharp, almost delta-like peaks, which move very strongly under small variation in (ω, ε). No significant broadening of the peaks is observed in both the DOS and τ_{m}^{-1} graphs for resonance energies farther away from the zero energy.

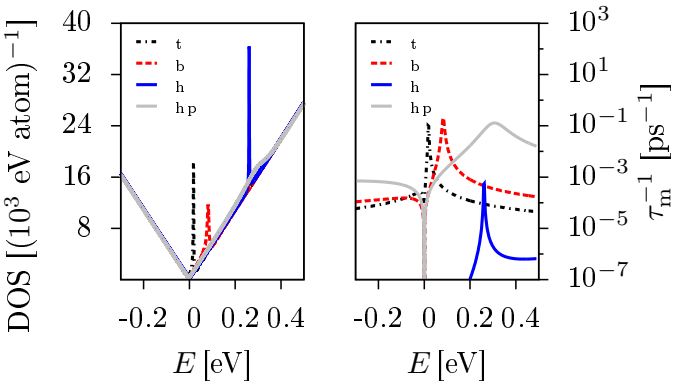

Figure 4.5: DOS and τ_{m}^{-1} for an adatom with $\omega = 0.54\,\mathrm{eV}$ and $\varepsilon = 0.02\,\mathrm{eV}$ in the adsorption positions top (t), bridge (b), and hollow ($m_z = 0$) (h). The resonant energies and width are, respectively, (t) $E_{\mathrm{res}} = 18\,\mathrm{meV}$, $\Gamma = 3\,\mathrm{meV}$, (b) $E_{\mathrm{res}} = 82\,\mathrm{meV}$, $\Gamma = 10\,\mathrm{meV}$, and (h) $E_{\mathrm{res}} = 261\,\mathrm{meV}$, $\Gamma \leq 2\,\mathrm{meV}$. A toy model calculation for the hollow position with $m_z = 1$ (hp) yields stronger coupling between the adatom and graphene compared to the case (h). The resonance level is found at $E_{\mathrm{res}} = 286\,\mathrm{meV}$ with $\Gamma = 114\,\mathrm{meV}$. For better visibility, a concentration of $\eta = 500\,\mathrm{ppm}$ is used in the DOS calculations, τ_{m}^{-1} data are shown for $\eta = 1\,\mathrm{ppm}$.

Instead, the peaks seem to sit on top of the DOS. In the top and bridge positions, in contrast, the resonance peaks broaden at higher energies where more graphene states are available to hybridize with the impurity. Correspondingly, at higher energies the top and bridge resonance levels become more buried in the background DOS of pristine graphene. The magnitudes of the hollow τ_{m}^{-1} rates are furthermore significantly smaller than in the other adsorption configurations of top and bridge. The hollow τ_{m}^{-1} curves increase in magnitude only for higher energies. Figure 4.5 shows the three adsorption positions of top, bridge, and hollow[10] in a direct comparison with the DOS and τ_{m}^{-1} curves for one chosen parameter pair of $\omega = 0.54\,\mathrm{eV}$ and $\varepsilon = 0.02\,\mathrm{eV}$. Both the sensitivity to the parameter strengths and the different magnitude in the momentum relaxation rates are apparent. As was also noted by Duffy *et al.* [6] in a detailed study of the scattering cross section, we observe that a $m_z = 0$ orbital in the hollow position acts only as a weak scatterer in graphene.

The decoupling of the impurity state from the graphene states is also clearly visible in large-supercell TB calculations for an adatom concentration of 312 ppm, as shown in the left panel of Fig. 4.6. In the single adatom limit, the parameters $\omega = 0.54\,\mathrm{eV}$ and $\varepsilon = 0.02\,\mathrm{eV}$ lead to a resonance level at $E_{\mathrm{res}} = 261\,\mathrm{meV}$ in the DOS. A very flat band appears precisely at this energy in the supercell calculation, lying on top of the graphene band structure.

In the following we will show that the decoupling of the hollow adatom is closely

[10] Also the result of a toy model calculation, which will be introduced later in the text, is included in Fig. 4.5. The discussion of the graphs will follow below.

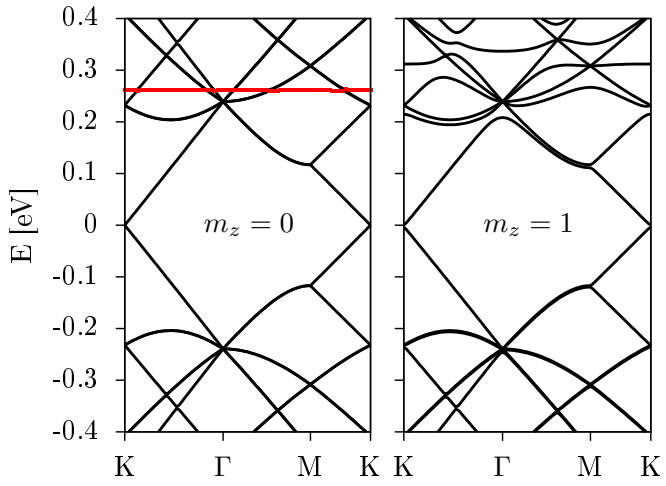

Figure 4.6: Left and right panel show the TB band structure of graphene with adatoms in the hollow position with a $m_z = 0$ and $m_z = 1$ orbital, respectively, for a 40×40 supercell. For $m_z = 0$, the graphene band structure is almost undisturbed and a flat non-dispersive band (red) occurs at about $E = 261\,\text{meV}$. For $m_z = 1$, band anti-crossings appear for energies above 200 meV, which reflects a strong hybridization of the impurity state with graphene.

related to the symmetry of the impurity orbital. For this, we consider as a toy model an adatom in hollow position where the effective adatom orbital has the magnetic quantum number $m_z = 1$ which explicitly breaks the C_{6v} symmetry. The Hamiltonian describing this adatom orbital in the hollow position on graphene is given by

$$H' = \varepsilon \left|O\right\rangle \left\langle O\right| + \sum_{l=1}^{6} \omega_l \left(\left|O\right\rangle \left\langle Y_l\right| + \text{H.c.}\right) + \mathcal{H}_0\,, \tag{4.31}$$

where $\mathcal{H}_0$ describes graphene as before. The hybridization coupling now depends on the neighboring carbon site $|Y_l\rangle$ on the hexagon ring through $\omega_l = \omega \exp[i(l-1)\phi]$, where $\phi = \pi/6$. The phase dependence originates in the transformation properties of the $m_z = 1$ orbital under the angular momentum operator L_z.

The right panel of Fig. 4.6 shows the toy model induced band structure of a supercell calculation with $\eta = 312\,\text{ppm}$, $\omega = 0.54$ and $\varepsilon = 0.02\,\text{eV}$. Comparing the left and right panels, i.e., the cases of an $m_z = 0$ and $m_z = 1$ orbital in the hollow position, we see that in the latter case a strong coupling between the impurity induced state and graphene is established, which alters the graphene bands for energies above 200 meV. Anti-crossings appear around the resonance level of $E_{\text{res}} = 285\,\text{meV}$ as found from the DOS calculation in the single adatom limit. The DOS and the momentum relaxation rate for the same parameter realization were already shown in Fig. 4.5. The DOS reveals that the resonance peak is with $\Gamma = 114\,\text{meV}$

significantly broader than in the $m_z = 0$ case and more buried in the background of the graphene DOS. Also the magnitude of the momentum relaxation rate is now comparable to the one observed for the top and bridge position. By breaking the C_{6v} symmetry of the hybridization between the hollow adatom and graphene, we restored the effective coupling of the impurity to the states of graphene.

Figure 4.7(a) displays the resonance maps for the $m_z = 1$ orbital in the hollow position. Compared to the $m_z = 0$ case, a wider parameter range leads to resonance levels appearing within $[-0.3, 0.3]$ eV. However, the resonance levels are still more sensitive to the variation of ω and ε than it is the case for the top and bridge configurations (with an $m_z = 0$ orbital on the adatom). Both the resonance energy and the width of the resonance peaks behave under variation of the orbital parameters qualitatively in the same way as in the bridge position, see Fig. 4.7(b).

4.4 Localization of resonant states

In the previous section, we have concentrated on the position and width of resonance peaks occurring in the DOS and the momentum relaxation rate due to adatoms in the top, bridge, or hollow positions. We now want to learn more about the resonant state itself, i.e., the eigenstate of the system at the resonance energy, by taking a closer look at its spatial distribution around the impurity.

In the single adatom limit, the eigenstate amplitude at a lattice site X_m^α can be calculated from the LDOS $\rho^{m,\alpha}(E_{\mathrm{res}})$, Eq. (4.25). On the other hand, we can also extract the LDOS from supercell calculations mimicking a dilute adatom concentration of $\eta = 312\,\mathrm{ppm}$. The LDOS is evaluated by applying the triangle method (or two-dimensional tetrahedron method) for the Brillouin zone integration [84]. We will employ the TB supercell calculations to quantitatively analyze LDOS magnitudes in the vicinity of the adatom along selected directions. The LDOS is extracted at the peak energies $E_{\mathrm{res}}^{\mathrm{tb}}$ of the supercell DOS. We find that these peak energies are for all investigated parameter configurations close to the resonance energies E_{res} predicted for the single adatom limit. Therefore, we do not expect qualitative changes between the two cases of dilute and single adatom limit. However, due to the finite size of the supercells we are limited in our investigation to the distance dependence of the LDOS around the impurity. As we approach the supercell boundary, the LDOS saturates.

Figure 4.8 presents the profile of the resonant states for exemplary parameters ω and ε for the top, bridge, and hollow positions along certain directions. The local point group symmetries of C_{3v}, C_{2v}, and C_{6v}, classifying the three adsorption positions, are reflected in the LDOS distribution around the impurities. The symmetrical behavior is visible in both the supercell calculations (not shown) and the T-matrix based LDOS calculation for the down-folded Hamiltonian (insets in Fig. 4.8). We have to keep in mind that we work with a graphene-only system in

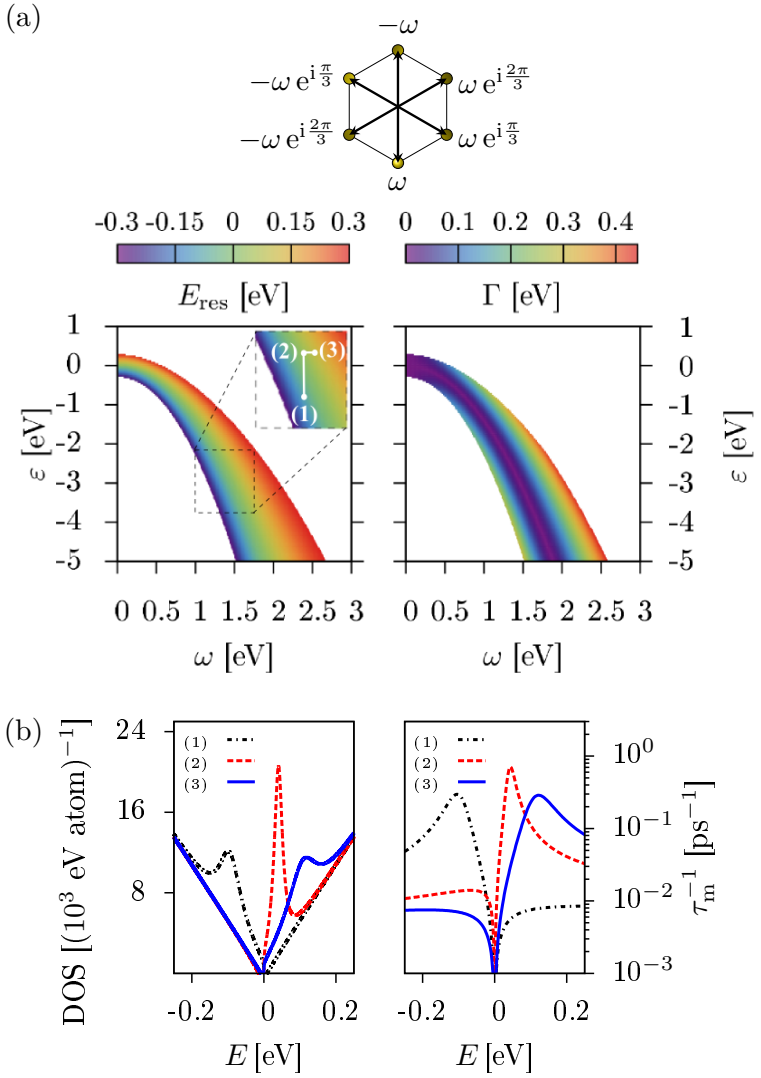

Figure 4.7: Resonance and momentum relaxation characteristics induced by a $m_z = 1$ orbital in the hollow position. (a) On top, a pictorial view of the phase-dependent coupling between the $m_z = 1$ orbital and its carbon hybridization partners is provided. The dependence of the resonance energy E_{res} and resonance width Γ on ε and ω are shown underneath. (b) Snapshots of DOS and τ_{m}^{-1} for the three parameter realizations (1) $\omega = 1.4\,\mathrm{eV}$, $\varepsilon = -3.3\,\mathrm{eV}$, (2) $\omega = 1.4\,\mathrm{eV}$, $\varepsilon = -2.5\,\mathrm{eV}$, and (3) $\omega = 1.5\,\mathrm{eV}$, $\varepsilon = -2.5\,\mathrm{eV}$. The chosen parameters give rise to resonance levels with (1) $E_{\mathrm{res}} = -94\,\mathrm{meV}$, $\Gamma = 72\,\mathrm{meV}$, (2) $E_{\mathrm{res}} = 40\,\mathrm{meV}$, $\Gamma = 28\,\mathrm{meV}$, and (3) $E_{\mathrm{res}} = 107\,\mathrm{meV}$, $\Gamma = 92\,\mathrm{meV}$, respectively. An adatom concentration of $\eta = 500\,\mathrm{ppm}$ is used for the DOS data, for better resolution, and a more realistic concentration of $\eta = 1\,\mathrm{ppm}$ for τ_{m}^{-1}.

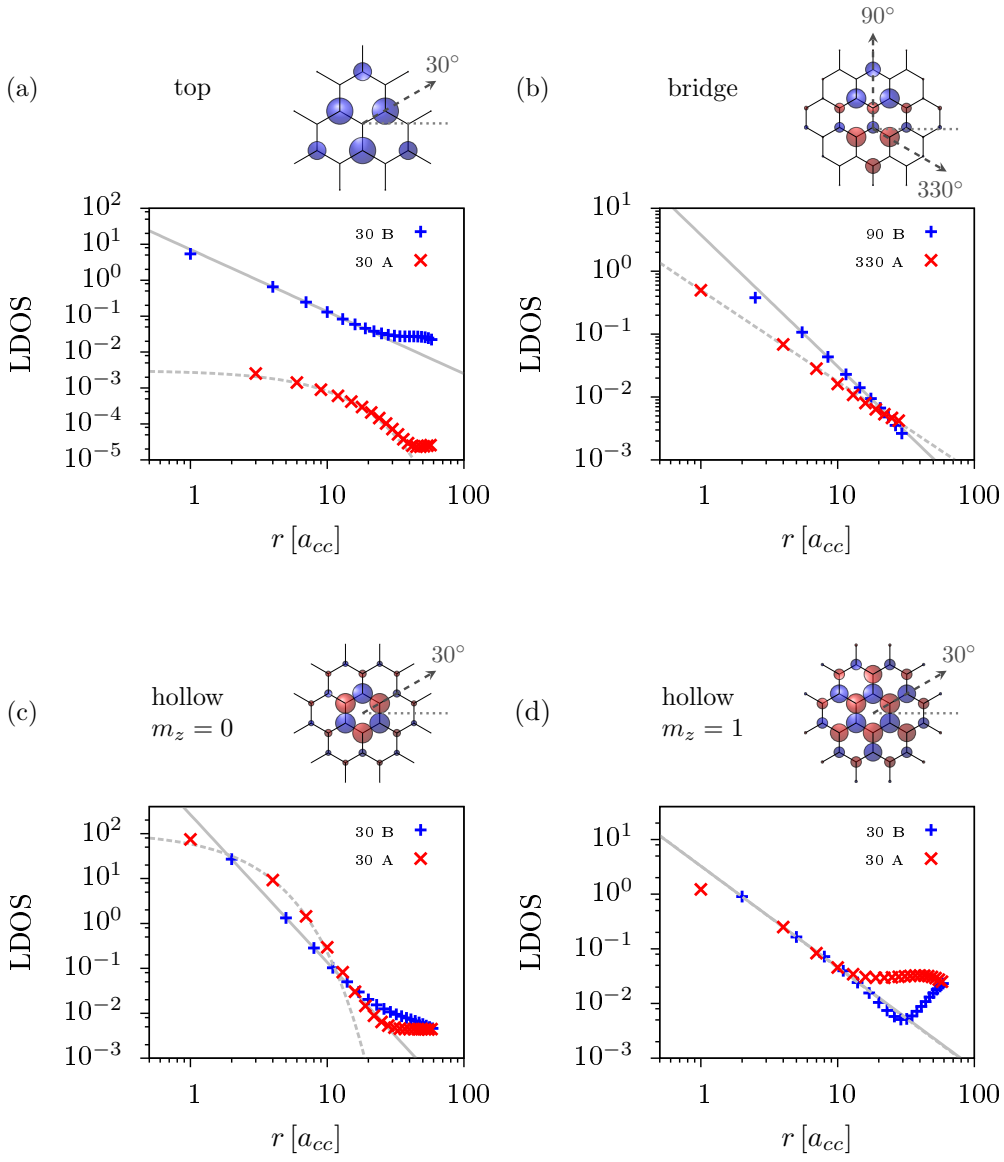

Figure 4.8: Localization of resonant states along selected directions in the lattice for adatoms with, (a)-(b), $\omega = 0.54\,\text{eV}$ and $\varepsilon = 0.02\,\text{eV}$ in the top and bridge positions, respectively, and with, (c)-(d), $\omega = 0.3\,\text{eV}$ and $\varepsilon = 0.02\,\text{eV}$ in the hollow position for the cases $m_z = 0$ and $m_z = 1$. The insets show the LDOS in the vicinity of the impurity site as obtained from the down-folded Hamiltonian in the T-matrix formalism. The spheres' radii indicate the LDOS magnitude on the corresponding site, the colors refer to the two sublattices A (red) and B (blue). The quantitative analysis of the LDOS is based on 40×40 supercell calculations. Power-law decay is observed in the dominant directions for the top and bridge positions. No clear tendency is found for the $m_z = 0$ orbital in the hollow position, in contrast to the result for $m_z = 1$ in the same configuration. Consult the main text for the resonance levels and the decay exponents.

the T-matrix approach. Therefore, no LDOS contribution for the adatom site itself is extracted. The observed symmetry implies that the decay of the resonant states depends for all adsorption position on the direction of the selected path leading away from the adatom site, as was already noted by Liang *et al.* [175] for the top position.

A strong scatterer represented by an adatom in the top position [186], or similarly by substitutional impurity [183], on sublattice A induces a resonant state which is more localized on the opposite sublattice B and vice versa. In the case of a vacancy in the lattice, the state exclusively populates sites on the opposite sublattice, and it was shown that the LDOS decays as r^{-2} [173, 174, 181], where r denotes the distance from the vacancy. For a general adatom in the top position, both the sublattice population and the decay exponent depend on the orbital parameters characterizing the adatom. We here chose as an example $\omega = 0.54\,\mathrm{eV}$ and $\varepsilon = 0.02\,\mathrm{eV}$ which yields a peak in the DOS at $E_{\mathrm{res}}^{\mathrm{tb}} = 19\,\mathrm{meV}$. Figure 4.8(a) displays the LDOS profile along the 30° line (with respect to the x axis, as shown in the inset) on the two sublattices B and A, where the latter hosts the adsorption position of the adatom. On the B sublattice, we observe a power-law decay $|\psi|^2 \propto r^{-p}$, $p \simeq 1.72$, where r is given in units of the carbon-carbon distance. On the A sublattice, however, a tendency to exponential decay is found, $|\psi|^2 \propto \exp(-qr)$, $q \approx 0.12$. Note that the amplitude of the resonant state is significantly smaller on the A sublattice to which the adatom is adsorbed. If we choose orbital parameters which lead to a larger resonance energy, the width of the resonant peak broadens and the difference in the population of the two sublattices diminishes, as was also observed in Ref. [175].

The situation for the bridge position, for the same parameter choice of $\omega = 0.54\,\mathrm{eV}$ and $\varepsilon = 0.02\,\mathrm{eV}$, is shown in Fig. 4.8(b). The peak in the DOS is now located at $E_{\mathrm{res}}^{\mathrm{tb}} = 83\,\mathrm{meV}$. The LDOS around the adatom resembles the shape of a diamond (see inset in the figure), which is built of two intertwined triangles with their centers placed on neighboring carbon sites of the A and B sublattice. Naively thinking of the bridge adatom as two neighboring top adatoms or a double substitutional impurity [183], this distribution looks natural. The amplitude of the LDOS is decreased on the hybridization partners of the bridge adatom due to the adatom mediated effective coupling between them [see Eq. (4.8)]. Extracting the decay of the LDOS on the B sublattice along the direction of 90° and the LDOS decay on the A sublattice along 330°, we find again clear power-law decay, $|\psi|^2 \propto r^{-p}$, with $p \approx 2.09$ and $p \approx 1.45$, respectively.

Similarly to the bridge adatom, a hollow adatom does not distinguish the sublattices for equivalent directions. This is clearly visible in the six-fold rotational symmetry of the LDOS distribution displayed in Fig. 4.8(c). We change now the orbital parameters to $\omega = 0.3\,\mathrm{eV}$ and $\varepsilon = 0.02\,\mathrm{eV}$ which results in a resonance peak at $E_{\mathrm{res}}^{\mathrm{tb}} = 99\,\mathrm{meV}$ for an orbital with $m_z = 0$ in the hollow position. For this configuration, we find along the 30° direction no clear tendency in the LDOS decay. The LDOS amplitude has the same order of magnitude on the A and B sublattice sites,

while there are hints to an exponential decay, $|\psi|^2 \propto \exp(-qr)$, with $q \approx 0.62$ for the A sites, and to a power-law decay, $|\psi|^2 \propto r^{-p}$, with $p \approx 3.29$ for B. This behavior is in clear contrast to the bridge configuration with a comparable peak energy and we may suspect that it is related to the effective decoupling of the orbital from the graphene states as discussed above. Comparing this hollow case to the top and bridge realizations for even smaller adatom concentrations, we observed that the adatom site loses the LDOS contribution much faster than the top or bridge adatom site. However, if we consider a $m_z = 1$ orbital in the hollow position with the same orbital parameters, see Fig. 4.8(d), the picture changes. At the extracted peak energy of $E_{\text{res}}^{\text{tb}} = 129\,\text{meV}$, we now find that the LDOS distribution on both sublattices can be fitted to a power-law decay with the exponent $p \approx 3.3$. We saw before that for the $m_z = 1$ orbital in the hollow position the destructive interference effects of the $m_z = 0$ case are gone and the effective coupling to the graphene states is restored.

4.5 Adatoms, vacancies, and the model of a strong midgap scatterer

A well studied structural defect in graphene is the vacancy, which describes the missing of one carbon atom in the graphene lattice. This defect was shown to induce a sharp state at zero energy [173, 174, 181, 189, 193] and is therefore understood as the prototype of a strong resonant scatterer. Simple models ignore the probable reconstruction of the defect [203, 204] and treat the vacancy either explicitly as a missing carbon atom or, which is equivalent, assign a local potential U to the vacancy site and take the limit $U \to \infty$ [174, 189, 193]. This forces an eigenstate of the system to vanish there, just as if the site was removed from the lattice.

Top positioned adatoms which act as strong resonant scatterers in graphene are often compared to a vacancy. The connection is apparent in our graphene-only model description as by the down-folding process the top adatom induces an effective on-site potential $|\omega|^2/(E-\varepsilon)$ on the adsorption site, see Eq. (4.8). Taking the limit $|\omega|^2/(E-\varepsilon) \to \infty$ removes the adsorption site from the graphene states as done in the vacancy models. The T-matrix expression of Eq. (4.20) reduces in this limit, representing an ideal vacancy, to [177, 189]

$$\mathcal{T}_{vac} = -\frac{1}{G_{00}(E)} \, |Y\rangle \langle Y| \, . \tag{4.32}$$

The sharp resonance peak at zero energy arising from the vacancy state according to Eq. (4.32) is visible in both the DOS and τ_{m}^{-1} graphs shown in Fig. 4.9(a). We note that the peak is fully symmetric with respect to positive and negative energies which does not hold for resonance peaks originating from general adatoms in the

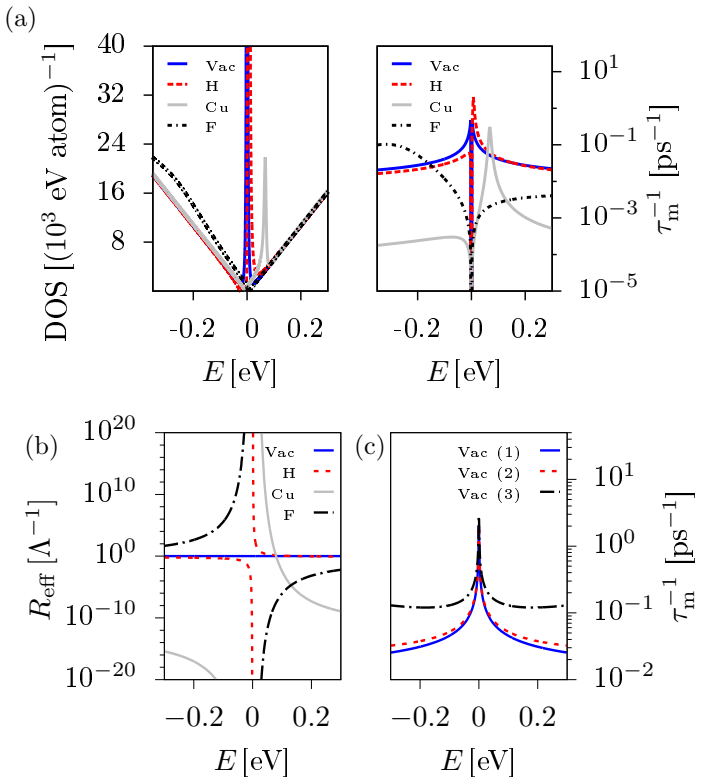

Figure 4.9: Signatures of top adatoms in the DOS and τ_{m}^{-1} in comparison to the model of a vacancy and the strong midgap scatterer. (a) DOS and τ_{m}^{-1} for a vacancy (Vac) and selected adatoms in the top position, i.e., hydrogen adatom (H) with $\omega = 7.5\,\mathrm{eV}$, $\varepsilon = 0.16\,\mathrm{eV}$, copper adatom (Cu) with $\omega = 0.81\,\mathrm{eV}$ $\varepsilon = 0.08\,\mathrm{eV}$ and fluorine (F) with $\omega = 5.5\,\mathrm{eV}$, $\varepsilon = -2.2\,\mathrm{eV}$. An adatom concentration of $\eta = 10^3$ ppm is used in the DOS, τ_{m}^{-1} data are shown for $\eta = 1$ ppm. Fluorine in the top position induces a broad resonance, $\Gamma = 277\,\mathrm{meV}$, at about $E_{\mathrm{res}} = -262\,\mathrm{meV}$, which induces a small shoulder in the DOS and τ_{m}^{-1} at negative energies. More pronounced features at lower energies are visible for copper and hydrogen. Copper induces a resonance level at $E_{\mathrm{res}} = 68\,\mathrm{meV}$ with $\Gamma = 9\,\mathrm{meV}$, hydrogen yields $E_{\mathrm{res}} = 7\,\mathrm{meV}$ with $\Gamma = 5\,\mathrm{meV}$. The signatures of hydrogen are comparable to the ones of a vacancy at zero energy, yielding graphs that are fully symmetric with respect to negative and positive energies. (b) Energy dependence of the effective impurity radius R_{eff} for a vacancy as well as hydrogen, copper, and fluorine adatoms. (c) τ_{m}^{-1} for a vacancy under different approximations to Eq. (4.35). Neglecting the imaginary part of G_{00}, graph (2), increases τ_{m}^{-1} slightly compared to the exact result, graph (1). Artificially increasing $R_{\mathrm{eff}} = 4.5\Lambda^{-1}$, enhances τ_{m}^{-1} significantly, graph (3).

top position such as fluorine and copper shown along with the vacancy result. The closer the resonance level of the adatom appears to the zero energy, the smaller the asymmetry is. Hydrogen, shown in the figure as well, induces a peak at 7 meV ($\Gamma = 5$ meV) and therefore looks very similar to a vacancy. The same observation would hold for the methyl group on graphene, of the previous chapter, which induces a resonance peak at $E_{\text{res}} = -7.9$ meV and a width of $\Gamma = 6$ meV. We further see that the τ_{m}^{-1} graph for the copper adatom lies for most energies below the graphs for the hydrogen and fluorine adatoms. This reflects the weak bond established between copper and graphene as found in Sec. 3.6 of the previous chapter.

We obtain the conductivity for graphene with adatoms in the top position from the Boltzmann formalism in the relaxation time approximation[11] taking into account the spin- and valley-degeneracy. In the low energy approximation, we obtain from the T-matrix the momentum relaxation rate (see Sec. 4.2.2),

$$\tau_{\text{m}}^{-1}(E) = \frac{2\pi}{\hbar}\,\eta\,\frac{|E|}{W^2}\left|\frac{|\omega|^2}{E-\varepsilon-|\omega|^2 G_{00}(E)}\right|^2 . \tag{4.33}$$

Inserting the analytic expression for the on-site Green's function G_{00} from Eq. (4.19),

$$\begin{aligned} G_{00}(E) &= \frac{E}{W^2}\ln\left|\frac{E^2}{W^2-E^2}\right| - i\pi\frac{|E|}{W^2}\Theta(W-|E|) \\ &\approx \frac{2E}{W^2}\ln\left(\frac{|E|}{W}\right) - i\pi\frac{|E|}{W^2}\Theta(W-|E|)\,, \end{aligned} \tag{4.34}$$

with the cut-off energy $W = \hbar v_F \Lambda$, into τ_{m}^{-1} one obtains the formula for the Boltzmann conductivity,

$$\begin{aligned} \sigma &= \frac{e^2}{h}\,\frac{2|E|\tau_{\text{m}}}{\hbar} \\ &= \frac{e^2}{h}\,\frac{4}{\pi\eta}\,\frac{E^2}{W^2}\left[\ln^2\left(\frac{|E|}{\hbar v_F}R_{\text{eff}}\right)+\frac{\pi^2}{4}\right], \end{aligned} \tag{4.35}$$

where we have introduced $R_{\text{eff}}(E)$ as

$$R_{\text{eff}}(E) = \Lambda^{-1}\exp\left[-\frac{1}{2}\frac{W^2}{|\omega|^2}\frac{(E-\varepsilon)}{E}\right]. \tag{4.36}$$

The quantity $R_{\text{eff}}(E)$ has the dimension of length and could be, therefore, interpreted as an effective radius of the top positioned scatterer. However, this effective radius is energy dependent and diverges at zero energy. If we consider, in contrast, a vacancy on graphene, i.e., if we use Eq. (4.32) in the derivation, we arrive at Eq. (4.35) with a constant effective radius $R_{\text{eff}}^{\text{Vac}} = \Lambda^{-1} \approx 0.9$ Å. Figure 4.9(b) shows

[11] For details on the Boltzmann formalism in general and for graphene see for example Ref. [85].

the energy dependence of the effective radius for the adatoms hydrogen, copper, and fluorine in comparison to the one for a vacancy. We note that the R_{eff} curves incorporate the asymmetry between negative and positive energies for the adatoms mentioned above.

In the broad literature on resonant scattering, vacancies, and adsorbates, one eventually comes across the SMS model [2, 176, 177]. In this description, the defect is treated as a potential disk with some finite (constant) radius R. From partial wave decomposition the cross-section and, finally, the conductivity are obtained [2, 176, 177, 189],

$$\begin{aligned}\sigma_{\text{SMS}} &= \frac{e^2}{h}\,\frac{2\,k_F^2}{\pi^2\,n_i}\,\ln^2(k_F R) \\ &= \frac{e^2}{h}\,\frac{2}{\pi}\,\frac{2}{n_i\,A_{\text{uc}}}\,\frac{E^2}{W^2}\ln^2\left(\frac{|E|}{\hbar v_F}R\right)\,. \end{aligned} \tag{4.37}$$

Here, n_i denotes the impurity concentration per unit area [177], $A_{\text{uc}} = 3(\sqrt{3}/2)a_{cc}^2$ is the unit cell area, and k_F represents the Fermi wave vector measured from the Dirac point. The two concentration measures n_i and η are related by $\eta = n_i A_{\text{uc}}/2$. We obtain $\sigma = 2\sigma_{\text{SMS}}$ by setting $R_{\text{eff}}(E) = R = \text{const}$ and neglecting the term $\pi^2/4$, which originates from the imaginary part of G_{00}, in our Boltzmann conductivity formula Eq. (4.35) for a general adsorbate in top position. Also Ref. [98] reports the additional factor of two.

Apart the neglected factors, the formula σ_{SMS} reflects our Boltzmann conductivity for a vacancy, Eq. (4.35), with $R_{\text{eff}} = R_{\text{eff}}^{\text{Vac}} = \text{const}$. The effective radius is in this case fixed to the inverse of the momentum cut-off, which guaranteed the conservation of states in the calculation of the on-site Green's function. The authors of Ref. [177] mention that "R has to be of the order of ~ 1 Å" in accordance with $R_{\text{eff}}^{\text{Vac}} = \Lambda^{-1} = 0.9$ Å. Experimental conductivity data is, however, often analyzed employing σ_{SMS} where both n_i and R are treated as fitting parameters [134, 190, 191] and R reaches values of few angstroms.

Figure 4.9(c) shows the momentum relaxation rate for a vacancy under different approximations to Eq. (4.35). Neglecting the term $\pi^2/4$ increases τ_{m}^{-1} only slightly, by about 20% at $E = 200$ meV. A more severe effect is obtained from artificially enhancing the effective vacancy radius to $R = 4.5\,\Lambda^{-1} \approx 4.1$ Å by which τ_{m}^{-1} for a vacancy is overestimated by a factor of four at $E = 200$ meV. The momentum relaxation rate is proportional to the impurity concentration n_i so that a simultaneous fit of n_i and $R > \Lambda^{-1}$ leads to an underestimation of n_i, or equivalently, to an overestimation of the impact of the impurities.

The SMS model was not designed to capture the effects of general adatoms with resonance energies significantly away from zero energy. We have also seen in the previous sections of this chapter that both the orbital adatom parameters and the adsorption position strongly influence the resonance levels. Fluorine, for example,

induces a resonance peak far off at negative energies, $E_{\mathrm{res}} = -262\,\mathrm{meV}$, which is at the same time very broad, $\Gamma = 277\,\mathrm{meV}$. Therefore, a notable asymmetry with respect to positive and negative energies appears in the momentum relaxation rate, see Fig. 4.9(a). Furthermore, the SMS model gives in general higher τ_{m}^{-1} magnitudes than it is the case for adsorbates, which can be understood as a consequence of several approximations in the calculation of G_{00}. From these observations, we see that single (or a dilute concentration of) fluorine adatoms on graphene are not sufficiently described by the SMS or vacancy model. The analysis of experimental data is further complexified since additionally to the suspected impurity type also charged impurities [180] or clusters of adsorbates [198, 199] can be present in the sample which are predicted to yield symmetric contributions to the conductivity similar as in the SMS model. An analysis of experimental data based on Eq. (4.37) should be, therefore, done very carefully keeping in mind its restrictions.

4.6 Concluding remarks

In this chapter, we have addressed the orbital resonance characteristics of adatoms on graphene for different adsorption positions by a scan of the parameter space (ω, ε) which models different adatoms. The DOS and the momentum relaxation rates were used for the analysis of the resonance levels. In the following, the main findings are shortly summarized.

For an adatom in the top position, the resonance level appears the closer to the zero energy the stronger is the adatom's bond to graphene (larger ω) or the smaller is its on-site energy. Furthermore, we saw that the resonance energy follows the relation $E_{\mathrm{res}}(\omega, \varepsilon) = -E_{\mathrm{res}}(\omega, -\varepsilon)$. The resonance peaks in the DOS broaden with increased resonance energy and electron-hole asymmetry gradually develops in the momentum relaxation rates.

In the bridge position, the resonance levels are more sensitive to the variation of the orbital adatom parameters compared to the top case. Negative on-site energies dominate the parameter region leading to a formation of resonance levels in the same energy interval as in the top position. Due to an effective coupling between the adatom's two hybridization partners, an enhanced ω shifts the resonance levels to even higher energies, which is in contrast to the observation for the top configuration.

An adatom with s or p_z orbital character in the hollow position is effectively decoupled from the states of graphene. The resonance peaks are very narrow and more δ-like and move quickly out of the investigated energy interval under the variation of the parameter pair (ω, ε). The momentum relaxation rates are significantly lower compared to adatoms in the top or bridge positions. While we observe for the top and bridge configuration a power-law decay of the resonant state around the impurity, no clear tendency appears for this hollow configuration. However, con-

sidering an adatom with an orbital of higher magnetic quantum number changes the situation significantly and the coupling of the adatom in the hollow position to the states of graphene is restored.

In the last section, we compared general adatoms in the top position to the case of a vacancy and the SMS model of Refs. [2, 176, 177]. Adatoms like hydrogen, which are strong resonant scatterers in graphene and induce resonance levels close to the zero energy, are closest resembled by vacancies as they approximately give rise to electron-hole symmetric momentum relaxation rates. We stressed that the SMS model does not sufficiently well describe adatoms with resonance energies significantly different from the zero energy and might even for strong resonant scatterer overestimate the impact of the impurity on the conductivity. The analysis of experimental data on adsorbates on graphene needs to be done carefully and should consider the particular limits of the different models. We will meet this issue again in the next chapter when we have a look on a spin relaxation experiment with fluorinated graphene samples.

5 Spin relaxation in bilayer graphene: Resonant scattering off magnetic moments

This chapter is based on the publication "Resonant scattering by magnetic impurities as a model for spin relaxation in bilayer graphene", PRL 115, 196601 (2015), by Denis Kochan, Susanne Irmer, Martin Gmitra, and Jaroslav Fabian. I contributed to this work with TB simulations. The second part of this chapter presents unpublished and ongoing work on spin relaxation in fluorinated single and bilayer graphene, which was done by Susanne Irmer, Denis Kochan, Martin Gmitra, and Jaroslav Fabian in collaboration with the experimental group of Jun Zhu at Penn State University. Therein, all presented experimental data are courtesy of the group of Jun Zhu and the DFT calculations were performed by Martin Gmitra. I was involved in both the TB simulations as well as the modeling of the experimental results.

5.1 Spin relaxation in graphene

Due to its small SOC [21] and negligible hyperfine interaction[1], graphene initially encouraged the hope for spintronics devices with long spin diffusion lengths and long spin relaxation times τ_s up to $1\,\mu$s [32, 206]. However the first experimental measurement of τ_s by Tombros *et al.* [23] yielded about $\tau_s \approx 100\,$ps, a value known from conventional metals and semiconductors [207]. Following experiments estimated values of the spin relaxation time ranging from 100 ps to few ns (see Refs. [25, 31] and references therein).

Additional to this discrepancy between theoretical prediction and experimental observation, the non-unique dependence of τ_s on the mobility or charge carrier density in the experiments provide another puzzle about the underlying spin relaxation mechanism. While some groups [27, 208] found results in agreement with the

[1] It was even shown experimentally by Wojtaszek *et al.* [205] in isotopically engineered ^{13}C graphene, hosting a high density of nuclear moments, that hyperfine interaction plays only a minor role in the spin dephasing in graphene.

Elliot-Yafet spin relaxation mechanism in SL and the Dyakonov-Perel mechanism[2] in BL graphene, other studies attributed the mechanisms to SL and BL devices in exactly the opposite way [209, 210] or could not find a clear signature of either of them [25]. Since the experiments differ from another, for example, by different sample fabrication, substrates, and contacts, the source of the observed spin relaxation in graphene experiments seems to be of extrinsic nature.

As a consequence, a joint force of theory and experiment was (and is) required to hunt down the underlying spin relaxation mechanism in the specific experimental studies. Substrates such as SiO_2, as used in Ref. [23], were shown to reduce the mobility in graphene samples [211]. Therefore, the attention was brought to the influence of charged impurities trapped in the substrate, as well as the substrate's roughness, surface phonons [32] and random SOC fields [212]. Turning, on the one hand, to suspended graphene [213] or graphene on (or encapsulated by) hBN [25, 30, 33] increases significantly the mobility of the samples, though, on the other hand, the spin relaxation times are comparable to the ones of samples with lower mobilities and remain quite off the first theoretical predictions. It was concluded that neither the surface roughness of the substrate [31] nor the trapped charged impurities represent the limiting factor to the observed τ_s values [25, 31], which was further confirmed in an experiment with tunable mobility by Han *et al.* [214]. Neither could be the discrepancy between theory and experiment fully explained by the influence of invasive contacts [33, 215], also if spin adsorption in the electrodes [216] was taken into account. Other studies focused on ripples, corrugations and strain, which are predicted to cause effective gauge fields, and lead, in combination with SOC, to relaxation of the electrons' spin [206, 217]. Over the time, possible contaminants on the graphene samples crystallized as potential culprits limiting τ_s.

We saw in Ch. 3 that local adsorbates on graphene such as hydrogen [21] or the methyl group [99] enhance graphene's SOC locally up to strengths on the order of 1 meV. A dilute concentration of about 1 to 10 ppm of these contaminants is likely present in most of the graphene samples, yet theoretical studies showed that such single adsorbates lead to $\tau_s \geq 100$ ns [170], and about 1000 ppm of hydrogen atoms would be needed to reach the experimental spin relaxation times [133]. On the other hand, the entanglement of spin and pseudospin due to a random SOC field caused, for example, by the heavier adatom gold with large SOC of about 50 meV, was considered as an important ingredient to spin relaxation [218]. Still, a concentration of randomly placed adatoms of 500 ppm was necessary to reach τ_s values of 200 ps. SOC from local adsorbates thus does not seem to play the leading part in the spin relaxation of clean graphene samples, and it was early realized that local magnetic moments are a significant source for dephasing. Indeed, they appear to be the dominant mechanism for spin relaxation [23, 27, 62, 166, 169].

[2]The Elliot-Yafet mechanism was initially derived for metals, while the Dyakonov-Perel mechanism is known for semiconductors with a large band gap [207].

Local magnetic moments can arise in graphene due to vacancies [219, 220], sp^3 defects such as hydrogen [115, 221, 222], molecular doping [99, 148], and graphene edges [223], and were also found to form after annealing of graphene samples [224]. Magnetic moments are experimentally detected in different ways. On the one hand, there are direct measurements of the magnetization via SQUID devices [137] and magnetic force microscopy [225]. On the other hand, magnetic moments influence also STM experiments [219, 220] and their signatures are found in the spin transport of spin valve samples [115]. Furthermore, transport experiments focusing on the aspect of quantum interference are helpful, as spin-flip scattering off magnetic moments influences both the universal conductance fluctuations and the low-field magnetoresistance [169]. In the latter, a fit of the magnetoresistance curves to the theory of weak localization (WL) [226, 227] allows to extract the phase coherence time and to analyze its dependence on the temperature. The presence of magnetic moments is usually attributed to a saturation of this time [134, 228, 229], although other mechanisms may lead to this behavior [169, 229, 230]. Recently, there appeared experimental studies [167, 231] on the anisotropy of spin relaxation in graphene which confirmed the presence of magnetic moments in their samples. Magnetic moments were further detected in the spin-dependent 1/f noise in graphene [168].

In this chapter, we focus on a spin relaxation mechanism for graphene which is based on resonant scattering off local magnetic moments in a dilute concentration. In contrast to a first study of Huertas-Hernando *et al.* [217], which considered localized magnetic moments at the graphene edges and found a spin relaxation time of 0.1 μs, we focus here on adsorbates that both induce local magnetic moments and are resonant scatterers in graphene, see Ch. 4. Due to their resonant feature, only a small fraction of about 1 ppm of local magnetic moments is needed to reproduce the experimental values of 100 ps [26, 27, 62, 165, 166]. The basic model was derived earlier for SL graphene [62] and we concentrate here on its extension to BL structures. The underlying idea is simple but very effective: The local magnetic moment gives rise to a local spin-flip field. As an electron scatters resonantly off the impurity site, its spin precesses around the impurity spin. As long as the resonance lifetime is long enough, the spin-flip probability for the electron reaches 50% and the electron spin is randomized on exiting the scattering region. The spin-flip time determines the spin relaxation time.

The model offers furthermore an answer to the puzzle of the different dependence of the spin relaxation rate on the carrier density in SL and BL graphene devices, as it considers the influence of electron-hole puddles on the relaxation rates. Although the magnitude of these fluctuations in the charge density are found to be very similar in SL and BL graphene (see for example Refs. [232, 233]), they induce a different Fermi level smearing due to the peculiarities of the DOS in both structures. As the smearing is more pronounced in the SL system, subtleties still observable in the τ_s to carrier density dependence in BL graphene are hidden in the SL counterpart.

While in SL graphene with a small concentration of hydrogen adatoms, the model predicts a continuous increase of τ_s with the carrier density, τ_s first decreases in BL graphene and increases after crossing a certain carrier density. Signatures of these tendencies were found in both SL [165] and BL [26, 27, 234] experiments.

In Sec. 5.2 we introduce the model in more detail and present resulting spin relaxation rates for hydrogenated SL and BL graphene. Based on this approach, we study in Sec. 5.3 fluorinated SL and BL graphene and the corresponding measurements of the group of Jun Zhu [134, 235]. In this second part, we try to answer whether fluorine induces local magnetic moments in graphene since there is no conclusive result found in DFT studies so far [148, 157]. We summarize and discuss observed agreements and disagreements with the experimental results in Sec. 5.4.

5.2 Spin relaxation by resonant scattering off magnetic moments

5.2.1 Adatom model with exchange

Tight-binding model for single and bilayer graphene

We consider an adatom binding in the top position to either single layer (SL) or AB-stacked (Bernal stacked) bilayer graphene (BL) where we account for a non-itinerant magnetic moment at the adatom site (spin-1/2 impurity) by an exchange coupling J [62, 166]. The full TB Hamiltonian is given by

$$H = \mathcal{H}_0 + \mathcal{H}_{\mathrm{orb}}^{\mathrm{ad}} + \mathcal{H}_{\mathrm{ex}} \,. \tag{5.1}$$

The term $\mathcal{H}_0$ describes the electronic structure of the π orbitals of either unperturbed SL graphene, $\mathcal{H}_0^{\mathrm{SL}}$, or BL graphene, $\mathcal{H}_0^{\mathrm{BL}}$. For the SL configuration, we employ the nearest neighbor approximation with $t_0 \equiv t = 2.6\,\mathrm{eV}$ so that[3]

$$\mathcal{H}_0^{\mathrm{SL}} = -t_0 \sum_{\langle l,m \rangle} |X_l\rangle \langle X_m| + \mathrm{H.c.}\,, \tag{5.2}$$

and for the BL configuration, we have[4]

$$\mathcal{H}_0^{\mathrm{BL}} = -t_0 \sum_{\langle l,m \rangle} \sum_{\beta \in \{\mathrm{t,b}\}} |X_l^\beta\rangle \langle X_m^\beta| + t_1 \sum_l |A_l^{\mathrm{t}}\rangle \langle B_l^{\mathrm{b}}| + \mathrm{H.c.}\,, \tag{5.3}$$

[3] For simplicity, we omit the electron spin σ in all parts of H, Eq. (5.1), which are diagonal in the electron spin space.

[4] More general forms of Eq. (5.3) can be found in the literature, e.g., in Refs. [10, 92, 236, 237] where additional interlayer couplings or potential offsets are employed.

where the symbol $\beta \in \{\mathrm{t}, \mathrm{b}\}$ specifies whether the corresponding site $X \in \{A, B\}$ lies in the top (t) or bottom (b) layer. In our convention for the AB-stacked bilayer graphene, an A^{t} site lies directly above a B^{b} site and those two sites are connected by the interlayer hopping $t_1 = 0.34\,\mathrm{eV}$. We refer to carbon sites coupled by t_1 as dimer sites, whereas the lattice positions A^{b} and B^{t} are called non-dimer carbon atoms since they have no partner directly above or below in the other layer [10].

As in the previous chapters, the hybridization of the impurity in the top position to graphene is described by $\mathcal{H}^{\mathrm{ad}}_{\mathrm{orb}}$,

$$\mathcal{H}^{\mathrm{ad}}_{\mathrm{orb}} = \omega \left(|O\rangle \langle Y| + |Y\rangle \langle O| \right) + \varepsilon \, |O\rangle \langle O| \;, \tag{5.4}$$

with the two orbital parameters which are the hybridization strength ω and the on-site energy ε. In the BL case, the impurity is considered to bind only to the top layer and, where needed, we explicitly distinguish whether the adsorption takes place on a dimer, Y_{d}, or non-dimer carbon site, Y_{nd}. The two situations are indicated by adding the subscripts d and nd to ω and ε.

The last term in Eq. (5.1),

$$\mathcal{H}_{\mathrm{ex}} = -J \, \hat{\boldsymbol{s}}.\hat{\boldsymbol{S}} \,, \tag{5.5}$$

describes the exchange interaction of strength J between the itinerant electron spin $\sigma \in \{\uparrow, \downarrow\}$ and the localized impurity spin $\Sigma \in \{\Uparrow, \Downarrow\}$. The symbols $\hat{\boldsymbol{s}}$ and $\hat{\boldsymbol{S}}$ refer to the array of Pauli matrices in the corresponding spin space [see Eq. (2.12) for the employed convention]. We assume a constant value for J which is thus not depending on the Fermi energy or chemical potential.

T-matrix in the singlet and triplet basis

In analogy to Ch. 4, we can now proceed to obtain the T-matrix and the relaxation rates. In the present chapter, we explicitly take into account the spin degree of freedom since we are interested in the spin-flip scattering due to the interaction of the electron spin with the local magnetic moment.

In the singlet ($\ell = 0$) and triplet ($\ell = 1$) spinor basis $|\ell, \mu_\ell\rangle$ ($\mu_\ell = -\ell, ..., \ell$),

$$\begin{aligned}
|0, 0\rangle &= \frac{1}{\sqrt{2}} \left(|\uparrow\rangle \, |\Downarrow\rangle - |\downarrow\rangle \, |\Uparrow\rangle \right) \quad \text{(singlet)} \\
|1, +1\rangle &= |\uparrow\rangle \, |\Uparrow\rangle \\
|1, \;\; 0\rangle &= \frac{1}{\sqrt{2}} \left(|\uparrow\rangle \, |\Downarrow\rangle + |\downarrow\rangle \, |\Uparrow\rangle \right) \quad \text{(triplet)} \\
|1, -1\rangle &= |\downarrow\rangle \, |\Downarrow\rangle \;,
\end{aligned} \tag{5.6}$$

the exchange term, Eq. (5.5), obtains the convenient form [196]

$$\mathcal{H}_{\mathrm{ex}} = -J \sum_{\ell=0}^{1} \sum_{\mu_\ell=-\ell}^{\ell} (4\ell - 3) \, |O, \ell \, \mu_\ell\rangle \langle O, \ell \, \mu_\ell| \;, \tag{5.7}$$

in the new one-particle basis $|O,\ell\,\mu_\ell\rangle = |O\rangle\otimes|\ell,\mu_\ell\rangle$, $|X_l,\ell\,\mu_\ell\rangle = |X_l\rangle\otimes|\ell,\mu_\ell\rangle$. The orbital contributions of $\mathcal{H}_0$ and $\mathcal{H}_{\rm orb}^{\rm ad}$ are diagonal in the $|\sigma\rangle\otimes|\Sigma\rangle$ spin space and, therefore, remain unchanged under the transformation to the singlet-triplet basis.

Following the down-folding procedure of Sec. 4.2.1, we obtain the (SL or BL) graphene-only Hamiltonian composed of $\mathcal{H}_0$ and the energy-dependent perturbation[5] [62, 166, 196]

$$\mathcal{V}(E) = \sum_{\ell,\mu_\ell} \mathcal{V}_\ell(E)\,|Y,\ell\,\mu_\ell\rangle\,\langle Y,\ell\,\mu_\ell| = \sum_{\ell,\mu_\ell} \frac{|\omega|^2}{E-\varepsilon+(4\ell-3)J}\,|Y,\ell\,\mu_\ell\rangle\,\langle Y,\ell\,\mu_\ell|\ . \tag{5.8}$$

Correspondingly, the T-matrix reads

$$\mathcal{T}(E) = \sum_{\ell,\mu_\ell} \mathcal{T}_\ell(E)\,|Y,\ell\,\mu_\ell\rangle\,\langle Y,\ell\,\mu_\ell| = \sum_{\ell,\mu_\ell} \frac{\mathcal{V}_\ell}{E-\mathcal{V}_\ell\,G_{\rm C}(E)}\,|Y,\ell\,\mu_\ell\rangle\,\langle Y,\ell\,\mu_\ell|\ , \tag{5.9}$$

with the (retarded) on-site Green's function $G_{\rm C}(E) = \lim_{\delta\to 0}\langle Y|(E+i\delta-\mathcal{H}_0)^{-1}|Y\rangle$ of unperturbed (SL or BL) graphene.

Green's function $G_{\rm C}(E)$ for BL graphene and DOS

To obtain the real-space representation of the on-site Green's function for BL graphene, we first transform the BL Hamiltonian $\mathcal{H}_0$ to the four dimensional Bloch basis[6] $\{|A_{\boldsymbol{q}}^{\rm t}\rangle, |B_{\boldsymbol{q}}^{t}\rangle, |A_{\boldsymbol{q}}^{\rm b}\rangle, |B_{\boldsymbol{q}}^{b}\rangle\}$,

$$\mathcal{H}_0(\boldsymbol{q}) = -t_0 \sum_{\beta\in\{\rm t,b\}} \left(\tilde{f}_{\rm orb}(\boldsymbol{q})\ |A_{\boldsymbol{q}}^{\beta}\rangle\,\langle B_{\boldsymbol{q}}^{\beta}| + \text{H.c.}\right) + t_1(|A_{\boldsymbol{q}}^{\rm t}\rangle\,\langle B_{\boldsymbol{q}}^{\rm b}| + \text{H.c.})\,. \tag{5.10}$$

Here, $\tilde{f}_{\rm orb}(\boldsymbol{q}) = \exp(i\boldsymbol{q}.\boldsymbol{\delta}_1)+\exp(i\boldsymbol{q}.\boldsymbol{\delta}_2)+\exp(i\boldsymbol{q}.\boldsymbol{\delta}_3)$ is the orbital structural function of Eq. (4.12) and $\boldsymbol{\delta}_m$ are the vectors connecting nearest carbon neighbors in the same layer.

The diagonalization of Eq. (5.10) yields four spin-degenerate eigenenergies given by

$$\epsilon_n^\alpha(\boldsymbol{q}) = \frac{n}{2}(\alpha t_1 + \sqrt{t_1^2 + 4\,t_0^2\,|\tilde{f}_{\rm orb}(\boldsymbol{q})|^2})\,, \tag{5.11}$$

where the symbol $n=\pm1$ labels the conduction and valence branch of the spectrum and $\alpha=\pm1$ addresses the high and low energy bands[7], respectively. Note that by

[5] In the following, we will omit the limits for the ℓ and μ_ℓ summations. Symbol ℓ can take the values 0 and 1, μ_ℓ lies in the interval from $-\ell$ to ℓ.

[6] Here, we follow the convention of Eq. (4.11) of the Bloch transform for SL graphene. It is important to note that there are twice as many carbon atoms in the BL graphene unit cell than in the one for SL graphene, which requires an additional factor of $1/\sqrt{2}$ in Eq. (4.11).

[7] To be explicit, the low energy bands are given by the lowest conduction and highest valence bands whereas the high energy bands are built from the highest conduction and lowest valence bands in the spectrum.

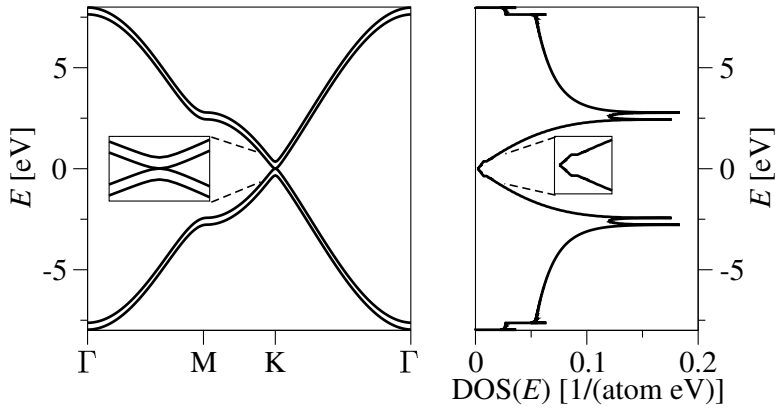

Figure 5.1: (a) Electronic band structure of AB-stacked BL graphene with the TB parameters $t_0 = 2.6\,\mathrm{eV}$ and $t_1 = 0.34\,\mathrm{eV}$. The high energy valence and conduction bands begin to form at $E = \pm t_1$. Around the zero energy, the band structure is approximately parabolic and the valence and conduction bands touch (see inset). (b) Density of states of BL graphene. The DOS remains finite at zero energy (see inset).

setting $t_1 = 0$ we obtain two copies of the SL graphene dispersion given in Eq. (4.13). Figure 5.1 shows the band structure of BL graphene and the corresponding DOS. The separation of the spectrum into low and high energy bands arises due to the finite interlayer coupling t_1. Around the $\boldsymbol{K}$ point, the high energy bands are built from the bonding and anti-bonding states formed by the p_z orbitals on dimer sites, whereas the low energy bands are equivalently formed by the orbitals on nondimer sites [10].

The eigenvectors corresponding to the spectrum in Eq. (5.11) are given by

$$|n\,\alpha\,q\rangle = \frac{\epsilon_n^\alpha(\boldsymbol{q})^2}{2\left(\epsilon_n^\alpha(\boldsymbol{q})^2 + t_0^2|\tilde{f}_{\mathrm{orb}}(\boldsymbol{q})|^2\right)} \left\{ |A_{\boldsymbol{q}}^{\mathrm{t}}\rangle + n\alpha\,|B_{\boldsymbol{q}}^{\mathrm{b}}\rangle \right. \\ \left. -t_0 \left[\frac{\overline{\tilde{f}_{\mathrm{orb}}(\boldsymbol{q})}\,|B_{\boldsymbol{q}}^{\mathrm{t}}\rangle + n\alpha\tilde{f}_{\mathrm{orb}}(\boldsymbol{q})\,|A_{\boldsymbol{q}}^{\mathrm{b}}\rangle}{\epsilon_n^\alpha(\boldsymbol{q})} \right] \right\} . \quad (5.12)$$

The on-site Green's function, projected to a dimer ($C = \mathrm{d}$) or nondimer site ($C = \mathrm{nd}$), is calculated from

$$G_C(E) = \lim_{\delta\to 0} \sum_{n,\alpha,\boldsymbol{q}} \langle C|n\,\alpha\,q\rangle \left\langle n\,\alpha\,q|[E^+ - \mathcal{H}_0(\boldsymbol{q})]^{-1}|n\,\alpha\,q\right\rangle \langle n\,\alpha\,q|C\rangle \; . \quad (5.13)$$

which involves an integration over the first Brillouin zone. For simplification, we use the spectrum $\epsilon_n^\alpha(\boldsymbol{q})$ linearized around the two inequivalent corners of the Brillouin zone, $\boldsymbol{q} = \pm\boldsymbol{K} + \boldsymbol{k}$,

$$\epsilon_n^\alpha(\pm\boldsymbol{K} + \boldsymbol{k}) \approx \frac{n}{2}(\alpha t_1 + \sqrt{t_1^2 + 4\,t_0^2\,\hbar^2 v_F^2|\boldsymbol{k}|^2}) \, , \quad (5.14)$$

and separate the Brillouin zone integral into two integrals around the $\pm\boldsymbol{K}$ points using the energy cut-off energy $W = \sqrt{\sqrt{3}\pi t_0}$. One then arrives at $G_C(E) = \Lambda_C(E) - i\pi\lambda_C(E)$ with

$$\Lambda_C(E) = \frac{E}{2W^2} \ln\left|\frac{E^2(E^2 - t_1^2)}{(W^2 - E^2)^2}\right| + \frac{t_1\Delta_C}{2W^2} \ln\left|\frac{E + t_1}{E - t_1}\right|, \tag{5.15}$$

$$\lambda_C(E) = \sum_{\alpha=\pm} \frac{|E| - \alpha\Delta_C t_1}{2W^2}\, \Theta\big(W - |E|\big)\Theta\big(|E| - \alpha t_1\big), \tag{5.16}$$

where $\Delta_C = 0$ if the on-site Green's function is evaluated for a dimer site, and $\Delta_C = 1$ if it is calculated for a nondimer site. By setting $t_1 = 0$ we obtain the SL case, $G_C(E, t_1 = 0) \equiv G_{00}(E)$, see Eq. (4.19).

From the imaginary part of the Green's function $G_C(E)$ we directly obtain the C-site resolved DOS of unperturbed BL graphene per spin, $\nu_0^C(E)$, [166]

$$\begin{aligned}\nu_0^C(E) &= \sum_{\alpha=\pm} \frac{|E| - \alpha\Delta_C t_1}{2W^2}\, \Theta\big(W - |E|\big)\Theta\big(|E| - \alpha t_1\big) \\ &= \sum_{\alpha=\pm} P_C^\alpha(E)\nu_0^\alpha(E)\,.\end{aligned} \tag{5.17}$$

In the last line, we rewrote the expression for $\nu_0^C(E)$ by introducing the quantities $\nu_0^\alpha(E)$ and $P_C^\alpha(E)$. By taking the average of the C-site resolved DOS contributions for the dimer and nondimer sites, we defined the DOS of unperturbed BL graphene per atom and spin of the band α,

$$\nu_0^\alpha(E) = \frac{2|E| - \alpha t_1}{4W^2}\, \Theta\big(W - |E|\big)\, \Theta\big(|E| - \alpha t_1\big)\,. \tag{5.18}$$

In Eq. (5.17), the contribution of the site C to the low and high energy bands α at a given energy E is then accounted for with the projection factor $P_C^\alpha(E)$,

$$P_C^\alpha(E) = \frac{2(|E| - \alpha\Delta_C t_1)}{2|E| - \alpha t_1}\, \Theta\big(W - |E|\big)\, \Theta(|E| - \alpha t_1)\,. \tag{5.19}$$

In the case of SL graphene, where there is no distinction between dimer and nondimer sites and $t_1 = 0$, we have $\nu_0^+(E) = \nu_0^-(E)$ and $P_C^+(E) = P_C^-(E)$.

Using the expression for the T-matrix, Eq. (5.9), and following the procedure outlined in Sec. 4.2.2, we arrive at the perturbed DOS per atom and spin, $\nu^C(E)$, describing SL or BL graphene in the presence of a magnetic impurity,

$$\nu^C(E) = \sum_{\alpha=\pm} \nu_0^\alpha(E) - \frac{1}{\pi}\frac{\eta}{4} \operatorname{Im} \sum_\ell \left[-\frac{\partial G_C(E)}{\partial E}\right] (2\ell + 1)\, \mathrm{T}_\ell(E)\,. \tag{5.20}$$

As in Ch. 4, the adatom concentration η is defined as the number of adatoms divided by the number of carbon atoms in the structure. The quantity η is related to the areal impurity concentration, n_i, via $\eta^{\mathrm{SL}} = n_i A_{\mathrm{uc}}/2$ for SL graphene and $\eta^{\mathrm{BL}} = n_i A_{\mathrm{uc}}/4$ for BL graphene, where $A_{\mathrm{uc}} = 3(\sqrt{3}/2)a_{cc}^2$ is the area of one graphene unit cell.

5.2.2 Relaxation rates

The scattering rates are obtained from the generalized Fermi's golden rule. Unlike in Ch. 4, we want to investigate the relaxation of the electron spin in SL and BL graphene due to spin-flip scattering at the local magnetic moment. Therefore, the (electron) spin-dependent transition rates are calculated from

$$W_{n\,\alpha\,q\,\sigma|n'\alpha'q'\sigma'} = \frac{2\pi}{\hbar}\frac{1}{2}\,\mathrm{Tr}_\Sigma\Big[\langle n'\alpha'q'\sigma'|\,\mathcal{T}(\varepsilon^\alpha_{nq})\,|n\,\alpha\,q\,\sigma\rangle^\dagger \times \langle n'\alpha'q'\sigma'|\,\mathcal{T}(\varepsilon^\alpha_{nq})\,|n\,\alpha\,q\,\sigma\rangle\Big]\,\delta(\epsilon^\alpha_{nq} - \epsilon^{\alpha'}_{n'q'})\,, \tag{5.21}$$

where $\epsilon^\alpha_{nq} \equiv \epsilon^\alpha_n(\boldsymbol{q})$. In Eq. (5.21) we explicitly trace out the Σ spin degree of freedom of the impurity. Note that an external magnetic field is not considered here, which would polarize the impurity spin. Using the linearized spectrum around the $\boldsymbol{K}^\pm$ points, integrating over all final states and averaging over the Fermi contour for a given energy E, we finally obtain the spin-dependent relaxation rate[8], [62, 166, 196]

$$\frac{1}{\tau^C_{\sigma\sigma'}} = \frac{\eta}{2}\frac{2\pi}{\hbar}\left\{\delta_{\sigma\sigma'}|\mathcal{T}_1(E)|^2 + \frac{1}{4}|\mathcal{T}_1(E) + (\sigma.\sigma')\mathcal{T}_0(E)|^2\right\} \times \frac{\left[P^+_C(E)\nu^+_0(E) + P^-_C(E)\nu^-_0(E)\right]^2}{\nu^+_0(E) + \nu^-_0(E)}\,. \tag{5.22}$$

Here, the spin labels are $\sigma = +1$ for the electron spin $\uparrow$ and $\sigma = -1$ for the electron spin $\downarrow$.

The spin-dependent relaxation rates, Eq. (5.22), enter the definition of the spin relaxation rate $1/\tau^C_{\mathrm{s}}$ and the momentum relaxation rate $1/\tau^C_{\mathrm{m}}$ via

$$\frac{1}{\tau^C_{\mathrm{s}}} = \frac{1}{\tau^C_{\uparrow\downarrow}} + \frac{1}{\tau^C_{\downarrow\uparrow}} \tag{5.23}$$

$$\frac{1}{\tau^C_{\mathrm{m}}} = \frac{1}{\tau^C_{\uparrow\uparrow}} + \frac{1}{\tau^C_{\downarrow\downarrow}}\,, \tag{5.24}$$

which both depend on the adsorption site of the impurity.

[8] In Eq. (5.22), the expression including the T-matrix elements stems from evaluating the trace over Σ, the last factor, containing the C-site projected DOS of BL or SL graphene, ν^C_0, originates from the summation over the final states and the average over the Fermi contour.

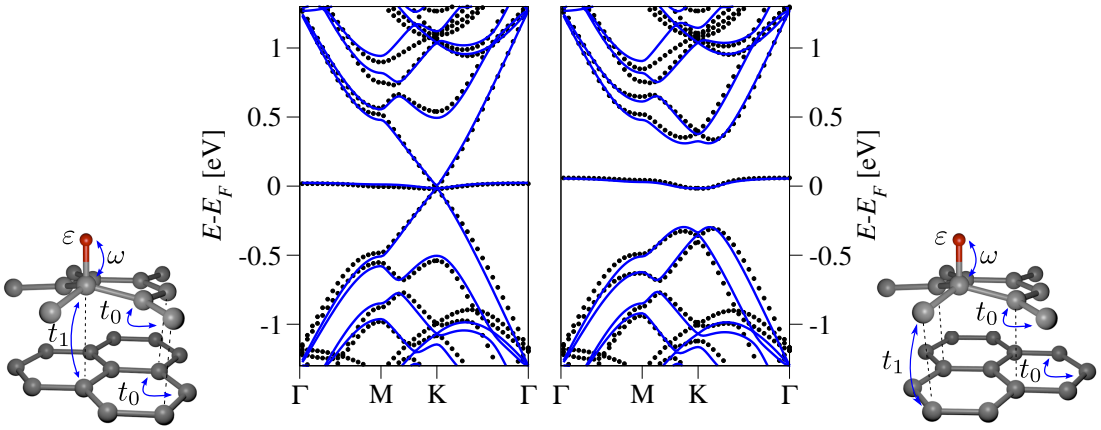

Figure 5.2: Electronic band structure of a 7×7 supercell of BL graphene with one hydrogen adatom in the dimer (left) and nondimer (right) adsorption position on the top layer. Shown are both DFT (black dotted) and TB data (blue solid) with the TB parameters $\omega_\mathrm{d} = 6.5\,\mathrm{eV}$ and $\varepsilon_\mathrm{d} = 0.25\,\mathrm{eV}$ for the dimer configuration, and $\omega_\mathrm{nd} = 5.5\,\mathrm{eV}$, $\varepsilon_\mathrm{nd} = 0.35\,\mathrm{eV}$ for the nondimer configuration.

Example: Hydrogen adatom on bilayer graphene

In the following, we will consider as an example an hydrogen adatom adsorbing on bilayer graphene in the dimer and nondimer position. We find suitable TB parameters ω_d, ε_d, ω_nd, and ε_nd, describing the adatom adsorption, by comparing the TB band structure to spin-unpolarized DFT data [166] for a 7×7 supercell calculation. A least-square fit to the three bands around the Fermi level for each adsorption position did not give a unique result. Out of a larger neighborhood of TB parameters, which yield similar good agreement to the DFT data, we select for hydrogen in the dimer position $\omega_\mathrm{d} = 6.5\,\mathrm{eV}$ and $\varepsilon_\mathrm{d} = 0.25\,\mathrm{eV}$, and for the same adatom in the nondimer position $\omega_\mathrm{nd} = 5.5\,\mathrm{eV}$ and $\varepsilon_\mathrm{nd} = 0.35\,\mathrm{eV}$. Figure 5.2 displays the resulting band structures in comparison to the DFT data.

In both the dimer and nondimer configuration, hydrogen induces a local magnetic moment of $1\,\mu_\mathrm{B}$ [166, 238]. We use an exchange coupling strength of $J = -0.4\,\mathrm{eV}$ to account for the magnetic moment, which agrees with the findings for hydrogen on SL graphene [62] where the TB parameters are given by $\omega = 7.5\,\mathrm{eV}$ and $\varepsilon = 0.16\,\mathrm{eV}$ [52].

Signatures of dimer and nondimer adsorption

Figure 5.3 presents the effect of the exchange parameter J on the DOS of hydrogenated SL and BL graphene. In SL graphene, the narrow resonance peak close to zero energy is split into two broader ones, which correspond to the singlet and triplet states. The same effect is visible in the BL configurations of hydrogen dimer and nondimer adatoms. However, the dimer and nondimer adsorption positions are

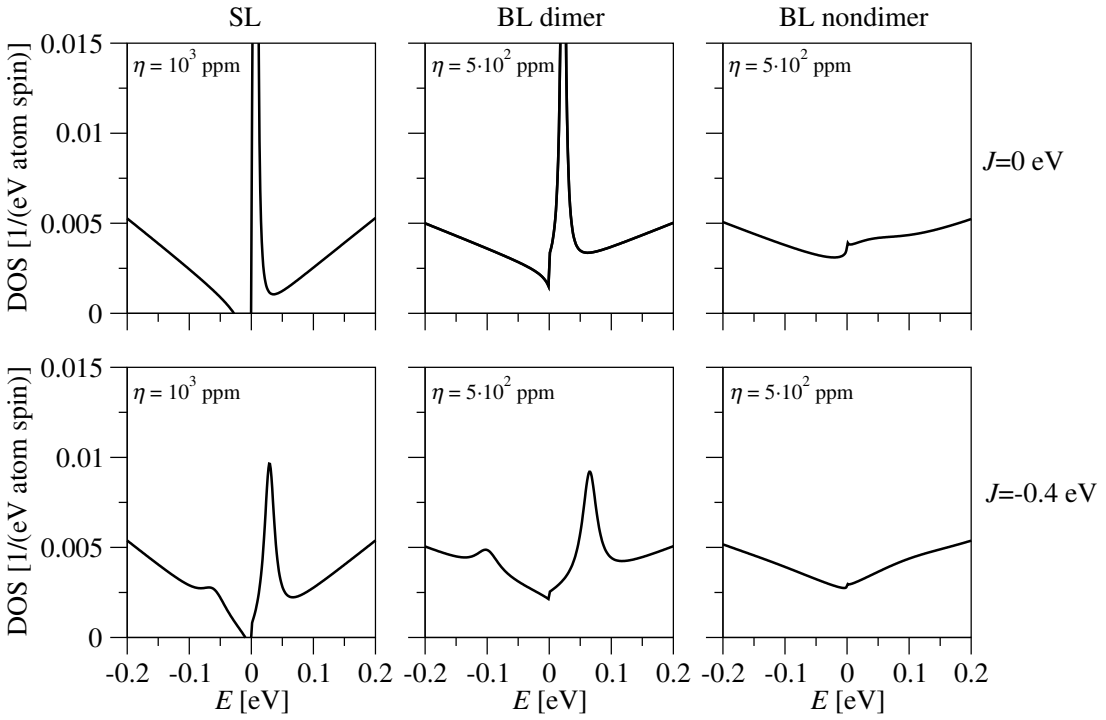

Figure 5.3: Effect of the exchange coupling on the DOS of hydrogenated SL and BL graphene. Hydrogen adsorbing in the top position on SL graphene with $\omega = 7.5\,\mathrm{eV}$, $\varepsilon = 0.16\,\mathrm{eV}$ [52] is shown in the first column. A finite exchange coupling $J = -0.4\,\mathrm{eV}$ (second row) splits the singlet and triplet states, and leads to the formation of two resonance peaks, $E_{\mathrm{res}}^{\ell=0} = -60\,\mathrm{meV}$ with $\Gamma^{\ell=0} = 41\,\mathrm{meV}$ and $E_{\mathrm{res}}^{\ell=1} = 29\,\mathrm{meV}$ with $\Gamma^{\ell=1} = 19\,\mathrm{meV}$. These peaks are broader than the single peak, $E_{\mathrm{res}} = 7\,\mathrm{meV}$ with $\Gamma = 5\,\mathrm{meV}$, in the $J = 0\,\mathrm{eV}$ case. Hydrogen in the dimer position of BL graphene (second column) exhibits similar resonance features as in the SL case. The sharp resonance peak for $J = 0\,\mathrm{eV}$, $E_{\mathrm{res}} = 23\,\mathrm{meV}$ with $\Gamma = 22\,\mathrm{meV}$, is split into two for $J = -0.4\,\mathrm{eV}$, $E_{\mathrm{res}}^{\ell=0} = -100\,\mathrm{meV}$ with $\Gamma^{\ell=0} = 43\,\mathrm{meV}$ and $E_{\mathrm{res}}^{\ell=1} = 65\,\mathrm{meV}$ with $\Gamma^{\ell=1} = 28\,\mathrm{meV}$. The nondimer position (third column), on the contrary, induces a shallow and broad resonance, $E_{\mathrm{res}} = 19\,\mathrm{meV}$ with $\Gamma = 108\,\mathrm{meV}$, so that the singlet-triplet splitting, resulting from setting $J = -0.4\,\mathrm{eV}$, is hidden from the eyes of the observer. An artificially increased adatom concentration of $\eta = 10^3\,\mathrm{ppm}$ and $\eta = 500\,\mathrm{ppm}$ were used in the calculation for the SL and BL cases, respectively.

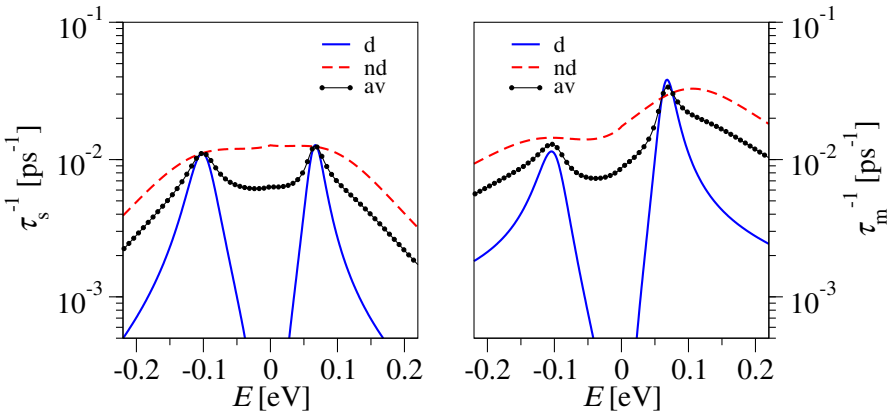

Figure 5.4: Spin and momentum relaxation rates, τ_s^{-1} and τ_m^{-1}, of hydrogenated BL graphene with local magnetic moments. Shown are the relaxation rates for the dimer (blue solid), nondimer (red dashed) configuration and their unbiased average (black dotted). The clear relaxation shoulders in the dimer case, resulting from the singlet-triplet splitting, are blurred for hydrogen in the nondimer position. Both the τ_s^{-1} and τ_m^{-1} values have the same order of magnitude, though the τ_m^{-1} curve appears more asymmetric with respect to the zero energy than τ_s^{-1}. An adatom concentration of $\eta = 0.17\,\text{ppm}$ was used in the calculation of the relaxation rates.

clearly distinct regarding their appearance in the DOS. While the dimer hydrogen adatom leads to a narrow resonance comparable to the SL case, the resonance peak for the nondimer position is significantly broader and more shallow. While the exchange splitting of the dimer resonance is clearly visible, the singlet and triplet peaks for the nondimer configuration overlap and are not distinguishable in the DOS.

It was discussed in Ch. 4 that for SL graphene a strong resonant scatterer, or in the extreme case, a vacancy, induces a resonant state which occupies mainly the sublattice not hosting the impurity. The SL explanation can be directly transferred to our BL situation. Hydrogen in the dimer position induces a resonant state which occupies mainly nondimer sites in the top layer. Hydrogen in the nondimer position, on the other hand, induces a resonant state which occupies mainly dimer sites in the top layer. However, the dimer sites are coupled to the lower layer of the BL structure via t_1 and the resonant state can leak to the layer underneath. In fact, we checked by LDOS calculations for a large supercell with $\eta \approx 0.02\%$ (not shown) that for the nondimer position the resonant state is quasilocalized in the top layer and delocalized in the bottom layer. This observation is also in accordance with the main result of Ref. [239] which studies vacancies in multilayer graphene. The leakage of the nondimer resonant state to the lower layer causes the broad and shallow resonance peak in the DOS.

The expression for the spin-dependent relaxation rate, Eq. (5.22), contains the

perturbed DOS per atom and spin, ν^C, and we therefore expect that also the (spin and momentum) relaxation rates exhibit two peaks originating in the singlet and triplet splitting by $J \neq 0$. Furthermore, the dimer and nondimer relaxation rates will look different in general. Figure 5.4 presents the relaxation rates for hydrogen on BL graphene assuming the orbital parameters and exchange coupling as given above. Following our expectation, the dimer rates exhibit a clear distinction of the singlet and triplet induced peaks as observed in the DOS. Corresponding resonance features in the nondimer curves are less pronounced due to larger broadening of the resonances.

Despite the shallow resonance in the DOS, the nondimer hydrogen adatom induces still a $1/\tau_{\mathrm{s}}^{\mathrm{nd}}$ lying slightly above the dimer rate. For $|E| < t_1 = 0.34\,\mathrm{eV}$, only the term proportional to the projection factor P_C^- survives in the spin-dependent relaxation rate $1/\tau_{\sigma\sigma'}^C$, Eq. (5.22). Since $P_{\mathrm{nd}}^- > P_{\mathrm{d}}^-$, the nondimer rates reach the high values compared to the dimer rates. Equivalently, we can argument that the nondimer adatom strongly perturbs the low energy states since they are built from the carbon nondimer sites. We note that the momentum relaxation rate is of the same order of magnitude as the spin relaxation rates. In Fig. 5.4, also the unbiased average of the dimer and nondimer rates, $\tau_{\mathrm{s/m}}^{-1} \equiv (1/\tau_{\mathrm{s/m}}^{\mathrm{d}} + 1/\tau_{\mathrm{s/m}}^{\mathrm{nd}})/2$, is shown, based on the assumption that in a real sample hydrogen adsorbs equally likely to dimer and nondimer carbon atoms.

Effect of electron-hole puddles

Graphene samples exhibit electron-hole puddles which are fluctuations in the Fermi level around its average value, or, equivalently, fluctuations in the local carrier density. Throughout the years, charged impurities in the environment of the graphene sample (e.g. the substrate) were identified as the main contributors to the spatial inhomogeneity of the carrier density [180, 240, 241] while subdominant contributions might stem from ripples and short-range scatterers in graphene [242, 243]. Close to the charge neutrality point, where in perfect SL graphene the carrier density vanishes and in BL graphene it acquires a finite but its smallest value, the fluctuations dominantly affect the physics. The most prominent example is the experimentally observed minimum conductivity at the charge neutrality point in SL graphene. The random network of electron and hole conducting puddles present in the realistic graphene sample gives rise to a finite conductivity [241, 244, 245].

While transport measurements yield an indirect proof of the presence of the electron-hole puddles, direct experimental observation can be achieved by scanning tunneling microscopy (STM) [232, 246, 247], Kelvin probe microscopy [248], or scanning single electron transistor (SET) measurements [211]. Depending on the spatial and energetic resolution of the different approaches[9], surveys of SL graphene

[9]Ref. [232] points out that the smaller spatial resolution of the SET measurements ($\sim 150\,\mathrm{nm}$),

found fluctuations Δn in the carrier density from $4 \cdot 10^{10}\,\mathrm{cm}^{-2}$ to $4 \cdot 10^{11}\,\mathrm{cm}^{-2}$. In samples of BL graphene, the puddles are found to be of smaller size [249], and typical carrier density fluctuations are similar to the ones of SL graphene, for example, about $8 \cdot 10^{11}\,\mathrm{cm}^{-2}$ [233, 235].

However, due to the different dependence of the DOS on the energy in the two systems, the same carrier density fluctuation Δn yields a different magnitude for the fluctuation or smearing in the Fermi level. While in SL graphene, the carrier density (per unit area) depends on the Fermi level as

$$n = \frac{1}{\pi}\left(\frac{E_F}{\hbar v_F}\right)^2 , \tag{5.25}$$

the corresponding relation for BL graphene is given by

$$n = \frac{1}{\pi(\hbar v_F)^2}\left\{|E_F|\,(|E_F| + t_1) + |E_F|\,(|E_F| - t_1)\,\Theta(|E_F| - t_1)\right\} . \tag{5.26}$$

For a density fluctuation of $\Delta n = 8.5{\cdot}10^{11}\,\mathrm{cm}^{-2}$ the values for the energy broadening are $\sigma_{\mathrm{br}}^{\mathrm{SL}} = 91\,\mathrm{meV}$ and $\sigma_{\mathrm{br}}^{\mathrm{BL}} = 23\,\mathrm{meV}$ for the SL and BL case, respectively. We implement the effect of the electron-hole puddles by applying to the rates a Gaussian broadening [62],

$$\frac{1}{\tau_{\mathrm{s}}(E_F)} = \frac{1}{\sqrt{2\pi\sigma_{\mathrm{br}}^2}}\int_{-\infty}^{\infty} \mathrm{d}E \frac{1}{\tau_{\mathrm{s}}(E)} \exp\left[-\frac{(E - E_F)^2}{2\sigma_{\mathrm{br}}^2}\right] . \tag{5.27}$$

For a given exchange parameter, the singlet-triplet splitting is slightly larger in the hydrogenated BL case than in the SL one due to an effective energy renormalization by the interlayer coupling t_1. However, the large energy broadening in the SL system completely masks the splitting effect which yields a qualitatively different picture of the hydrogen induced relaxation rates around the charge neutrality point, see the scheme presented in Fig. 5.5. In the vicinity of the charge neutrality point, the broadened rate for hydrogenated SL graphene decreases with increasing the Fermi energy. In contrast, for the BL structure, the broadened rate increases with increasing the Fermi energy until the maximum of the resonance induced shoulders are met. At high energies (or charge carrier densities), both the SL and BL spin relaxation rates decrease with increasing energy.

In Fig. 5.6, we provide the calculated (broadened and unbroadened) spin relaxation rates of hydrogenated SL and BL graphene assuming an energy broadening as specified above and, in both cases, a concentration of 0.17 ppm. The broadening of the rates follows the scheme as presented above. Hydrogen adatoms (or the methyl

compared to the resolution in the STM approach ($\sim 2\,\mathrm{nm}$) of the authors of Ref. [232], yield smaller estimates for Δn due to spatial averaging effects.

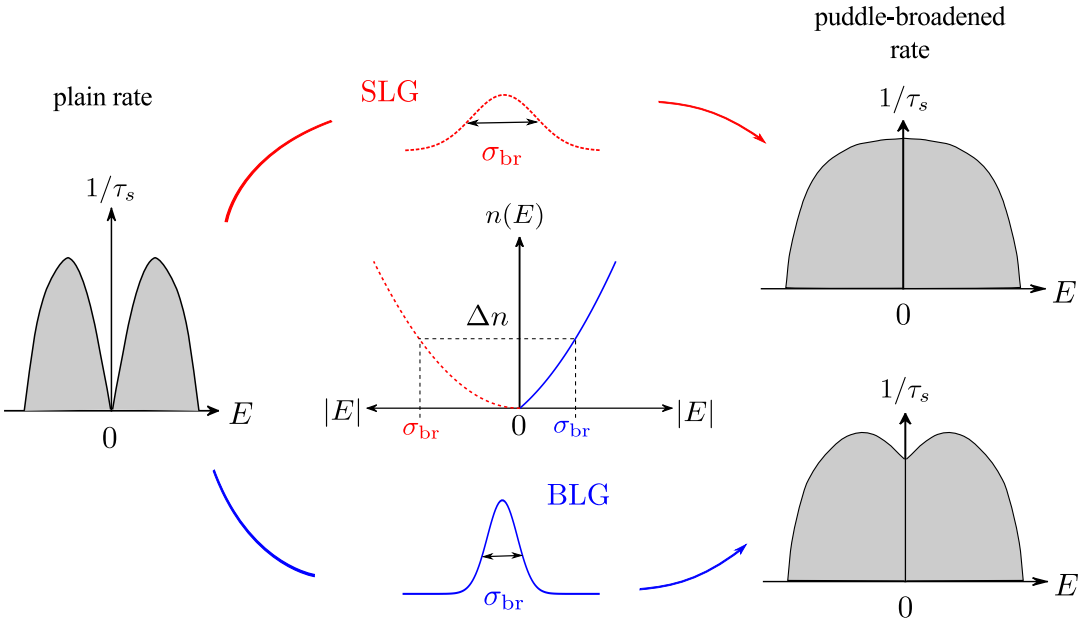

Figure 5.5: Scheme of the influence of electron-hole puddles on the spin relaxation rates. The different DOS of SL and BL graphene lead for the same carrier density fluctuation Δn to a larger energy broadening $\sigma_{\rm br}$ in the SL case than in the BL one (center). While the unbroadened relaxation rate shows for both SL and BL graphene clear singlet and triplet resonances (left), the singlet-triplet signature survives only in the BL graphene case (right). Adapted from Ref. [166].

group), appearing at the order of 1 ppm, are likely contaminants of experimental SL and BL graphene samples. Indeed, comparing[10] the hydrogen computed spin relaxation rates to experimental SL [62, 165] and BL [26, 166] graphene data yields very good agreement (see Refs. [62, 166] for a direct comparison). This is a strong indication that a ppm concentration of local magnetic moments arising from the production process of the experimental samples gives rise to the measured spin relaxation rates.

5.3 Is fluorine a magnetic resonant scatterer in graphene?

In the remainder of this chapter, we will address the question, whether fluorine induces magnetic moments in graphene. Approaching this issue with theoretical

[10] In the SL graphene case, Refs. [62, 165], additional energy broadening appears due to a finite temperature of 300 K. The electron-hole puddles were estimated to give $\sigma_{\rm br} = 110$ meV for the considered sample and a concentration of $\eta = 0.36$ ppm was extracted in the comparison of model and experiment.

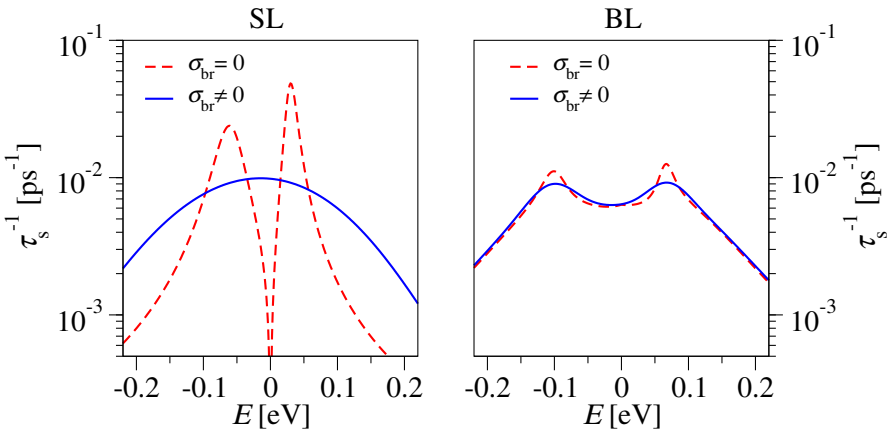

Figure 5.6: Spin relaxation rates of hydrogenated SL (left) and BL (right) graphene with an exchange coupling of $J = -0.4\,\mathrm{eV}$. In the BL case, an unbiased average over dimer and nondimer adsorption positions was applied. Taking into account a carrier density fluctuation of $\Delta n = 8.5 \cdot 10^{11}\,\mathrm{cm}^{-2}$ ($\sigma_{\mathrm{br}}^{\mathrm{SL}} = 91\,\mathrm{meV}$ and $\sigma_{\mathrm{br}}^{\mathrm{BL}} = 23\,\mathrm{meV}$) yields different trends of τ_{s}^{-1} around the charge neutrality point. An adatom concentration of $\eta = 0.17\,\mathrm{ppm}$ was used in the calculation of the relaxation rates.

DFT calculations did, so far, not provide a conclusive answer. For example, Santos *et al.* [148] do not find fluorine induced magnetic moments, while Kim *et al.* [157], performing a hybrid DFT study, come to the opposite result. A possible culprit for the discrepancy in the results is the self-interaction error appearing in the exchange-correlation functionals [158, 159]. However, experiments found indications that fluorine does indeed induce magnetic moments in graphene [134, 137, 160, 235].

Below, we choose a path between a full theoretical and experimental treatment of fluorinated graphene. On the one hand, we take DFT calculations as a backbone for the orbital part of the fluorine adatom model. On the other hand, we apply the previously discussed model of resonant scattering off magnetic moments to experimental spin relaxation data of the group of Jun Zhu at Penn State University on fluorinated SL [134, 160] and BL [235, 250] graphene. Knowing from the experimental characterization of the samples the fluorine concentration, we aim to extract the value for the exchange coupling by comparing model and experiment.

The following sections summarize the current status of the project. While the model works successfully in some aspects, we find discrepancies between theory and experiment that are not yet satisfyingly resolved.

5.3.1 Experiment at Penn State University

The experiments on fluorinated SL and BL graphene were conducted in the group of Jun Zhu at Penn State University. We were provided with experimental data sets of the samples A [134] and W03 [250] of the SL and BL fluorinated graphene

experiments. In the following, we will give a short overview on the preparation of the samples and applied measurement methods as reported by the Penn State group in Refs. [134, 160, 235, 250].

Sample preparation and characterization

Starting point are exfoliated graphene samples on SiO_2/doped Si substrates which are fluorinated in a reactive ion etching chamber with a CF_4 plasma [251] at room temperature. An earlier experiment showed that this fluorination method is clean and reversible [160]. Varying the exposure time of the graphene sample to the plasma, different fluorine concentrations on the samples are realized. The BL graphene samples are found to be harder to fluorinate, which might be related to a flatter surface of the BL samples on the substrate than the SL ones [235, 250]. Defluorinated control samples are produced by annealing at about 370 °C (in Ar/H_2 gas flow) for 12 h (BL) and 24 h (SL).

STM measurements, performed on the SL graphene samples, indicate the covalent bonding of adsorbates on the graphene sheet [142, 160]. These adsorbates are interpreted as fluorine atoms. The concentration of the fluorine adatoms, on the other hand, is extracted from Raman spectroscopy measurements. By analyzing the intensity ratio of the Raman D to G peak [252, 253], a fluorine concentration of $n_F = 5 \cdot 10^{11}\,\mathrm{cm}^{-2}$ is deduced for sample A (SL) and $n_F = 4.4 \cdot 10^{12}\,\mathrm{cm}^{-2}$ for sample W03 (BL). As in the defluorinated samples the Raman D peak almost vanishes, only few residual defects such as vacancies are expected. The Penn State group estimates a residual defect concentration of $6 \cdot 10^{11}\,\mathrm{cm}^{-2}$ in the BL graphene device.

After the defluorination process, the graphene samples are fabricated into field effect transistors in the Hall Bar geometry by standard electron-beam lithography. Applying a perpendicular magnetic field, magnetoresistance measurements at low field strengths are carried out in order to extract the spin relaxation rates in the samples.

Weak localization measurements

Weak localization (WL) is a quantum interference effect of electrons diffusing on closed or self-crossing paths in the sample [254–256]. It was first observed experimentally in weakly disordered thin metallic films and semiconductor inversion layers in the 1980s as resistance anomalies in the temperature and magnetic field dependence [254]. In the presence of time reversal symmetry, the diffusion along closed paths leads to an enhanced backscattering probability of the electrons [254, 255]. The WL is therefore a precursor of the Anderson localization [257] which describes the absence of diffusion [255].

Being a quantum interference effect, WL strongly relies on the phase coherence

of the electron and its time-reversed counterpart[11] diffusing along a closed trajectory. The phase coherence time of the electron is a temperature dependent quantity due to electron-electron and electron-phonon interactions [241] in the sample. Furthermore, an external magnetic field destroys time reversal symmetry and induces a phase shift between the two counterpropagating paths for the closed loop. Therefore, an important experimental tool for the investigation of phase breaking mechanisms in the sample are the magnetoresistance measurements at low magnetic fields, i.e. when quantizing effects of the Landau level formation are not yet dominating [254, 255, 258].

Negative magnetoresistance is a signature of the suppression of WL under increasing magnetic field strength. If spin-orbit scattering is present, however, the spin state of the electron, diffusing along the closed loop, undergoes a relative rotation by 2π. An enhanced forward scattering probability is the consequence. This effect is commonly called weak anti-localization (WAL) [254] and is observed as a positive magnetoresistance.

Theoretically, pristine SL and BL graphene exhibit the WAL and WL effects, respectively [226, 227, 259, 260]. The reason lies in the Berry phases of SL and BL graphene of π and 2π, respectively, which is acquired by the electrons diffusing on the closed paths [256] due to the rotation of momentum around a Dirac point. Here, one can draw (specifically for SL graphene) an analogy to the spin-rotation induced WAL mentioned in thin films. In SL graphene, the pseudospin, carrying information about the sublattice population of the lattice, is either parallel or anti-parallel to the momentum of the charge carrier[12] (depending on the considered Dirac valley and the conduction or valence band). This alignment of pseudospin and momentum is often referred to as the chiral nature or symmetry of graphene [256]. The rotation of the momentum is therefore directly connected to the rotation of the pseudospin. In both SL and BL graphene, SOC of the Rashba type (affecting the real physical spin of the electrons) was predicted to induce WAL [261].

The chiral symmetry of SL and BL graphene can be broken by inter- and intravalley scattering processes due to, for example, surface ripples, atomic defects, boundaries, random bond disorder etc. [230, 262, 263]. Intravalley scattering affects directly the pseudospin, and counterpropagating partial waves (electron and time-reversed partner on the closed loop) acquire different phases. This leads to a suppression of the WAL or WL effect. Intervalley scattering, on the other hand, can restore the WL effect. If the counterpropagating states live in different valleys they have different pseudospin orientation and correspondingly, due to a total phase shift of 0, constructive interference can occur between the two partial waves [256].

[11] If the electron traverses the closed path in clock wise orientation, its time-reversed partner diffuses in the counter clockwise direction. In the presence of time-reversal symmetry, both diffusion paths have the same return probability and are phase coherent.

[12] This can be seen by calculating the expectation value of the pseudospin Pauli matrices σ with the low energy states.

Furthermore, SL graphene (at high charge carrier densities) and BL graphene are subject to trigonal warping of the Fermi contours around the valleys [227, 262]. This effect also breaks the chiral symmetry and suppresses the WL effects.

Realistic, weakly disordered graphene samples can exhibit a complex interplay of different phase-breaking effects [230, 263] which lead to observations contradicting the theoretical predictions for the ideal situations. For example, first measurements for SL graphene showed WL instead of WAL [77, 264]. Improving the sample quality and thus changing the ratio of the dephasing time and the inter- and intravalley scattering times, Tikhonenko *et al.* [265] were able to tune between WL and WAL behavior in their SL graphene device.

WL measurement in the Penn State experiment

The fluorinated SL and BL graphene devices of the Penn State group exhibit the characteristics of WL [134, 235]. Fitting the magnetoconductance correction,

$$\Delta\sigma(B,n) = \sigma(B,n) - \sigma(0,n) \tag{5.28}$$

at different charge carrier densities n to the theoretical WL model of Refs. [226, 227], the phase coherence length $L_\phi(T)$ and the corresponding dephasing rate $\tau_\phi^{-1}(T) = D/L_\phi^2$ in the sample is extracted at different temperatures T. Here, D denotes the diffusion constant which is determined by the mean free path. In order to avoid effects of strong localization, all measurements are performed at high carrier densities where $n > n_F$.

The dephasing rate increases with temperature. This behavior of $\tau_\phi^{-1}(T)$ can be attributed to inelastic scattering processes due to electron-electron interaction [134, 230]. At low T, large momentum-transfer collisions due to direct Coulomb interaction are found to be negligible in accordance with measurements on pristine graphene samples [264, 266]. Furthermore, in this low temperature range the contribution from electron-phonon scattering is subdominant. Approaching the zero temperature ($T \in [1, 10]\,\mathrm{K}$), the dephasing rate saturates to a constant value τ_{sat}^{-1} which depends approximately linearly on the fluorine concentration in the samples [134]. No saturation is observed in the WL measurements of the defluorinated control samples.

In the literature, several candidates explaining the saturation behavior can be found [229, 230]. On the one hand, additional dephasing can occur at the sample boundaries, for example in the electric contacts. This typically happens for sample sizes L where $L_\phi \gtrsim L$, which is not the case for the investigated fluorinated samples of the Penn State experiment [134, 235]. Electron-hole puddles could also give rise to additional dephasing. However, in this scenario the dephasing would start at different temperatures T_{sat} depending on the charge carrier concentration [230]. This n dependence is not observed in the data. As the value of τ_{sat}^{-1} seems to be directly connected to the fluorine concentration, a third mechanism is probably

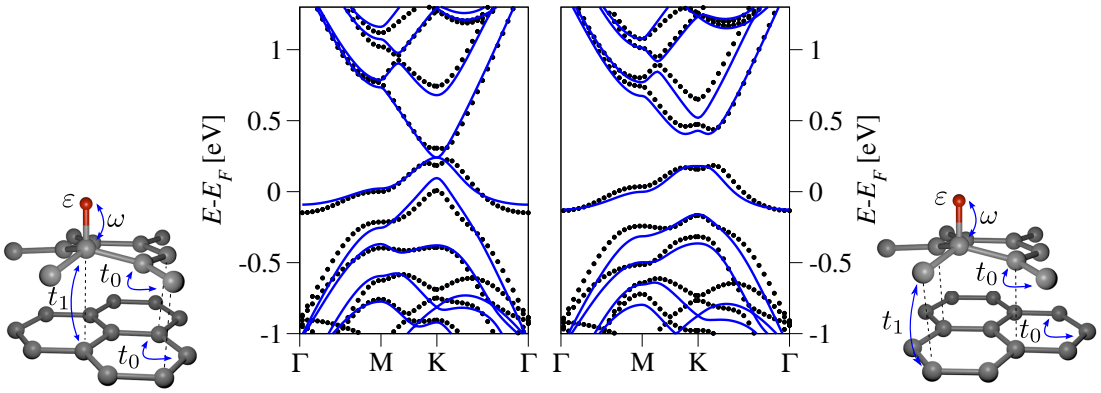

Figure 5.7: Electronic band structure of a 7×7 supercell of BL graphene with one fluorine adatom in the dimer (left) and nondimer (right) adsorption position on the top layer. Shown are both DFT (black dotted) and TB data (blue solid) with the TB parameters $\omega_\mathrm{d} = 7.0\,\mathrm{eV}$ and $\varepsilon_\mathrm{d} = -2.5\,\mathrm{eV}$ for the dimer configuration, and $\omega_\mathrm{nd} = 8.0\,\mathrm{eV}$, $\varepsilon_\mathrm{nd} = -3.0\,\mathrm{eV}$ for the nondimer configuration. Aside a good overall agreement between the TB and DFT band structures, the gap at the $\boldsymbol{K}$ point between the two bands above the Fermi energy is not recovered in the simple TB model.

responsible [134, 235]. This mechanism is spin-flip scattering off local magnetic moments. Pierre *et al.* [228] showed earlier that spin-flip scattering off a dilute concentration of magnetic impurities can explain the saturation of τ_ϕ^{-1} in metal wires. Also Kozikov *et al.* [229] employ this explanation for their observations in SL graphene. In the following, we interpret τ_sat^{-1} as the spin relaxation rate and investigate its dependence on the charge carrier density.

5.3.2 DFT and TB input

Below, we model a dilute concentration of fluorine adatoms in both SL and BL graphene as a source of local magnetic moments. The orbital parameters for the TB model are extracted from DFT calculations by Martin Gmitra of a SL 10×10 [100] and a BL 7×7 supercell calculation. The results regarding the SL supercell were already presented in Sec. 3.5.1, where we found fluorine being well described by the orbital parameters $\omega = 5.5\,\mathrm{eV}$ and $\varepsilon = -2.2\,\mathrm{eV}$.

In the case of BL graphene, we compare the orbital part of the TB model, Eq. (5.1), to the three bands around the Fermi level of the DFT computed spectrum. However, as in the case of hydrogenated BL graphene, Sec. 5.2.2, we do not achieve a unique fit. Instead, we select for the dimer and nondimer configuration adatom parameters which are close to the SL (unique) fit and which are best suited for the description of the experimental spin relaxation data as presented below. Following this approach, we describe fluorine in the dimer position with $\omega_\mathrm{d} = 7.0\,\mathrm{eV}$ and $\varepsilon_\mathrm{d} = -2.5\,\mathrm{eV}$, and nondimer fluorine with $\omega_\mathrm{nd} = 8.0\,\mathrm{eV}$ and $\varepsilon_\mathrm{nd} = -3.0\,\mathrm{eV}$. Both

DFT and TB band structures are displayed in Fig. 5.7. We note a good overall agreement for both adsorption positions. However, in the dimer case, the model does not recover the small gap at the $\boldsymbol{K}$ point occurring between the two DFT bands above the Fermi level. This discrepancy cannot be cured by introducing standard additional interlayer hoppings[13], and local modifications of them, in the BL graphene model.

Without doubt, we employ a rather simple TB model to describe fluorine on BL graphene and there might be some component missing. Furthermore, the DFT calculation cannot mimic the (by a factor of 10) smaller fluorine concentrations in the BL graphene samples of the Penn State experiment due to computational costs. In the experimental limit of adatom coverage, recovering the gap might be of small importance. For simplicity, we first stick to the simple model in the following and address a possible extension later.

Resonances with exchange

We found in Ch. 4 that fluorine on SL graphene induces a very broad resonance, $\Gamma \approx 280\,\mathrm{meV}$, in the DOS which lies about 260 meV below the zero energy. Placing fluorine on BL graphene, the resonance peak appears at similar energies for the dimer, $E_{\mathrm{res}} = -253\,\mathrm{meV}$, and nondimer, $E_{\mathrm{res}} = -247\,\mathrm{meV}$, adsorption configuration. Also the resonance widths are comparable to the SL case. As it is displayed in Fig. 5.8, a nonzero exchange coupling splits the resonance peaks in their respective singlet and triplet contributions which are further broadened. This is in accordance with our findings for hydrogen shown in Fig. 5.3. Here, we chose for illustration the same exchange parameter $J = 0.47\,\mathrm{eV}$ for SL and BL graphene. As we will see below, we recover the experimental BL spin relaxation data best with this value for J in the simple model description.

5.3.3 Spin relaxation in fluorinated BL and SL graphene

Figure 5.9 shows the spin relaxation data of the fluorinated BL graphene sample from the Penn State group. The data is taken for charge carrier concentrations in the interval $[5 \cdot 10^{12}\,\mathrm{cm}^{-2}, 13 \cdot 10^{12}\,\mathrm{cm}^{-2}]$ (electron doped sample [235]) and thus covers energy values from about 0.1 to 0.22 eV. In this interval, the extracted spin relaxation rates yield values from about 0.15 to $0.5\,\mathrm{ps}^{-1}$. For the modeling part, we assume that the fluorine adsorption occurs in a statistically equal manner[14] to dimer and non-dimer sites in the top layer such that the total spin relaxation rate

[13] See, for example, the interlayer hoppings γ_0, γ_1, γ_3, and γ_4 of Ref. [10] where $\gamma_0 \equiv t_0$, $\gamma_1 \equiv t_1$.

[14] In the DFT calculation, the nondimer configuration is by about 40 meV lower in energy than the dimer one. We checked that a variation of the occupation to dimer and nondimer sites did not affect our results on τ_{s}^{-1} and τ_{m}^{-1} significantly.

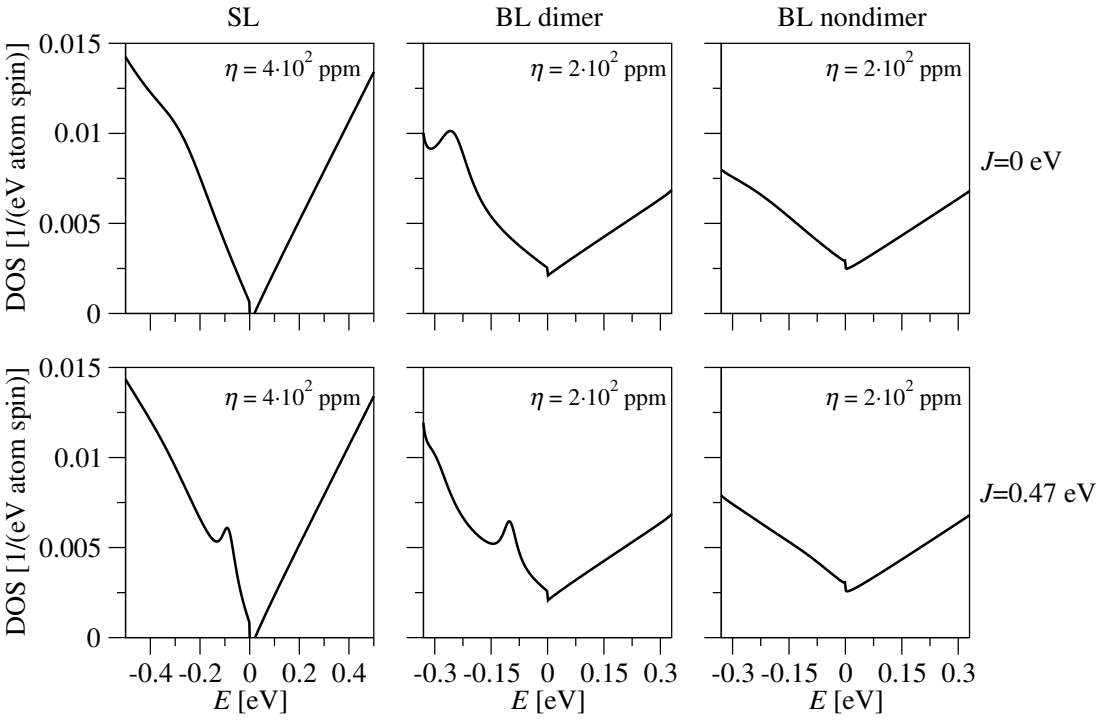

Figure 5.8: Effect of the exchange coupling on the DOS of fluorinated SL and BL graphene. The first column addresses fluorine on SL graphene with $\omega = 5.5\,\mathrm{eV}$, $\varepsilon = -2.2\,\mathrm{eV}$. The adatom induces a broad resonance far off the zero energy ($E_{\mathrm{res}} \approx 260\,\mathrm{meV}$), see Ch. 4. On BL graphene, fluorine related resonances appear at about $E_{\mathrm{res}} = -253\,\mathrm{meV}$ and $E_{\mathrm{res}} = -247\,\mathrm{meV}$ for the dimer and nondimer configuration, respectively. Under the influence of the exchange coupling $J = 0.47\,\mathrm{eV}$, the peaks are split. However, since the appearing resonances are very broad, the individual width of the singlet and triplet resonances are not sufficiently resolved. For fluorine on SL graphene, the resonance energies are $E_{\mathrm{res}}^{\ell=0} = -85\,\mathrm{meV}$ and $E_{\mathrm{res}}^{\ell=1} = 323\,\mathrm{meV}$. For fluorinated BL graphene, one can read off $E_{\mathrm{res}}^{\ell=0} = -101\,\mathrm{meV}$ and $E_{\mathrm{res}}^{\ell=1} \approx -305\,\mathrm{meV}$ in the dimer configuration. The singlet-triplet splitting in the nondimer configuration is hidden due to the shallow and broad resonance. An artificially increased adatom concentration of $\eta = 400\,\mathrm{ppm}$ and $\eta = 200\,\mathrm{ppm}$ were used in the calculation for the SL and BL cases, respectively.

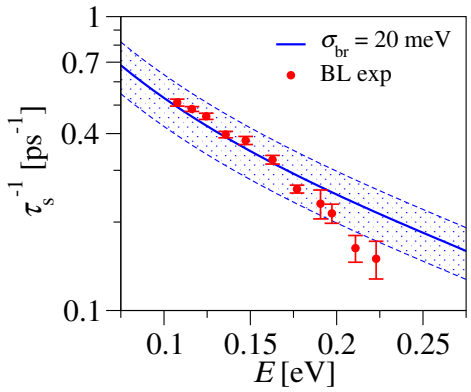

Figure 5.9: Spin relaxation rate of fluorinated BL graphene. Aside the experimental data from the Penn State group [235] (red symbols), the model calculated data is shown (blue solid). The model parameters are $\omega_{\rm d} = 7.0\,{\rm eV}$, $\varepsilon_{\rm d} = -2.5\,{\rm eV}$, $\omega_{\rm nd} = 8.0\,{\rm eV}$, $\varepsilon_{\rm nd} = -3.0\,{\rm eV}$, and $J = 0.47\,{\rm eV}$. The fluorine concentration of $\eta = 572\,{\rm ppm}$ ($n_F = 4.4 \cdot 10^{12}\,{\rm cm}^{-2}$) follows the experimental estimate, and an energy broadening of $\sigma_{\rm br} = 20\,{\rm meV}$ is employed. A variation of $\pm 20\%$ in η is indicated by the dashed lines.

is given by the unbiased average over the two adsorption configurations,

$$1/\tau_s \equiv 1/\left(2\tau_s^{\rm C_d}\right) + 1/\left(2\tau_s^{\rm C_{nd}}\right) . \tag{5.29}$$

Employing the orbital TB parameters for fluorine as discussed above and the experimental estimate for the fluorine concentration, $\eta = 572\,{\rm ppm}$ ($n_F = 4.4 \cdot 10^{12}\,{\rm cm}^{-2}$), we find good agreement between model and experiment for the exchange parameter $J = 0.47\,{\rm eV}$. The employed energy broadening of $\sigma_{\rm br} = 20\,{\rm meV}$ [235] affects the spin relaxation data only marginally. In Fig. 5.9 we also show the model rates for a variation of the fluorine concentration by $\pm 20\%$ which takes into account the uncertainty in the experimental estimation of η [235].

Taking into account only the $\tau_{\rm s}^{-1}$ data of the BL sample, one would conclude that fluorine indeed seems to induce local magnetic moments in the BL graphene with an exchange value close to the one for hydrogenated graphene. However, we should find a similar result for the spin relaxation data [134] of SL graphene first. And that is exactly the problem, as we see in Fig. 5.10. According to Ref. [235], the SL $\tau_{\rm s}^{-1}$ data was extracted in the hole-doped region for carrier concentrations ranging from 0.6 to $3.9 \cdot 10^{12}\,{\rm cm}^{-2}$ (energies lie in $[-0.2\,{\rm eV}, -0.07\,{\rm eV}]$) and $\tau_{\rm s}^{-1}$ values from to 0.07 up to $0.6\,{\rm ps}^{-1}$ are found. The model data does not recover these magnitudes of the rates. Neglecting at the moment the exchange parameter, the orbital parameters of fluorine on SL graphene, as extracted from the DFT/TB study in Sec. 3.5, lead to a broad resonance at large negative energy, see Fig. 5.8. In Ch. 4, we saw that this leads to a pronounced asymmetry in the momentum relaxation rate. The value of the relaxation rate is significantly higher for negative energies than for positive ones. Here, we now observe a similar tendency in the

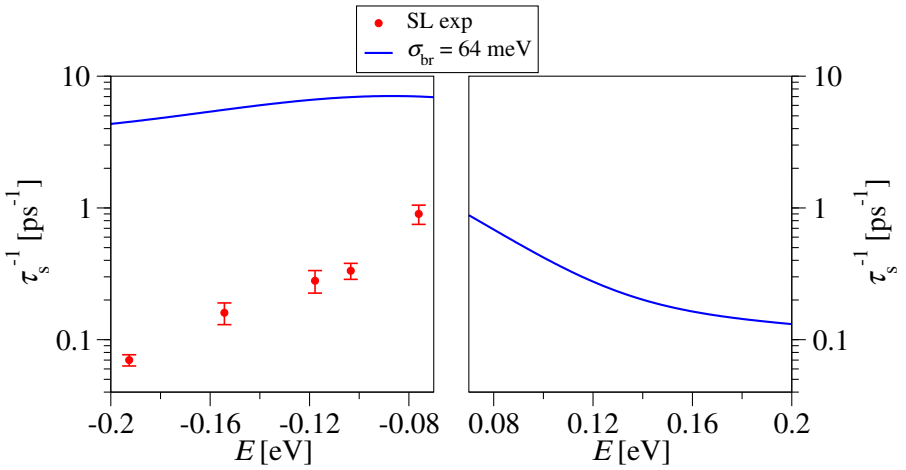

Figure 5.10: Spin relaxation rate of fluorinated SL graphene. Aside the experimental data from the Penn State group [134, 235] (red symbols), the model calculated data is shown(blue solid). The model parameters are $\omega = 5.5\,\mathrm{eV}$, $\varepsilon = -2.2\,\mathrm{eV}$, and $J = 0.56\,\mathrm{eV}$. The fluorine concentration of $\eta = 131\,\mathrm{ppm}$ ($n_F = 5 \cdot 10^{11}\,\mathrm{cm}^{-2}$) follows the experimental estimate and an energy broadening of $\sigma_{\mathrm{br}} = 64\,\mathrm{meV}$ is employed. The experimental data is taken in the hole-doped region [235] where the model does not match the experimental data (left panel). Agreement between model and experiment can only be found assuming that the experimental data was taken in the electron-doped region (right panel).

spin relaxation rate for a finite exchange coupling.

As an example, we take $J = 0.56\,\mathrm{eV}$ and an energy broadening of $\sigma_{\mathrm{br}} = 64\,\mathrm{meV}$ for the experimental fluorine concentration of $\eta = 131\,\mathrm{ppm}$ ($n_F = 5 \cdot 10^{11}\,\mathrm{cm}^{-2}$). Figure 5.10 presents that the model recovers the magnitude of the experimental τ_{s}^{-1} data only at positive energies but overestimates the real experimental data by a factor of 10 to 40. This overestimation persists under variation of J and σ_{br} in reasonable intervals. At this stage of the investigation, one way to fix this discrepancy in our model would be to assume that only a fraction of the fluorine adatoms induce local magnetic moments which then contribute to the observed spin relaxation. To support this hypothesis, knowledge of the experimental τ_{s}^{-1} data for positive energies would be required since we should still observe the pronounced asymmetry with respect to zero energy as in the model.

Strong midgap scatterer model

As it is shown in Ref. [134] by the Penn State group, the experimental conductivity data of SL fluorinated graphene lacks pronounced asymmetry with respect to negative and positive energies and can be fitted to the SMS model [2, 176, 177, 189], see Eq. (4.37) and Fig. 5.11(a). In order to rule out localization effects, the authors of Ref. [134] fit the data for a temperature of 200 K to the corresponding

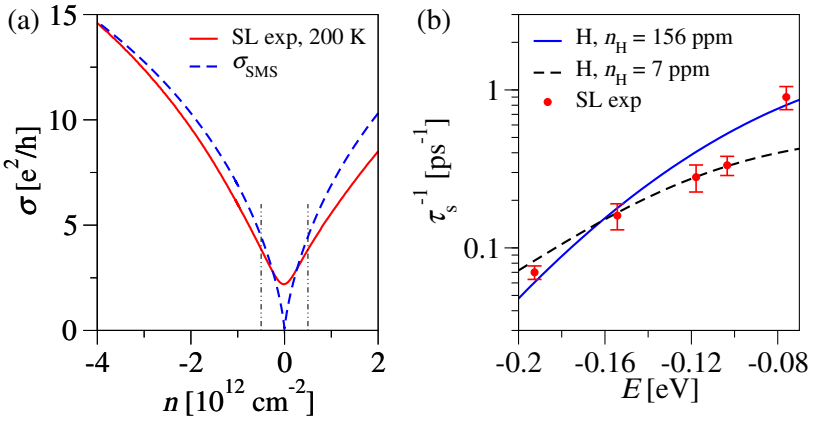

Figure 5.11: (a) Experimental conductivity data [134, 235] of fluorinated SL graphene at 200 K (red solid) in comparison with the SMS model (blue dashed) [see Eq. (4.37) in Sec. 4.5]. For $|n| \gtrsim n_F$ (vertical dashed lines), the SMS model parameters $n_i = 6 \cdot 10^{11}\,\mathrm{cm}^{-2}$ and $R = 4.4\,\text{Å}$ were extracted in Ref. [134]. (b) Spin relaxation rate for a hydrogen-like adsorbate on SL graphene with $\omega = 7.5\,\mathrm{eV}$, $\varepsilon = 0.16\,\mathrm{eV}$ in comparison to the experimental relaxation rate of SL fluorinated graphene [134, 235]. Data are shown for $\sigma_{\mathrm{br}} = 80\,\mathrm{meV}$, $\eta = 156\,\mathrm{ppm}$ (n_i), and $J = 7\,\mathrm{meV}$ (blue solid) as well as for $\sigma_{\mathrm{br}} = 60\,\mathrm{meV}$, $\eta = 7\,\mathrm{ppm}$, and $J = -0.4\,\mathrm{eV}$ (black dashed).

SMS formula and extract an effective disk radius of $R = 4.4\,\text{Å}$ for an impurity concentration of $n_i = 6 \cdot 10^{11}\,\mathrm{cm}^{-2}$. The value of n_i is close to the estimate of the fluorine concentration, $n_F = 5 \cdot 10^{11}\,\mathrm{cm}^{-2}$, which is extracted from Raman measurements. The authors conclude in their work that fluorine acts like a SMS impurity on SL graphene. As we elucidated in Sec. 4.5, the SMS model can be used for the description of vacancies or strong resonant scatterers, such as hydrogen, in SL graphene. However, the model does not catch the situation of adatom induced resonances significantly away from zero energy, which is exactly what we found for fluorine in our combined DFT/TB analysis, Sec. 3.5.

Ignoring for a moment our knowledge on the orbital parameters of fluorine, we calculate the spin relaxation rate assuming a hydrogen-like adsorbate, $\omega = 7.5\,\mathrm{eV}$ and $\varepsilon = 0.16\,\mathrm{eV}$, for an adatom concentration of $\eta = 156\,\mathrm{ppm}$ (corresponding to n_i). Indeed, applying an energy broadening of $\sigma_{\mathrm{br}} = 80\,\mathrm{meV}$ the model spin relaxation rate reaches the experimental results, see Fig. 5.11(b). However, this is achieved at the cost of a very small exchange parameter[15] of $J = 7\,\mathrm{meV}$. Alternatively, we fix the exchange parameter to the hydrogen value of $J = -0.4\,\mathrm{eV}$ [62] and allow the concentration of the impurity to vary. For $\sigma_{\mathrm{br}} = 60\,\mathrm{meV}$ we need only $\eta = 7\,\mathrm{ppm}$ to obtain a good agreement between model and experiment, see Fig. 5.11(b).

Interestingly, the experimental conductivity data of fluorinated BL graphene [250]

[15] An equally good alignment between model and experiment can be achieved for $J \approx -6\,\mathrm{meV}$.

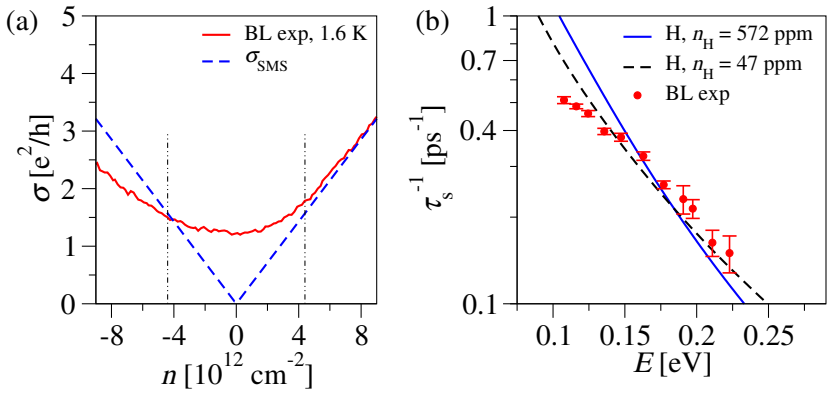

Figure 5.12: (a) Experimental conductivity data [235, 250] of fluorinated BL graphene at 1.6 K (red solid) in comparison with the SMS model (blue dashed) of Eq. (5.30). For $|n| \gtrsim n_F$ (vertical dashed lines), the SMS model parameter $n_i = 4.4 \cdot 10^{12}\,\mathrm{cm}^{-2}$ is extracted in Ref. [250]. (b) Spin relaxation rate for a hydrogen-like adsorbate on BL graphene with $\omega_\mathrm{d} = 6.5\,\mathrm{eV}$, $\varepsilon_\mathrm{d} = 0.25\,\mathrm{eV}$, $\omega_\mathrm{nd} = 5.5\,\mathrm{eV}$, $\varepsilon_\mathrm{nd} = 0.35\,\mathrm{eV}$ in comparison to the experimental relaxation rate of BL fluorinated graphene [235]. Data are shown for $\sigma_\mathrm{br} = 20\,\mathrm{meV}$, $\eta = 572\,\mathrm{ppm}$ (n_F), and $J = -40\,\mathrm{meV}$ (blue solid) as well as for $\sigma_\mathrm{br} = 20\,\mathrm{meV}$, $\eta = 47\,\mathrm{ppm}$, and $J = -0.4\,\mathrm{eV}$ (black dashed).

can also be fit by the BL version of the SMS model of Ref. [177][16],

$$\sigma_\mathrm{SMS}^\mathrm{BL} = \frac{e^2}{h}\,\frac{\pi}{2}\,\frac{|n|}{n_i}\,. \tag{5.30}$$

Figure 5.12(a) displays the experimental conductivity at $T = 1.6\,\mathrm{K}$ and the corresponding fit[17] to the SMS model with $n_i = n_F$ as presented in Ref. [250]. Again, the authors of Ref. [250] relate the observed conductivity data to a strong resonant nature of fluorine on BL graphene. As before, we try to obtain an agreement with this experimentally motivated assumption by using the orbital parameters of hydrogen on graphene ($\omega_\mathrm{d} = 6.5\,\mathrm{eV}$, $\varepsilon_\mathrm{d} = 0.25\,\mathrm{eV}$, $\omega_\mathrm{nd} = 5.5\,\mathrm{eV}$, $\varepsilon_\mathrm{nd} = 0.35\,\mathrm{eV}$). Figure 5.12(b) shows that with an exchange parameter of $J = -40\,\mathrm{meV}$ the model and experimental data reach the same order of magnitude. Similarly as for the SL relaxation data, we also consider the hydrogen attributed exchange parameter $J = -0.4\,\mathrm{eV}$ (see Sec. 5.2.2) and need only $\eta = 47\,\mathrm{ppm}$ to tune the model to the experimental data.

However, let us stress that the SMS model (or strong resonant scatterer) approach is in conflict with the DFT results on fluorinated SL and BL graphene. Figure 5.13

[16] Note that the additional factor of 2 in Eq. (5.30) (compared to Ref. [177]) appears due to the one-sided fluorination of the experimental sample [250].

[17] The experimental conductivity data for $T = 200\,\mathrm{K}$ is about a factor of 2 larger than the low temperature data [235, 250]. Correspondingly, a fit of σ_SMS to the high temperature σ curve would result in 2 times smaller impurity concentration n_i.

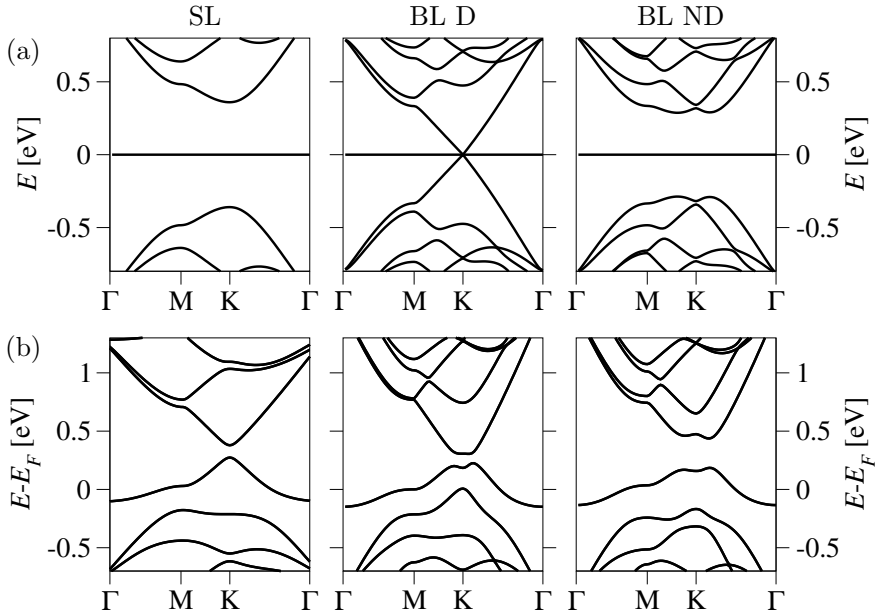

Figure 5.13: (a) Electronic band structures as obtained from a TB implementation of a disk scatterer with radius $R = 4\,\text{Å}$ on a 10×10 supercell of SL and BL graphene. In the latter, the disk center was placed on a dimer (D) or nondimer (ND) site. (b) DFT calculated band structures of fluorinated SL (see Sec. 3.5) and BL graphene (see Sec. 5.3.2). A 10×10 supercell was used for SL graphene, a 7×7 one for BL graphene.

presents a direct comparison of the DFT computed band structure of fluorinated (SL and BL) graphene with a TB implementation of a disk scatterer with effective radius $R = 4\,\text{Å}$. In the TB model, all carbon atoms within the disk radius are shifted to large positive energy and are decoupled from the rest of graphene. Furthermore, for BL graphene, the disk center coincides either with a dimer or a nondimer site. The disk scatterer model exhibits similarities with hydrogenated[18] SL [52] or BL (Fig. 5.2) graphene, but it is clearly distinct from fluorine on SL or BL graphene.

5.3.4 Momentum relaxation in fluorinated SL and BL graphene

Experimental τ_s^{-1}/τ_m^{-1} ratio

Another puzzle is provided by the experimental ratio of the spin to the momentum relaxation rate[19], see Fig. 5.14. The ratios yield values of 10^{-3} to 10^{-2} in SL fluorinated graphene, and around 10^{-3} in BL fluorinated graphene. We compare

[18] Compare also to the band structure of methyl functionalized SL graphene in Fig. 3.3.

[19] The momentum relaxation rate is extracted by the Penn State group for both SL and BL configuration from the 200 K conductivity data applying the Drude formula [235].

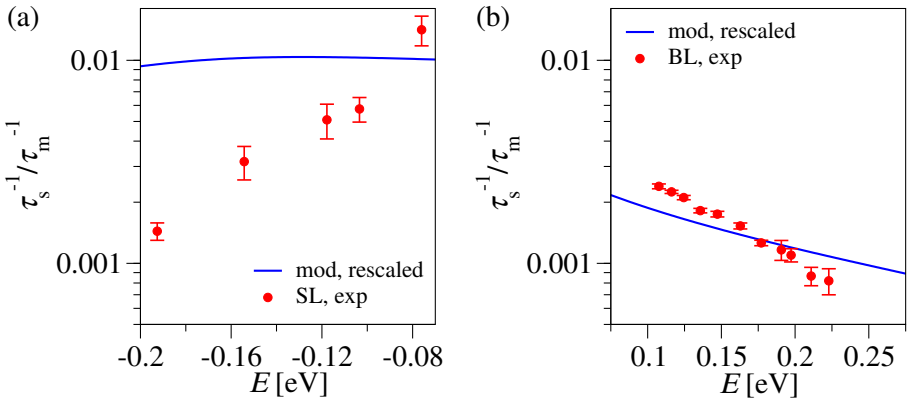

Figure 5.14: Ratio of spin to momentum relaxation rate in fluorinated (a) SL and (b) BL graphene. Together with the experimental data (red symbols) the model calculated ratios (blue solid) are plotted. The parameters are the same as in Fig. 5.9 and Fig. 5.10 for the BL and SL case, respectively. The model ratios are rescaled by a factor of (a) 1/100 and (b) 1/40 to obtain the experimental order of magnitude. The experimental momentum relaxation rate is extracted from the 200 K conductivity data [235], while the model considers $T = 0\,\mathrm{K}$ as a first estimate.

the experimental data to the model calculations of fluorine on SL ($\omega = 5.5\,\mathrm{eV}$, $\varepsilon = -2.2\,\mathrm{eV}$, $J = 0.56\,\mathrm{eV}$, $\sigma_{\mathrm{br}} = 64\,\mathrm{meV}$) and on BL ($\omega_{\mathrm{d}} = 7.0\,\mathrm{eV}$, $\varepsilon_{\mathrm{d}} = -2.5\,\mathrm{eV}$, $\omega_{\mathrm{nd}} = 8.0\,\mathrm{eV}$, $\varepsilon_{\mathrm{nd}} = -3.0\,\mathrm{eV}$, $J = 0.47\,\mathrm{eV}$, $\sigma_{\mathrm{br}} = 20\,\mathrm{meV}$) graphene. While in the SL configuration a rescaling by a factor of 1/100 is needed to reach the order of magnitude of the experimental data, a rescaling of 1/40 is required in the BL case. A match for SL fluorinated graphene is not to be expected, since we did not recover τ_{s}^{-1} with the model (Fig. 5.10). In fluorinated BL graphene, however, we found good agreement between experiment and model for τ_{s}^{-1} (Fig. 5.9). The rescaling therefore implies that there is a source for additional momentum scattering present in the experimental sample which does not affect the spin relaxation rate.

The Penn State group analyzed three different samples of BL graphene with different fluorination degrees, ranging from $n_F = 2.2 \cdot 10^{12}\,\mathrm{cm}^{-2}$ to $n_F = 4.4 \cdot 10^{12}\,\mathrm{cm}^{-2}$ [235, 250]. Performing the same measurements on the different samples, they find that the $\tau_{\mathrm{s}}^{-1}/\tau_{\mathrm{m}}^{-1}$ ratio does not depend on n_F [235]. The source of the enhanced momentum relaxation appears to be linked directly to the source of the spin relaxation in the fluorinated BL sample.

Charge redistribution and charged impurity scattering due to fluorine

All experimental samples show a conductivity curve being almost symmetric with respect to the charge neutrality point [250]. However, we know from our DOS analysis that fluorine induces in BL graphene broad resonances away from the charge neutrality point. These resonances influence highly the momentum scattering, mak-

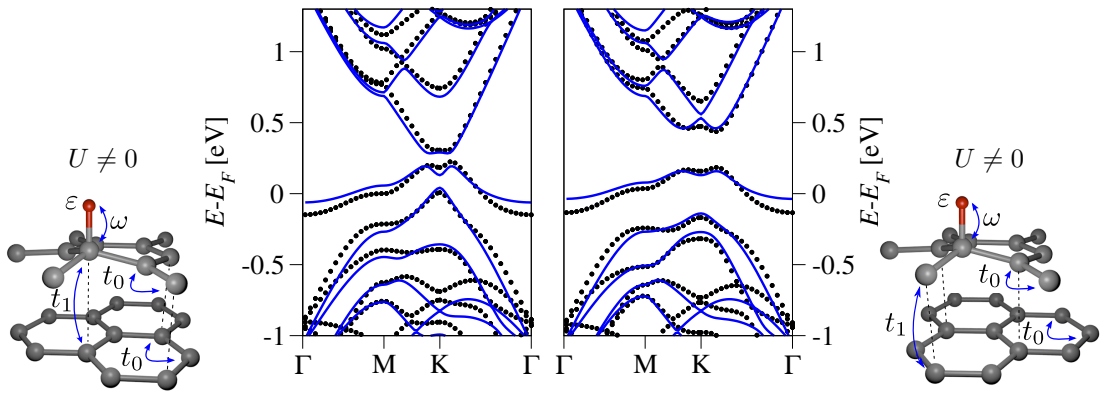

Figure 5.15: Electronic band structure of a 7×7 supercell of BL graphene with one fluorine adatom in the dimer (left) and nondimer (right) adsorption position on the top layer. Shown are both DFT (black dotted) and TB data (blue solid) with the TB parameters $\omega_\mathrm{d} = 7\,\mathrm{eV}$ and $\varepsilon_\mathrm{d} = -2.5\,\mathrm{eV}$ for the dimer configuration, and $\omega_\mathrm{nd} = 8\,\mathrm{eV}$, $\varepsilon_\mathrm{nd} = -3\,\mathrm{eV}$ for the nondimer configuration. A finite potential offset $U = 0.16\,\mathrm{eV}$ was assigned to the top layer of BL graphene in the TB calculation which opens a gap at the $\boldsymbol{K}$ point between the two bands above the Fermi energy.

ing the momentum relaxation rate rather asymmetric.

Apart the SMS scenario also charged impurities are predicted to give a symmetric contribution to the conductivity [180, 244, 267, 268]. Due to its high electronegativity, it is likely that fluorine indeed leads to charged impurity scattering in graphene. In the SL case, the DFT calculations predict a finite charge transfer from graphene to fluorine (Sec. 3.5). In BL graphene, the DFT calculations also provide hints on a charge redistribution between the bottom and top layer due to fluorine. We recall that our earlier TB model of fluorine in the dimer position of BL graphene does not reproduce the DFT gap between the two bands above the Fermi energy at the $\boldsymbol{K}$ point (Fig. 5.7). If we instead introduce, in a first approximation, an overall potential offset of $U = 0.16\,\mathrm{eV}$ for the top layer (compared to the lower one) in the TB model, a gap is opened as desired, see Fig. 5.15.

In the following, we model fluorine as a charged impurity scatterer following Refs. [244, 267, 269, 270] in the approximation of zero temperature. For simplicity, we assume a charge of $1\,e$ per fluorine adatom, neglect the finite distance (see Sec. 3.5) of fluorine to graphene, and set the relative permittivity of the fluorine environment to graphene on SiO_2 [180]. Finally, we combine the momentum relaxation rates—short range due to resonant scattering, τ_m^{-1}, and long range due to charged impurity scattering, τ_ch^{-1}—according to Matthiesen's rule: $\tau_\mathrm{m,eff}^{-1} = \tau_\mathrm{m}^{-1} + \tau_\mathrm{ch}^{-1}$. Figure 5.16 displays the resulting ratios $\tau_\mathrm{s}^{-1}/\tau_\mathrm{m,eff}^{-1}$ for both the SL and BL case. The additional contribution of charged impurity scattering to τ_m^{-1} reduces the magnitude of the ratios, though the model values are still significantly larger than the experimental ones. For the SL case, a rescaling by 1/50 is needed.

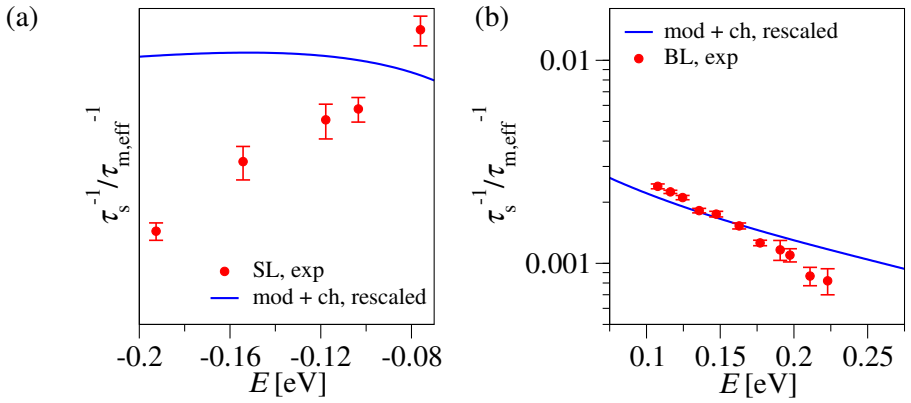

Figure 5.16: Ratio of spin to momentum relaxation rate in fluorinated (a) SL and (b) BL graphene considering fluorine as a charged impurity. Together with the experimental data (red symbols) the model calculated ratios (blue solid) are plotted. The parameters for the short range scattering contribution are the same as in Fig. 5.9 and Fig. 5.10 for the BL and SL case, respectively. The charged impurity scattering is modeled according to Refs. [244, 267]. The model ratios $\tau_s^{-1}/\tau_{m,eff}^{-1}$ are rescaled by a factor of (a) 1/50 and (b) 1/15 to obtain the experimental order of magnitude. The experimental momentum relaxation rate is extracted from the 200 K conductivity data [235], while the model considers $T = 0$ K as a first estimate.

In the BL configuration, the rescaling factor reduces to 1/15. We conclude that charged impurity scattering off fluorine cannot cure the discrepancies in the spin to momentum relaxation rate ratio between model and experiment. The origin of the discrepancies between the experimental and model data is thus still open for discussion.

5.4 Concluding remarks

In the first part of this chapter, we introduced the model of spin relaxation off local magnetic moments in BL and SL graphene. Taking into account the impurity spin, the model is derived from the T-matrix formalism for the single adatom limit. A finite value for the exchange parameter splits the orbital resonance peak in the singlet and triplet contributions which leads to two shoulders in the relaxation rate.

As an example, we took hydrogen adsorbing on BL graphene as a source for local magnetic moments. Indeed, experimental spin relaxation data [26, 166] can be matched with the model assuming a small hydrogen concentration of below 1 ppm. Comparing to the case of SL graphene, the role of energy broadening due to electron hole puddles becomes clear. Due to the different DOS of SL and BL graphene, the same fluctuation in the carrier density leads to larger fluctuation in the Fermi energy in SL graphene devices than in BL ones. The singlet-triplet

splitting in the spin relaxation rate is washed out in the SL case and the spin relaxation rate decreases with increasing charge carrier density. In BL graphene, on the contrary, the singlet and triplet resonance peaks are still well separated and the spin relaxation rate increases first at low carrier densities. However, our model based on resonant scattering off local magnetic moments predicts that at high carrier densities both SL and BL devices should exhibit qualitatively the same dependence on the charge carrier concentration.

In the second part of this chapter, we focused on fluorine and the possibility of it inducing local magnetic moments in SL and BL graphene. We chose a combined DFT/TB analysis of fluorine adsorbing on SL and BL graphene in modeling fluorinated graphene devices of the Penn State group. From a theoretical point of view, the DFT support is a clear strength of our approach. It allows us to narrow down the set of free parameters and gives us a basic understanding of the influence of fluorine on the electronic structure. However, we find that the experimental data are often at odds with our predictions for the impact of single fluorine atoms on, for example, the momentum relaxation (SL and BL device) and spin relaxation rate (SL device).

Our model calculation for the spin relaxation rate due to local magnetic moments can explain the BL spin relaxation data for reasonable parameters of exchange and adatom concentration. On the contrary, the experimental τ_s^{-1} data of the fluorinated SL device are overestimated. This is due to the large asymmetry in the spin relaxation which originates in the fluorine induced resonance level at large negative energy. The asymmetry is not confirmed from the experimental side since, on the one hand, the SL τ_s^{-1} data is extracted only in the hole doped range of charge carrier concentrations. On the other hand, the conductivity data of both the fluorinated SL and BL devices appears rather symmetric.

The second large discrepancy relies on the τ_s^{-1}/τ_m^{-1} ratio in both the SL and BL samples. Even in the BL configuration, where τ_s^{-1} is satisfyingly reproduced by our model, the momentum relaxation rate due to electrons scattering off the fluorine adatoms is by a factor of 40 smaller than the experimentally extracted value. Furthermore, τ_s^{-1}/τ_m^{-1} is independent of the fluorine concentration in the experimental devices [235]. This indicates that both the spin and momentum relaxation rates stem from the same source. Inspired by the symmetric appearance of the experimental conductivity and an observed charge transfer in the DFT calculations for fluorinated SL and BL graphene, we modeled fluorine as a charged impurity. However, even this extra contribution to momentum scattering does not resolve the τ_s^{-1}/τ_m^{-1} ratio issue.

The experimental interpretation of the data was based in Refs. [134, 250] on fluorine being a strong midgap scatterer. However, this is in deep contrast to our DFT results. Of course, there is still the possibility that the DFT calculation does not mimic the real experimental situation (or the dominant, crucial adsorbate in the devices). For example, we do not investigate or model the formation of small

fluorine clusters ($< 2\,\mathrm{nm}$ [235]) on graphene. Clusters are also predicted to give rise to a symmetric appearance of the conductivity [198, 199]. Magnetic moments stemming from fluorine would probably be quenched in the cluster configuration [137, 271], influencing both the magnitude of τ_s^{-1} and the relaxation rate ratio. Furthermore, our model assumed for simplicity that all fluorine adatoms in the device can be explained by the same exchange parameter, which is also not depending on the carrier concentration.

All in all, we conclude from the above statements that the question of fluorine induced magnetic moments in SL and BL graphene, which we addressed in the second part of this chapter, is not yet answered. Instead, further thorough theoretical and experimental investigations are needed.

6 | Summary

This chapter summarizes our theoretical investigations of orbital and spin-orbital effects in functionalized graphene presented in the preceding chapters. We laid the focus on the description of SOC in graphene, induced by proximity or local adsorbates, as well as resonant scattering off adsorbates and their role in spin relaxation in graphene in the presence of local magnetic moments.

After a short introduction in Ch. 1 to the status and prospects for graphene in the field of spintronics, Ch. 2 presented an intuitive guide for deriving effective SOC Hamiltonians from symmetry arguments. A clear strength of this approach is that only little knowledge from group theory is needed to infer the presence of different SOC hoppings from the crystal's point group symmetry. In particular, we started with pristine graphene (point group D_{6h}), which exhibits only the intrinsic SOC term, and followed the rise of the Rashba and PIA contributions to SOC upon decreasing the point group symmetry to D_{3d}, D_{3h}, C_{6v}, and C_{3v}. Using the same approach, but taking further into account the lack of translational symmetry, local adsorbates on graphene were considered. Here, the local point group symmetry is dictated by the adsorption position of the impurity. The effective Hamiltonians derived in this chapter are helpful in spin transport simulations (see for example Refs. [41, 50, 272]) or can be easily implemented in quantum transport simulation packages such as Kwant [113]. Furthermore, these Hamiltonians are useful to extract the strength of SOC hoppings directly from DFT calculations [45, 52, 75, 76].

In the following chapter, Ch. 3, we demonstrated the successful application of the local effective SOC Hamiltonians of Ch. 2 to three specific adsorbates. We considered the methyl group binding in the top position, fluorine (also in the top position), and the adatom copper. For the latter, we analyzed both the top and bridge position as the binding energies for both are very alike and differ only by few meV. Leaning on DFT calculations, we first learned about the adsorption specifics for each considered impurity. While, for example, methyl and fluorine establish a strong covalent bond with graphene, copper is only weakly bond and van der Waals interactions have to be considered in the DFT calculations. Nevertheless, we found that all three candidates lead to a strong enhancement of the SOC in graphene in the vicinity of the impurity. The SOC strengths reach values of 0.1 to 1 meV in the case of methyl, 1 to 10 meV in the case of fluorine, and even 10 to 50 meV

for copper. Compared to the value of the intrinsic SOC in pristine graphene of about 10 μeV [21], the studied adsorbates therefore enhance the SOC locally by two (methyl) to three (fluorine and copper) orders of magnitude. This naturally gives rise to the question about the origin of this enhancement. While the local sp^3 distortion [51] induced by the adsorbate can be hold accountable for the extracted SOC strengths in the case of methyl, intra-atomic SOC of the adatom itself is the dominant factor for fluorine and copper. In particular, fluorine's p orbitals and copper's p and d orbitals lead to the effective transfer of large SOC to graphene. These local SOC case studies are, on the one hand, interesting for spin Hall effect studies as for example done in the experiments on graphene functionalized by hydrogen or copper adatoms in Refs. [53, 54]. On the other hand, locally enhanced SOC also leaves traces in the spin relaxation rates of functionalized graphene [170]. However, how strong the effect will be, depends both on the magnitude of the SOC strengths (compared to other possible factors such as magnetic moments), which is mainly determined by the atomic number of an adatom, and on how effective the spins of the itinerant electrons in graphene is flipped during scattering off the impurity.

Resonant scattering off adsorbates on graphene offers a possible mechanism for an effective interaction between an itinerant electron and the impurity, and was subject of Ch. 4. Focusing on the orbital resonance characteristics, we presented a comprehensive analysis of adatoms on graphene distinct by their different adsorption position top, bridge, or hollow. Subject of the considerations were adatoms with s or p orbital character, which are described by the two orbital parameters of on-site energy and hybridization strength. We described that in the top position an adatom with small on-site energy or large hybridization strength induces a resonance level close to zero energy. Depending on the sign of the on-site energy, which indicates partial electron donation to or extraction from graphene, the resonance level appears at positive or negative energy. The larger the resonance energy the broader the resonance peaks appear in the DOS or momentum relaxation rate, and a pronounced asymmetry is observed in the relaxation rate with respect to positive and negative energies. In the bridge configuration, the impurity binds to two neighboring carbon sites in graphene and thus mediates an effective coupling between these two atoms. Due to this coupling, an increase in the hybridization strength shifts the resonance level to higher energies and, furthermore, the resonance energy is more sensitive to the variation of the orbital parameters than for the top case. The relation between partial charge transfer and appearance of the resonance at positive or negative energy observed in the top configuration does not hold. However, for both adsorption cases, the resonant state is power-law localized around the impurity. Finally, an adatom with s or p orbital character sitting in the most symmetric adsorption position, the hollow position, is effectively decoupled from graphene. Higher orbital quantum numbers have to be considered to see a notable effect of the adsorbate to the DOS or momentum relaxation rate. At the end of Ch. 4, a comparison between general top adatoms, vacancies, and the model

of a SMS impurity [2, 176, 177] was drawn. While the latter relies on a strong resonant character of the impurity, inducing a resonance level at zero energy, caution needs to be exercised when using this model to describe general adsorbates, for which the resonance lies significantly off the zero energy. Since the SMS model seems to be often applied in the experimental analysis [134, 190, 191] of graphene with adsorbates in order to, for example, extract the impurity concentration, the understanding of induced resonance levels is a relevant factor.

In Ch. 5 we finally turned to the topic of spin relaxation in BL graphene. Based on an earlier promising explanation of the magnitude of spin relaxation observed in experiments on SL graphene [62], we investigated the effect of resonant scattering off local magnetic moments in BL graphene. While the magnetic moment flips the spins of itinerant electrons, the resonant aspect of the scattering event makes it possible that already a small concentration (of the order of 1 ppm) of resonant scatterers like hydrogen induces significant spin relaxation. Furthermore, taking into account the energy broadening introduced by electron-hole puddles in the graphene sample, the model recovers the different dependence of the spin relaxation rate on the charge carrier density observed in experimental SL and BL devices [26, 27, 165]. In the second part of this chapter we focused on experiments by the group of Jun Zhu, which consider spin relaxation in fluorinated SL and BL graphene [134, 235]. By testing with the aforementioned model for spin relaxation their hypothesis that the spin relaxation rate is due to fluorine induced magnetic moments, we further wanted to resolve the theoretical debate, whether fluorine gives rise to magnetic moments or not. However, we found that while the BL graphene data can be reproduced by the model, a significant overestimation of the spin relaxation rate is observed for the SL sample. Furthermore, the ratio of spin to momentum relaxation rate from the model does not match the experimentally extracted values by one to two orders of magnitude. Extending the description of the momentum relaxation rate to the charged nature of fluorine, reduces this large discrepancy but does not resolve it. We should view this failure of the model analysis of the experimental data as an opportunity and motivation to carry out further investigations on this topic, including additional experimental tests and possible extensions of the theoretical model, for example, by allowing the exchange parameter to depend on the charge carrier density, or investigating the interplay of potential magnetic moments and SOC induced by fluorine.

7 | Bibliography

[1] K. S. Novoselov, A. K. Geim, S. V. Morozov, D. Jiang, Y. Zhang, S. V. Dubonos, I. V. Grigorieva, and A. A. Firsov. "Electric field effect in atomically thin carbon films". In: *Science* 306 (2004), p. 666.

[2] M. I. Katsnelson and K. S. Novoselov. "Graphene: New bridge between condensed matter physics and quantum electrodynamics". In: *Solid State Commun.* 143 (2007), p. 3.

[3] A. H. Castro Neto, F. Guinea, N. M. R. Peres, K. S. Novoselov, and A. K. Geim. "The electronic properties of graphene". In: *Rev. Mod. Phys.* 81 (2009), p. 109.

[4] H. Jang, Y. J. Park, X. Chen, T. Das, M.-S. Kim, and J.-H. Ahn. "Graphene-based flexible and stretchable electronics". In: *Adv. Mater.* 28 (2016), p. 4184.

[5] F. Schedin, A. K. Geim, S. V. Morozov, E. W. Hill, P. Blake, M. I. Katsnelson, and K. S. Novoselov. "Detection of individual gas molecules adsorbed on graphene". In: *Nat. Mater.* 6 (2007), p. 652.

[6] J. Duffy, J. Lawlor, C. Lewenkopf, and M. S. Ferreira. "Impurity invisibility in graphene: Symmetry guidelines for the design of efficient sensors". In: *Phys. Rev. B* 94 (2016), p. 045417.

[7] G. F. Schneider, S. W. Kowalczyk, V. E. Calado, G. Pandraud, H. W. Zandbergen, L. M. K. Vandersypen, and C. Dekker. "DNA translocation through graphene nanopores". In: *Nano Lett.* 10 (2010), p. 3163.

[8] K. S. Novoselov, A. K. Geim, S. V. Morozov, D. Jiang, M. I. Katsnelson, I. V. Grigorieva, S. V. Dubonos, and A. A. Firsov. "Two-dimensional gas of massless Dirac fermions in graphene". In: *Nature* 438 (2005), p. 197.

[9] Y. Zhang, Y.-W. Tan, H. L. Stormer, and P. Kim. "Experimental observation of the quantum Hall effect and Berry's phase in graphene". In: *Nature* 438 (2005), p. 201.

[10] E. McCann and M. Koshino. "The electronic properties of bilayer graphene". In: *Rep. Prog. Phys.* 76 (2013), p. 056503.

[11] E. McCann and V. I. Fal'ko. "Landau-level degeneracy and quantum Hall effect in a graphite bilayer". In: *Phys. Rev. Lett.* 96 (2006), p. 086805.

[12] K. S. Novoselov, E. McCann, S. V. Morozov, V. I. Fal'ko, M. I. Katsnelson, U. Zeitler, D. Jiang, F. Schedin, and A. K. Geim. "Unconventional quantum Hall effect and Berry's phase of 2π in bilayer graphene". In: *Nat. Phys.* 2 (2006), p. 177.

[13] T. Ohta, A. Bostwick, T. Seyller, K. Horn, and E. Rotenberg. "Controlling the electronic structure of bilayer graphene". In: *Science* 313 (2006), p. 951.

[14] E. V. Castro, K. S. Novoselov, S. V. Morozov, N. M. R. Peres, J. M. B. Lopes dos Santos, J. Nilsson, F. Guinea, A. K. Geim, and A. H. Castro Neto. "Biased bilayer graphene: Semiconductor with a gap tunable by the electric field effect". In: *Phys. Rev. Lett.* 99 (2007), p. 216802.

[15] Y. Cao, V. Fatemi, S. Fang, K. Watanabe, T. Taniguchi, E. Kaxiras, and P. Jarillo-Herrero. "Unconventional superconductivity in magic-angle graphene superlattices". In: *Nature* 556 (2018), p. 43.

[16] H. B. Heersche, P. Jarillo-Herrero, J. B. Oostinga, L. M. K. Vandersypen, and A. F. Morpurgo. "Bipolar supercurrent in graphene". In: *Nature* 446 (2007), p. 56.

[17] V. E. Calado, S. Goswami, G. Nanda, M. Diez, A. R. Akhmerov, K. Watanabe, T. Taniguchi, T. M. Klapwijk, and L. M. K. Vandersypen. "Ballistic Josephson junctions in edge-contacted graphene". In: *Nat. Nanotechnol.* 10 (2015), p. 761.

[18] M. B. Shalom et al. "Quantum oscillations of the critical current and high-field superconducting proximity in ballistic graphene". In: *Nat. Phys.* 12 (2016), p. 318.

[19] D. K. Efetov et al. "Specular interband Andreev reflections at van der Waals interfaces between graphene and $NbSe_2$". In: *Nat. Phys.* 12 (2016), p. 328.

[20] S. Ichinokura, K. Sugawara, A. Takayama, T. Takahashi, and S. Hasegawa. "Superconducting calcium-intercalated bilayer graphene". In: *ACS Nano* 10 (2016), p. 2761.

[21] M. Gmitra, S. Konschuh, C. Ertler, C. Ambrosch-Draxl, and J. Fabian. "Band-structure topologies of graphene: Spin-orbit coupling effects from first principles". In: *Phys. Rev. B* 80 (2009), p. 235431.

[22] L. D. Landau and E. M. Lifshitz. *Lehrbuch der theoretischen Physik: Quantenmechanik*. Berlin: Akademie Verlag Berlin, 1971.

[23] N. Tombros, C. Jozsa, M. Popinciuc, H. T. Jonkman, and B. J. van Wees. "Electronic spin transport and spin precession in single graphene layers at room temperature". In: *Nature* 448 (2007), p. 571.

[24] W. Han, K. Pi, K. M. McCreary, Y. Li, J. J. I. Wong, A. G. Swartz, and R. K. Kawakami. "Tunneling spin injection into single layer graphene". In: *Phys. Rev. Lett.* 105 (2010), p. 167202.

[25] P. J. Zomer, M. H. D. Guimarães, N. Tombros, and B. J. van Wees. "Long-distance spin transport in high-mobility graphene on hexagonal boron nitride". In: *Phys. Rev. B* 86 (2012), p. 161416.

[26] T.-Y. Yang et al. "Observation of long spin-relaxation times in bilayer graphene at room temperature". In: *Phys. Rev. Lett.* 107 (2011), p. 047206.

[27] W. Han and R. K. Kawakami. "Spin relaxation in single-layer and bilayer graphene". In: *Phys. Rev. Lett.* 107 (2011), p. 047207.

[28] B. Dlubak et al. "Highly efficient spin transport in epitaxial graphene on SiC". In: *Nat. Phys.* 8 (2012), p. 557.

[29] A. L. Friedman, O. M. J. van't Erve, C. H. Li, J. T. Robinson, and B. T. Jonker. "Homoepitaxial tunnel barriers with functionalized graphene-on-graphene for charge and spin transport". In: *Nat. Commun.* 5 (2014), p. 3161.

[30] M. Gurram, S. Omar, and B. J. van Wees. "Bias induced up to 100% spin-injection and detection polarizations in ferromagnet/bilayer-hBN/graphene-/hBN heterostructures". In: *Nat. Commun.* 8 (2017), p. 248.

[31] W. Han, R. K. Kawakami, M. Gmitra, and J. Fabian. "Graphene spintronics". In: *Nat. Nanotechnol.* 9 (2014), p. 794.

[32] C. Ertler, S. Konschuh, M. Gmitra, and J. Fabian. "Electron spin relaxation in graphene: The role of the substrate". In: *Phys. Rev. B* 80 (2009), p. 041405.

[33] M. Drögeler, C. Franzen, F. Volmer, T. Pohlmann, L. Banszerus, M. Wolter, K. Watanabe, T. Taniguchi, C. Stampfer, and B. Beschoten. "Spin lifetimes exceeding 12 ns in graphene nonlocal spin valve devices". In: *Nano Lett.* 16 (2016), p. 3533.

[34] A. G. Swartz, P. M. Odenthal, Y. Hao, R. S. Ruoff, and R. K. Kawakami. "Integration of the ferromagnetic insulator EuO onto graphene". In: *ACS Nano* 6 (2012), p. 10063.

[35] K. Zollner, M. Gmitra, T. Frank, and J. Fabian. "Theory of proximity-induced exchange coupling in graphene on hBN/(Co, Ni)". In: *Phys. Rev. B* 94 (2016), p. 155441.

[36] J. Lee and J. Fabian. "Magnetotransport signatures of the proximity exchange and spin-orbit couplings in graphene". In: *Phys. Rev. B* 94 (2016), p. 195401.

[37] J. Schliemann. "Spin Hall effect". In: *Int. J. Mod. Phys. B* 20 (2006), p. 1015.

[38] T. Völkl, T. Rockinger, M. Drienovsky, K. Watanabe, T. Taniguchi, D. Weiss, and J. Eroms. "Magnetotransport in heterostructures of transition metal dichalcogenides and graphene". In: *Phys. Rev. B* 96 (2017), p. 125405.

[39] B. Yang, M.-F. Tu, J. Kim, Y. Wu, H. Wang, J. Alicea, R. Wu, M. Bockrath, and J. Shi. "Tunable spin-orbit coupling and symmetry-protected edge states in graphene/WS_2". In: *2D Mater.* 3 (2016), p. 031012.

[40] Z. Wang, D.-K. Ki, J. Y. Khoo, D. Mauro, H. Berger, L. S. Levitov, and A. F. Morpurgo. "Origin and magnitude of 'designer' spin-orbit interaction in graphene on semiconducting transition metal dichalcogenides". In: *Phys. Rev. X* 6 (2016), p. 041020.

[41] J. H. Garcia, A. W. Cummings, and S. Roche. "Spin Hall effect and weak antilocalization in graphene/transition metal dichalcogenide heterostructures". In: *Nano Lett.* 17 (2017), p. 5078.

[42] A. Avsar et al. "Spin-orbit proximity effect in graphene". In: *Nat. Commun.* 5 (2014), p. 4875.

[43] M. Offidani, M. Milletarì, R. Raimondi, and A. Ferreira. "Optimal charge-to-spin conversion in graphene on transition-metal dichalcogenides". In: *Phys. Rev. Lett.* 119 (2017), p. 196801.

[44] T. Frank, P. Högl, M. Gmitra, D. Kochan, and J. Fabian. "Protected pseudohelical edge states in $\mathbb{Z}_2$-trivial proximitized graphene". In: *Phys. Rev. Lett.* 120 (2018), p. 156402.

[45] M. Gmitra and J. Fabian. "Graphene on transition-metal dichalcogenides: A platform for proximity spin-orbit physics and optospintronics". In: *Phys. Rev. B* 92 (2015), p. 155403.

[46] Y. K. Luo, J. Xu, T. Zhu, G. Wu, E. J. McCormick, W. Zhan, M. R. Neupane, and R. K. Kawakami. "Opto-valleytronic spin injection in monolayer MoS_2/few-layer graphene hybrid spin valves". In: *Nano Lett.* 17 (2017), p. 3877.

[47] A. Avsar, D. Unuchek, J. Liu, O. Lopez Sanchez, K. Watanabe, T. Taniguchi, B. Özyilmaz, and A. Kis. "Optospintronics in graphene via proximity coupling". In: *ACS Nano* 11 (2017), p. 11678.

[48] T. S. Ghiasi, J. Ingla-Aynés, A. A. Kaverzin, and B. J. van Wees. "Large proximity-induced spin lifetime anisotropy in transition-metal dichalcogenide/graphene heterostructures". In: *Nano Lett.* 17 (2017), p. 7528.

[49] L. A. Benítez, J. F. Sierra, W. Savero Torres, A. Arrighi, F. Bonell, M. V. Costache, and S. O. Valenzuela. "Strongly anisotropic spin relaxation in graphene-transition metal dichalcogenide heterostructures at room temperature". In: *Nat. Phys.* 14 (2018), p. 303.

[50] A. W. Cummings, J. H. Garcia, J. Fabian, and S. Roche. “Giant spin lifetime anisotropy in graphene induced by proximity effects”. In: *Phys. Rev. Lett.* 119 (2017), p. 206601.

[51] A. H. Castro Neto and F. Guinea. “Impurity-Induced Spin-Orbit Coupling in Graphene”. In: *Phys. Rev. Lett.* 103 (2009), p. 026804.

[52] M. Gmitra, D. Kochan, and J. Fabian. “Spin-orbit coupling in hydrogenated graphene”. In: *Phys. Rev. Lett.* 110 (2013), p. 246602.

[53] J. Balakrishnan, G. K. W. Koon, M. Jaiswal, A. H. Castro Neto, and B. Özyilmaz. “Colossal enhancement of spin–orbit coupling in weakly hydrogenated graphene”. In: *Nat. Phys.* 9 (2013), p. 284.

[54] J. Balakrishnan et al. “Giant spin Hall effect in graphene grown by chemical vapour deposition”. In: *Nat. Commun.* 5 (2014), p. 4748.

[55] C. Weeks, J. Hu, J. Alicea, M. Franz, and R. Wu. “Engineering a robust quantum spin Hall state in graphene via adatom deposition”. In: *Phys. Rev. X* 1 (2011), p. 021001.

[56] Y. Wang, X. Cai, J. Reutt-Robey, and M. S. Fuhrer. “Neutral-current Hall effects in disordered graphene”. In: *Phys. Rev. B* 92 (2015), p. 161411.

[57] A. A. Kaverzin and B. J. van Wees. “Electron transport nonlocality in monolayer graphene modified with hydrogen silsesquioxane polymerization”. In: *Phys. Rev. B* 91 (2015), p. 165412.

[58] D. V. Tuan, J. M. Marmolejo-Tejada, X. Waintal, B. K. Nikolić, S. O. Valenzuela, and S. Roche. “Spin Hall effect and origins of nonlocal resistance in adatom-decorated graphene”. In: *Phys. Rev. Lett.* 117 (2016), p. 176602.

[59] Z. Jia, B. Yan, J. Niu, Q. Han, R. Zhu, D. Yu, and X. Wu. “Transport study of graphene adsorbed with indium adatoms”. In: *Phys. Rev. B* 91 (2015), p. 085411.

[60] U. Chandni, E. A. Henriksen, and J. P. Eisenstein. “Transport in indium-decorated graphene”. In: *Phys. Rev. B* 91 (2015), p. 245402.

[61] F. J. dos Santos, D. A. Bahamon, R. B. Muniz, K. McKenna, E. V. Castro, J. Lischner, and A. Ferreira. “The impact of complex adatom-induced interactions on quantum spin Hall phases”. In: *arXiv:1712.07827* (2017).

[62] D. Kochan, M. Gmitra, and J. Fabian. “Spin relaxation mechanism in graphene: Resonant scattering by magnetic impurities”. In: *Phys. Rev. Lett.* 112 (2014), p. 116602.

[63] P. R. Wallace. “The band theory of graphite”. In: *Phys. Rev.* 71 (1947), p. 622.

[64] J. C. Slonczewski. "Band theory of graphite". PhD thesis. Rutgers University of New Jersey, 1955.

[65] J. W. McClure and Y. Yafet. "Theory of the g-factor of the current carriers in graphite single crystals". In: *Proceedings of the Fifth Conference on Carbon.* Pergamon, 1962, p. 22.

[66] G. Dresselhaus and M. S. Dresselhaus. "Spin-orbit interaction in graphite". In: *Phys. Rev.* 140 (1965), A401.

[67] C. L. Kane and E. J. Mele. "Quantum spin Hall effect in graphene". In: *Phys. Rev. Lett.* 95 (2005), p. 226801.

[68] D. Huertas-Hernando, F. Guinea, and A. Brataas. "Spin-orbit coupling in curved graphene, fullerenes, nanotubes, and nanotube caps". In: *Phys. Rev. B* 74 (2006), p. 155426.

[69] H. Min, J. E. Hill, N. A. Sinitsyn, B. R. Sahu, L. Kleinman, and A. H. MacDonald. "Intrinsic and Rashba spin-orbit interactions in graphene sheets". In: *Phys. Rev. B* 74 (2006), p. 165310.

[70] Y. Yao, F. Ye, X.-L. Qi, S.-C. Zhang, and Z. Fang. "Spin-orbit gap of graphene: First-principles calculations". In: *Phys. Rev. B* 75 (2007), p. 041401.

[71] S. Konschuh, M. Gmitra, and J. Fabian. "Tight-binding theory of the spin-orbit coupling in graphene". In: *Phys. Rev. B* 82 (2010), p. 245412.

[72] J. C. Boettger and S. B. Trickey. "First-principles calculation of the spin-orbit splitting in graphene". In: *Phys. Rev. B* 75 (2007), p. 121402.

[73] S. Y. Zhou, G.-H. Gweon, A. V. Fedorov, P. N. First, W. A. de Heer, D.-H. Lee, F. Guinea, A. H. Castro Neto, and A. Lanzara. "Substrate-induced bandgap opening in epitaxial graphene". In: *Nat. Mater.* 6 (2007), p. 770.

[74] Y. S. Dedkov, M. Fonin, U. Rüdiger, and C. Laubschat. "Rashba effect in the graphene/Ni(111) system". In: *Phys. Rev. Lett.* 100 (2008), p. 107602.

[75] T. Frank, M. Gmitra, and J. Fabian. "Theory of electronic and spin-orbit proximity effects in graphene on Cu(111)". In: *Phys. Rev. B* 93 (2016), p. 155142.

[76] M. Gmitra, D. Kochan, P. Högl, and J. Fabian. "Trivial and inverted Dirac bands, and emergence of quantum spin Hall states in graphene on transition-metal dichalcogenides". In: *Phys. Rev. B* 93 (2016), p. 155104.

[77] S. V. Morozov, K. S. Novoselov, M. I. Katsnelson, F. Schedin, L. A. Ponomarenko, D. Jiang, and A. K. Geim. "Strong suppression of weak localization in graphene". In: *Phys. Rev. Lett.* 97 (2006), p. 016801.

[78] M. Ishigami, J. H. Chen, W. G. Cullen, M. S. Fuhrer, and E. D. Williams. "Atomic structure of graphene on SiO_2". In: *Nano Lett.* 7 (2007), p. 1643.

[79] A. Fasolino, J. H. Los, and M. I. Katsnelson. “Intrinsic ripples in graphene”. In: *Nat. Mater.* 6 (2007), p. 858.

[80] A. Pachoud, A. Ferreira, B. Özyilmas, and A. H. Castro Neto. “Scattering theory of spin-orbit active adatoms on graphene”. In: *Phys. Rev. B* 90 (2014), p. 035444.

[81] L. Brey. “Spin-orbit coupling in graphene induced by adatoms with outer-shell p orbitals”. In: *Phys. Rev. B* 92 (2015), p. 235444.

[82] R. Saito, G. Dresselhaus, and M. S. Dresselhaus. *Physical properties of carbon nanotubes*. London: Imperial College Press, 1998.

[83] See http://www.netlib.org/lapack/.

[84] S. I. Kurganskii, O. I. Dubrovskii, and E. P. Domashevskaya. “Integration over the two-dimensional Brillouin zone”. In: *Phys. Stat. Sol. (B)* 129 (1985), p. 293.

[85] L. E. F. Foa Torres, S. Roche, and J.-C. Charlier. *Introduction to graphene-based nanomaterials*. Cambridge: Cambridge University Press, 2014.

[86] M. S. Dresselhaus, G. Dresselhaus, and A. Jorio. *Group Theory: Application to the Physics of Condensed Matter*. Berlin: Springer, 2008.

[87] J. O. Sofo, A. S. Chaudhari, and G. D. Barber. “Graphane: A two-dimensional hydrocarbon”. In: *Phys. Rev. B* 75 (2007), p. 153401.

[88] K. Takeda and K. Shiraishi. “Theoretical possibility of stage corrugation in Si and Ge analogs of graphite”. In: *Phys. Rev. B* 50 (1994), p. 14916.

[89] S. Cahangirov, M. Topsakal, E. Aktürk, H. Şahin, and S. Ciraci. “Two- and one-dimensional honeycomb structures of silicon and germanium”. In: *Phys. Rev. Lett.* 102 (2009), p. 236804.

[90] G. F. Koster, J. O. Dimmock, R. G. Wheeler, and H. Statz. *Properties of the thirty-two point groups*. Cambridge, Massachusetts: MIT Press, 1963.

[91] J. Zhou, Q. Wang, Q. Sun, X. S. Chen, Y. Kawazoe, and P. Jena. “Ferromagnetism in semihydrogenated graphene sheet”. In: *Nano Lett.* 9 (2009), p. 3867.

[92] S. Konschuh, M. Gmitra, D. Kochan, and J. Fabian. “Theory of spin-orbit coupling in bilayer graphene”. In: *Phys. Rev. B* 85 (2012), p. 115423.

[93] C.-C. Liu, H. Jiang, and Y. Yao. “Low-energy effective Hamiltonian involving spin-orbit coupling in silicene and two-dimensional germanium and tin”. In: *Phys. Rev. B* 84 (2011), p. 195430.

[94] Y. A. Bychkov and E. I. Rashba. “Properties of a 2D electron gas with lifted spectral degeneracy”. In: *Pis’ma Zh. Eksp. Teor. Fiz.* 39 (1983), p. 66.

[95] C. L. Kane and E. J. Mele. "Z_2 topological order and the quantum spin Hall effect". In: *Phys. Rev. Lett.* 95 (2005), p. 146802.

[96] Z. Wang, D.-K. Ki, H. Chen, H. Berger, A. H. MacDonald, and A. F. Morpurgo. "Strong interface-induced spin-orbit interaction in graphene on WS2". In: *Nat. Commun.* 6 (2015), p. 8339.

[97] J. P. Robinson, H. Schomerus, L. Oroszlány, and V. I. Fal'ko. "Adsorbate-limited conductivity of graphene". In: *Phys. Rev. Lett.* 101 (2008), p. 196803.

[98] T. O. Wehling, S. Yuan, A. I. Lichtenstein, A. K. Geim, and M. I. Katsnelson. "Resonant scattering by realistic impurities in graphene". In: *Phys. Rev. Lett.* 105 (2010), p. 056802.

[99] K. Zollner, T. Frank, S. Irmer, M. Gmitra, D. Kochan, and J. Fabian. "Spin-orbit coupling in methyl functionalized graphene". In: *Phys. Rev. B* 93 (2016), p. 045423.

[100] S. Irmer, T. Frank, S. Putz, M. Gmitra, D. Kochan, and J. Fabian. "Spin-orbit coupling in fluorinated graphene". In: *Phys. Rev. B* 91 (2015), p. 115141.

[101] T. Frank, S. Irmer, M. Gmitra, D. Kochan, and J. Fabian. "Copper adatoms on graphene: Theory of orbital and spin-orbital effects". In: *Phys. Rev. B* 95 (2017), p. 035402.

[102] K. T. Chan, J. B. Neaton, and M. L. Cohen. "First-principles study of metal adatom adsorption on graphene". In: *Phys. Rev. B* 77 (2008), p. 235430.

[103] Y. Mao, J. Yuan, and J. Zhong. "Density functional calculation of transition metal adatom adsorption on graphene". In: *J. Phys. Condens. Matter* 20 (2008), p. 115209.

[104] O. Leenaerts, B. Partoens, and F. M. Peeters. "Adsorption of H_2O, NH_3, CO, NO_2, and NO on graphene: A first-principles study". In: *Phys. Rev. B* 77 (2008), p. 125416.

[105] D. W. Boukhvalov, M. I. Katsnelson, and A. I. Lichtenstein. "Hydrogen on graphene: Electronic structure, total energy, structural distortions and magnetism from first-principles calculations". In: *Phys. Rev. B* 77 (2008), p. 035427.

[106] M. Wu, E.-Z. Liu, and J. Z. Jiang. "Magnetic behavior of graphene absorbed with N, O, and F atoms: A first-principles study". In: *Appl. Phys. Lett.* 93 (2008), p. 082504.

[107] H. Şahin, M. Topsakal, and S. Ciraci. "Structures of fluorinated graphene and their signatures". In: *Phys. Rev. B* 83 (2011), p. 115432.

[108] M. Wu, E.-Z. Liu, M. Y. Ge, and J. Z. Jiang. "Stability, electronic, and magnetic behaviors of Cu adsorbed graphene: A first-principles study". In: *Appl. Phys. Lett.* 94 (2009), p. 102505.

[109] M. Amft, S. Lebègue, O. Eriksson, and N. V. Skorodumova. "Adsorption of Cu, Ag, and Au atoms on graphene including van der Waals interactions." In: *J. Phys. Condens. Matter* 23 (2011), p. 395001.

[110] T. O. Wehling, M. I. Katsnelson, and A. I. Lichtenstein. "Impurities on graphene: Midgap states and migration barriers". In: *Phys. Rev. B* 80 (2009), p. 085428.

[111] R. M. Guzmán-Arellano, A. D. Hernández-Nieves, C. A. Balseiro, and G. Usaj. "Gate-induced enhancement of spin-orbit coupling in dilute fluorinated graphene". In: *Phys. Rev. B* 91 (2015), p. 195408.

[112] P. O. Löwdin. "A note on the quantum-mechanical perturbation theory". In: *J. Chem. Phys.* 19 (1951), p. 1396.

[113] C. W. Groth, M. Wimmer, A. R. Akhmerov, and X. Waintal. "Kwant: a software package for quantum transport". In: *New J. Phys.* 16 (2014), p. 063065.

[114] T. O. Wehling, B. Grundkötter-Stock, B. Aradi, T. Frauenheim, and T. Niehaus. "Charge-doping-induced phase transitions in hydrogenated and fluorinated graphene". In: *Phys. Rev. B* 90 (2014), p. 085422.

[115] K. M. McCreary, A. G. Swartz, W. Han, J. Fabian, and R. K. Kawakami. "Magnetic moment formation in graphene detected by scattering of pure spin currents". In: *Phys. Rev. Lett.* 109 (2012), p. 186604.

[116] C. S. Praveen, S. Piccinin, and S. Fabris. "Adsorption of alkali adatoms on graphene supported by the Au/Ni(111) surface". In: *Phys. Rev. B* 92 (2015), p. 075403.

[117] A. Khademi, E. Sajadi, P. Dosanjh, D. A. Bonn, J. A. Folk, A. Stöhr, U. Starke, and S. Forti. "Alkali doping of graphene: The crucial role of high-temperature annealing". In: *Phys. Rev. B* 94 (2016), p. 201405.

[118] Y. Ferro, N. Fernandez, A. Allouche, and C. Linsmeier. "Adsorption of beryllium atoms and clusters both on graphene and in a bilayer of graphite investigated by DFT". In: *J. Phys. Condens. Matter* 25 (2013), p. 015002.

[119] A. G. Swartz, J.-R. Chen, K. M. McCreary, P. M. Odenthal, W. Han, and R. K. Kawakami. "Effect of *in situ* deposition of Mg adatoms on spin relaxation in graphene". In: *Phys. Rev. B* 87 (2013), p. 075455.

[120] A. Londono-Hurtado, D. Morgan, and I. Szlufarska. "First-principles study of Cs and Sr sorption on carbon structures". In: *J. Appl. Phys.* 111 (2012), p. 094912.

[121] A. L. Kozub, A. B. Shick, F. Máca, J. Kolorenč, and A. I. Lichtenstein. "Electronic structure and magnetism of samarium and neodymium adatoms on free-standing graphene". In: *Phys. Rev. B* 94 (2016), p. 125113.

[122] H. Zhang, C. Lazo, S. Blügel, S. Heinze, and Y. Mokrousov. "Electrically tunable quantum anomalous Hall effect in graphene decorated by 5*d* transition-metal adatoms". In: *Phys. Rev. Lett.* 108 (2012), p. 056802.

[123] J. A. Elias and E. A. Henriksen. "Electronic transport and scattering times in tungsten-decorated graphene". In: *Phys. Rev. B* 95 (2017), p. 075405.

[124] V. S. Anithaa, R. Shankar, and S. Vijayakumar. "Adsorption of Mn atom on pristine and defected graphene: a density functional theory study". In: *J. Mol. Model* 23 (2017), p. 132.

[125] C. Cao, M. Wu, J. Jiang, and H.-P. Cheng. "Transition metal adatom and dimer adsorbed on graphene: Induced magnetization and electronic structures". In: *Phys. Rev. B* 81 (2010), p. 205424.

[126] J. Hu, J. Alicea, R. Wu, and M. Franz. "Giant topological insulator gap in graphene with 5*d* adatoms". In: *Phys. Rev. Lett.* 109 (2012), p. 266801.

[127] V. W. Brar et al. "Gate-controlled ionization and screening of cobalt adatoms on a graphene surface". In: *Nat. Phys.* 7 (2011), p. 43.

[128] P. Hota, A. J. Akhtar, S. Bhattacharya, M. Miah, and S. K. Saha. "Ferromagnetism in graphene due to charge transfer from atomic Co to graphene". In: *Appl. Phys. Lett.* 111 (2017), p. 042402.

[129] W. X. Wang, S. H. Liang, T. Yu, D. H. Li, Y. B. Li, and X. F. Han. "The study of interaction between graphene and metals by Raman spectroscopy". In: *J. Appl. Phys.* 109 (2011), p. 07C501.

[130] Y. Wang, S. Xiao, X. Cai, W. Bao, J. Reutt-Robey, and M. S. Fuhrer. "Electronic transport properties of Ir-decorated graphene". In: *Sci. Rep.* 5 (2015), p. 15764.

[131] D. Ma, Z. Li, and Z. Yang. "Strong spin-orbit splitting in graphene with adsorbed Au atoms". In: *Carbon* 50 (2012), p. 297.

[132] R. Varns and P. Strange. "Stability of gold atoms and dimers adsorbed on graphene". In: *J. Phys. Condens. Matter* 20 (2008), p. 225005.

[133] D. V. Fedorov, M. Gradhand, S. Ostanin, I. V. Maznichenko, A. Ernst, J. Fabian, and I. Mertig. "Impact of electron-impurity scattering on the spin relaxation time in graphene: A first-principles study". In: *Phys. Rev. Lett.* 110 (2013), p. 156602.

[134] X. Hong, K. Zou, B. Wang, S.-H. Cheng, and J. Zhu. "Evidence for spin-flip scattering and local moments in dilute fluorinated graphene". In: *Phys. Rev. Lett.* 108 (2012), p. 226602.

[135] H. Şahin and S. Ciraci. "Chlorine adsorption on graphene: chlorographene". In: *J. Phys. Chem. C.* 116 (2012), p. 24075.

[136] M. F. Craciun, I. Khrapach, M. D. Barnes, and S. Russo. "Properties and applications of chemically functionalized graphene". In: *J. Phys. Condens. Matter* 25 (2013), p. 423201.

[137] R. R. Nair, M. Sepioni, I.-L. Tsai, O. Lehtinen, J. Keinonen, A. V. Krasheninnikov, T. Thomson, A. K. Geim, and I. V. Grigorieva. "Spin-half paramagnetism in graphene induced by point defects". In: *Nat. Phys.* 8 (2012), p. 199.

[138] G. R. Berdiyorov, M. V. Milošević, F. M. Peeters, and C. T. van Duin. "Stability of CH_3 molecules trapped on hydrogenated sites of graphene". In: *Phys. B Condens. Matter* 455 (2014), p. 60.

[139] T. O. Wehling, H. P. Dahal, A. I. Lichtenstein, M. I. Katsnelson, H. C. Manoharan, and A. V. Balatsky. "Theory of Fano resonances in graphene: The influence of orbital and structural symmetries on STM spectra". In: *Phys. Rev. B* 81 (2010), p. 085413.

[140] B. Uchoa, L. Yang, S.-W. Tsai, N. M. R. Peres, and A. H. Castro Neto. "Theory of scanning tunneling spectroscopy of magnetic adatoms in graphene". In: *Phys. Rev. Lett.* 103 (2009), p. 206804.

[141] K. Saha, I. Paul, and K. Sengupta. "Unconventional scanning tunneling conductance spectra for graphene". In: *Phys. Rev. B* 81 (2010), p. 165446.

[142] K. F. Kelly, E. T. Mickelson, R. H. Hauge, J. L. Margrave, and N. J. Halas. "Nanoscale imaging of chemical interactions: Fluorine on graphite". In: *Proc. Natl. Acad. Sci. U.S.A.* 97 (2000), p. 10318.

[143] A. C. Ferrari. "Raman spectroscopy of graphene and graphite: Disorder, electron-phonon coupling, doping and nonadiabatic effects". In: *Solid State Commun.* 143 (2007), p. 47.

[144] A. Eckmann, A. Felten, A. Mishchenko, L. Britnell, R. Krupke, K. S. Novoselov, and C. Casiraghi. "Probing the nature of defects in graphene by Raman spectroscopy". In: *Nano Lett.* 12 (2012), p. 3925.

[145] J. Moser, A. Verdaguer, D. Jiménez, A. Barreiro, and A. Bachtold. "The environment of graphene probed by electrostatic force microscopy". In: *Appl. Phys. Lett.* 92 (2008), p. 123507.

[146] W. Zhao et al. "Low-energy transmission electron diffraction and imaging of large-area graphene". In: *Sci. Adv.* 3 (2017), e1603231.

[147] D. Halbertal et al. "Imaging resonant dissipation from individual atomic defects in graphene". In: *Science* 358 (2017), p. 1303.

[148] E. J. G. Santos, A. Ayuela, and D. Sánchez-Portal. "Universal magnetic properties of sp^3-type defects in covalently functionalized graphene". In: *New J. Phys.* 14 (2012), p. 043022.

[149] J. O. Sofo, G. Usaj, P. S. Cornaglia, A. M. Suarez, A. D. Hernández-Nieves, and C. A. Balseiro. "Magnetic structure of hydrogen-induced defects on graphene". In: *Phys. Rev. B* 85 (2012), p. 115405.

[150] L. Pauling. *The nature of the chemical bond*. Ithaka, NY: Cornell University Press, 1972.

[151] W. H. Press, S. A. Teukolsky, W. T. Vetterling, and B. P. Flannery. *Numerical Recipes in Fortran 77: The Art of Scientific Computing*. Cambridge: Cambridge University Press, 1992.

[152] S. Bae et al. "Roll-to-roll production of 30-inch graphene films for transparent electrodes". In: *Nat. Nanotechnol.* 5 (2010), p. 574.

[153] L. Huai, W. Qingwei, and L. Lixin. "An improvement on the formula for group electronegativity". In: *J. Chem. Educ.* 69 (1992), p. 783.

[154] L. C. Allen. "Electronegativity is the average one-electron energy of the valence-shell electrons in ground-state free atoms". In: *J. Am. Chem. Soc.* 111 (1989), p. 9003.

[155] D. O'Hagan. "Understanding organofluorine chemistry. An introduction to the C-F bond". In: *Chem. Soc. Rev.* 37 (2008), p. 308.

[156] O. Leenaerts, H. Peelaers, A. D. Hernández-Nieves, B. Partoens, and F. M. Peeters. "First-principles investigation of graphene fluoride and graphane". In: *Phys. Rev. B* 82 (2010), p. 195436.

[157] H.-J. Kim and J.-H. Cho. "Fluorine-induced local magnetic moment in graphene: A hybrid DFT study". In: *Phys. Rev. B* 87 (2013), p. 174435.

[158] P. Mori-Sánchez, A. J. Cohen, and W. Yang. "Localization and delocalization errors in density functional theory and implications for band-gap prediction". In: *Phys. Rev. Lett.* 100 (2008), p. 146401.

[159] S. Casolo, E. Flage-Larsen, O. M. Løvvik, G. R. Darling, and G. F. Tantardini. "Role of the self-interaction error in studying chemisorption on graphene from first-principles". In: *Phys. Rev. B* 81 (2010), p. 205412.

[160] X. Hong, S.-H. Cheng, C. Herding, and J. Zhu. "Colossal negative magnetoresistance in dilute fluorinated graphene". In: *Phys. Rev. B* 83 (2011), p. 085410.

[161] H. Y. Liu, Z. F. Hou, C. H. Hu, Y. Yang, and Z. Z. Zhu. "Electronic and magnetic properties of fluorinated graphene with different coverage of fluorine". In: *J. Phys. Chem. C* 116 (2012), p. 18193.

[162] R. F. W. Bader. *Atoms in Molecules: A Quantum Theory*. Oxford: Oxford University Press, 1990.

[163] J. Sugar and A. Musgrove. “Energy levels of copper, Cu I through Cu XXIX”. In: *J. Phys. Chem. Ref. Data* 19 (1990), p. 527.

[164] V. I. Anisimov, J. Zaanen, and O. K. Andersen. “Band theory and Mott insulators: Hubbard U instead of Stoner I”. In: *Phys. Rev. B* 44 (1991), p. 943.

[165] M. Wojtaszek, I. J. Vera-Marun, T. Maassen, and B. J. van Wees. “Enhancement of spin relaxation time in hydrogenated graphene spin-valve devices”. In: *Phys. Rev. B* 87 (2013), p. 081402.

[166] D. Kochan, S. Irmer, M. Gmitra, and J. Fabian. “Resonant scattering by magnetic impurities as a model for spin relaxation in bilayer graphene”. In: *Phys. Rev. Lett.* 115 (2015), p. 196601.

[167] B. Raes, J. E. Scheerder, M. V. Costache, F. Bonell, J. F. Sierra, J. Cuppens, J. Van de Vondel, and S. O. Valenzuela. “Determination of the spin-lifetime anisotropy in graphene using oblique spin precession”. In: *Nat. Commun.* 7 (2016), p. 11444.

[168] S. Omar, M. H. D. Guimarães, A. Kaverzin, B. J. van Wees, and I. J. Vera-Marun. “Spin relaxation 1/f noise in graphene”. In: *Phys. Rev. B* 95 (2017), p. 081403.

[169] M. B. Lundeberg, R. Yang, J. Renard, and J. A. Folk. “Defect-mediated spin relaxation and dephasing in graphene”. In: *Phys. Rev. Lett.* 110 (2013), p. 156601.

[170] J. Bundesmann, D. Kochan, F. Tkatschenko, J. Fabian, and K. Richter. “Theory of spin-orbit induced spin relaxation in functionalized graphene”. In: *Phys. Rev. B* 92 (2015), p. 081403.

[171] A. C. Hewson. *The Kondo Problem to Heavy Fermions*. Cambridge: Cambridge University Press, 1997.

[172] G. D. Mahan. *Many-particle physics*. New York: Kluwer, 2000.

[173] V. M. Pereira, F. Guinea, J. M. B. Lopes dos Santos, N. M. R. Peres, and A. H. Castro Neto. “Disorder induced localized states in graphene”. In: *Phys. Rev. Lett.* 96 (2006), p. 036801.

[174] V. M. Pereira, J. M. B. Lopes dos Santos, and A. H. Castro Neto. “Modeling disorder in graphene”. In: *Phys. Rev. B* 77 (2008), p. 115109.

[175] S.-Z. Liang and J. O. Sofo. “Impurity state and variable range hopping conduction in graphene”. In: *Phys. Rev. Lett.* 109 (2012), p. 256601.

[176] T. Stauber, N. M. R. Peres, and F. Guinea. “Electronic transport in graphene: A semiclassical approach including midgap states”. In: *Phys. Rev. B* 76 (2007), p. 205423.

[177] A. Ferreira, J. Viana-Gomes, J. Nilsson, E. R. Mucciolo, N. M. R. Peres, and A. H. Castro Neto. "Unified description of the dc conductivity of monolayer and bilayer graphene at finite densities based on resonant scatterers". In: *Phys. Rev. B* 83 (2011), p. 165402.

[178] M. Monteverde, C. Ojeda-Aristizabal, R. Weil, K. Bennaceur, M. Ferrier, S. Guéron, C. Glattli, H. Bouchiat, J. N. Fuchs, and D. L. Maslov. "Transport and elastic scattering times as probes of the nature of impurity scattering in single-layer and bilayer graphene". In: *Phys. Rev. Lett.* 104 (2010), p. 126801.

[179] M. Trushin and J. Schliemann. "Conductivity of graphene: How to distinguish between samples with short- and long-range scatterers". In: *EPL* 83 (2008), p. 17001.

[180] S. Adam, E. H. Hwang, V. M. Galitski, and S. Das Sarma. "A self-consistent theory for graphene transport". In: *Proc. Natl. Acad. Sci. USA* 104 (2007), p. 18392.

[181] B. R. K. Nanda, M. Sherafati, Z. S. Popović, and S. Satpathy. "Electronic structure of the substitutional vacancy in graphene: density-functional and Green's function studies". In: *New J. Phys.* 14 (2012), p. 083004.

[182] D. M. Basko. "Resonant low-energy scattering on short-range impurities in graphene". In: *Phys. Rev. B* 78 (2008), p. 115432.

[183] T. O. Wehling, A. V. Balatsky, M. I. Katsnelson, A. I. Lichtenstein, K. Scharnberg, and R. Wiesendanger. "Local electronic signatures of impurity states in graphene". In: *Phys. Rev. B* 75 (2007), p. 125425.

[184] Y. V. Skrypnyk and V. M. Loktev. "Impurity effects in a two-dimensional system with the Dirac spectrum". In: *Phys. Rev. B* 73 (2006), p. 241402.

[185] S. Ihnatsenka and G. Kirczenow. "Dirac point resonances due to adatoms and molecules adsorbed on graphene and transport gaps and conductance quantization in graphene nanoribbons with covalently bonded adsorbates". In: *Phys. Rev. B* 83 (2011), p. 245442.

[186] M. Farjam, D. Haberer, and A. Grüneis. "Effect of hydrogen adsorption on the quasiparticle spectra of graphene". In: *Phys. Rev. B* 83 (2011), p. 193411.

[187] D. A. Ruiz-Tijerina and L. G.G. V. Dias da Silva. "Symmetry-protected coherent transport for diluted vacancies and adatoms in graphene". In: *Phys. Rev. B* 94 (2016), p. 085425.

[188] B. Uchoa, L. Yang, S.-W. Tsai, N. M. R. Peres, and A. H. Castro Neto. "Orbital symmetry fingerprints for magnetic adatoms in graphene". In: *New J. Phys.* 16 (2014), p. 013045.

[189] N. M. R. Peres, F. Guinea, and A. H. Castro Neto. "Electronic properties of disordered two-dimensional carbon". In: *Phys. Rev. B* 73 (2006), p. 125411.

[190] J.-H. Chen, W. G. Cullen, C. Jang, M. S. Fuhrer, and E. D. Williams. "Defect scattering in graphene". In: *Phys. Rev. Lett.* 102 (2009), p. 236805.

[191] Z. H. Ni et al. "On resonant scatterers as a factor limiting carrier mobility in graphene". In: *Nano Lett.* 10 (2010), p. 3868.

[192] Y. V. Skrypnyk and V. M. Loktev. "Electrical conductivity in graphene with point defects". In: *Phys. Rev. B* 82 (2010), p. 085436.

[193] F. Ducastelle. "Electronic structure of vacancy resonant states in graphene: A critical review of the single-vacancy case". In: *Phys. Rev. B* 88 (2013), p. 075413.

[194] Z. F. Wang, R. Xiang, Q. W. Shi, J. Yang, X. Wang, J. G. Hou, and J. Chen. "Modeling STM images in graphene using the effective-mass approximation". In: *Phys. Rev. B* 74 (2006), p. 125417.

[195] Á. Bácsi and A. Virosztek. "Local density of states and Friedel oscillations in graphene". In: *Phys. Rev. B* 82 (2010), p. 193405.

[196] D. Kochan, M. Gmitra, and J. Fabian. "Resonant scattering off magnetic impurities in graphene: Mechanism for ultrafast spin relaxation". In: *Symmetry, Spin Dynamics and the Properties of Nanostructures*. World Scientific, 2015. Chap. 7, p. 136.

[197] S. Das Sarma, S. Adam, E. H. Hwang, and E. Rossi. "Electronic transport in two-dimensional graphene". In: *Rev. Mod. Phys.* 83 (2011), p. 407.

[198] K. M. McCreary, K. Pi, A. G. Swartz, W. Han, W. Bao, C. N. Lau, F. Guinea, M. I. Katsnelson, and R. K. Kawakami. "Effect of cluster formation on graphene mobility". In: *Phys. Rev. B* 81 (2010), p. 115453.

[199] M. I. Katsnelson, F. Guinea, and A. K. Geim. "Scattering of electrons in graphene by clusters of impurities". In: *Phys. Rev. B* 79 (2009), p. 195426.

[200] K. Tahara, T. Iwasaki, S. Furuyama, A. Matsutani, and M. Hatano. "Asymmetric transport property of fluorinated graphene". In: *Appl. Phys. Lett.* 103 (2013), p. 143106.

[201] B. Uchoa, T. G. Rappoport, and A. H. Castro Neto. "Kondo quantum criticality of magnetic adatoms in graphene". In: *Phys. Rev. Lett.* 106 (2011), p. 016801.

[202] D. A. Ruiz-Tijerina and L. G.G. V. Dias da Silva. "Transport signatures of Kondo physics and quantum criticality in graphene with magnetic impurities". In: *Phys. Rev. B* 95 (2017), p. 115408.

[203] A. A. El-Barbary, R. H. Telling, C. P. Ewels, M. I. Heggie, and P. R. Briddon. "Structure and energetics of the vacancy in graphite". In: *Phys. Rev. B* 68 (2003), p. 144107.

[204] H. Amara, S. Latil, V. Meunier, P. Lambin, and J.-C. Charlier. "Scanning tunneling microscopy fingerprints of point defects in graphene: A theoretical prediction". In: *Phys. Rev. B* 76 (2007), p. 115423.

[205] M. Wojtaszek, I. J. Vera-Marun, E. Whiteway, M. Hilke, and B. J. van Wees. "Absence of hyperfine effects in ^{13}C-graphene spin-valve devices". In: *Phys. Rev. B* 89 (2014), p. 035417.

[206] D. Huertas-Hernando, F. Guinea, and A. Brataas. "Spin-orbit-mediated spin relaxation in graphene". In: *Phys. Rev. Lett.* 103 (2009), p. 146801.

[207] J. Fabian, A. Matos-Abiague, C. Ertler, P. Stano, and I. Žutić. "Semiconductor Spintronics". In: *Acta Phys. Slovaca* 57 (2007), p. 565.

[208] A. Avsar et al. "Toward wafer scale fabrication of graphene based spin valve devices". In: *Nano Lett.* 11 (2011), p. 2363.

[209] F. Volmer, M. Drögeler, E. Maynicke, N. von den Driesch, M. L. Boschen, G. Güntherodt, and B. Beschoten. "Role of MgO barriers for spin and charge transport in Co/MgO/graphene nonlocal spin-valve devices". In: *Phys. Rev. B* 88 (2013), p. 161405.

[210] T. Maassen, F. K. Dejene, M. H. D. Guimarães, C. Józsa, and B. J. van Wees. "Comparison between charge and spin transport in few-layer graphene". In: *Phys. Rev. B* 83 (2011), p. 115410.

[211] J. Martin, N. Akerman, G. Ulbricht, T. Lohmann, J. H. Smet, K. von Klitzing, and A. Yacoby. "Observation of electron-hole puddles in graphene using a scanning single-electron transistor". In: *Nat. Phys.* 4 (2008), p. 144.

[212] D. V. Tuan, F. Ortmann, A. W. Cummings, D. Soriano, and S. Roche. "Spin dynamics and relaxation in graphene dictated by electron-hole puddles". In: *Sci. Rep.* 6 (2016), p. 21046.

[213] M. H. D. Guimarães, A. Veligura, P. J. Zomer, T. Maassen, I. J. Vera-Marun, N. Tombros, and B. J. van Wees. "Spin transport in high-quality suspended graphene devices". In: *Nano Lett.* 12 (2012), p. 3512.

[214] W. Han, J.-R. Chen, D. Wang, K. M. McCreary, H. Wen, A. G. Swartz, J. Shi, and R. K. Kawakami. "Spin relaxation in single-layer graphene with tunable mobility". In: *Nano Lett.* 12 (2012), p. 3443.

[215] G. Stecklein, P. A. Crowell, J. Li, Y. Anugrah, Q. Su, and S. J. Koester. "Contact-induced spin relaxation in graphene nonlocal spin valves". In: *Phys. Rev. Appl.* 6 (2016), p. 054015.

[216] H. Idzuchi, A. Fert, and Y. Otani. "Revisiting the measurement of the spin relaxation time in graphene-based devices". In: *Phys. Rev. B* 91 (2015), p. 241407.

[217] D. Huertas-Hernando, F. Guinea, and A. Brataas. “Spin relaxation times in disordered graphene”. In: *Eur. Phys. J. Spec. Top.* 148 (2007), p. 177.

[218] D. V. Tuan, F. Ortmann, D. Soriano, S. O. Valenzuela, and S. Roche. “Pseudospin-driven spin relaxation mechanism in graphene”. In: *Nat. Phys.* 10 (2014), p. 857.

[219] M. M. Ugeda, I. Brihuega, F. Guinea, and J. M. Gómez-Rodríguez. “Missing atom as a source of carbon magnetism”. In: *Phys. Rev. Lett.* 104 (2010), p. 096804.

[220] H. González-Herrero, J. M. Gómez-Rodríguez, P. Mallet, M. Moaied, J. J. Palacios, C. Salgado, M. M. Ugeda, J.-Y. Veuillen, F. Yndurain, and I. Brihuega. “Atomic-scale control of graphene magnetism by using hydrogen atoms”. In: *Science* 352 (2016), p. 437.

[221] E. J. Duplock, M. Scheffler, and P. J. D. Lindan. “Hallmark of perfect graphene”. In: *Phys. Rev. Lett.* 92 (2004), p. 225502.

[222] O. Yazyev. “Emergence of magnetism in graphene materials and nanostructures”. In: *Rep. Prog. Phys* 73 (2010), p. 056501.

[223] Y.-W. Son, M. L. Cohen, and S. G. Louie. “Half-metallic graphene nanoribbons”. In: *Nature* 444 (2006), p. 347.

[224] B. Birkner, D. Pachniowski, A. Sandner, M. Ostler, T. Seyller, J. Fabian, M. Ciorga, D. Weiss, and J. Eroms. “Annealing-induced magnetic moments detected by spin precession measurements in epitaxial graphene on SiC”. In: *Phys. Rev. B* 87 (2013), p. 081405.

[225] J. Červenka, M. I. Katsnelson, and C. F. J. Flipse. “Room-temperature ferromagnetism in graphite driven by two-dimensional networks of point defects”. In: *Nat. Phys.* 5 (2009), p. 840.

[226] E. McCann, K. Kechedzhi, V. I. Fal’ko, H. Suzuura, T. Ando, and B. L. Altshuler. “Weak-localization magnetoresistance and valley symmetry in graphene”. In: *Phys. Rev. Lett.* 97 (2006), p. 146805.

[227] K. Kechedzhi, V. I. Fal’ko, E. McCann, and B. L. Altshuler. “Influence of trigonal warping on interference effects in bilayer graphene”. In: *Phys. Rev. Lett.* 98 (2007), p. 176806.

[228] F. Pierre, A. B. Gougam, A. Anthore, H. Pothier, D. Esteve, and N. O. Birge. “Dephasing of electrons in mesoscopic metal wires”. In: *Phys. Rev. B* 68 (2003), p. 085413.

[229] A. A. Kozikov, D. W. Horsell, E. McCann, and V. I. Fal’ko. “Evidence for spin memory in the electron phase coherence in graphene”. In: *Phys. Rev. B* 86 (2012), p. 045436.

[230] D.-K. Ki, D. Jeong, J.-H. Choi, and H. Lee. "Inelastic scattering in a monolayer graphene sheet: a weak-localization study". In: *Phys. Rev. B* 78 (2008), p. 125409.

[231] S. Ringer, S. Hartl, M. Rosenauer, T. Völkl, M. Kadur, F. Hopperdietzel, D. Weiss, and J. Eroms. "Measuring anisotropic spin relaxation in graphene". In: *arXiv:1711.06472* (2017).

[232] A. Deshpande, W. Bao, Z. Zhao, C. N. Lau, and B. J. LeRoy. "Imaging charge density fluctuations in graphene using Coulomb blockade spectroscopy". In: *Phys. Rev. B* 83 (2011), p. 155409.

[233] K. Zou and J. Zhu. "Transport in gapped bilayer graphene: The role of potential fluctuations". In: *Phys. Rev. B* 82 (2010), p. 081407.

[234] A. Avsar, I. J. Vera-Marun, J. Y. Tan, G. K. W. Koon, K. Watanabe, T. Taniguchi, S. Adam, and B. Özyilmaz. "Electronic spin transport in dual-gated bilayer graphene". In: *NPG Asia Mater.* 8 (2016), e274.

[235] Private communication with Jun Zhu.

[236] L. G. Johnson and G. Dresselhaus. "Optical properties of graphite". In: *Phys. Rev. B* 7 (1973), p. 2275.

[237] A. Grüneis, C. Attaccalite, L. Wirtz, H. Shiozawa, R. Saito, T. Pichler, and A. Rubio. "Tight-binding description of the quasiparticle dispersion of graphite and few-layer graphene". In: *Phys. Rev. B* 78 (2008), p. 205425.

[238] M. Moaied, J. V. Alvarez, and J. J. Palacios. "Hydrogenation-induced ferromagnetism on graphite surfaces". In: *Phys. Rev. B* 90 (2014), p. 115441.

[239] E. V. Castro, M. P. López-Sancho, and M. A. H. Vozmediano. "New type of vacancy-induced localized states in multilayer graphene". In: *Phys. Rev. Lett.* 104 (2010), p. 036802.

[240] Q. Li, E. H. Hwang, and S. Das Sarma. "Disorder-induced temperature-dependent transport in graphene: Puddles, impurities, activation, and diffusion". In: *Phys. Rev. B* 84 (2011), p. 115442.

[241] N. M. R. Peres. "Colloquium: The transport properties of graphene: An introduction". In: *Rev. Mod. Phys.* 82 (2010), p. 2673.

[242] E. Rossi, S. Adam, and S. Das Sarma. "Effective medium theory for disordered two-dimensional graphene". In: *Phys. Rev. B* 79 (2009), p. 245423.

[243] E.-A. Kim and A. H. Castro Neto. "Graphene as an electronic membrane". In: *EPL* 84 (2008), p. 57007.

[244] E. H. Hwang, S. Adam, and S. Das Sarma. "Carrier transport in two-dimensional graphene layers". In: *Phys. Rev. Lett.* 98 (2007), p. 186806.

[245] M. I. Katsnelson, K. S. Novoselov, and A. K. Geim. "Chiral tunnelling and the Klein paradox in graphene". In: *Nat. Phys.* 2 (2006), p. 620.

[246] A. Deshpande, W. Bao, F. Miao, C. N. Lau, and B. J. LeRoy. "Spatially resolved spectroscopy of monolayer graphene on SiO_2". In: *Phys. Rev. B* 79 (2009), p. 205411.

[247] Y. Zhang, V. W. Brar, C. Girit, A. Zettl, and M. F. Crommie. "Origin of spatial charge inhomogeneity in graphene". In: *Nat. Phys.* 5 (2009), p. 722.

[248] A. E. Curtin, M. S. Fuhrer, J. L. Tedesco, R. L. Myers-Ward, C. R. J. Eddy Jr., and D. K. Gaskill. "Kelvin probe microscopy and electronic transport in graphene on SiC(0001) in the minimum conductivity regime". In: *Appl. Phys. Lett.* 98 (2011), p. 243111.

[249] G. M. Rutter, S. Jung, N. N. Klimov, D. B. Newell, N. B. Zhitenev, and J. A. Stroscio. "Microscopic polarization in bilayer graphene". In: *Nat. Phys.* 7 (2011), p. 649.

[250] A. A. Stabile, A. Ferreira, J. Li, N. M. R. Peres, and J. Zhu. "Electrically tunable resonant scattering in fluorinated bilayer graphene". In: *Phys. Rev. B* 92 (2015), p. 121411.

[251] K. Shoda, H. Kohno, Y. Kobayashi, D. Takagi, and S. Takeda. "Feasibility study for sidewall fluorination of SWCNTs in CF_4 plasma". In: *J. Appl. Phys.* 104 (2008), p. 113529.

[252] M. Lucchese, F. Stavale, E. H. Martins Ferreira, C. Vilani, M. V. O. Moutinho, R. B. Capaz, C. A. Achete, and A. Jorio. "Quantifying ion-induced defects and Raman relaxation length in graphene". In: *Carbon* 48 (2010), p. 1592.

[253] L. G. Cançado, A. Jorio, E. H. Martins Ferreira, F. Stavale, C. A. Achete, R. B. Capaz, M. V. O. Moutinho, A. Lombardo, T. S. Kulmala, and A. C. Ferrari. "Quantifying defects in graphene via Raman spectroscopy at different excitation energies". In: *Nano Lett.* 11 (2011), p. 3190.

[254] G. Bergmann. "Weak localization in thin films: a time-of-flight experiment with conduction electrons". In: *Phys. Rep.* 107 (1984), p. 1.

[255] B. Kramer and A. MacKinnon. "Localization: theory and experiment". In: *Rep. Prog. Phys.* 56 (1993), p. 1469.

[256] E. McCann. "Staying or going? Chirality decides!" In: *Physics* 2 (2009), p. 98.

[257] P. W. Anderson. "Absence of diffusion in certain random lattices". In: *Phys. Rev.* 109 (1958), p. 1492.

[258] M. Hilke, M. Massicotte, E. Whiteway, and V. Yu. "Weak localization in graphene: theory, simulations, and experiments". In: *Sci. World J.* 2014 (2014), p. 737296.

[259] H. Suzuura and T. Ando. "Crossover from symplectic to orthogonal class in a two-dimensional honeycomb lattice". In: *Phys. Rev. Lett.* 89 (2002), p. 266603.

[260] T. Ando, T. Nakanishi, and R. Saito. "Berry's phase and absence of back scattering in carbon nanotubes". In: *J. Phys. Soc. Jpn.* 67 (1998), p. 2857.

[261] E. McCann and V. I. Fal'ko. "$z \to -z$ symmetry of spin-orbit coupling and weak localization in graphene". In: *Phys. Rev. Lett.* 108 (2012), p. 166606.

[262] V. I. Fal'ko, K. Kechedzhi, E. McCann, B. L. Altshuler, H. Suzuura, and T. Ando. "Weak localization in graphene". In: *Solid State Commun.* 143 (2007), p. 33.

[263] A. F. Morpurgo and F. Guinea. "Intervalley scattering, long-range disorder, and effective time-reversal symmetry breaking in graphene". In: *Phys. Rev. Lett.* 97 (2006), p. 196804.

[264] F. V. Tikhonenko, D. W. Horsell, R. V. Gorbachev, and A. K. Savchenko. "Weak localization in graphene flakes". In: *Phys. Rev. Lett.* 100 (2008), p. 056802.

[265] F. V. Tikhonenko, A. A. Kozikov, A. K. Savchenko, and R. V. Gorbachev. "Transition between electron localization and antilocalization in graphene". In: *Phys. Rev. Lett.* 103 (2009), p. 226801.

[266] R. V. Gorbachev, F. V. Tikhonenko, A. S. Mayorov, D. W. Horsell, and A. K. Savchenko. "Weak localization in bilayer graphene". In: *Phys. Rev. Lett.* 98 (2007), p. 176805.

[267] S. Das Sarma, E. H. Hwang, and E. Rossi. "Theory of carrier transport in bilayer graphene". In: *Phys. Rev. B* 81 (2010), p. 161407.

[268] S. Xiao, J.-H. Chen, S. Adam, E. D. Williams, and M. S. Fuhrer. "Charged impurity scattering in bilayer graphene". In: *Phys. Rev. B* 82 (2010), p. 041406.

[269] E. H. Hwang and S. Das Sarma. "Single-particle relaxation time versus transport scattering time in a two-dimensional graphene layer". In: *Phys. Rev. B* 77 (2008), p. 195412.

[270] S. Das Sarma, S. Adam, E. H. Hwang, and E. Rossi. "Electronic transport in two-dimensional graphene". In: *Rev. Mod. Phys.* 83 (2011), p. 407.

[271] J. Wilhelm, M. Walz, and F. Evers. "*Ab initio* spin-flip conductance of hydrogenated graphene nanoribbons: Spin-orbit interaction and scattering with local impurity spins". In: *Phys. Rev. B* 92 (2015), p. 014405.

[272] K. Song, D. Soriano, A. W. Cummings, R. Robles, P. Ordejón, and S. Roche. "Spin proximity effects in graphene/topological insulator heterostructures". In: *Nano Lett.* 18 (2018), p. 2033.

Acknowledgments

This work would not have been possible without my professor Dr. Jaroslav Fabian, whom I would like to thank at this point for his committed mentoring and expertise. His office door was always open for discussions, advice, and encouragement.

I also want to thank all present and former members of our group for close collaboration, critical questions, motivation, or the casual chat on the corridor. Regarding this manuscript, I am grateful to Phillipp Reck for proofreading the second chapter at an early stage.

Last but not least, I want to mention the support and encouragement of my family, friends and dear one (and a half), which has been and will always be essential for me.